TECHNISCHE
UNIVERSITÄT
WIEN

DISSERTATION

Plasmonics for Mid-infrared Photonic Integrated Circuits

A thesis submitted for the degree of
Doctor of Technical Sciences (Dr. Techn.)

at
Technische Universität Wien

Faculty of Electrical Engineering and Information Technology
Institute of Solid State Electronics

under supervision of
Univ. Prof. Dr. Gottfried Strasser
&
Dr. Borislav Hinkov

defended by

Mauro David, M.Sc.
Mat. Nr. 51833273

Vienna, August 2023

Reviewers: Prof. Dr. Adrian Hierro
Institute for Optoelectronic Systems and Microtechnology,
Universidad Politécnica de Madrid, Spain

Ao. Univ. Prof. Dr. Alois Lugstein
Institute of Solid State Electronics, TU Wien, Austria

" Someone is sitting in the shade today because someone planted a tree a long time ago "
WARREN BUFFET

Abstract

The field of photonics has transformed global communication and data processing, changing how we connect and interact in the digital age. Photonic integrated circuits (PICs) further revolutionized the field, enabling compact and cost-efficient sensors and optical systems. While visible and near-infrared photonics have been extensively explored, mid-infrared (mid-IR) photonics has only recently emerged as a rapidly growing area of interest due to its unique potential for various groundbreaking applications.

The mid-IR spectral region offers sensitive and selective detection of important molecules for many applications in environmental monitoring, medical diagnostics, and security screening. It simultaneously enables optical free-space communication in atmospheric transparency windows. However, the development of mid-IR PICs remains untapped due to the lack of suitable materials and strategies for efficient monolithic integration, which can be considered the best solution to overcome costly and time-consuming sub-micrometer alignment procedures and additionally increase the overall robustness of the system. Plasmonics offers a promising solution to this problem, by guiding and manipulating light with metallic-like structures coupled with dielectric ridges. Dielectric-loaded surface plasmon polariton waveguides (DLSPPWs) have been proposed as a promising platform for mid-IR PICs, but challenges remain in terms of materials and their fabrication.

The primary focus of this work is to address the challenges in mid-IR integrated photonics and pave the way for the next generation of fully integrated, miniaturized mid-IR PICs through the use of DLSPPWs. In this thesis, two distinct materials, germanium (Ge) and polyethylene (PE), were investigated in combination with gold layers to analyze their potential for mid-IR sensing and on-chip mode guiding. The research demonstrated that PE, a transparent and low refractive index polymer, is a promising choice for dielectric loading, especially in the long-wave infrared (LWIR) range. PE's efficient trade-off between propagation length and mode confinement results in high performance at wavelengths above 9 µm, comparable to traditional materials like PMMA (at telecom wavelengths) or SiN_x (between 3-7 µm). Additionally, Ge slabs provide a high refractive index alternative, enabling low-loss (<0.015 dB/µm) broadband (5.6-11.2 µm) propagation with high tunability, making them highly suitable for sensing applications. The integration of Pd with Ge further enhances compatibility with CMOS technology, facilitating large-scale production and integration of DLSPPWs-based photonic devices. Furthermore, this work explores the potential of DLSPPWs for mid-IR sensors by functionalizing the Ge-based waveguide sensors. By leveraging the combination of low-loss Ge waveguides with on-chip integrated micro-mirrors, a compact, monolithic integrated LWIR heterodyne detector is realized, with room temperature operation. Overall, this dissertation lays the foundation for the development of highly integrated, monolithic mid-IR PICs for communication and sensing applications, in combination with quantum cascade intersubband devices.

Keywords: mid-infrared optoelectronics, quantum cascade devices, plasmonics, photonic integration, photonic integrated circuits, polymers

Kurzfassung

Die Photonik hat die globale Kommunikation und die Datenverarbeitung transformiert und dabei geändert, wie wir im digitalen Zeitalter miteinander interagieren. Photonisch integrierte Schaltungen (PICs) haben das Feld weiter revolutioniert, und ermöglichen kompakte kostengünstige Sensoren und optische Systeme. Während die Photonik im sichtbaren und nahen Infrarot Spektralbereich bereits ausgiebig untersucht wurde, ist der mid-infrarot (mid-IR) Bereich ein noch recht junges Feld, das schnell an Interesse wächst, auf Grund seines einzigartigen Potentials für verschiedenste bahnbrechende Applikationen.

Der mid-IR Spektralbereich erlaubt die sensitive und selektive Detektion wichtiger Moleküle für verschiedenste Anwendungen in der Umwelt-Sensorik, medizinischen Diagnostik und Sicherheits-Überwachung. Gleichzeitig ermöglicht er die optische Datenübertragung in den spektralen Wasser-Transparenz-Fenstern der Atmosphäre. Jedoch wird die Entwicklung neuer mid-IR PICs durch fehlende, passende Materialien und Strategien für effiziente monolithische Integration stark behindert. Diese können als beste Lösung angesehen werden, um teure und zeitaufwendige sub-Mikrometer genaue Alienier-Prozeduren zu vermeiden und zusätzlich um die Robustheit des gesamten Systems zu erhöhen. Die Plasmonik bietet hier eine vielversprechende Lösung für dieses Problem, indem Licht in metallischen und metall-ähnlichen Strukturen, die mit dielektrischen Rippenwellenleitern gekoppelt werden, geführt und manipuliert werden kann. Dielektrisch-geladene Oberflächen-Plasmon-Polariton Wellenleiter (DLSPPWs) wurden als erfolgversprechende Plattform für mid-IR PICs vorgeschlagen, jedoch verbleiben noch weitere Herausforderungen bezüglich des Materials und Ihrer Herstellung.

Der Hauptfokus der vorliegenden Arbeit liegt eben darin, diese Herausforderungen in der mid-IR integrierten Photonik aufzunehmen, und den Weg für die nächste Generation voll-integrierter, miniaturisierter mid-IR PICs durch Verwendung der DLSPPWs zu ebnen. In dieser Thesis werden die zwei Materialien Germanium (Ge) und Polyethylene (PE) in Kombination mit Gold-Schichten untersucht, zusammen mit ihrem Potential für die mid-IR Sensorik und on-chip Lichtleitung. Die Ergebnisse demonstrieren, dass PE, ein transparentes Polymer mit geringem Brechungsindex, eine vielversprechende Wahl für das Konzept des dielektrischen ladens ist, besonders im langwelligen IR-Bereich (LWIR). Polyethylens effizienter trade-off zwischen Propagationslänge und Moden-Beschränkung resultiert in hoher Performance bei 9 µm Wellenlänge, vergleichbar mit traditionellen Materialien wie PMMA im Telekom-Wellenlängen-Bereich oder SiN zwischen 3 µm und 7 µm Wellenlänge. Zusätzlich bieten

Ge-Rippen-Strukturen eine weitere hoch-Index Alternative, für breitbandige (5.6 µm – 11.2 µm) Licht-Leitungsstrukturen mit geringen Verlusten (<0.015 dB/µm) und großer Durchstimmbarkeit, was ein weiterer Vorteil für Anwendungen in der Sensorik ist. Die Integration von Palladium (Pd) mit Ge verbessert weiter die CMOS-Kompatibilität, was die Produktion großer Stückzahlen und die weitere Integration der DLSPPW-basierten photonischen Strukturen erlaubt. Darüber hinaus, untersucht diese Arbeit das Potential der DLSPPWs für mid-IR Sensoren mit funktionalisierten Ge-basierten Wellenleiter-Sensoren. Durch Ausnutzung der Kombination von Ge Wellenleitern mit niedrigen Verlusten mit on-chip integrierten mikro-Spiegeln, wird ein kompakter, monolithisch-integrierter LWIR heterodyner Detektor realisiert, der bei Raumtemperatur operabel ist.

In Summe legt diese Dissertation die Grundlage für die Entwicklung hoch-integrierter, monolithischer mid-IR PICs für die Kommunikation und Sensor-Anwendungen, in Kombination mit Quanten Kaskaden Intersubband Bauteilen.

Schlagworte: mid-infrared optoelectronics, quantum cascade devices, plasmonics, photonic integration, photonic integrated circuits, polymers

Acknowledgments

Embarking on this PhD journey has been one of the most challenging, yet rewarding experiences of my life. Its success would not have been possible without the immense support, help, encouragement, and guidance of numerous individuals. I am deeply grateful to each of them and here I would like to extend my heartfelt appreciation.

First and foremost, I want to express my profound gratitude to Gottfried Strasser, for offering me the opportunity to undertake this PhD in the first place. His help, wisdom, and contagious humor have been a guiding light during this process. I am extremely grateful to Borislav Hinkov, who has been a pillar of strength during my research journey. His enormous support throughout my PhD, his availability, and his unyielding optimism and humor made even the toughest days bearable. Thank you, Borislav, for being such a great reserch fellow, for the incredible opportunities you gave me, for the effort in aligning the research needs and my interests, and for your always encouraging words.

I want to extend my gratitude to several professors, without whom this work would not have been possible. In particular, Bernhard Lendl played a pivotal role in many of my projects. Spending three months in his laboratories was not only profoundly educational but also memorable, thanks to his wonderful sense of humor and his spirited group. Secondly, I would like to thank Ulrich Schmid, that allowed me to bring the polyethylene project to fruition in his labs. I am deeply grateful to Walter M. Weber for facilitating the success of the projects through our collaborations. I am thankful to Benedikt Schwarz for his helpful input and for consistently bringing forward intelligent suggestions. I want to thank Aaron Maxwell Andrews for always eagerly sharing his knowledge, engaging in helpful discussions, and the fun times we had playing disc golf. A big thank you also to Erich Gornik for insightful discussions and feedback. Lastly, I want to thank Alois Lugstein and Adrian Hierro for reviewing this thesis.

I owe a huge debt of gratitude to Masiar Sistani, for sharing his expertise and support, and precious help in the clean room, especially in the early days of my PhD. I would also like to thank Daniele Nazzari. His assistance with the passivation experiments was crucial, and I'm grateful for the friendship we have developed. I extend my gratitude to Hermann Detz, for his assistance with the ellipsometry measurements and for the fun times in Brno, and to Hanh T. Hoang for her help in the initial stages of the polyethylene project.

In research, there are often uncelebrated heroes working behind the scenes, making significant technical contributions. I would like to thank Werner Schrenk whose vast knowledge never ceases to amaze me. I have learned so much from our discussions. Along with Markus Schinnerl and Anton Tsenov, Werner has kept our clean room in top condition, playing a decisive role in the success of most of the projects presented in this thesis. Andreas Linzer also deserves special thanks for his skills in developing customized mechanical parts, which are essential for the lab.

Next, I thank the entire QCL group for their mutual support, fruitful discussions, and the friendly atmosphere they created. These interactions have led to friendships that I hope will extend beyond graduation. I want to express my sincere gratitude to my friend Elena Arigliani for being with me from the beginning to the end of my academic education. Her support has meant a lot to me, both in my personal and professional life. We worked closely over the last two years, which helped us achieve more in our scientific work while improving the working environment. I'll always remember with affection our "pizza meetings" and the time we spent in California. A heartfelt thank you to Anna Lardschneider for her significant contributions during the fabrication of the polyethylene waveguides and for sharing both the challenges and laughter along the way. I want to thank Georg Marschick for his valuable work in the cleanroom and relaxed spirit, which has helped build the foundation for great teamwork and enjoyable moments. I'm grateful to Florian Pilat, with whom I've talked about many things throughout the entire time during the PhD, whether they were relevant or not. I appreciate his constant support and our amazing music jam sessions. I want to express my thanks to Stefania Isceri for openly sharing both the positive and challenging aspects of the research journey, and for also becoming a friend in the process. I want to thank Nikola Opačak for the enjoyable conversations and the pleasant times we've spent working out together. I want to thank Sandro Dal Cin for his precious assistance in the lab and for the funny moments. I'd like to express my gratitude to Rolf Szedlak for being so supporting, honest, and direct. His openness has truly enhanced our deep discussions. His adventurous mindset has encouraged me to discover new possibilities and think differently. I'm grateful to Mikołaj Piotrowski for always brightening my days and sharing his expertise, which has brought both humor and valuable advices along the way. I'm thankful to Andreas Windischhofer for sharing enjoyable moments and engaging discussions. I want to thank Johannes Hillbrand for making me laugh, and helping me at the beginning of the PhD. I'm thankful to Hedwig Knoeting for encouraging me to join the team and for our pleasant chats. My sincere thanks goes also to Miriam Giparakis, for her help and assistance during these last years we worked together. I want to thank I. Cem Doganlar for his genuine friendship. Finally, I want to thank Dominik Koukola, Xaver Gsodam, and Niklas Brandacher for the nice times we've had together, both in and outside the labs.

I want to thank some other people who played a significant role in the success of my research. Without their contributions, achieving these results would have been extremely challenging, if not impossible. A special thanks go to my friend Alicja Dabrowska, for sharing her contagious enthusiasm for science since our master's studies. I will always be grateful for her initial help in the optical lab. I also thank Dominik Wacht for his solid and quick support. His valuable feedback has enriched my research, and I'm grateful for the friendship that has developed between us. Thanks to everyone in the CAVS team. I really enjoyed my time in the chemistry department, where they made me feel at home, even during the challenging COVID times. In particular, Davide Pinto and Giovanna Ricchiuti, for the countless funny moments we shared and for becoming good friends. Lastly, I cannot forget Davide Disnan. His extensive knowledge of polymers has been a great asset to my research. More importantly, I cherish the genuine and committed friendship he offered, especially during tough times.

Finally, my heartfelt gratitude goes to my family. Their sacrifices, patience, and love have paved the way for this achievement. To my dear sister, Anna David, your constant belief in me fueled my determination. Our discussions and your patience in listening to my ideas were invaluable.

In the mosaic that is this journey, some tiles gleam brightly, while others have fractured. To those shadows that brought light in times of darkness and the anchors that held steady among life's tempests: thank you. Though names may fade, the essence remains, deeply etched. To memories that scaffolded my path, and the unsung muses, I owe my gratitude.

TABLE OF CONTENTS

List of abbreviations

Abbreviation	Full description
AFM	Atomic Force Microscopy
ALD	Atomic Layer Deposition
AR	Anti-Reflection
ATR	Attenuated Total Reflection
BSA	Bovine Serum Albumin
CMOS	Complementary Metal-Oxide-Semiconductor
CVD	Chemical Vapor Deposition
CW	Continuous Wave
DFB	Distributed Feedback
DI	Deionized
DLSPPW	Dielectric-Loaded Surface Plasmon Polariton Waveguide
EC	External Cavity
FEM	Finite Element Method
FIB	Focused Ion Beam
FOM	Figure of Merit
FSO	Free-Space Optical
FTIR	Fourier Transform Infrared Spectroscopy
HDPE	High-Density Polyethylene
HSPPW	Hybrid Surface Plasmon Polariton Waveguide
IBAD	Ion Beam-Assisted Deposition
ICL	Interband Cascade Laser
IMI	Insulator-Metal-Insulator
IR	Infrared
ITO	Indium Tin Oxide
LDPE	Low-Density Polyethylene
LLDPE	Linear Low-Density Polyethylene
LOC	Lab-on-a-Chip
LP	Propagation Length
LRSP	Long-Range Surface Plasmon
LSP	Localized Surface Plasmon
LWIR	Long-Wave Infrared
MBE	Molecular Beam Epitaxy
MCT	Mercury Cadmium Telluride
MEMS	Microelectromechanical System

MFD	Mode Field Diameter
MI	Metal-Insulator
MIM	Metal-Insulator-Metal
MOCVD	Metal-Organic Chemical Vapor Deposition
MOSFET	Metal-Oxide-Semiconductor Field-Effect Transistor
MZI	Mach-Zehnder Interferometer
near-IR	Near-Infrared
PE	Polyethylene
PECVD	Plasma-Enhanced Chemical Vapor Deposition
PIC	Photonic Integrated Circuit
PMMA	Polymethyl Methacrylate
PVD	Physical Vapor Deposition
QC	Quantum Cascade
QCD	Quantum Cascade Detector
QCL	Quantum Cascade Laser
QCLD	Quantum Cascade Laser & Detector
QW	Quantum Well
RF	Radio Frequency
RI	Refractive Index
RIE	Reactive Ion Etching
RMS	Root Mean Square
RPM	Rounds Per Minute
SEM	Scanning Electron Microscopy
SERS	Surface-Enhanced Raman Scattering
SLSPP	Semiconductor-Loaded Surface Plasmon Polariton
SOI	Silicon-On-Insulator
SPP	Surface Plasmon Polariton
SPR	Surface Plasmon Resonance
TCO	Transparent Conducting Oxide
TM	Transverse Magnetic
UV	Ultraviolet
VIS	Visible
VLDPE	Very Low-Density Polyethylene

1
INTRODUCTION

This dissertation focuses on the design, fabrication, and characterization of surface plasmon polariton (SPP) waveguides for mid-infrared (mid-IR) applications. Specifically, the research addresses the need for mid-IR integrated optical interconnects for monolithic photonic integrated circuits (PICs). The aims and objectives are to design and fabricate dielectric-loaded SPP waveguides (DLSPPWs) for the mid-IR spectral band, with a particular focus on the critical long-wave infrared (LWIR) band. These waveguides will be optimized for on-chip liquid spectroscopy applications and integrated with active photonic devices to realize versatile PICs. The dissertation is organized into nine chapters that cover the different aspects of the design and realization of the plasmonic waveguides based on the use of two dielectric loads, polyethylene (PE) and germanium (Ge), implemented on a gold (Au) platform, and discusses their implications for the field of mid-IR photonics.

1.1 Background and Motivation

The field of photonics has revolutionized our world, enabling high-speed, low-loss communication and data processing. The recent development of PICs has further reshaped the field by combining multiple photonic components on a single chip and resulting in optical systems that are affordable, compact, and more robust. The reduced device size, and consequent reduced power consumption, opened new opportunities across multiple fields, significantly impacting our daily lives. As a result, photonics has become an essential technology for a wide range of applications such as telecommunication, data centers, biomedical devices, and many others. While visible (VIS) and near-IR (near-IR) photonics have been extensively studied and have reached a significant level of advancement, including the commercialization of PICs [1], the field of mid-IR photonics has emerged as a rapidly growing area of interest only in recent years. Despite being in the early stages of development, mid-IR photonics has the potential to provide unique and complementary advantages that can make it superior in certain applications and fields. In fact, the mid-IR spectral region (2-20 µm) offers several advantages over near-IR and VIS photonics. Firstly, in the mid-IR, the fundamental absorptions of many important molecules are located, including those found in environmental pollutants [2], biological tissues [3,4], and explosives [5,6] (see Figure 1.1). This means that mid-IR sensing can provide sensitive and selective detection of these molecules, leading to a range of potential applications in environmental monitoring [7], non-invasive medical diagnostics [8,9], and security screening [10].

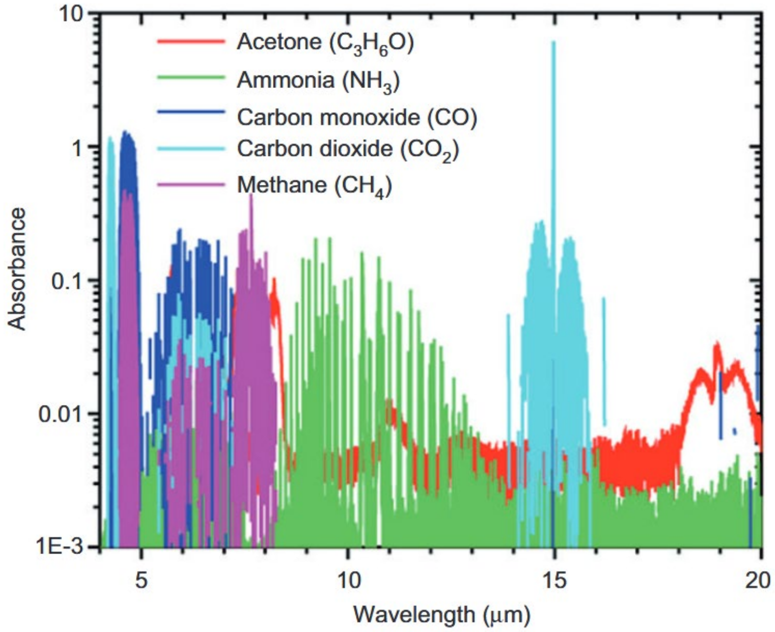

Figure 1.1 The absorbance spectra in the mid-IR range for five specific molecules relevant to medical, environmental, and industrial sensing applications. Image taken from [11]. The data was sourced from the EPA spectral database [12].

Secondly, the mid-IR region is less affected by scattering from molecules and particles in the atmosphere compared to the near-IR and VIS regions, enabling the use of mid-IR radiation for remote sensing applications, such as monitoring the Earth's atmosphere and surfaces [13–15], as well as offering optical free-space communication links in the "atmospheric windows" of low water vapor absorptions [16,17] (Figure 1.2).

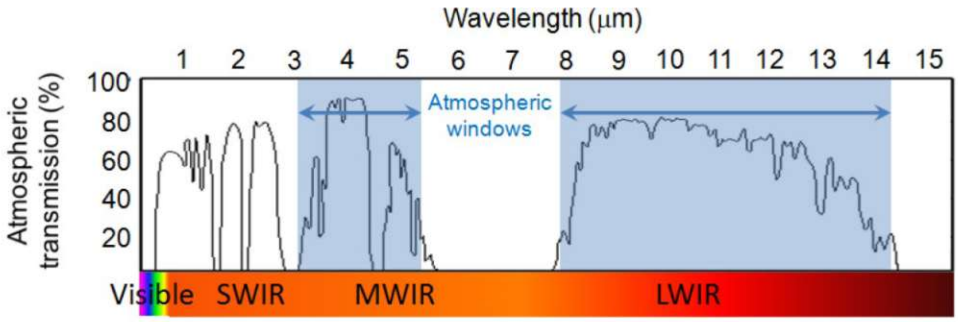

Figure 1.2 The atmospheric transmission spectrum reveals the presence of two distinct mid-IR windows, one spanning the wavelength range of 3-5 μm and another ranging from 8-14 μm. Image taken from [18].

However, the progress of mid-IR systems has been hindered by the absence of a suitable materials infrastructure that matches its technological significance. In comparison to their near-IR/VIS counterparts, basic optical and optoelectronic components for the mid-IR are either significantly more expensive or not readily available. To bridge this gap, considerable research efforts have been dedicated to the development of mid-IR detectors, sources, and optoelectronic devices over the past few decades [11]. Probably, the most ground-breaking result that has played a significant role in driving a renovated enthusiasm for mid-IR research is the development of the first quantum cascade laser (QCL) nearly 30 years ago [19]. The QCL is a semiconductor laser source that utilizes transitions between quantized states in complex multi-period quantum well (QW) heterostructures within the conduction band (i.e., intersubband transitions) to generate light (Figure 1.3).

QCLs offer a compact and powerful coherent source for a wide range of mid-IR applications. With their high power and wavelength flexibility, QCLs have become commercially available, providing optical systems developers and researchers with a valuable tool to explore novel phenomena, study materials and structures, and develop advanced sensing and countermeasure systems in the mid-IR spectrum [11]. The specific emission wavelength of a QCL depends on the design and composition of the active region and can be tailored to target specific wavelengths, covering a wide range of the IR, from 2.63 [20] to 250 μm [21].

Similarly to QCLs, Interband Cascade Lasers (ICLs) [22–24] are also emerging as a promising technology for the mid-IR. ICLs utilize an interband cascade design that allows for efficient multi-stage electron transitions, generating coherent light in a modest portion of the mid-IR region (3-6 μm [25]) with lower power consumption than QCLs.

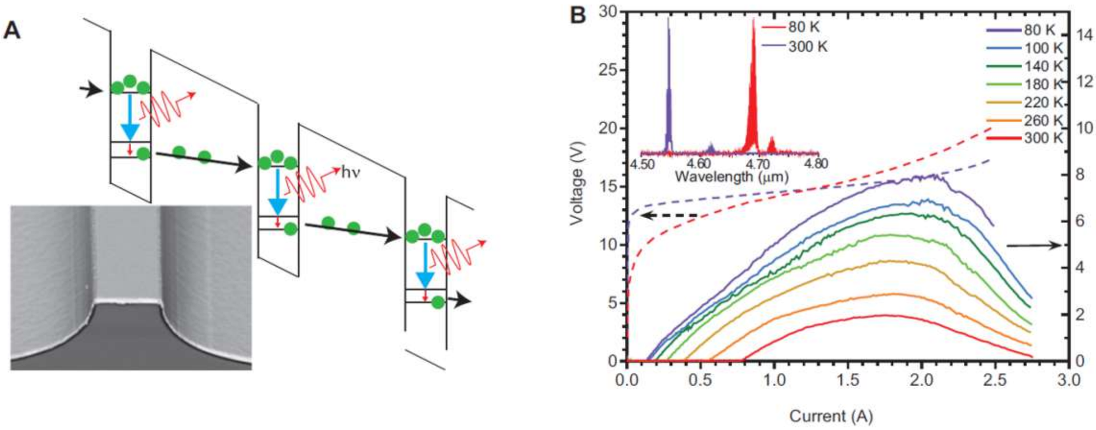

Figure 1.3 (a) Electron transport (black arrows) and optical transitions (red arrows) in a QCL, with an inset displaying the front facet of a typical fabricated QCL. (b) The light output and applied bias are plotted as a function of current (I) and temperature (T) for a specific QCL emitting at a wavelength of approximately 4.6 μm, as shown in the inset of Figure 1. Additionally, the inset presents the emission spectra of the QCL at 80 K (red) and 300 K (purple). Image taken from [11].

However, despite all the advancements, the development of mid-IR PICs is still limited because implementing existing integrated photonics solutions remains a challenging task [26]. The main reason is the lack of materials that enable efficient integration of passive waveguides with active components [27]. These challenges include the requirement for compatible materials [28], and advanced fabrication schemes, particularly for developing LWIR passive optical interconnects, that are currently lacking as final elements for fully integrated functional devices. This is true, for example, for dielectric waveguides based on Ge [29,30], Si [31,32], halides [33], chalcogenides [34], or heavy metal oxides [35]. Recent work made significant progress by integrating InGaAs/InP passive dielectric waveguides with InP-based mid-IR QCLs [36,37]. However, this integration method requires complex post-regrowth schemes that can potentially decrease fabrication yield [38] and substantially increase device costs.

The field of plasmonics may offer a solution to this problem. Plasmonics is an interdisciplinary area of research that explores the interaction of light with metallic structures. A particular solution of the Maxwell equations for electromagnetic fields interacting with metallic/dielectric surfaces leads to the so-called SPPs [39]. SPPs are the collective oscillations of free electrons between a metallic and a dielectric interface that can be used to guide and manipulate light at sub-wavelength scales. By engineering the geometry and materials, it is possible to create waveguides that guide SPPs along a desired path. The inherent support of only TM modes in conventional plasmonic waveguides and the TM emission characteristics of QCLs present an interesting alignment that makes them an ideal combination for mid-IR PICs.

SPP waveguides offer several advantages over traditional dielectric waveguides, including the possibility of easily integrating them with other photonic components [40–43]. However, unlike VIS and near-IR plasmonics, noble metals in the mid-IR have a much larger negative permittivity. This results in weakly-bound surface waves that penetrate deep into the dielectric medium. Several approaches have been proposed to address this issue. One proposed solution is the spoof plasmon polaritons, which consist of patterning a metal surface with resonant grooves to modify the propagation properties so that electromagnetic waves are strongly bound to the interface [44]. Alternatively, surface phonon polaritons [45] in polar dielectrics or graphene and 2D materials can serve as alternative materials for mid-IR plasmonics, offering strong confinement and electrostatic tunability. Highly doped semiconductors can also be designed to be used as metals, enabling a wide control of plasma frequency via manipulation of the carrier density [46]. Another approach to increase the confinement of mid-IR plasmons is through dielectric loading, which involves applying a dielectric ridge on top of an unpatterned metal surface to increase the effective mode index and support well-confined mid-IR plasmon waves on noble metals [47]. In fact, recent studies have utilized plasmonic waveguides based on silicon nitride (Si_3N_4, SiNx)/Au architecture based on DLSPPWs for proof-of-concept monolithic mid-IR sensors [48–50]. In their simple form of having laser, detector and passive waveguide on the same epitaxially grown chip, they have paved the way to a new class of monolithic mid-IR PICs. They are based on a specifically engineered quantum cascade active region that allows emission and detection in the same spectral range, depending on the applied bias. It is commonly referred to as quantum cascade laser and detector (QCLD) material [51,52].

However, the use of SiNx and other commonly used dielectrics is limited in the LWIR band due to their higher losses, which poses challenges for some applications [53]. Specifically, the losses of these dielectrics increase in the 6-12 µm band [53], which is crucial for developing sensors for the detection of important molecules in medicine, disease diagnosis, and life sciences (such as glucose and body fluids) [54]. Newly proposed plasmonic waveguides employing advanced plasmonic materials have mainly only been investigated theoretically so far [55]. Moreover, their fabrication and integration with typical QCL substrate platforms (i.e., for example, InP or GaAs) pose significant challenges. Instead, the integration of DLSPPWs with existing QCL/QCD materials is a compelling approach. This integration is made feasible by incorporating a Au layer as the plasmonic material, which is deposited during the fabrication process and serves as both a plasmonic element and electrical contact.

Although plasmonic waveguides offer moderate propagation lengths (with losses in the order of a few dB/mm, against dB/cm losses of the dielectric waveguides), they represent a highly favorable method for attaining high-density photonic integration. Therefore, one of the critical challenges is the need to improve waveguide performance by implementing materials with broadband mid-IR transparency and low refractive index (RI) dispersion over the entire mid-IR range. The research presented in this thesis addresses these challenges. It proposes novel solutions for the creation of advanced monolithic mid-IR PICs for sensing and telecommunication applications, specifically designed in combination with intersubband devices.

1.2 Research Objectives & Achievements

As discussed in the previous section, DLSPPWs have significant potential to enhance the performance of a wide range of optoelectronic devices.

Considering the trends and problems discussed in the previous section, the following objectives are set for this work:

i. *Designing and fabricating passive SPP components, including waveguide bends and splitters, optimized for the mid-IR spectral band, with a particular focus on the LWIR band*
ii. *To assess the capability of the proposed structures, including for broadband on-chip liquid spectroscopy applications*
iii. *To demonstrate the integration of these components with other active photonic devices, such as lasers and detectors, to realize a proof-of-concept monolithically integrated PIC with advanced functionalities.*

A range of waveguides has been proposed and fabricated through the use of standard and novel nanofabrication techniques and characterized by the use of a custom-built setup. The achievements of the thesis include:

i. *Broadband Semiconductor-Loaded SPP (SLSPP) waveguides based on Ge*
ii. *Novel and efficient processing techniques for fabricating high-quality and transparent PE thin films*
iii. *Photolithographic patterning of PE ridges*
iv. *Design and fabrication of low-loss LWIR polymeric-based DLSPP components, including waveguides and S-bends (double bend)*
v. *Integration of the aforementioned SLSPP waveguides with QCLs and QCDs.*

vi. *The introduction of novel concepts (on-chip integrated micro-mirrors) as a possible trade-off solution for balanced low-loss guiding and routing for the realization of monolithically integrated mid-IR PICs*

These newly developed waveguides hold promise for a variety of applications, particularly those in the LWIR band. The use of SLSPP waveguides based on Ge is a novel approach that opens up new possibilities for mid-IR photonics. The SLSPP platform's functionality was broadened by encapsulating devices in different ALD protective coatings, and the resulting architectures' optical properties were evaluated. The devices' protection and surface activation capabilities for liquid-based water experiments were also tested, resulting in functionalized LWIR plasmonic waveguide sensors. Additionally, the efficient processing techniques for highly transparent PE thin films and the development of DLSPPWs based on their photolithographic patterning provide further opportunities to realize high-performance and low-cost mid-IR PICs. Finally, the integration of the SLSPP waveguides with QCLs and QCDs represents a significant step towards the practical implementation of mid-IR PICs based on the plasmonic interconnects shown in this thesis.

1.3 Thesis Organization

The dissertation thesis is organized into nine chapters that cover the various aspects of design, materials selection, fabrication, and characterization of surface plasmon waveguides investigated for mid-IR photonics applications. Following the thesis introduction (Chapter 1), Chapter 2 offers an overview of plasmonics. Chapter 3 delves into the theory and design of integrated plasmonic components. Chapter 4 discusses the selection and comparison of materials for mid-IR plasmonic waveguides. Chapter 5 covers the techniques used for fabricating and characterizing plasmonic waveguides. Chapter 6 presents the developed dielectric-loaded plasmonic waveguides based on organic (PE) material, discussing the thin film preparation and the DLSPPWs fabrication and characterization. Chapter 7 discusses the dielectric-loaded plasmonic waveguides based on a Ge/Au architecture, outlining design optimization for broadband sensing applications, device protection for water-based spectroscopy applications, device functionalization, and shows the potential of the use of on-chip routing via integrated micro-mirrors. Chapter 8 compares and discusses each loading approach, outlining the advantages and disadvantages, and explores various applications and future directions of the investigated approaches, outlining their potential use for various more advanced

PICs. Finally, Chapter 9 presents the conclusion of the dissertation, summarizing the findings and discussing their implications for the field of mid-IR photonics.

2
PRINCIPLES OF SURFACE PLASMON WAVEGUIDING

In recent years, plasmonic waveguides have been extensively investigated for their potential applications in nanophotonic circuits [56], sensing [57], and energy harvesting in thin-film solar cells [58,59]. By properly designing the geometry and material properties involved, it is possible to achieve strong confinement and control of the electromagnetic fields in the vicinity of the metal-dielectric interface. This chapter discusses the basic principles and fundamental concepts of surface plasmon waveguiding. Furthermore, some of the latest advances in the field of mid-IR plasmonics will be presented. The primary sources used for the fundamentals covered in this chapter are the book of S. A. Maier [60], and S. Bozhevolnyi [61]. Additionally, notable contributions from S. Hayashi et al. [58], Zhong et al. [62], and Law et al. [11] have been incorporated, as these review papers offer valuable insights into the plasmonics field and its specific opportunities in the mid-IR range.

2.1 Overview of Plasmonics

2.1.1. Introduction

At its most fundamental level, the field of plasmonics can be described as the study of plasmons, the collective oscillation of free electrons in a conductive media. These hybrid excitations, commonly referred as surface plasmons, are accompanied by electromagnetic oscillations due to the induced variations of electric charge at surfaces. Therefore, surface plasmons are often called SPPs, where the term "polaritons" denotes the coupled oscillations of electromagnetic waves and charged particles within solid materials.

SPPs are a widely studied topic, particularly when coupled with VIS or near-IR light. They exhibit localized electromagnetic fields at metallic surfaces, which are significantly enhanced compared to the excitation field. The localization of fields at the nanoscale enabled the development of nano-optics, extending beyond the diffraction limit of conventional light waves.

Surface plasmons have a rich history dating back to the early 20th century. In 1902, Wood [63] observed the anomalous decrease in reflected light intensity from a metallic grating, which can be attributed to the excitation of SPPs, even though the term did not exist at the time. Maxwell-Garnett [64] developed the theory of effective dielectric constant in 1904, enabling to explain the color of glasses containing metallic particles. Mie's electromagnetic theory of light scattering and absorption by spherical particles [65] further contributed to understand the behavior of metallic colloidal particles. These studies laid the foundation for discussing the optical properties of small metallic particles in terms of localized surface plasmons (LSPs).

Advances in the physics of surface plasmons continued with Ritchie [66] deriving dispersion relations for SPPs in metallic films in 1957, later confirmed experimentally [67]. The attenuated total reflection (ATR) method, demonstrated by Otto [68] and Kretschmann-Raether [69] in 1968, became a sensitive tool for surface sensing, known as the surface plasmon resonance (SPR) sensor [57]. In 1974, Fleischmann et al. [70] developed the surface-enhanced Raman scattering (SERS) technique. Since then, SERS has led to diverse applications in various fields, benefiting from enhanced local fields in nanoparticles.

Around 1990, the field of surface plasmons began expanding into various interdisciplinary research fields, particularly in biology. The close connection between surface plasmons, near-field optics, and nano-optics emerged, leading to the development of tip-enhanced spectroscopy [71,72] and optical nanoscale antennas [73]. The progress of plasmonics also relied on the advancement of fabrication techniques for metallic nanostructures, such as electron-beam lithography, focused ion beam (FIB) etching, and advanced chemical synthesis methods. Furthermore, the availability of advanced and affordable numerical simulation tools facilitated visualization and analysis of the interactions of the electromagnetic fields with plasmonic structures. The improvement of fabrication techniques and computational tools helped to rapidly expand the field, driving surface plasmons toward numerous applications, including biosensors, nano-imaging, waveguides, data storage, photovoltaics, light-emitting devices, and many others.

Surface plasmons can be categorized into two main types: SPPs and LSPs. SPPs propagate along a planar interface between a metal and a dielectric, while LSPs are confined to metallic nanoparticles. Despite their different appearances, both SPPs and LSPs exhibit enhanced electromagnetic fields localized at metal surfaces. Given the emphasis of this thesis on mid-IR plasmonic waveguides, the following sections will delve into the fundamentals of plasmonics, with a particular focus on the characteristics of SPPs. We will begin covering the fundamentals, starting from Maxwell's equations and material properties, and discussing surface wave propagation. Finally, this chapter will conclude by providing an overview of recent advances and techniques for plasmonics in the mid-IR.

2.1.2. Maxwell’s Equations

The interaction of light with metals and dielectrics can be described by Maxwell's equations, which provide the mathematical framework to describe the behavior of the electric field $\vec{E}$ and magnetic field $\vec{H}$ to their sources. At their fundamental level, Maxwell's equations are formulated without the consideration of specific material properties [60]:

$$\begin{gathered}\vec{\nabla} \times \vec{E} = -\frac{\partial \vec{B}}{\partial t} \\ \vec{\nabla} \cdot \vec{B} = 0 \\ \vec{\nabla} \cdot \vec{D} = \rho \\ \vec{\nabla} \times \vec{H} = \vec{J} + \frac{\partial \vec{D}}{\partial t}\end{gathered} \tag{2.1}$$

where $\vec{B}$ is the magnetic flux density, ρ is the charge density, $\vec{J}$ is the current density, and $\vec{D}$ is the electric displacement field. When considering electromagnetic fields in a vacuum, these equations can be expressed as follows:

$$\begin{gathered}\vec{\nabla} \times \vec{E} = -\frac{\partial \vec{B}}{\partial t} \\ \vec{\nabla} \cdot \vec{B} = 0 \\ \vec{\nabla} \cdot \vec{D} = \rho \\ \frac{1}{\mu_0}\vec{\nabla} \times \vec{B} = \vec{J} + \varepsilon_0 \frac{\partial \vec{E}}{\partial t}\end{gathered} \tag{2.2}$$

where, in the last equation, the constants ε_0 and μ_0 represent the vacuum electrical permittivity and vacuum magnetic permeability, respectively.

In vacuum, the relationship between electric displacement and electric field, and the magnetic flux density and the magnetic field is:

$$\begin{aligned}\vec{D} &= \varepsilon_0 \vec{E} \\ \vec{B} &= \mu_0 \vec{H}\end{aligned} \tag{2.3}$$

2.1.3. Material Properties

Equations (2.2) can be used to calculate the fields where all sources are known. In bulk materials, this would mean knowing the exact charges and positions of all atoms at any given time. However, computing the exact number of individual contributions when dealing with complex systems is often impossible and unnecessary. Instead, it is common practice to calculate average macroscopic fields using material equations. These equations express the impact of the fields on the material's structure observed over large distances. By employing material equations, one can effectively describe the effects of the material's microstructure without needing to consider every individual component. In this case, equations (2.3) can be reformulated as follow [74]:

$$\begin{aligned}\vec{D} &= \varepsilon_0 \vec{E} + \vec{P} = \varepsilon_0 (1 + \chi_e) \vec{E} \\ \vec{B} &= \mu_0 \vec{H} + \vec{M} = \mu_0 (1 + \chi_m) \vec{H}\end{aligned} \tag{2.4}$$

where $\vec{P}$ is the polarization, χ_e is the electric susceptibility tensor, χ_m is the magnetic susceptibility tensor, and $\vec{M}$ is the magnetization. Polarization and magnetization represent the distribution of electric and magnetic dipole moments that arise in response to an external field. This implies that both of these vectors are functions of the external field. As a result, when the expressions (2.4) for the electric displacement and magnetic field are substituted into the equations (2.1), the Maxwell's equations in the medium have a similar form to those in a vacuum. For non-magnetic materials and most materials within the optical frequency spectrum, the magnetization component $\vec{M}$ can be neglected. Two new constants can be introduced:

$$\begin{aligned}\varepsilon &= 1 + \chi_e \\ \mu &= 1 + \chi_m\end{aligned} \tag{2.5}$$

called electric permittivity and magnetic permeability. Using these notations, the displacement and magnetic induction can be written in a simpler form:

$$\begin{aligned}\vec{D} &= \varepsilon_0 \varepsilon \vec{E} \\ \vec{B} &= \mu_0 \mu \vec{H}\end{aligned} \tag{2.6}$$

In real materials, the permittivity is frequency-dependent and expressed as a complex function $\varepsilon(\omega) = \varepsilon'(\omega) + j\varepsilon''(\omega)$. This complex function comprises two components: the real part, which represents the material's polarization, and the imaginary part, which accounts for the material's losses. The combination of these two components, ε' and ε'', plays a crucial role in determining the appearance of materials in the VIS range. Transparent materials typically have low values of ε'' and refractive indices close to unity. These materials allow light to pass through with minimal absorption, resulting in a transparent or translucent appearance. In contrast, materials with higher values of ε'' in the VIS range tend to absorb light more strongly. This absorption can cause them to appear darker or opaque, as they absorb a significant portion of the incident light. The color of an opaque material is determined by the wavelengths of light that are not absorbed but are instead reflected or scattered back to our eyes.

Metals have the unique property of having a negative permittivity, and for this reason are used in the field of plasmonics [60]. Figure 2.1 shows an example of the permittivity of bulk Au from the UV to the mid-IR wavelengths [75]. The losses are relatively low in the VIS range, with the imaginary part of the permittivity around 1. However, as the wavelength extends to the IR region, the real part of the permittivity becomes more negative, reaching values as low as -1000 to -2000, and the losses increase as well. In the radio-frequency range, metals are considered as perfect conductors, due to their highly negative permittivity, which prevents the penetration of waves into the metal.

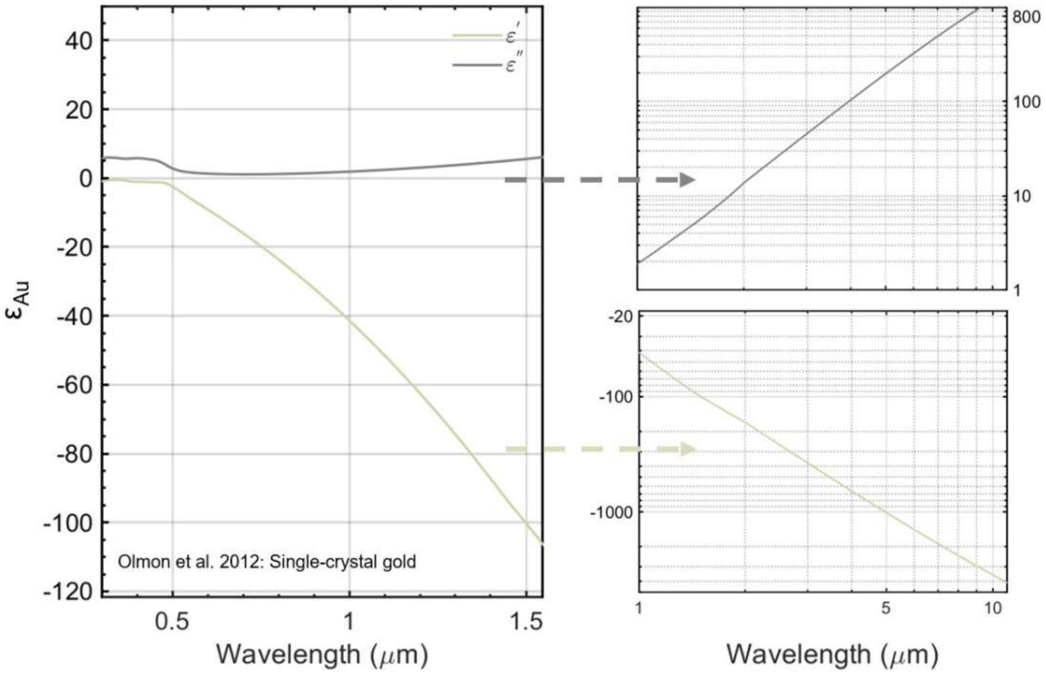

Figure 2.1 Real (ε') and imaginary(ε'') values of permittivity of Au in the UV to near-IR range (left) and mid-IR (right). Data taken from [75].

To accurately predict and understand the behavior of surface plasmons, it is necessary to model metals and understand their behavior in response to an external electromagnetic field. Most metals crystallize with atoms arranged in a periodic structure called crystal lattice. The majority of metals exhibit a cubic face-centered cubic (FCC) lattice, where the unit cell is a cube, and atoms are located at the corners and centers of the faces. The lattice constant for most metals falls within the range of 0.35-0.4 nm. This lattice structure is among the densest possible, explaining their weight and solidity. In addition to bound electrons localized around atoms, metals also have free electrons that can move freely within the material. These free electrons form the so-called "free electron gas" enabling metals to conduct electrical currents. The typical concentration of electrons in metals is on the order of around 10^{21} - 10^{23} electrons/cm^3 [76]. The response of metals to an external electromagnetic field is primarily governed by the behavior of the electron gas within the material, which gives the main contribution to the permittivity. The movement of charge carriers in the presence of electromagnetic waves can be expressed as [77]:

$$m_e\vec{r}'' + b\vec{r}' + a\,\vec{r} \;= -|e|\vec{E} \tag{2.7}$$

where the charged particles with a mass m_e are elastically connected to their equilibrium position by a restoring force ($a\vec{r}$) that is proportional to the displacement ($\vec{r}$) of the particles. Any motion of the particles is attenuated by a damping term ($b\overrightarrow{r'}$), which increases linearly with velocity. The influence of the light field on the charged particles is mediated through the Coulomb force ($\vec{F_C} = -|e|\vec{E}$), while the Lorentz force is typically considered negligible in comparison to the Coulomb force [77]. For periodic exitation $\vec{E} = \overrightarrow{E_0}e^{-i\omega t}$, and the solution is:

$$\vec{r}(\omega) = \frac{-|e|}{m_e\left[\left(\frac{a}{m_e}\right)^2 - \omega^2 + J\omega\left(\frac{b}{m_e}\right)\right]}\vec{E}(\omega) \tag{2.8}$$

Introducing the charge carrier density n$_e$, the resonance frequency of the linear oscillator $\omega_0 = \frac{a}{m_e}$, the electric dipole moment $\vec{p} = -|e|\vec{r}$ and the damping coefficient $\Gamma = \frac{b}{m_e}$, the corresponding polarization density $\overrightarrow{P}(\omega)$ can be written as [77]:

$$\overrightarrow{P}(\omega) = n_e\,\vec{p}(\omega) = \; -n_e|e|\,\vec{r}(\omega) = \frac{n_e|e|^2}{(\omega_0^2 - \omega) + J\omega\Gamma}\vec{E}(\omega) \tag{2.9}$$

Therefore, using equation (2.4), the permittivity can be expressed as:

$$\varepsilon(\omega) = \left(1 + \frac{|e|^2 n_e}{m_e \varepsilon_0} \frac{1}{(\omega_0^2 - \omega^2) + J\omega\Gamma}\right) \tag{2.10}$$

Thus, we can represent the permittivity of a metal using the following simplified form:

$$\varepsilon(\omega) = 1 + \frac{\omega_p^2}{(\omega_0^2 - \omega^2) + J\omega\Gamma}$$
$$\omega_p = \sqrt{\frac{|e|^2 n_e}{\varepsilon_0 m_e}} \tag{2.11}$$

where ω_p is called plasma frequency. Therefore, the permittivity of an electron gas can be entirely determined by a single parameter which depends on factors such as the charge, mass, and concentration of the carriers.

As a complex function, the permittivity can be further separated into its real and imaginary components:

$$\varepsilon' = 1 + \frac{\omega_P^2(\omega_0 - \omega^2)}{(\omega_0^2 - \omega^2)^2 + \omega^2\Gamma^2}$$
$$\varepsilon'' = -\frac{\Omega_P^2 \omega\Gamma}{(\omega_0^2 - \omega^2)^2 + \omega^2\Gamma^2} \tag{2.12}$$

In the IR region, highly conducting metals can be simplified by assuming that the resonance frequency of bound electrons ω_0 is negligible (i.e., $\omega_0 = 0$) [78]. As a result, equations (2.12) can be rewritten in a simplified form.

$$\varepsilon' = 1 - \frac{\omega_P^2}{\omega^2 + \Gamma^2}$$
$$\varepsilon'' = -\frac{\Omega_P^2 \Gamma}{\omega^3 + \omega\Gamma^2} \tag{2.13}$$

Therefore, at low frequencies, below the plasma frequency, the permittivity is negative and it tends to minus infinity for a static case (see Figure 2.2). At higher frequencies significantly surpassing the plasma frequency, the permittivity approaches unity, indicating that the electron gas becomes nearly transparent to electromagnetic waves. In the vicinity of the plasma frequency, the permittivity of the electron gas approaches zero, forming what is known as the epsilon-near-zero regime. This regime is of great interest and subject to active research, particularly within the metamaterial community.

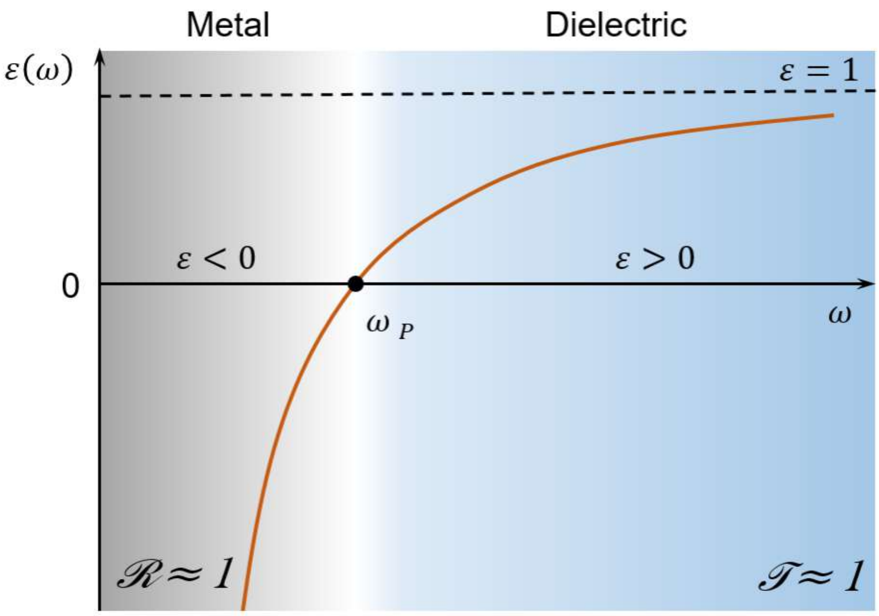

Figure 2.2 Frequency-dependent permittivity $\varepsilon(\omega)$ predicted by the Drude model. The region of transparency of metallic materials is highlighted in reference to the plasma frequency. Below the plasma frequency (on the left side), the metal exhibits near-perfect conductivity (R≈1). Above the transparency region, the material allows for transmission (T≈1). Image adapted from [79].

The complex permittivity is related to the complex refractive index through the following equations [77]:

$$\begin{gathered} \tilde{n} = n + jk \\ n = \sqrt{\frac{1}{2}\sqrt{\varepsilon'^2 + \varepsilon''^2} + \varepsilon'} \\ k = \sqrt{\frac{1}{2}\sqrt{\varepsilon'^2 + \varepsilon''^2} - \varepsilon'} \end{gathered} \tag{2.14}$$

where the imaginary part k represents the extinction coefficient and is responsible for an exponential decay of the electric field amplitute in the media.

In the opposite manner, the permittivity is linked by the refractive index by:

$$\begin{gathered} \varepsilon' = n^2 - k^2 \\ \varepsilon'' = -2nk \end{gathered} \tag{2.15}$$

The extinction coefficient (k) characterizes the attenuation of a propagating wave within a material. It is important to note that the sign convention for k differs across literature and simulation models. In COMSOL Multiphysics [80], the software employed for optical simulations in this thesis, the imaginary part ε'' (representing the loss) and the extinction coefficient k of absorbing materials are defined as negative.

2.1.4. Surface Wave Propagation

SPPs are longitudinal surface waves that propagate along the interface between a dielectric and a metal. In the absence of magnetizable materials and external current densities, equations (2.1) can be expressed as follows [77]:

$$\begin{gathered}\vec{\nabla} \times \vec{E} = -\mu_0 \frac{\partial \vec{H}}{\partial t} \\ \vec{\nabla} \times \vec{H} = \frac{\partial \vec{D}}{\partial t}\end{gathered} \tag{2.16}$$

By applying the curl operator to both sides of the first expression and utilizing the second expression, the following is obtained:

$$\vec{\nabla} \times \vec{\nabla} \times \vec{E} = -\mu_0 \frac{\partial^2 \vec{D}}{\partial t^2} \tag{2.17}$$

The expression can be rewritten by using the following mathematical identity:

$$\vec{\nabla} \times \left(\vec{\nabla} \times \vec{f}\right) = \vec{\nabla}\left(\vec{\nabla} \cdot \vec{f}\right) - \nabla^2 \vec{f} \tag{2.18}$$

and considering the absence of charge accumulation (i.e., $\vec{\nabla} \cdot \vec{D} = 0$):

$$-\nabla^2 \vec{E} = -\mu_0 \frac{\partial^2 \vec{D}}{\partial t^2} \tag{2.19}$$

When using $c_0 = \frac{1}{\sqrt{\varepsilon_0 \mu_0}}$, we obtain the wave equation for the electric field in linear isotropic media:

$$\nabla^2 \vec{E} - \frac{\varepsilon}{c_0^2} \frac{\partial^2 \vec{E}}{\partial t^2} = 0 \tag{2.20}$$

When expressed in complex notation with ${}^{\partial}/_{\partial t} = j\omega$ and $\vec{E} = \overrightarrow{E_0} e^{-i\omega t}$

$$\nabla^2 E^2 + \varepsilon k_0^2 \vec{E} = 0 \tag{2.21}$$

This last equation is known as the Helmholtz equation, where $k_0 = \frac{\omega}{c_0}$ represents the wave vector of the propagating wave in a vacuum.

If we consider the simple propagation geometry of Figure 2.3, the permittivity ε only varies along one spatial coordinate. Assuming that the propagation direction is along the y-axis in a Cartesian coordinate system, with no variation in the x-axis (in-plane) and z = 0 defining the interface, we can express ε as a function of z, i.e., $\varepsilon = \varepsilon(z)$. The propagating wave can therefore be described as $\vec{E}(x, y, z) = E(z)e^{-J\beta y}$. The component of the wave vector aligned with the propagation direction, k_y, is referred to as the propagation constant β of the traveling wave. Substituting this expression into equation (2.21):

$$\frac{\partial^2 \vec{E}}{\partial z^2} + (k_0^2\varepsilon - \beta^2)\vec{E} = 0 \tag{2.22}$$

which represents the wave equation governing the electric field of a propagating wave on the interface between a metal and air.

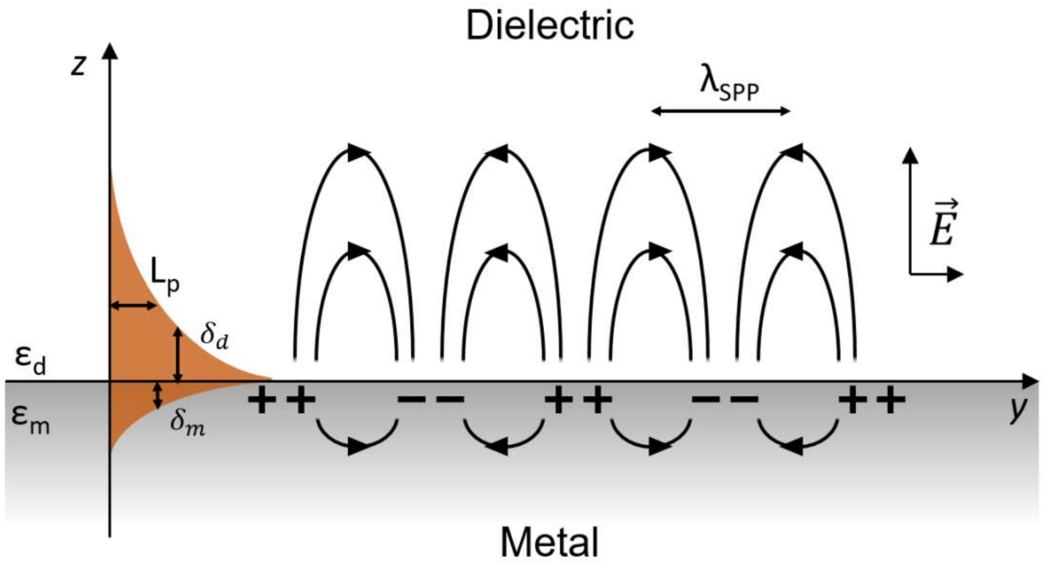

Figure 2.3 Schematic representation of a SPP wave propagating along the metal-dielectric interface. The electric field, denoted as $\vec{E}$, exhibits an exponential decay as the distance increases. L_p is the propagation length. δ_d, δ_m represent the penetration depth in the dielectic (with permettivity ε_d) and the metal (with permettivity ε_m), respectively. The surface wave propagate at the interface with wavelegnth λ_{SPP}.

An analogous equation for the magnetic field can also be derived. As SPPs are characterized by TM polarization, their propagating direction in the y-axis only induces non-zero field components $\vec{H}_x, \vec{E}_y, \vec{E}_z$. The equation governing the propagation of TM waves in the y direction is given by [60]:

$$\begin{gathered}
\frac{\partial^2 \vec{H}_x}{\partial z^2} + (k_0^2 \varepsilon - \beta^2)\vec{H}_x = 0 \\
\vec{E}_y = -J \frac{1}{\omega\varepsilon} \frac{\partial \vec{H}_x}{\partial z} \\
\vec{E}_x = -\frac{\beta}{\omega\varepsilon} \vec{H}_x
\end{gathered} \tag{2.23}$$

It can be demonstrated that a non-magnetic medium does not have a solution for the given form of TE-polarization. By using the following assumption for the metal:

$$\begin{gathered}
H_x = A_1 e^{J\beta y} e^{k_m z} \\
E_y = -jA_1 \frac{1}{\omega\varepsilon_m} k_m e^{J\beta y} e^{k_m z} \\
E_z = -A_1 \frac{\beta}{\omega\varepsilon_m} e^{J\beta y} e^{k_m z}
\end{gathered} \tag{2.24}$$

Similarly, applying the same approach to the dielectric component of the interface

$$\begin{gathered}
H_x = A_2 e^{J\beta y} e^{-k_d z} \\
E_y = jA_2 \frac{1}{\omega\varepsilon_d} k_m e^{J\beta y} e^{-k_d z} \\
E_z = -A_1 \frac{\beta}{\omega\varepsilon_d} e^{J\beta y} e^{-k_d z}
\end{gathered} \tag{2.25}$$

The continuity of the magnetic field component H_x and $\varepsilon_i E_z$ at the interface requires that $A_1 = A_2$, and

$$\frac{k_d}{k_m} = -\frac{\varepsilon_d}{\varepsilon_m} \tag{2.26}$$

The expression for H_y must satisfy the wave equation, leading to [60]:

$$\begin{gathered}
k_d^2 = \beta^2 - k_0^2 \varepsilon_d \\
k_m^2 = \beta^2 - k_0^2 \varepsilon_m
\end{gathered} \tag{2.27}$$

By combining (2.26) and (2.27), we obtain the dispersion relation governing the propagation of SPPs at the interface between the metal/dielectric interface:

$$\beta = k_0 \sqrt{\frac{\varepsilon_d \varepsilon_m}{\varepsilon_d + \varepsilon_m}} \tag{2.28}$$

In order for SPPs to be confined to the metal-dielectric interface, it is essential that the real parts of the permittivities, $Re\,\{\varepsilon_d\}$ and $Re\,\{\varepsilon_m\}$, have opposite signs. This condition is satisfied by commonly used metals in plasmonics. A similar methodology can be applied to TE modes, leading to the conclusion that propagating TE modes are prohibited at a metal/dielectric interface.

Figure 2.4 illustrates the behavior of a lossless Drude metal at an air interface ($\varepsilon_d = 1$) and a fused silica interface ($\varepsilon_d = 2.25$). The frequency (ω) and wave vector in the direction of propagation ($\beta = k_y$) are normalized to the plasma frequency. The real part of β is represented by continuous curves, while the imaginary part is depicted by dashed lines. Within the frequency range $\omega < \omega_p$, the permittivity ε_m is negative, satisfying the condition $\beta^2 - k_0\varepsilon_m > 0$. However, since SPP excitations always occur below their corresponding light lines (gray dashed lines in the graph), specific phase-matching techniques are required to excite them.

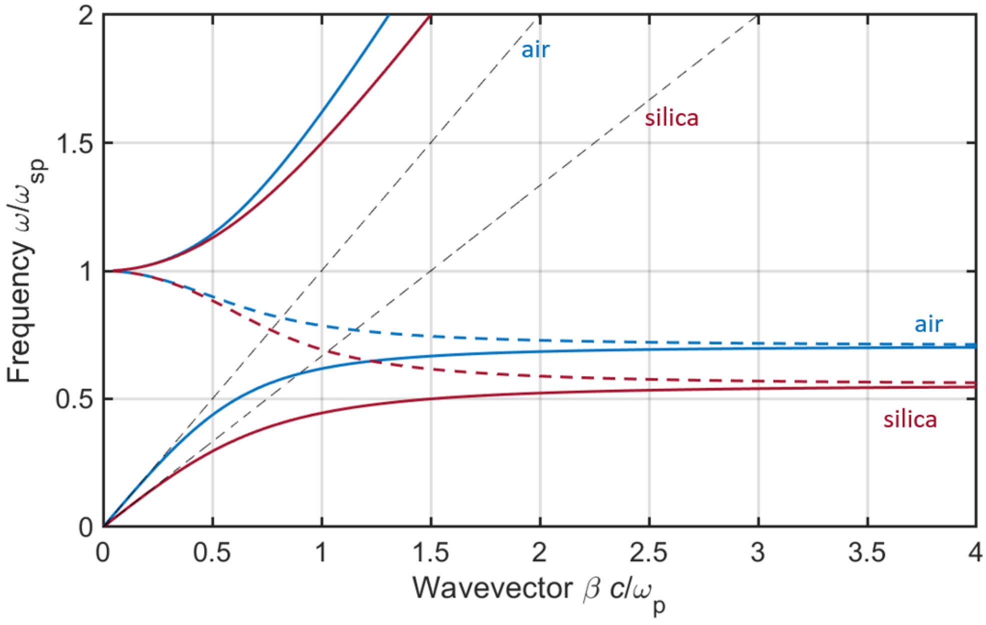

Figure 2.4 The dispersion relation of a typical SPP confined by a Drude metal with negligible damping frequency is shown for the interface of air (blue curve) and silica (red curve). The dashed line represents the imaginary part of β.

The frequency at which propagating modes can no longer exist is commonly referred to as the surface plasmon frequency:

$$\omega_{\mathrm{sp}} = \frac{\Omega_p}{\sqrt{1+\varepsilon_d}} \tag{2.29}$$

and at this particular frequency, the mode exhibits an electrostatic nature. Damping effects in real metals results in attenuation of SPPs. The attenuation is quantified by the propagation length L_p, which accounts for the decay of SPP intensity along the propagation direction:

$$L_p = \frac{1}{2\,\mathrm{Im}(\beta)} \tag{2.30}$$

At lower frequencies, the propagation constant of SPPs closely follows the trajectory of the light line, leading to weakly bound modes. These SPPs, also known as Sommerfeld-Zenneck waves [60], exhibit a characteristic of penetrating the dielectric over multiple wavelengths. This work specifically investigates the properties of SPPs in the mid-IR regime. Therefore, in the next section, we will discuss different techniques in order to achieve highly bound modes in the mid-IR with novel materials and spoof plasmons.

2.2 Mid-IR Plasmonics

There is a growing interest in plasmonics within the mid-IR spectral region [11,62]. However, as discussed in the previous section, conventional metals exhibit a large negative real part of their permittivity (see Figure 2.1), leading to different optical behavior compared to shorter wavelengths (VIS or near-IR). As an example, considering the simple dielectric/metal interface, and assuming air as the dielectric medium ($\varepsilon_d = 1$), the penetration depths into the metal (δ_m) and the dielectric (δ_d) can be expressed as [62]:

$$\begin{aligned} \delta_m &= \frac{1}{\mathrm{Re}\left\{k_0\sqrt{\frac{-\varepsilon_m^2}{1+\varepsilon_m}}\right\}} \\ \delta_d &= \frac{1}{\mathrm{Re}\left\{k_0\sqrt{\frac{-1}{1+\varepsilon_m}}\right\}} \end{aligned} \tag{2.31}$$

As a result, SPP modes in the mid-IR have limited penetration into the metal (i.e., lower losses compared to the VIS and near-IR SPP modes, see Figure 2.1b) but greater depths into the dielectric (see Figure 2.5a), resulting in a weak confinement and limited utility for many applications.

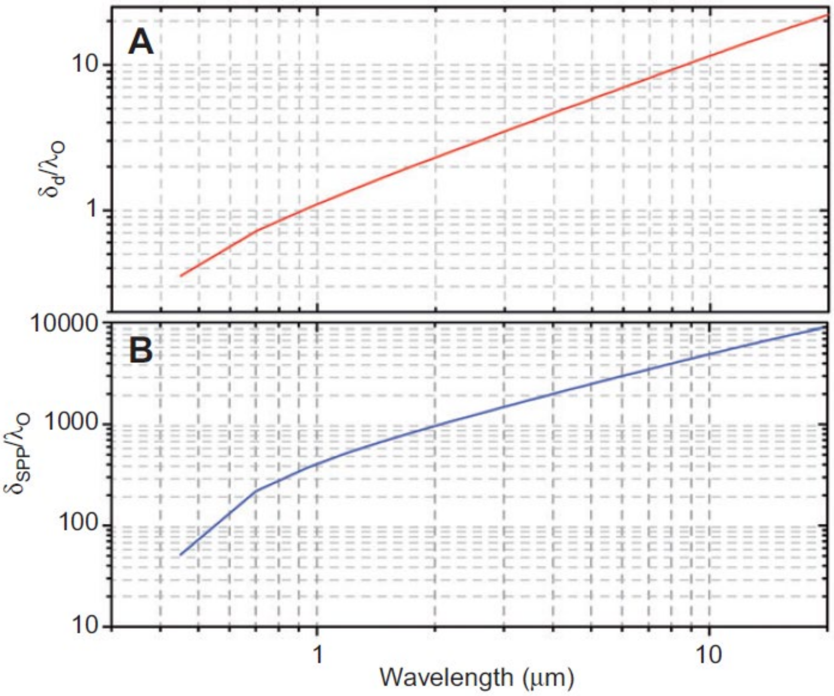

Figure 2.5 Spectral depenedent behavior of a SPP mode at an Ag/air interface: a) penetration of the SPP mode into the dielectric material, normalized to the free-space wavelength λ_0 calculated for an SPP at an Ag/air interface. b) propagation length (normalized to the free-space wavelength λ_0). It is worth noting the significant penetration depth and propagation length at mid-IR wavelengths. Image taken from [11].

An additional consequence of this behavior is that traditional metals cannot support strong sub-wavelength LSP modes at mid-IR wavelengths. While localized modes on metallic structures can be achieved, they resemble more antennas than LSP resonances and scale linearly with antenna dimension. Consequently, the optical properties of traditional metals significantly differ at longer wavelengths, necessitating the development of new plasmonic materials that mimic the behavior of traditional metals at shorter wavelengths. The next sections will discuss four classes of recently developed mid-IR plasmonic materials: spoof plasmons, graphene, engineered metals, and surface phonon polaritons.

2.2.1. Spoof Plasmons

The significant disparity between SPPs in the VIS and mid-IR frequency ranges has motivated to find alternative approaches to confine propagating radiation at sub-wavelength scales in the mid-IR. While the confinement of LSP resonances primarily relies on selecting alternative material platforms, achieving enhanced mode confinement for SPPs in the mid-IR can be achieved by using structured systems based on conventional metals to replicate SPP behavior in the mid-IR frequency range. The concept of the spoof SPP was first introduced in 2004 [81] and involves the collective excitation of waveguide modes in perforated films. Figure 2.6 illustrates an example of such a structure.

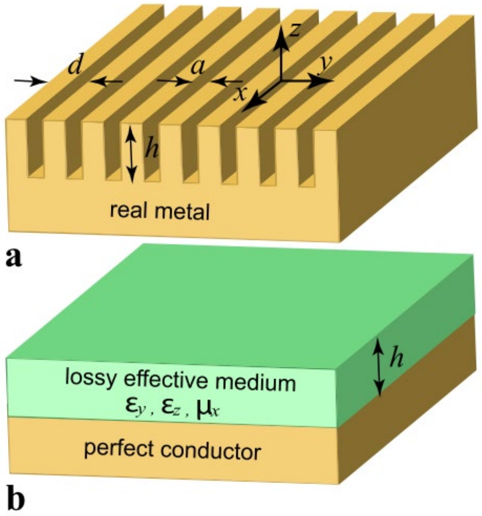

Figure 2.6 (a) THz spoof SPP structure. It consists of an array of grooves cut into a real metal with width a, depth h, and periodicity d. (b) shows the structure with grooves approximated as an effective medium (metamaterial). Image taken from [44].

Each corrugation within the system can be viewed as a sub-wavelength waveguide characterized by permittivity ε_h and permeability μ_h. As a result, the field inside a corrugation can be expressed as a linear combination of individual waveguide modes. When the size of the corrugation a is much smaller than the free-space wavelength, the contribution from the fundamental mode becomes the most significant. As a result, the collective response of multiple corrugations can be approximated using effective medium theory, leading to a plasma-like response characterized by an effective plasma frequency (2.32) [11].

$$\omega_p^2 = \frac{\pi^2 c}{\varepsilon_h \mu_h} \tag{2.32}$$

Corrections to the effective medium theory to account for the finite conductivity of noble metals in the mid-IR frequency range were addressed by Rusina et al. [44]. These corrections result in absorption losses similar to the propagation losses observed in VIS-frequency SPPs. However, spoof plasmons typically exhibit lower quality factors compared to their counterparts in the VIS-frequency range. Additionally, the limited bandwidth of spoof SPPs may impose constraints on the range of frequencies over which they can efficiently couple and interact with light, potentially limiting their versatility in certain applications. Nevertheless, spoof SPP structures offer substantial design flexibility and can be tailored across a wide range of wavelengths, particularly those where metals exhibit large negative permittivity, such as Au and silver (Ag). This enables the spoof SPP mode to mimic the highly confined and lossy characteristics of classical SPPs at shorter wavelengths.

2.2.2. Graphene

Graphene is a 2D monolayer of carbon atoms. It has gained significant attention in recent years due to its unique electronic, mechanical, and thermal properties [82–84]. Additionally, graphene exhibits extraordinary optical properties, making it an attractive alternative plasmonic material for long-wavelength applications. Graphene's unusual band structure, high mobility and tunable carrier concentration result in extreme strong confinement and long propagation lengths of SPPs have contributed to its growing interest in the field of plasmonics. The ability to vary the 2D carrier concentration of graphene allows for electrostatic control of the plasma frequency, offering exciting possibilities for IR plasmonic applications and fundamental investigations of 2D plasmons [11].

2.2.3. Engineered Metals

In addition to traditional noble metals, such as Au and Ag, a new class of materials has emerged in the field of plasmonics. Highly doped semiconductors offer unique advantages and novel opportunities for tailoring plasmonic responses in the mid-IR. The optical behavior of a doped semiconductor can be described using the Drude model, similarly to conventional metals, where the permittivity can be described as:

$$\begin{gathered} \varepsilon(\omega) = \varepsilon_b \left(1 - \frac{\Omega_p^2}{\omega(\omega + i\Gamma)}\right) \\ \Omega_p^2 = \frac{e^2 n}{m * \varepsilon_0 \varepsilon_s} \end{gathered} \tag{2.33}$$

Where ε_b is the background permittivity from the bound electrons in the crystal, and ε_s is the undoped semiconductor's relative permittivity. The plasma frequency deviates from the traditional expression, demonstrating two key aspects. Firstly, the carrier density (n) and charge polarity can be controlled through dopant selection (n-type or p-type) and doping density, during the growth or fabrication process. Secondly, the electron (or hole) mass needs to be substituted with a frequency-dependent effective mass ($m^* = m^*(\omega)$), which accounts for the influence of the semiconductor's band structure on the plasmonic response. By incorporating high levels of doping and utilizing semiconductors with small effective masses, it becomes possible to achieve mid-IR plasma frequencies in materials like group IV and III/V semiconductors. However, the concept of engineering plasmonic metals extends beyond semiconductors [11].

Recent studies have demonstrated the potential of transparent conducting oxides (TCOs), such as indium tin oxide (ITO), and nitrides to exhibit plasma frequencies in the near-IR to VIS region [85]. Doped TCOs exhibit a plasma wavelength typically around 1.5 µm, indicating the potential for strong confinement of plasmonic modes in the near-IR region, in contrast with the relatively weaker confinement observed in traditional metals like Au and Ag [11]. The doping of TCOs during growth allows for the tuning of the plasma frequency over a wide range of wavelengths.

Nitride-based materials (i.e., TiN) have also shown remarkable performance, achieved by sputtering a pure metal target with a nitrogen-argon gas mixture, allowing precise control of film properties through the adjustment of the nitrogen:argon ratio [86].

Recent studies have shown that CdZnO alloy shows tunable plasma frequency in the mid-IR [87]. The recent integration of Cd(Zn)O films on GaAs platforms presents a compelling option for future hybrid Cd(Zn)O/GaAs for the mid-IR technology [88,89].

Additionally, traditional semiconductors offer several advantages as potential mid-IR designer metals, with plasma wavelengths in the range of 3 - 30 µm. Other doping techniques, such as ion-implantation or thermal diffusion, offer lateral patterning capabilities. Moreover, traditional semiconductors benefit from well-established processing and fabrication infrastructure, high mobility, and potential integration with electronic and optoelectronic devices. Doped semiconductors like silicon (Si) [90] and Ge [46] have been proposed as candidates for mid-IR plasmonic devices. Si, in particular, offers advantages due to its well-understood properties and established fabrication infrastructure. Mid-IR plasmonic behavior has been achieved in ion-implanted Si [91] and commercially-doped Si wafers [92], allowing for tunability of the plasma wavelength within the range of approximately 4 µm to 11 µm using both n- and p-type materials. III/V semiconductor materials have also been explored as engineered metals. These materials offer advantages over Si, including high doping concentrations and small electron effective masses, enabling flexibility across the entire mid-IR wavelength range. Furthermore, III/V materials benefit from bottom-up growth techniques such as molecular beam epitaxy (MBE) or metal-organic chemical vapor deposition (MOCVD), allowing for precise control of layer thicknesses and integration with complex optoelectronic devices. In this context, doped InAs is a promising mid-IR plasmonic material [93], with a tunable plasma wavelength ranging from 5.5 µm to 17 µm or longer (see Figure 2.7). These films also exhibit low losses at their plasma frequency, comparable to TCOs, making them attractive alternatives to traditional metals, which exhibit interband absorption near the plasma frequency.

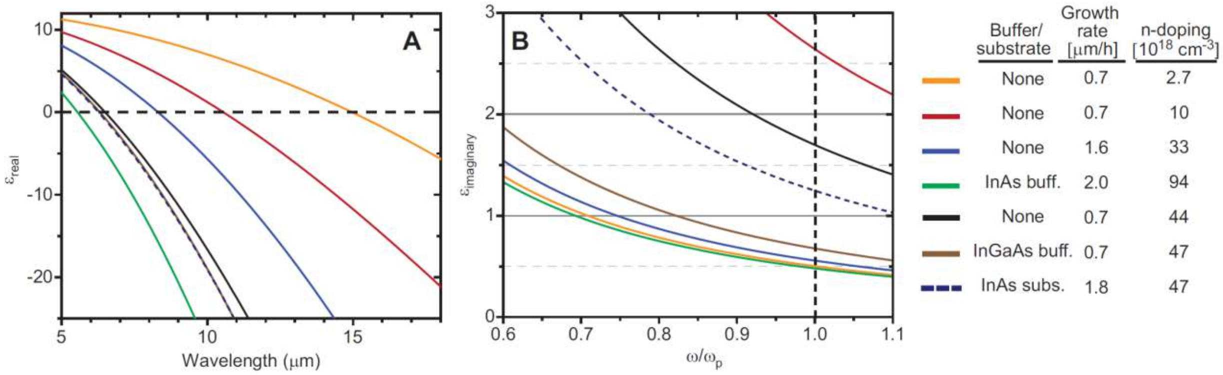

Figure 2.7 a) The real and b) imaginary part of heavily doped InAs permittivity. Image taken from [11].

In conclusion, the development of "mid-IR metals" capable of replicating the optical properties of classical metals at shorter wavelengths has opened up new possibilities for achieving sub-wavelength optical mode confinement. By designing metals with similar permittivity characteristics to the surrounding dielectric medium in the mid-IR range, it also becomes feasible to support LSP resonances at longer wavelengths [94].

2.2.4. Surface Phonon Polariton

Negative permittivity can also arise from lattice vibrations in polar dielectrics. These modes, surface phonon polaritons (SPhPs) modes, can exist in the Reststrahlen region of polar dielectrics between the frequencies of their longitudinal optical (LO) and transverse optical (TO) modes [95]. As a result, they naturally encompass the mid-IR (e.g., 0.2 eV in calcite and hexagonal boron nitride [96,97]) and terahertz (e.g., 10 meV in InSb [98]) spectral ranges. While SPhPs may not possess the same level of frequency tunability as plasmons, there is the availability of various polar materials, including SiC, GaN, SiO_2, Al_2O_3, GaAs, among others [95]. SPhPs, for example, have been observed in SiC at approximately 11 µm. These surface phonon polaritons offer strong confinement and low damping [45,99]. However, their spectral range is limited to a narrow band.

3

THEORY AND DESIGN OF MID-IR INTEGRATED PLASMONIC COMPONENTS

The need for extreme confinement and efficient propagation of light has prompted extensive research on plasmonic waveguides. In literature, various plasmonic structures with remarkable confinement capabilities have been reported, including metallic nanowires [100], metallic nanoparticles [101], V-shaped grooves [102], and wedges [103]. This chapter focuses on the types of integrated plasmonic components. It concludes with some considerations about the numerical simulation tools used in this work and the description of the figure of merits used to evaluate the performance of the waveguides. Sources used for this chapter are the reviews of S. Hayashi et al. [58] and Z. Han and S. Bozhevolnyi [104].

3.1 Types of SPP Waveguides

Surface plasmons find direct applications in the field of metal-based waveguides, offering a pathway towards efficient light guiding at sub-wavelength scales. Extensive research resulted in a multitude of SPP waveguide designs. Typically, SPP waveguides exhibit higher losses (in the order of ~100 dB/mm) compared to photonic waveguides (in the order of a few dB/cm, in the case of integrated photonic components). On the other hand, plasmonic waveguides provide strong field confinement up to the sub-wavelength scale, high surface sensitivity, super broad bandwidth transmission capacity, and a high level of miniaturization [58].

Photonic waveguides (i.e., dielectric waveguides, photonic crystal waveguides, fibers) are based on the total internal reflection (TIR) propagation mechanism, making them ideal for mm- to cm- distance transmission. The primary limitation of these components is that they are diffraction-limited, making PICs based on these components larger, more challenging to integrate monolithically with active components, and are typically less sensitive to the surrounding environment [105–107]. Ultimately, the choice between plasmonic and photonic waveguides depends on various factors, including the need for miniaturization, sensitivity, propagation efficiency, fabrication feasibility, and integration strategy.

In this section, we will begin by examining the simplest plasmonic waveguide architectures that offer 2D mode confinement (i.e., thereby forming two-dimensional boundwaves propagating along the metal–dielectric interfaces) [58]. Subsequently, we will examine SPP waveguides with 3D (mode) confinement, which additionally provide lateral mode confinement.

3.1.1. Planar (2D) SPP Modes

As we have seen in Chapter 2, metal/dielectric interfaces can support propagating modes bound at the metallic surface. These (TM-polarized SPP) modes exhibit exponential decay profiles into both media. Harnessing this principle, researchers have developed various plasmonic waveguide structures that exploit the interaction between plasmons and light. Among the plasmonic waveguide configurations, three are the most fundamental that show only 2D confinement: the metal-insulator (MI) waveguide, the metal-insulator-metal (MIM) waveguide, and the insulator-metal-insulator (IMI) waveguide. A schematic representation of these waveguide structures can be found in Figure 3.1.

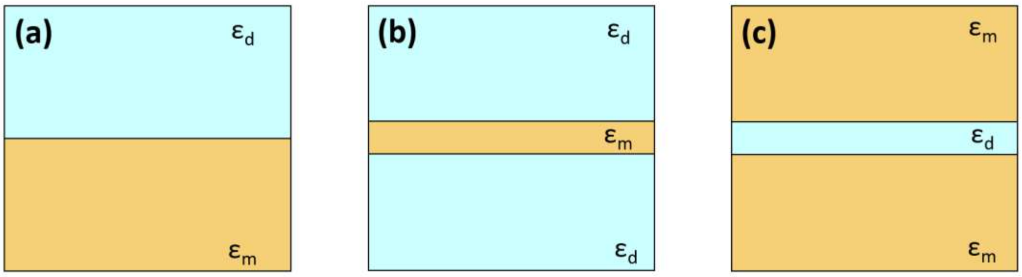

Figure 3.1 Cross sections of different fundamental plasmonic structure waveguide a) MI structure, b) IMI structure, featuring a metallic region sandwiched between two insulator regions, and c) MIM structure, consisting of two metal regions separated by an insulator region.

Plane Metal-Insulator (MI) interface

The MI waveguide (Figure 3.1a) was already analyzed in detail in the previous chapter. It consists of a metal and a dielectric layer, where the plasmonic mode is confined at the metal-dielectric interface. The influence of the ohmic losses on the surface plasmon significantly impacts its propagation performance. For instance, at telecom wavelengths (1.55 µm), the propagation length of an SPP mode supported by a Au-air interface is typically around 220 µm [104]. This propagation length provides a good spatial range for the implementation of SPP-based photonic components. At wavelengths closer to the plasma frequency (i.e., VIS range for conventional metals), the penetration of the electromagnetic wave in the metal is greater, and the mode exhibits a higher degree of confinement. However, this enhanced confinement comes at the expense of a reduced propagation length due to increased interaction with the metal layer, leading to higher losses. At longer wavelengths (i.e., in the mid-IR), the penetration of the SPP in the metal decreases, leading to increased propagation lengths. However, as the penetration in the dielectric layer increases as well (on the order of several free-space wavelengths, as illustrated in Figure 2.5), the practical utility of these structures may be limited without additional adjustments [48,108].

Although conceptually simple, the MI structure is widely employed in SPR sensors due to its exceptional sensitivity to refractive index changes facilitating highly sensitive and label-free detection of analyte concentrations and biomolecular interactions [109].

Insulator-Metal-Insulator (IMI) structure

Figure 3.1b shows an example of an IMI structure. In this plasmonic waveguide structure, a thin metal layer is sandwiched between two insulator layers. In this configuration, two distinct SPP modes propagate at the upper and lower interfaces. When the thickness of the film is sufficiently large (above the field penetration depth), these SPP modes exist independently of each other. However, as the film becomes thinner, a coupling effect occurs between the SPP modes, resulting in the generation of symmetric and antisymmetric SPP modes (Figure 3.2). The mechanism of mode coupling in plasmonic structures resembles the generation of bonding and antibonding states in quantum mechanics, when two atoms are brought into close proximity.

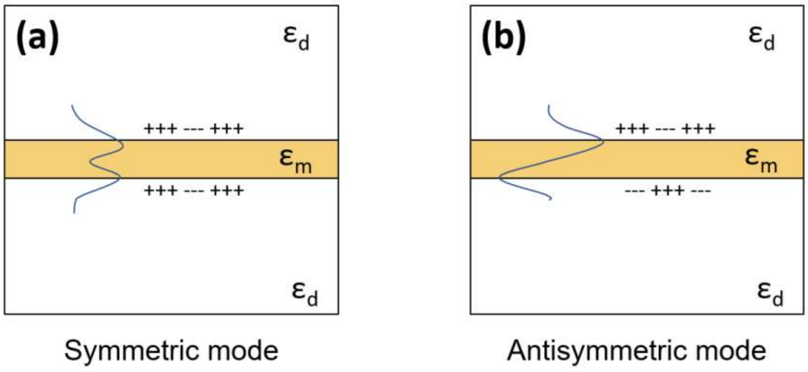

Figure 3.2 (a) Symmetric and (b) antisymmetric coupled SPP modes in IMI structures.

The antisymmetric SPP mode, originally predicted by Fukui et al. [110], exhibits a long propagation length and is commonly referred to as a long-range SPP (LR-SPP) mode [58]. The specific propagation length of this mode can vary significantly depending on factors such as the choice of metal and insulator materials, metal film thickness, and the operating wavelength. Theoretical predictions and experimental confirmations have shown typical values in the range of several hundreds of micrometers for a 15 nm-thick Ag film at a wavelength of 632.8 nm [111].

Metal-Insulator-Metal (MIM) structure

The MIM waveguide is the complementary structure of the IMI waveguide (Figure 3.1c). It consists of two metal layers separated by an insulating layer. The plasmonic mode in this structure is confined in the gap between the two metal surfaces, therefore called gap-SPP (G-SPP) mode, offering enhanced confinement compared to the MI waveguide. However, due to increased energy dissipation, the propagation length is typically shorter [104]. Within these structures, it is possible to achieve unlimited transversal compression of the G-SPP mode [104]. However, this enhanced confinement comes at the expense of a reduced propagation length. This trade-off is a fundamental characteristic of plasmonic surface guiding, where the pursuit of greater mode confinement is counterbalanced by an increase in propagation losses. As the thickness of the insulator layer decreases, the propagation loss of the symmetric mode in MIM structures increases.

3.1.2. SPP Guided by Dielectric Ridges

In the previous section, we considered 2D plasmonic structures that lack lateral confinement capabilities, which is an essential requirement for any integrated plasmonic concept. This and the next sections focus on the mode guiding mechanisms of the most popular 3D waveguide architectures, starting with the dielectric-loaded plasmonic waveguides. While the trade-off between propagation length and mode confinement also persists in 3D plasmonic waveguides, different architectures possess unique characteristics that make them suitable for specific applications. The most straightforward approach to achieve lateral mode confinement, therefore allowing radiation guiding along the SPP propagation direction, is to restrict the width of a dielectric layer on top of the metal surface. This structure is known as a DLSPP waveguide [47] (Figure 3.3a). Based on this initial concept, the fundamental idea has evolved, resulting in a series of distinct versions, each with its own unique properties. Examples of these approaches are shown in Figure 3.3b, c, and d.

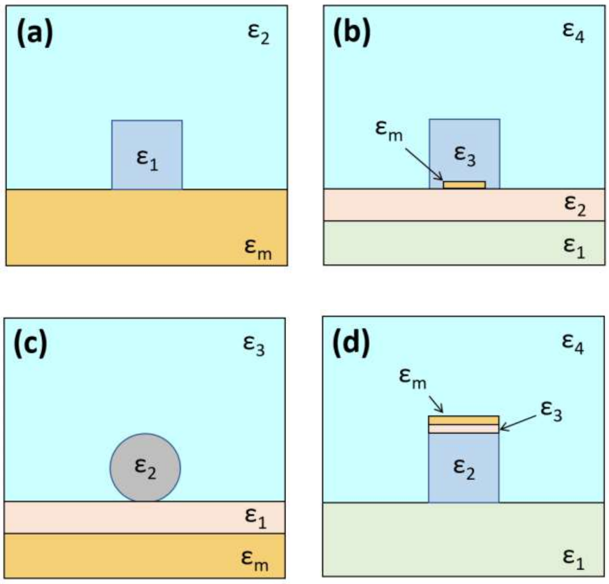

Figure 3.3 Cross sections of different plasmonic waveguides based on dielectric-loading. a) dielectric-loaded SPP waveguide (DLSPPW), b) Long range DLSPPW (LR-DLSPPW), c) Hybrid SPP waveguide (HSPPW) composed of a dielectric cylinder (ε_2) with a thin gap layer (ε_1) separating it from the metal (ε_m) and d) modified HSPPW on the silicon-on-insulator (SOI) platform.

Dielectric-Loaded SPP Waveguide

By introducing a dielectric stripe, often a polymer like polymethyl methacrylate (PMMA) on the metal surface, lateral confinement can be achieved. This is accomplished by taking advantage of the contrast in the effective index of the SPP mode at the metal/dielectric/air interface compared to the metal/air interface. This waveguide configuration, depicted schematically in Figure 3.3a, is known as a DLSPPW. It has gained significant popularity in recent years, with various fabrication methods being employed [112–114]. The use of polymers such as PMMA, which can work as both the UV-light sensitive resist and the dielectric core, offers a convenient and straightforward fabrication process [115].

The core geometry and material of the waveguide significantly impact its effective mode index and propagation length. By adjusting the parameters of the ridge, it becomes possible to tune the properties of the DLSPPW. The dielectric region above the metal layer can be considered as an effective medium, with its effective index influenced by the thickness of the dielectric. Calculations show that DLSPPWs with larger thickness exhibit stronger mode confinement but higher propagation losses due to larger real and imaginary parts of N_{SPP}. Conversely, DLSPPWs with smaller thicknesses are expected to have longer propagation lengths. These assumptions have been experimentally demonstrated and verified in previous studies [116]. Typical sub-wavelength ridge dimensions for telecom wavelengths, assuming a PMMA stripe on a thin Au layer, are approximately 600 nm × 600 nm, and the corresponding propagation lengths are around 50 µm. Moreover, the incorporation of optically active media into the polymer matrix of DLSPPWs allows for partial loss compensation through stimulated emission [117]. Experimental results have showed successful partial loss compensation in DLSPPWs using quantum dots as the gain medium, achieving a noteworthy increase of approximately 30% in propagation length at both telecom [118] and near-IR wavelengths [119]. In addition to their role in supporting plasmonic modes, the metallic component of a DLSPPW can also serve as a conductor for electrical signals, facilitating the integration of photonics and electronics on the same platform [120].

Long-Range DLSPP waveguide

Continuous efforts to enhance the propagation length of DLSPPWs have led to the development of the Long-Range DLSPPWs (LR-DLSPPWs) [121]. LR-DLSPPWs (Figure 3.3b) combine the advantages of having a long propagation length and the technological simplicity of DLSPPWs. These waveguides exhibit significantly reduced propagation losses, as the lateral component of the electric field within the metal is minimized. However, LR-SPPWs suffer from weaker mode confinement, where typically, the mode size is much larger than the wavelength of light, limiting their use in compact devices [122]. Recent experimental investigation of LR-SPP plasmonic interconnect structure utilizing TiN at a wavelength of 1.55 µm demonstrated impressive performance, achieving propagation lengths of up to 5.5 mm and a mode size (defined as $1/e^2$ decay of the power in the vertical direction) of 9.8 µm [123]. With further optimization of the geometry and cladding, it was projected that the TiN waveguide could surpass a propagation length of 10 mm, outperforming comparable devices employing Au as plasmonic material. Furthermore, the potential for loss compensation through the stimulated emission of LR-DLSPPW modes adds another degree to improving the performance of these circuits [124].

Hybrid SPP waveguide

LR-DLSPPWs have shown limited optical confinement compared to conventional dielectric waveguides. A new approach that combines the benefits of both (dielectric and plasmonic) waveguide types is the hybrid SPP waveguide (HSPPW) [125]. This waveguide exhibits sub-wavelength confinement capabilities, surpassing the diffraction limit, while maintaining relatively long propagation lengths compared to other plasmonic waveguides. Initially proposed as dielectric nanowires with a higher refractive index separated from a metal surface by a nanoscale dielectric gap [125] (see Figure 3.3c), the HSPPW was believed to arise from the coupling of photonic and plasmonic modes [58,104]. However, further analysis revealed that it is actually based on a 2D conductor-gap-dielectric (CGD) mode. The CGD mode exploits the high permittivity discontinuity between the central gap layer and the outer metal/high-index dielectric layer, resulting in a highly enhanced electric-field component perpendicular to the metal surface. The effective index of the CGD mode decreases with an increasing thickness of the gap layer.

Numerical simulations were conducted to analyze the characteristics of a modified HSPPW on a SOI platform. The cross-section of the waveguide is illustrated in Figure 3.3d. The results indicate that there is no critical thickness at which the mode loss significantly decreases for this configuration. However, a minimum loss is observed for the original HSPPW, as shown in Figure 3.3c. This discrepancy is attributed to the patterning of the high-index dielectric in these waveguides, preventing the ideal case of the CGD mode. The HSPPW offers sub-wavelength confinement and relatively low propagation loss, making it an attractive choice for many applications. Experimental demonstrations have shown the realization of a plasmon laser at a deep sub-wavelength scale, utilizing a high-gain cadmium sulfide (CdS) semiconductor nanowire separated from a Ag surface by a thin Magnesium Fluoride (MgF_2) gap [126]. Another advantage of the HSPPW is the incorporation of high refractive index materials that are not in direct contact with the metal, circumventing the challenges associated with SPPs on the metal-high-index material interface. Recently, a modified form of sub-wavelength HSPPW on an SOI platform, composed of a thin SiO_2 gap between the top Au layer and the underlying Si core, has been experimentally achieved. This HSPPW exhibits sub-wavelength confinement, a propagation length of 40 µm, at telecom wavelengths. Compact S-bends and Y splitters based on this waveguide configuration have also been demonstrated [127].

3.1.3. Other Types of Plasmonic Waveguides

Numerous other types of plasmonic waveguide structures have been extensively studied in the literature. In this section, we provide a summary of the key characteristics of some of the most fundamental ones, including slot waveguides, gap waveguides, wedges, v-grooves, and nanowires. These structures are schematically illustrated in Figure 3.4. Each waveguide configuration offers unique characteristics and properties that make them attractive for various applications in nanophotonics and integrated optics. The following sections will provide an overview of these waveguide structures and their respective capabilities in guiding and manipulating light at the sub-wavelength scale.

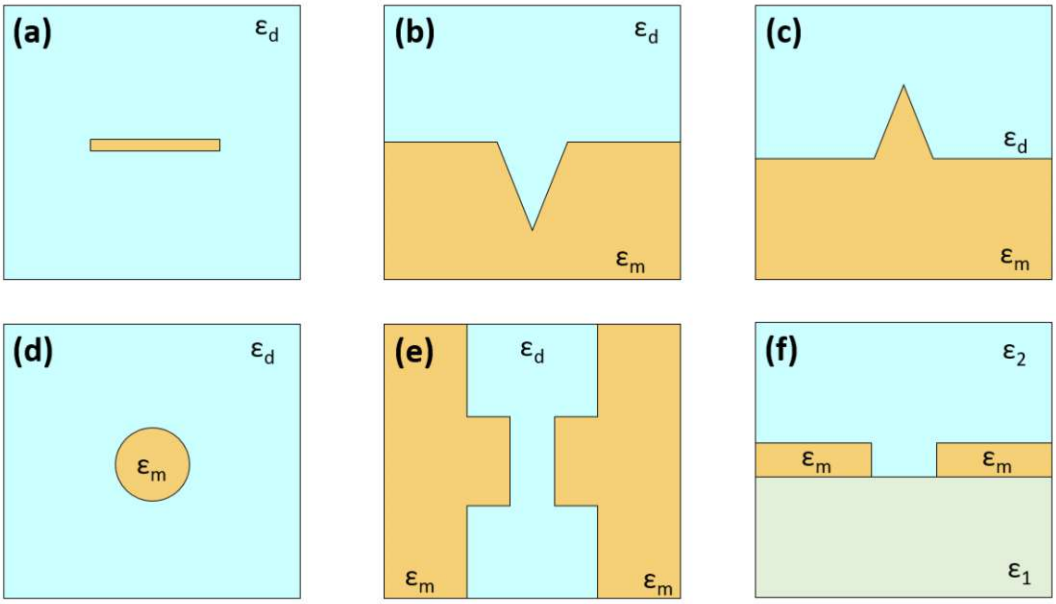

Figure 3.4 Schematic cross-section of different plasmonic waveguides, where the metallic regions are indicated by the yellow color. (a) IMI stripe, (b) V-groove, (c) Λ-wedge, (d) nanowire, (e) gap waveguide, and (f) slot waveguide.

SPP Guided by Metal Stripes

The simplest way to create lateral confinement in an IMI structure is to reduce the width of the metal that supports surface plasmons, creating a metal stripe, shown in Figure 3.4a. One notable example is the waveguide proposed by Berini [128], which consists of a thin metal strip surrounded by a homogeneous medium, enabling the support of Long-Range Surface Plasmons (LRSPs). This configuration exhibits reduced propagation loss, reaching values as low as 10 to 0.1 dB/cm at optical communication wavelengths, particularly when the strip has a thickness of 10 nm and a width of less than 1 µm. For a comprehensive review of thin metal strip waveguides, more details can be found in [129].

V-Grooves and Λ-Wedges

When a metal surface is shaped in a non-flat geometry, in some cases, it can also serve as a channel waveguide. Two commonly used geometries follow the letter 'V' (Figure 3.4b)[96] and the letter 'Λ' (Figure 3.4c) [130] shapes. These structures support surface plasmons known as channel plasmons and wedge plasmons, respectively. The confinement mechanism of channel plasmons in V-grooves was explained by Gramotnev [131] in terms of geometrical optics, where the effective index for gap mode plasmons plays a role similar to the refractive index in gradient-index optical fibers. The effective index of the antisymmetric mode in MIM structures increases as the gap width decreases, enabling the confinement of channel plasmons. A similar mechanism may apply to wedge plasmons, where symmetric modes in IMI structures are confined. Experimental observations by Bozhevolnyi et al. [132] demonstrated the confinement of channel plasmons in a V-groove with a propagation length of approximately 100 µm at telecommunication wavelengths. On the other hand, fabricating metallic Λ-wedges on a metal substrate to observe wedge plasmons requires more effort. Pile et al. [133] successfully sculptured a Λ-wedge on a 1.3 µm-thick Ag film using FIB milling and achieved a propagation length of 1.5 µm at a wavelength of 632.8 nm.

Nanowires

In contrast to the plasmonic waveguides discussed earlier, which confine surface plasmons at the metal-dielectric interface, Takahara et al. [134] introduced a different type of structure utilizing cylindrical metallic nanowires (Figure 3.4d). The TM_{01} mode is the fundamental mode in cylindrical metallic nanowires, exhibiting axisymmetric behavior with a vanishing radial component of the electric field at the wire's center. As the diameter of the nanowire decreases, the propagation constant increases while the penetration depth of the electromagnetic field into the surrounding dielectric decreases. Tong et al. [135] experimentally achieved a loss coefficient of 1.7 dB/mm in a cylindrical silica nanowire with a diameter of 190 nm at a wavelength of 633 nm. The main drawback of metallic nanowire waveguides is the increase in propagation loss as the wire diameter decreases. They can be synthesized chemically, resulting in high-quality nanowires. However, this method lacks the ability to create intricate plasmonic structures compared to other nanofabrication techniques. As a result, the manual micromanipulation technique needed to assemble the nanowires into the required geometry can be a challenging process.

Slot and Gap Waveguides

An approach to address the challenges associated with LR-SPP waveguide modes involves the utilization of MIM-like structures. Unlike the IMI structure, where LRSP modes with antisymmetric charge distribution experience lower propagation loss, in the MIM structure, modes with symmetric charge distribution exhibit reduced propagation loss [58]. However, both the propagation loss and propagation constant of the symmetric mode in a MIM structure increase as the insulator layer thickness decreases. The MIM structure confines the field within the metal layers, benefiting from the limited penetration of the field into the metal due to the large real parts of the dielectric constants of metals. Various plasmonic waveguide configurations based on the G-SPP mode have been investigated (for example, the SPP gap waveguide [136] of Figure 3.4e). However, some of these waveguides suffer from the problem of either fabrication infeasibility or characterization difficulty. Among them, the plasmonic slot waveguide (Figure 3.4f) has garnered significant attention due to its practicality and ability to support a fundamental mode with low bending loss even at small bend radii. Veronis et al. [137] have investigated the properties of plasmonic slot waveguides at telecom wavelengths. Propagation lengths are around 18 µm at 1.55 µm and can go up to 55 µm at 5 µm for gap sizes of 50 nm. The plasmonic slot waveguide offers tight confinement, low cross-talk, and low bending losses due to the relatively small penetration depth of light into the lateral metals. It allows for the integration of plasmonic devices with Silicon photonics, mitigating the high loss associated with traditional Si-based plasmonics. Fabrication techniques, such as focused ion beam milling and argon ion milling, have been employed to realize the small dimensions of the metal slot.

3.2 Simulation Tools

Numerical methods are powerful tools for modeling and simulating physics-based phenomena. Nowadays, modern simulation software can be highly precise in predicting waveguide losses, provided that the model accurately represents the physical geometry of the waveguide structure and the optical properties of the materials involved [138,139]. These methods can be employed to analyze the characteristics of optical devices. By utilizing numerical simulations, properties such as the mode field distribution, propagation constant, and attenuation coefficient can be accurately predicted, allowing for a deeper understanding of the optical device (or system) under investigation. However, there are several factors that can impact the accuracy of the simulation results. Among them, one critical factor is the quality of the input data, such as the refractive indices and other physical properties of the materials used.

Plasmonic mode properties in this thesis are calculated using the RF module of COMSOL Multiphysics software [80], employing the finite element method (FEM). Second-order scattering boundary conditions are utilized for all the simulations to mimic open boundaries. Convergence analyses have been performed to ensure the accuracy of the calculations by adjusting the simulation region until the effective indices show less than a 1% variation. To ensure the accuracy of our simulation results, we conducted mid-IR refractive index measurements with the ellipsometric technique for all the materials involved after the fabrication of plain layers (chip dimensions of at least 12x12 mm) in our cleanroom. This approach was undertaken to ensure precise input data and improve the reliability of our simulations and the success of our experiments.

3.3 Definition of Propagation Length and Mode Confinement

Propagation length

As described in Chapter 2, the propagation length is defined as:

$$L_p = \frac{1}{2\,\mathrm{Im}(\beta)} \tag{3.1}$$

where β is the propagation constant defined as $\beta = n_{eff} k_0$. It is defined as the distance that a mode can travel before the energy density decays to 1/e (approximately 37%) of its original value.

The attenuation in dB scale per meter can be calculated from the propagation constant using the formula:

$$\beta_{dB/m} = \ 20\beta \log e \tag{3.2}$$

Effective mode area

The existing definitions of modal area, derived from traditional waveguide theory, may not be suitable for accurately characterizing plasmonic modes due to the presence of sharp features and rapid sub-wavelength variations in their field distribution [140]. In order to consistently quantify the mode confinement in plasmonic waveguides, it is necessary to define a measure that takes into account the true extent of the electric field distribution. Among the various definitions proposed in the literature [140], we will focus on the one that we have found most useful for describing the mode in DLSPPWs [141]:

$$A_{eff} = \frac{1}{Max\{W(\vec{r})\}} \int_{A_\infty} W(\boldsymbol{r})\, \mathrm{d}A \tag{3.3}$$

where $W(\vec{r})$ is the energy density at position $\vec{r}$, expressed as:

$$W(\vec{r}) = \frac{1}{2} \mathrm{Re}\left\{\frac{\mathrm{d}[\omega\varepsilon(\vec{r})]}{\mathrm{d}\omega}\right\} \left|\vec{E}(\vec{r})\right|^2 + \frac{1}{2}\mu_0 \left|\vec{H}(\vec{r})\right|^2 \tag{3.4}$$

It should be noted, that the dependence of A_{eff} on the maximum energy density may lead to misleading results when dealing with waveguides that have sharp features. While this measure is helpful in quantifying the local field distribution, it does not necessarily indicate a strong confinement of total energy [140].

3.4 Figure of Merits

Plasmonic waveguides exhibit varying degrees of mode confinement and propagation losses, making direct comparisons complicated, due to the inherent trade-off between these two factors. To overcome this challenge, one or more figures of merit (FOM) are often employed to evaluate and assess plasmonic waveguide performance, taking into consideration both mode confinement and propagation losses. By utilizing the FOM, the performance of different plasmonic waveguides can be effectively compared and evaluated.

Several FOMs have been proposed in literature [140,142,143]. While plasmonic waveguides operate on similar plasmonic principles, they display distinct characteristics concerning propagation and confinement. It is crucial to consider all these effects when evaluating the FOM for a specific application. In this context, we use the following FOM, to quantify the trade-off between the propagation length normalized to the free-space wavelength and the mode size for the plasmonic materials under investigation in this thesis. It is defined as the ratio between the normalized propagation length and normalized mode area to the diffraction limit:

$$FOM = \frac{L_P \,/\, \lambda_0}{A_{eff} \,/\, A_0} \tag{3.5}$$

Where λ_0 is the free space wavelength, and A_0 is the diffraction-limited mode area, defined as:

$$A_0 = \left(\frac{\lambda_0}{2}\right)^2 = \frac{\lambda_0^2}{4} \tag{3.6}$$

4

MATERIAL CONSIDERATIONS FOR MID-IR PLASMONIC WAVEGUIDES

A major consideration in plasmonic waveguide design is the choice of materials. While the field of plasmonics has predominantly focused on shorter optical frequencies, there is significant untapped potential in the mid-IR wavelength range. To unlock the full potential of integrated plasmonic solutions, it is essential to engineer and employ suitable plasmonic materials (and material combinations), that offer favorable trade-offs for the specific application. Moreover, despite the significant advancements in integrated photonics for VIS and near-IR, the mid-IR has received less attention in the past, with new solutions being developed only in recent years. Traditional waveguide platforms, such as Silicon-On-Insulator (SOI), are not suitable for the entire mid-IR regime, necessitating the exploration of novel waveguide platforms, materials, and integration strategies. The ideal waveguiding solutions should meet at least three key requirements: low loss (allowing propagation for the desired distances), feasibility of fabrication and integration (for cost-effectiveness), and suitable mode confinement (for photonic circuit miniaturization). This chapter reviews available plasmonic materials for mid-IR photonic applications. As the field is rather broad, we will limit here the discussion to SPP waveguiding applications. The aim is to offer a concise overview of the current state of research on mid-IR plasmonic materials, along with a discussion of promising materials for mid-IR surface loading. The content of this chapter is derived from comprehensive reviews [62], [144] and [27].

4.1 Comparison of Different Mid-IR Plasmonic Materials

In contrast to LSPs, which require plasmonic/phononic materials with permittivity similar to the surrounding dielectric in the mid-IR, all conductive materials with a negative permittivity spectrum have the capability to support SPPs. Figure 4.1 presents a valuable summary of the wavelength-dependent characteristics of SPPs for different conductive materials [62]. It shows the SPP propagation length (L_{SPP}), mode penetration into the dielectric (i.e., air, here denoted as δ_{SPP}), and two FOMs: M_{1SPP} (= L_{SPP}/δ_{SPP}) and M_{2SPP} (= $\varepsilon_m''^2 / \varepsilon_m'$). These metrics help evaluate the confinement-to-propagation trade-off and determine a material's suitability for SPP-based applications. Specifically, M_{1SPP} is especially useful in evaluating the propagation length in relation to the extent of mode penetration within the dielectric.

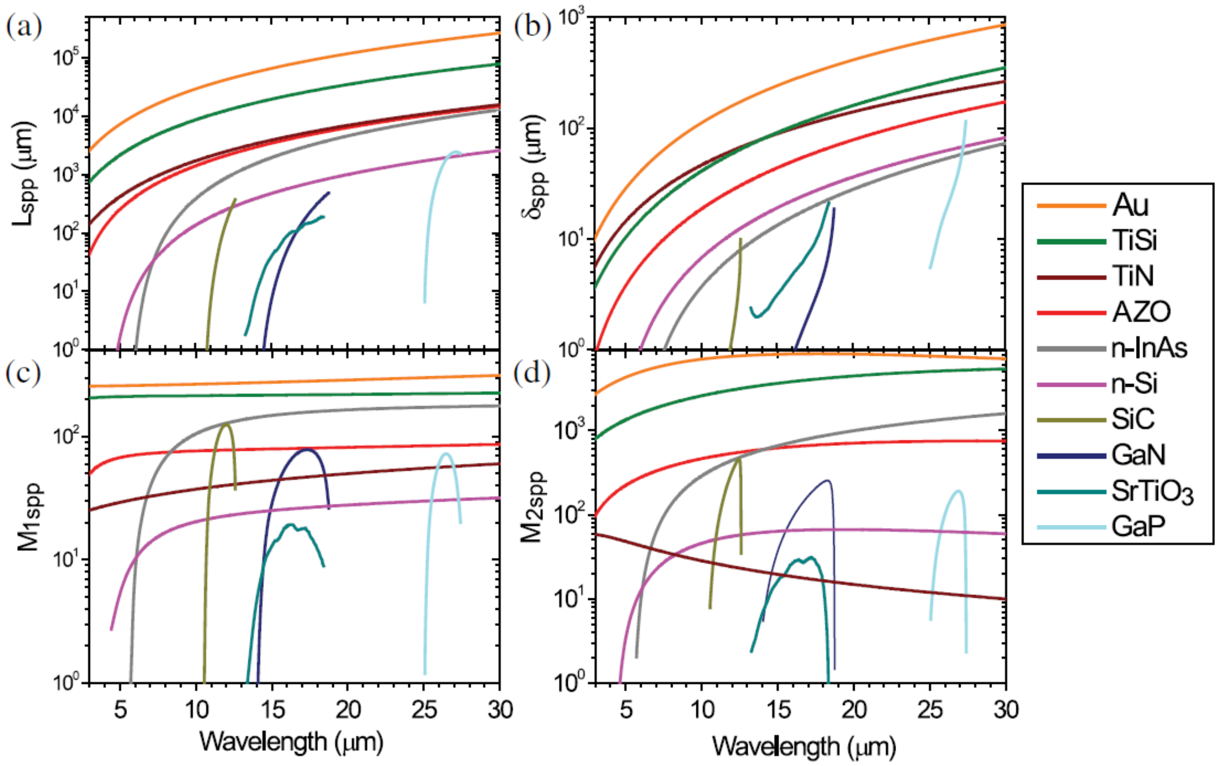

Figure 4.1 The SPP characteristics of different plasmonic materials. a) variation of the propagation length, b) mode confinement, c) figure of merit $M_{1SPP} = L_{SPP}/\delta_{SPP}$, and (d) figure of merit $M_{2SPP} = \varepsilon_m''^2 / \varepsilon_m'$ with respect to wavelength. Image taken from [62].

Among the materials investigated, Au demonstrates the highest FOMs for mid-IR SPPs due to their strongly negative permittivity in this spectral range [62]. However, as we have seen previously, noble metal-based SPP structures exhibit significant mode extension into the dielectric material, rendering them unsuitable for sub-wavelength optics at mid-IR wavelengths. To achieve confinement below a free-space wavelength, doped semiconductors and phononic materials emerge as viable options. However, recent modeling studies have shown that, for example, heavily doped Ge-based devices do not outperform Au-based sensing platforms in certain regimes [145]. Notably, the silicides, represented by TiSi in Figure 4.1, offer a favorable compromise between long propagation length, high FOM, and reasonable confinement factors across multiple wavelengths [62]. Their compatibility with Si-processing makes silicides promising candidates for plasmonic waveguiding materials in the IR frequency range.

On the other hand, the prevalence of Au as a preferred metal for electrical contacts in mid-to-far IR photonic devices motivates its choice as a plasmonic layer for surface waveguiding, also in the mid-IR range. However, in order to achieve a practical level of mode confinement, alternative approaches, such as the utilization of specialized waveguiding architectures introduced in Section 3.1 are necessary. Among these strategies, dielectric loading stands out as a particularly attractive approach due to its simplicity and effectiveness.

4.2 Comparison of Different Dielectric Materials for Surface Loading

4.2.1. Transparent Inorganic Materials

Passive components made of optically transparent materials play a critical role in light-transmitting networks within photonic circuits. However, in the mid-IR range, the transparency of materials is limited due to phonon absorption. To expand the transparency window in the mid-IR, lighter elements are substituted with heavier ones to lower the characteristic phonon frequency [26]. Figure 4.2 shows a comparison of the transparency windows of different optical materials. The figure provides valuable data for photonic designers, aiding them in selecting appropriate passive material platforms across different segments of the mid-IR range.

Ge exhibits transparency up to 14.6 µm in the mid-IR, surpassing the one of Si (6.8 µm) [146]. Similarly, replacing oxygen with heavier chalcogens extends the transmission window, overcoming the limited transmission capability of oxides beyond 5 µm. For wavelengths below 3.5 µm, standard SOI or SiNx on SiO_2 can be utilized, as the silicon dioxide cladding remains optically transparent in this range [147,148]. Several compositions of chalcogenide and halide materials are being utilized to create thin-film waveguides, leveraging the high refractive index contrast between the chalcogenide layer and a suitable substrate [149]. However, they present certain challenges in their fabrication process, as they can be rather complex [33] and, moreover, not compatible with CMOS foundry processes. Additionally, it is important to note that some of these materials may have toxic properties, requiring careful handling during manufacturing processes as well as particular consideration of environmental factors [27].

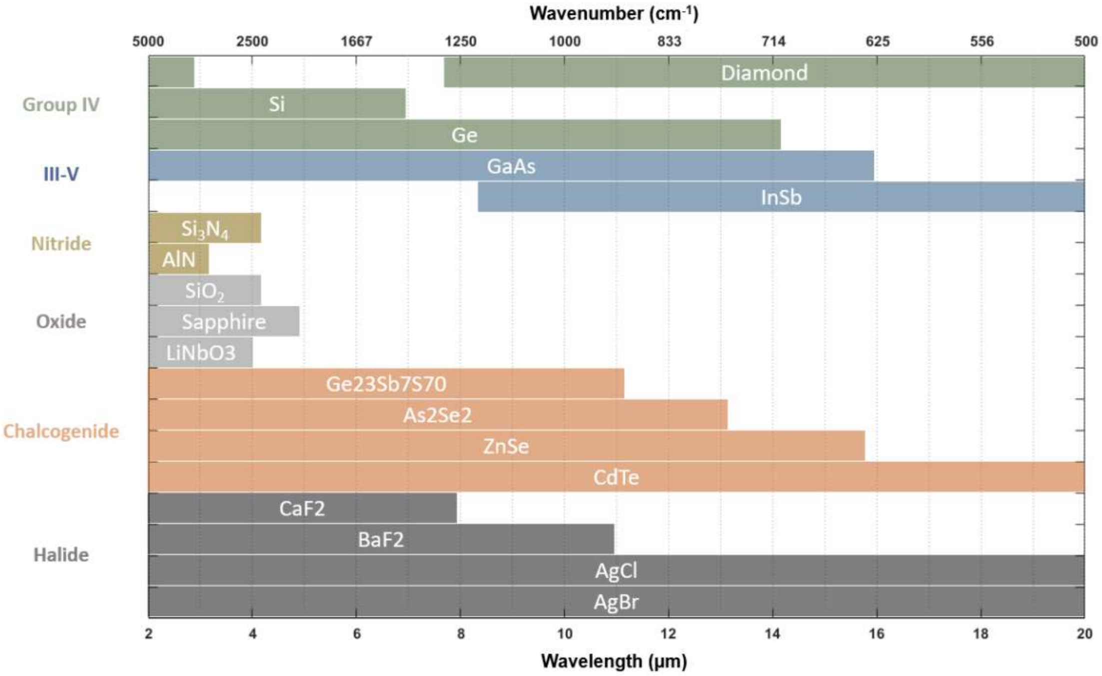

Figure 4.2 The figure provides an overview of the main mid-IR transmitting waveguide materials. The depicted bars illustrate the transparency windows of different materials, indicating regions where the material attenuation is below 1 dB/cm. The figure was derived from data published in [26].

Figure 4.3 illustrates the influence of the material losses on the propagation length of a DLSPPW based on Au and Ge and Au and SiNx for various mid-IR wavelengths. In this example, the waveguide geometry was adjusted by keeping the width equal to the wavelength (w=λ) and adjusting the thickness in order to maintain an almost constant effective mode area (A_{eff}). The A_{eff} was kept from 25 µm^2 to 45 µm^2. Therefore, the figure demonstrates that Ge exhibits superior performance above 6 µm wavelength in terms of both absolute propagation length (Figure 4.3a) and propagation per mode size (FOM, Figure 4.3b). The simulation results suggest that Ge can be a promising solution for mid-IR applications where longer propagation distances are desired.

Hence, considering the wide transparency range, the superior performance in the LWIR range, and the well-established processing protocols, together with its CMOS compatibility, Ge represents as a highly promising loading material for DLSPPWs for mid-IR PICs.

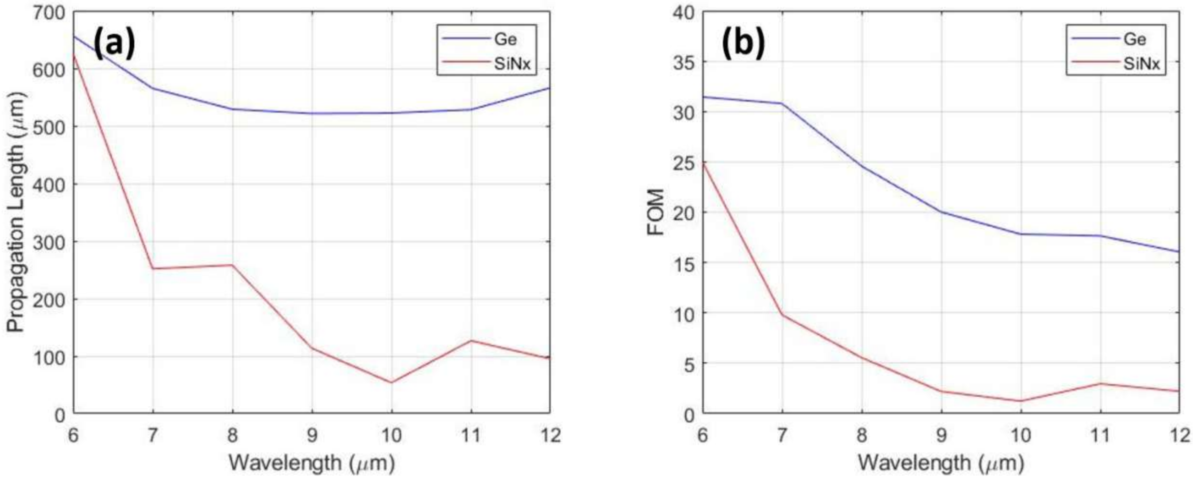

Figure 4.3 Simulations of the impact of the material losses on the propagation length of a DLSPPW based on Au and Ge (blue color) or Si_3N_4. (red color), for different mid-IR wavelengths. The dielectric geometry was adapted by keeping the width equal to the wavelength ($w = \lambda$) and asjusting the thickness in order to keep the A_{eff} almost constant (around 25-45 μm^2). Ge shows better performance in terms of a) propagation length. When considering the b) FOM (i.e., the propagation length normalized per Aff), Ge-loading surpasses Si_3N_4 for all the wavelengths between 6 and 12 μm.

4.2.2. Transparent Organic Materials

Polymers possess unique and adjustable properties that make them highly versatile for a wide range of applications. Their optical properties, in particular, along with the ability to develop novel composite materials, simple processing techniques, and diverse functionalization possibilities, position polymers as advantageous materials for many optoelectronic applications [150]. The use of polymers for waveguiding applications has several advantages. Firstly, they exhibit a low refractive index (useful to minimize interface reflections) and high transparency for wide spectral regions [151]. Secondly, polymers can be easily processed and fabricated using techniques such as spin coating, imprint lithography, or photolithography [152,153] (see Section 5.1 for more details about fabrication techniques). This enables cost-effective and scalable manufacturing of integrated photonic components, making them more accessible for practical fabrication [152]. High-quality thin films can be deposited with cost-effective spin-coating techniques that are routinely employed in the microelectronic industry. The thickness of the film can be achieved by manipulating the viscosity of the polymer solution and/or adjusting the speed of the spin-coating process. Thus, polymer films can be obtained rapidly and without the use of expensive deposition techniques, especially compared to SOI and III-V materials, that necessitate the use of epitaxial growth or physical or chemical vapor deposition (PVD or CVD). Some polymers can even be directly patterned using lithography and a wet development step, eliminating the need for costly plasma etching tools. Additionally, they offer flexibility and compatibility with various substrate materials, allowing for versatile integration into different photonic systems. Their mechanical flexibility enables the fabrication of bendable waveguides and fibers, and the integration on non-planar surfaces. Moreover, polymers can be engineered to have tunable optical properties through modifications in their chemical composition or by incorporating additives. This tunability allows for tailoring the refractive index, dispersion, and other optical characteristics of the polymer, enabling precise control over the waveguide's performance and functionality [117]. Lastly, polymers are considered lightweight, durable, biocompatible, and resistant to environmental factors, making them suitable for a wide range of applications, including sensing and bioengineering [154].

These factors collectively motivate the research of mid-IR transparent polymers for waveguides, offering a versatile and practical platform for integrated optics.

Mid-IR transparent polymers

Even though polymers have attracted significant attention for integrated optical applications for many years [152,155], most of the research and commercial products focus on the VIS and near-IR spectral ranges [156]. There has been limited progress in the development of polymer materials and waveguides specifically tailored for the mid-IR spectral range [26].

In the near-IR range, polymer materials such as PMMA and SU-8 are frequently selected for use in plasmonic devices [157–159]. However, neither of these materials can provide high transparency in the mid-IR spectral range (especially in the 6-12 µm band) due to the presence of multiple absorption lines situated in the LWIR (see Figure 4.4) [160,161].

In contrast, PE exhibits broad transparency across a wide spectral range [162,163]. Recently, it has been used as a broadband interconnector [164], flexible antenna [165], and sensor platform [166] in the THz spectral region (>20 µm). Moreover, theoretical studies have demonstrated its potential as a core material for DLSPPW also at telecom frequencies [167] and as a cladding layer for HSPPW waveguides for THz frequencies [168,169]. Therefore, in this thesis, considering the advantages of polymer-based waveguides and the desirable properties of polymers for dielectric loading, the focus has been directed towards examining the structural and optical characteristics of spin-coated PE films within the mid-IR frequency range. To achieve this, our research focuses on investigating novel fabrication techniques that enable repeatable and precise thin film deposition with excellent layer quality. Additionally, we explore the use of UV-lithographic patterning methods to provide the first experimental demonstration of the use of PE at mid-IR frequencies.

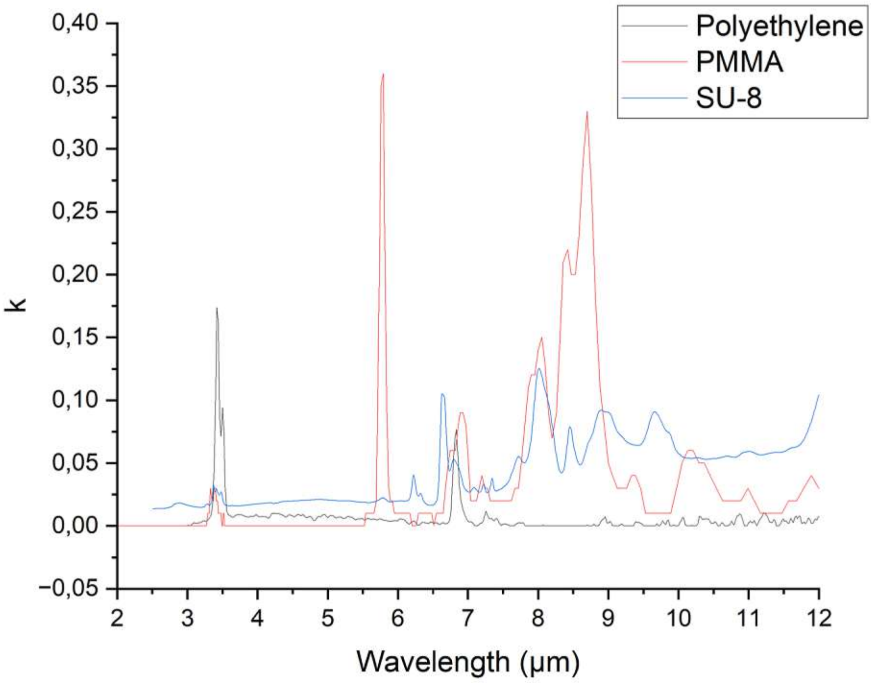

Figure 4.4 Imaginary part of the complex refractive index of the most used polymers in VIS and near-IR integrated photonics. PE is the only one that does not have absorption lines in the LWIR. Data taken from [160–162]

4.3 Final Considerations

So far, the majority of investigated plasmonic materials exhibit incompatibility with III-V substrate platforms. Given our aim to explore plasmonic solutions capable of enabling compact, low-loss optical interconnects for miniaturized mid-IR PICs, we chose to leverage the advantageous characteristics of conventional metals, such as their long propagation lengths, and employ loading techniques to enhance mode confinement. This approach not only enables to achieve mode sizes suitable for integration with mid-IR active components, specifically QCLs and QCDs, but also ensures a favorable balance between ease of integration and the necessary propagation length for on-chip applications.

When examining materials with high transparency in the mid-IR frequency range, particularly within the critical 6-12 µm region, Ge emerges as one of the most favorable options. It possesses low broadband absorption and relatively low refractive index dispersion, making it an excellent choice. Indeed, alongside Si, Ge is widely accepted as the optimal material platform for integrated photonics within this frequency range [170].

On the other hand, polymers have gained significant attention in the field of integrated photonics. When combined with the sub-wavelength properties of plasmonic structures, the challenges associated with their inherently low refractive index (larger device sizes, limiting integration density) can be counterbalanced. We will show in Chapter 6 that, when used in conjunction with Au layers in DLSPPWs configurations, they provide a favorable trade-off between low-loss and mode confinement.

Hence, in this thesis, the focus is directed towards two materials - Ge and PE - and their characteristics are examined when combined with Au for developing low-loss DLSPPWs for the mid-IR region.

5

FABRICATION AND CHARACTERIZATION TECHNIQUES

This chapter discusses the techniques used to fabricate and analyze PE-based and Ge-based DLSPPWs, including a concise overview of the various photonic integration strategies employed in the fabrication of photonic devices. The main source used for the fundamentals are the books by Peter M. Martin [171] and by M. Madou [172]. The final section of this chapter discusses the materials and characterization techniques used to analyze the properties and performance of the fabricated devices.

5.1 Fabrication Techniques

Fabrication techniques play a critical role in the development of photonic components. Their scope is to create complex and precise structures on a microscopic scale, in order to achieve the desired device functionality. A wide range of processes are typically performed during device fabrication, including photolithography, etching, material deposition, device cleaving, and bonding. These manufacturing procedures are typically sequentially executed in a unique and ordered combination to achieve the intended device architecture. In this section, the commonly employed fabrication techniques utilized in the manufacturing of photonic devices are discussed, with focus on the ones used for the waveguides fabricated in this thesis. Details about the clean room tools used can be found in *Appendix B:Clean Room Tools*.

5.1.1. Polymer Film Preparation

Polymers have been widely used for integrated photonics applications [152,173]. There are various methods of polymer thin film deposition.

Spin-coating

Spin-coating is a simple and versatile method for the fabrication of polymer thin films, and it is compatible with a wide range of substrates and polymer materials. In this technique, a polymer solution is dispensed onto a substrate, typically using a pipette. The solution can be dispensed using two primary methods: dynamic dispense, when the substrate is already rotating, or static dispense, when the substrate starts spinning after the deposition of the solution onto the substrate. The substrate is rotated at high speed, typically between a few hundred to a few thousand rounds per minute (RPM) [174]. The centrifugal force generated by the rotation causes the polymer solution to spread out and form a uniform thin film on the substrate. The thickness of the resulting film depends on several factors, including the viscosity of the polymer solution, the speed of rotation, and the concentration of the polymer in the solution [175]. After the spin-coating process is finished, the polymer film is typically annealed or cured to evaporate the remaining solvent [176]. The fabrication procedure is illustrated schematically in Figure 5.1.

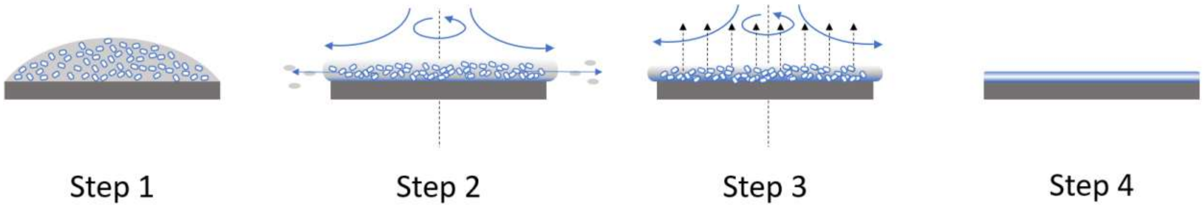

Figure 5.1 Demonstration of the spin coating technique using a static dispense method. Initially, the substrate is coated with the solution containing the molecules dissolved in a solvent with the target weight ratio (Step 1). Subsequently, the substrate is rotated at high speed, causing most of the solution to be expelled from the side due to centrifugal force (Step 2). Following this, airflow facilitates the evaporation process, removing the majority of the solvent, resulting in a plasticized film (Step 3). Finally, the film dries further until only the polymer molecules remain deposited on the surface (Step 4) [176].

Other techniques

Other techniques that can be used for polymer film preparation include dip coating, spray coating, and casting [177]. Dip coating consists of immersing a substrate into a polymer solution and then slowly withdrawing it to form a thin film. Spray coating involves spraying a polymer solution onto the substrate. Polymer deposition by casting is another common technique. It involves the process of pouring a liquid polymer solution or suspension onto a substrate and allowing it to spread and form a thin film as the solvent evaporates or undergoes a curing process.

However, compared to these techniques, spin-coating offers some advantages. Firstly, it produces films with a high degree of uniformity and thickness control, which is critical for microelectronic and photonics applications. In contrast, dip coating and spray coating can result in non-uniform thickness and poor film quality. Secondly, the spin-coating process is highly reproducible, efficient, and cost-effective, requiring only a spin-coater and a minimal amount of polymer solution compared to other techniques, like dip-coating. Finally, spin-coating is compatible with a wide range of substrates and polymer materials, making it a versatile technique for the preparation of thin films. Overall, the advantages inherent in spin-coating render it the optimal technique for preparing high-quality polymer thin films in the context of photonic applications [177,178].

The role of humidity

It is important to note that humidity can play a critical role in polymer film fabrication. High levels of humidity in the environment can affect the quality and properties of polymer thin films [179,180]. This is because some polymers are hygroscopic, meaning they can absorb moisture from the air, which can lead to changes in their chemical and physical properties. For example, high humidity can cause the formation of water droplets on the surface of the substrate during the spin-coating process, which can result in non-uniform film thickness and poor film quality. Additionally, high humidity can affect the adhesion between the polymer film and the substrate, which can lead to delamination or cracking of the film. Therefore, it is important to control the humidity levels during the fabrication of polymer films to ensure consistent and reproducible film quality. This can be achieved by using a controlled environment with low humidity or by using a humidity-controlled spin-coater.

Photoresists

Photoresists are light-sensitive polymers that are used to transfer a pattern onto a substrate. They are typically made up of a polymer matrix, which is combined with a photosensitive compound called a Photo-Active Compound (PAC). When exposed to light, the PAC in the photoresist undergoes a chemical change, which causes a change in the solubility of the resist material. As a result, the exposed regions of the resist experience selective changes in solubility, ultimately leaving behind a patterned layer of resist on the substrate after developing. There are two main types of photoresists: positive and negative. In positive photoresists, the areas exposed to light become more soluble and are removed during development, leaving behind the unexposed areas as the patterned layer [174]. In negative photoresists, the areas exposed to light become less soluble due to cross-linking of the polymer molecules under illumination and are retained during development, leaving behind the exposed areas as the patterned layer.

5.1.2. Optical Contact Lithography

Optical lithography is a key technique in the fabrication of photonic devices. It involves the use of light to transfer a pattern from a photomask onto a substrate coated with a photoresist. The process begins with the design of a photomask, a patterned template that is used to transfer the desired pattern on the chip substrate. The photomask is typically made of a thin layer of chrome (or other opaque material that blocks UV light), which is evaporated onto a UV-transparent glass substrate, allowing light to pass through in the areas without chrome. The photomask is then placed in close proximity to the substrate coated with the photoresist. Light is then shone through the photomask onto the photoresist, exposing it in the pattern defined by the mask. After exposure, the photoresist is developed, which selectively removes the exposed (or unexposed, in case of negative resist) areas, leaving behind a patterned layer on the substrate. The patterned layer can then be used as a template for further processing steps, such as etching or layer deposition, to create the final structured photonic device. In general, the theoretical limit of resolution for optical lithography is determined by the diffraction limit of light, which is given by the Rayleigh criterion [174]. For a given wavelength of light (λ) and numerical aperture (NA) of a lens, the resolution is given by:

$$\text{Resolution} \approx \lambda \,/\, (2 \text{ x NA}) \tag{5.1}$$

For VIS light with a wavelength of around 400-700 nm and a typical lens with a numerical aperture of 0.9, the theoretical limit of resolution is around 200-350 nm. However, in practice, the achievable resolution is often lower than this value due to various factors such as lens aberrations, resist performance, and process variations. With advanced techniques such as immersion lithography, multiple patterning, and resolution enhancement techniques, sub-100 nm feature sizes have been achieved using optical lithography [181]. It is worth noting that there are other lithographic techniques that can achieve higher resolution, such as electron beam lithography and deep UV lithography [174]. However, these techniques often require more complex and expensive equipment and may have lower throughput, making them less suitable for large-scale fabrication.

5.1.3. Layer Deposition Techniques

There are several deposition techniques used to create thin films or layers of materials on a substrate. In this section, we will discuss some of the commonly used ones (with the exception of spin coating, which is covered in the section *Polymer Film Preparation*).

Chemical Vapor Deposition (CVD)

CVD is a widely used fabrication technique in the manufacturing of semiconductors and optical coatings. Also known as vapor plating, it involves the deposition of atoms or molecules through the high temperature reduction or decomposition of a chemical vapor precursor species. This precursor contains the material intended for deposition, and reduction typically occurs through hydrogen at an elevated temperature. Thermal activation is employed for decomposition. During CVD, the deposited material may react with other gaseous species in the system, resulting in the formation of compounds such as oxides or nitrides. This process often produces volatile reaction byproducts and unused precursor species. Other variations of CVD include vapor phase epitaxy (VPE), which is utilized for depositing single crystal films, MOCVD when a metal-organic species serves as a precursor gas, plasma-enhanced CVD (PECVD) when plasma is employed to enhance decomposition and reaction, and low pressure CVD (LPCVD) when the pressure is below ambient [182].

Atomic Layer Deposition (ALD)

ALD is a gas-phase thin film deposition technique that relies on sequential, self-saturating surface reactions. During ALD, chemical precursors containing specific elements of the target material are introduced individually to the reactor chamber. With each introduction, the substrate surface becomes saturated, forming a monolayer of material on its surface. Short pulses of precursor chemicals are injected into the carrier gas flow, separated by brief purge or evacuation intervals. Each ALD cycle (consisting of a precursor 1 pulse, purge, precursor 2 pulse, and purge) leads to the growth of a precisely defined amount (typically around 1 Å) of the thin film material. The duration of each cycle ranges from one to several seconds, with process temperatures varying from room temperature to over 500°C. However, most ALD processes operate within the range of 200°C to 400°C. ALD techniques have been developed for various materials, including oxides, nitrides, carbides, fluorides, certain metals, II-VI and III-V compounds, and more recently, organic materials [171]. ALD is a deposition technique that is closely related to CVD. However, while both ALD and CVD rely on chemical reactions in a gas phase to deposit thin films, the key difference is that ALD is based on a self-limiting surface reaction, which enables precise control over the thickness and composition of the deposited film [183].

Physical Vapor Deposition (PVD)

PVD processes involve the deposition of material at the atomic or molecular level by vaporizing it from a solid or liquid source. This vapor then travels through a vacuum or low-pressure environment, such as a gas or plasma, to reach the substrate where it condenses. PVD is commonly employed for depositing thin films ranging from a few nanometers to thousands of nanometers in thickness. Additionally, PVD techniques can be utilized for creating multilayer coatings, graded composition deposits, thick deposits, and even freestanding structures. PVD processing techniques encompass a range of methods, including vacuum evaporation, sputter deposition in a plasma environment, sputter deposition in a vacuum, ion plating in a plasma environment with a thermal evaporation source, ion plating with a sputtering source, ion plating with an arc vaporization source, and ion beam-assisted deposition (IBAD) with a thermal evaporation source and ion bombardment from an ion gun [182].

Electroplating

Electroplating is a technique used to deposit metal films onto a substrate. In this method, an electric current is passed through an electrolyte solution containing the metal ions to be deposited. The metal ions then plate onto the substrate, forming a thin film [182].

5.1.4. Etching Techniques

Etching is a process used to selectively remove material from a substrate to create patterns, features, and structures. The choice of the chemicals to be used depends on the materials involved in the process. In this section, some of the commonly used etching techniques are briefly discussed.

Wet Etching

Wet etching is a technique that involves the use of liquid chemical solutions. The etchant solution chemically reacts with the material, dissolving it and leaving behind the desired pattern or structure. Wet etching is relatively simple, cost-effective, and widely used in the semiconductor industry for the production of simple and complex devices. However, its lack of precision can make it difficult to control the etching process, leading to non-uniform etching. In many cases, it can also be not selective enough to etch specific materials or patterns, and the chemical solutions used can be hazardous, corrosive, or incompatible with the substrate. Moreover, wet etching can cause under-etching, which can be problematic when high aspect ratio features are required. These drawbacks have led to the development of dry etching techniques, such as reactive ion etching (RIE), which offer more precise, selective, and controlled etching [184].

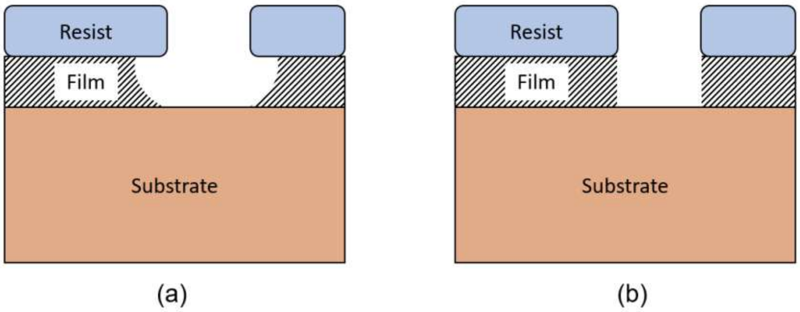

Figure 5.2 Difference in profile etched with (a) isotropic wet chemical etching and (b) dry anisotropic etching in a RIE etching system.

Dry Etching

Dry plasma etching is widely used in microelectronic and photonic fabrication to achieve highly anisotropic etching profiles with typically reduced undercutting known from wet etching processes (see Figure 5.2) the under-etching problem associated with wet processes (see Figure 5.2). It requires minimal reactant gases compared to wet etching, reducing liquid chemical waste disposal. Plasma systems utilize RF excitation to ionize various source gases in a vacuum. Operating at 13.56 MHz or at low frequencies of a few hundred kilohertz, these systems offer different modes based on pressure and chamber structure [184]. The standard plasma etching process, conducted at high pressure, employs a parallel-plate plasma-etching system. Free radicals generated in the plasma, such as fluorine or chlorine, react with the wafer surface to etch various materials. Isotropic etching is the primary process, but additional atomic species like argon, hydrogen, and oxygen can be introduced for improved etch rate [184]. Ion milling involves bombarding the wafer surface with energetic noble gas ions like Ar^+ to physically remove atoms. It offers highly anisotropic etching but typically lacks selectivity. Barrier materials, such as metals, can be utilized to protect the wafer from etching. Ion milling operates at low pressures and relies on an external dc-bias voltage to accelerate ions toward the surface [184].

Reactive-ion etching (RIE) combines plasma and sputter etching processes. Reactive gases are ionized in the plasma system, and the resulting ions are accelerated to bombard the surface. This process combines chemical reactions and momentum transfer for highly anisotropic etching. An asymmetrical plasma chamber structure with a larger grounded upper electrode, and the wafer placed on the RF-driven lower electrode enables the required acceleration potential for ion direction towards the wafer surface [184].

5.1.5. Device Dicing Methods

Device dicing is the process of separating individual components from a larger wafer or substrate. This is typically done after the components have been fabricated and before they are assembled into a complete device. Multiple techniques are employed for device dicing, which can be broadly categorized into mechanical dicing, laser dicing, and chemical etching [185,186].

Mechanical Dicing

Mechanical dicing is a simple and commonly used technique for separating components from larger wafers or substrates. It is usually performed by using a diamond-tipped tool (or saw) to scratch a line on the wafer (or part of it, in case of crystalline materials) and then applying pressure to break the material along the previously scratched line. Mechanical dicing can be used with a wide range of materials and is relatively inexpensive, but it can be difficult to control the cleave and can result in damage to the components [185].

Dicing can be performed either manually by hand or with the aid of specialized machines. In device prototyping, hand dicing is commonly favored, utilizing diamond pen scribers for placing fine marks and scribing the wafer surface. However, hand dicing may be less precise compared to machine dicing and not suitable for large fabrication volumes. Machine dicing provides distinct advantages in terms of superior precision and efficiency, thanks to the capability of scribing and breaking automation. This makes machine dicing particularly well-suited for large-scale production, and/or where consistent and precise results are essential.

Both techniques were used for creating the final devices. Figure 5.3 demonstrates the results of various dicing tests achieved with the Microtechnic Scriber S100, as well as images of waveguide samples specifically fabricated for this thesis.

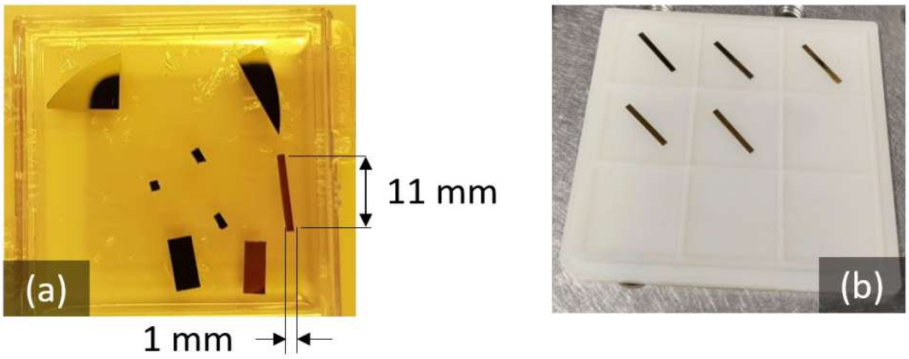

Figure 5.3 The figure shows (a) different dicing tests of a Si substrate obtained using the Microtechnich Scriber S100, highlighting the typical device aspect ratio of the devices presented in this thesis. (b) Typical waveguide samples fabricated through machine-assisted mechanical dicing for this thesis [141] from 2-inch size, 275 µm thick double-side polished Si 100 wafers.

Laser Dicing

Laser dicing is a technique for separating components from a larger wafer or substrate using a laser [187]. The laser is used to heat a small area of the wafer or substrate, causing it to expand and break along a predefined cleave line [185]. Laser dicing can be more precise and used with a wide range of materials. However, it requires specialized equipment and can be expensive [186].

Chemical Etching

Chemical etching is a technique for selectively removing material from a wafer or substrate to create a cleave line [185]. The wafer or substrate is typically coated with a mask material and then exposed to a chemical that selectively etches away the material not protected by the mask. The mask is then removed, and the wafer or substrate is cleaved along the etched line. Chemical etching can be precise and used with a wide range of materials, but it can be time-consuming and requires expensive tools [186].

5.1.6. Photonic Device Integration Strategies

Photonic device integration is the process of combining different components or devices on a single substrate in order to improve performance, reduce size and cost, and increase stability and functionality. Research in the field of photonic integration is quite active [188]. There are several approaches to photonic device integration, including monolithic, hybrid, and heterogeneous integration. In this section, we will briefly discuss each approach. Every technique has its own advantages and disadvantages, and the choice of the type of integration depends on the specific application requirements and design constraints.

Monolithic Integration

Monolithic integration involves fabricating all the components of an optical system on a single substrate (or material system) using a single technology platform at the packaging state. This technique offers the advantage of high integration density, low cost, and high reproducibility. The monolithic approach is typically the preferred choice, particularly well suited for applications where high-volume manufacturing is required. By fabricating all the components of an optical system on a single substrate, the production cost is reduced, as fewer processing steps are required, and the yield is improved, as there is less chance of misalignment or other errors during assembly. The stability and robustness of the devices are also typically superior compared to other approaches, which is of significant importance, especially for aerospace and satellite applications [189]. However, one of the critical challenges in monolithic integration is the limited choice of materials that can be integrated on a single substrate. This is because the different materials used for photonic devices often have different lattice constants, thermal expansion coefficients, and other properties that can lead to strain and defects during growth and processing [190,191]. To avoid these limitations hybrid and heterogeneous integration can be used [188].

Hybrid Integration

Hybrid integration is a post-processing step that involves combining two or more PIC or photonic devices from different materials on one single chip. This approach allows the integration of materials with complementary properties, enabling the creation of more complex and functional optical systems. Hybrid integration is typically performed using various bonding techniques. The components can be fabricated using technologies from different material systems, such as Si, InP, GaAs, or polymers, and combined on a single chip. The main advantage over monolithic integration is the ability to combine materials with different properties, which can enable the creation of devices with higher performance and functionality. Therefore hybrid integration allows for more flexibility in the design and fabrication process, as different components can be optimized independently, unlike monolithic integration, where the optimization process must accommodate all components using the same fabrication process. Another advantage of hybrid integration is the ability to use off-the-shelf components, which can reduce the time and cost associated with developing and fabricating custom components. However, hybrid integration also has some drawbacks. One of the main challenges is ensuring the precise alignment of the different components. The bonding process can also introduce additional loss and other performance limitations, impacting the overall device performance. Moreover, the photonic device alignment and integration process is a serial process, which can lead to limited fabrication throughput. This makes this process less attractive for PICs for large production volumes. Despite these challenges, hybrid integration has been successfully used in a range of applications. Examples of hybrid integrated devices include Si photonic circuitry and III-V lasers [38], which are widely used in optical communications, and Silicon photonics with $LiNbO_3$ modulators [192].

Heterogeneous Integration

Heterogeneous integration, like hybrid integration, involves combining different materials and devices on a single chip. However, unlike hybrid integration, the process is generally performed at the early- to mid stages of fabrication. The key benefit is that it can provide functionalities similar to the monolithic integration (high alignment accuracy and high volume production) while also presenting similar advantages to the hybrid integration (combination of different materials, as, for example, wafer-scale integration of III-V lasers on Si [193]). However, while hybrid integration requires less specialized equipment, which makes it less expensive and more flexible, heterogeneous integration is more suitable for mass production.

In conclusion, hybrid integration may be a suitable approach for prototyping and low-volume production. Monolithic or heterogeneous integration may be the better choice for mass production and high-performance devices.

5.2 Characterization Methods

Material characterization is an essential aspect of the development and optimization of photonic devices. Various characterization techniques have been developed over the years to provide information on the properties of materials, such as their thickness, refractive index, and surface roughness. Some of the most commonly used techniques for material characterization include profilometry, atomic force microscopy (AFM), scanning electron microscopy (SEM), and ellipsometry [171]. In addition to material characterization, it is also crucial to characterize the performance of passive photonic devices. One powerful technique for characterizing these devices is the effective cut-back method, which involves measuring the transmission through a series of waveguides of varying lengths. This technique allows for the determination of key parameters such as waveguide loss, coupling loss, and bend loss, providing valuable insights into the overall device performance. This section briefly explains materials and device characterization techniques used to evaluate material quality as well as the waveguide losses of the devices investigated in this work.

5.2.1. Material Characterization

The fabrication process can have a significant impact on the final properties of a material, including its structural, optical, and electrical properties. For instance, in deposition techniques such as physical vapor deposition (PVD) or CVD, changing the deposition temperature and pressure can alter the packing density of the deposited material, which in turn affects its optical and mechanical properties. Therefore, it follows that the technique selected for the fabrication may play a crucial role, as a change in the material properties can lead to a high degree of divergence from simulations results and device performance. In other words, the success of the designed device heavily depends on selecting an appropriate fabrication technique that can produce the desired material properties with high accuracy and high repeatability. To investigate the surface and optical properties of the materials fabricated used for dielectric loading in this work, several material techniques were used. During and after fabrication, the final devices were analyzed by optical microscopy to briefly verify their compliance with the intended design. The profilometer was used to quickly assess the height of the ridge structures, as well as surface waviness. AFM was used to get more precise information on surface roughness. SEM was utilized as an additional technique for detailed structure and fabrication defects analysis.

Optical Microscopy

Optical microscopy is one of the most commonly used techniques for material and device characterization. It provides high-resolution images of the fabricated surface, which can be used to study its microstructures. It allows a quick and easy investigation of the sample under analysis. As an example, Figure 5.4 presents two examples of 3 μm wide PE waveguides. Figure 5.4(a) demonstrates a successfully fabricated waveguide, while (b) exhibits mouse bite defects (darker parts) resulting from under-etching. Further information on these defects can be found in Section 6.3.

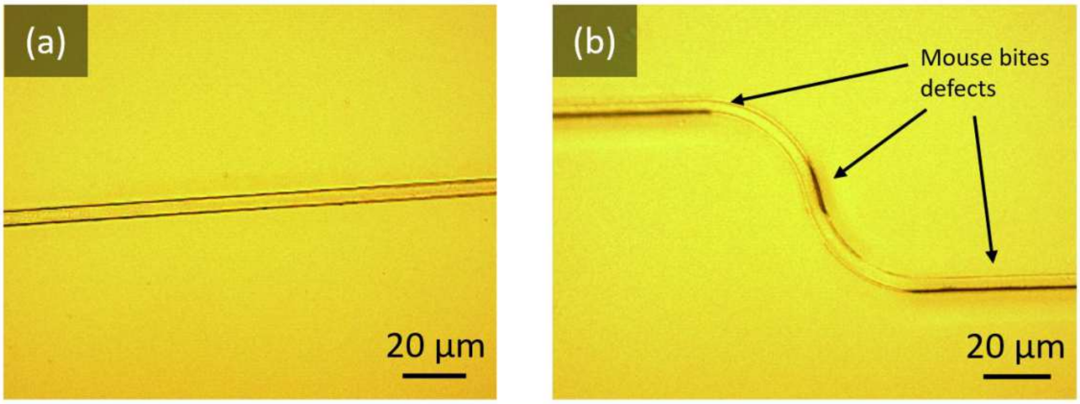

Figure 5.4 The figure captures two examples of 3 µm wide PE waveguides. In (a), a well-fabricated waveguide is shown, while (b) displays an example with mouse bite defects caused by underetching.

Scanning Electron Microscopy (SEM)

SEM is another widely used technique for material and device characterization, which uses a focused beam of electrons to examine the surface of the material. It is used to perform 3D microstructural analysis of a sample. Many systems have capabilities to study the chemical composition of the material by using energy-dispersive X-ray spectroscopy (EDXS) [171]. Figure 5.5 illustrates SEM images of dielectric waveguides [194]. These include a Si photonic wire waveguide with 400×200 nm² core (Figure 5.5a), a 80-nm-wide taper tip (Figure 5.5b), and a silica waveguide core (Figure 5.5c). SEM surpasses visible light microscopy in resolution and magnification.

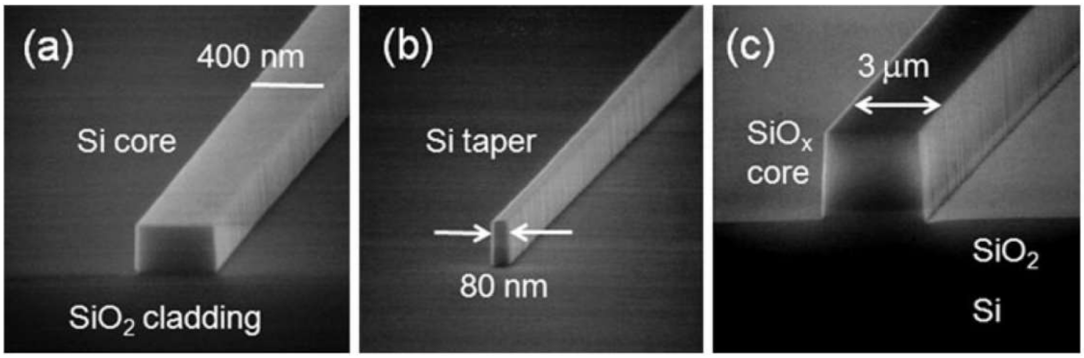

Figure 5.5 SEM images of several photonic wire waveguides based on Si/SiO_2. The images include (a) the Si photonic wire waveguide core, (b) a Si taper along the waveguide, and (c) the core of a SiO_2 waveguide. Image taken from [194].

Atomic Force Microscopy (AFM)

AFM is a type of scanning probe microscopy that uses a small tip to scan the surface of the material. This technique provides high-resolution images of the surface, which can be used to study the microstructure and topography of the material [171]. As an example, Figure 5.6 shows an AFM image for Sample C0817, which consisted of a 300 nm layer of Ge on a 200 nm layer of Au with an 8 nm Ti sticking layer on an InP substrate. The deposition method used was evaporation with a flux rate of 0.15 nm/s, and the sample was processed at a temperature of 44°C. The Root Mean Square (RMS) roughness of the surface was measured to be 1.903 nm.

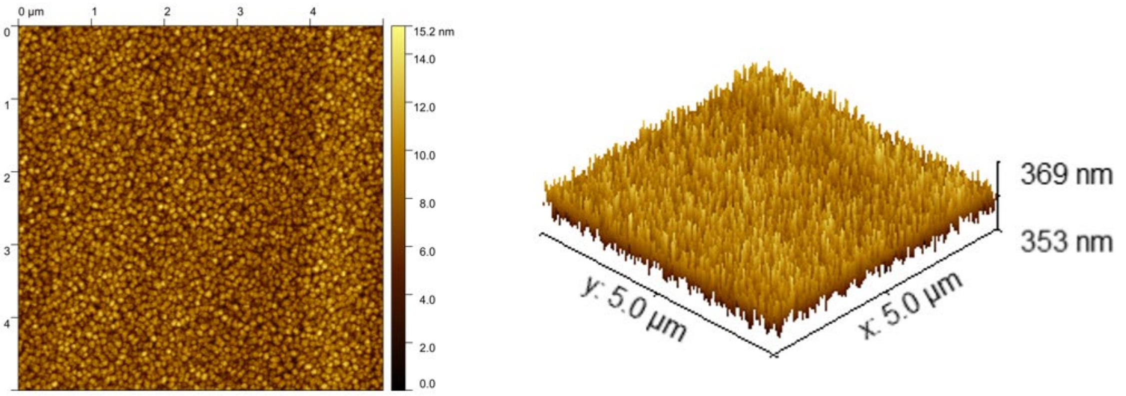

Figure 5.6 AFM images of Sample C0817, which consists of a 300 nm layer of Ge on a 200 nm layer of Au with an 8 nm Titanium (Ti) layer on an InP substrate. The deposition method used was evaporation with a flux rate of 0.15 nm/s. The sample was processed at a temperature of 44°C. The Root Mean Square (RMS) roughness of the surface is measured to be 1.903 nm.

Contact Profilometry

Profilometry is a technique that uses a stylus tip to measure the surface profile of the material. This technique provides high-precision measurements of the surface topography and can be used to study the roughness and waviness of the surface.

Ellipsometry

Ellipsometry is a characterization technique that has gained increasing significance in the analysis of various types of thin films due to advancements in computer control and data processing techniques [171]. This approach involves examining polarized light reflected from the sample, enabling the investigation of the complex refractive index (or dielectric function tensor). When light is incident on a surface, it exhibits both reflection and transmission characteristics, as depicted in Figure 5.7.

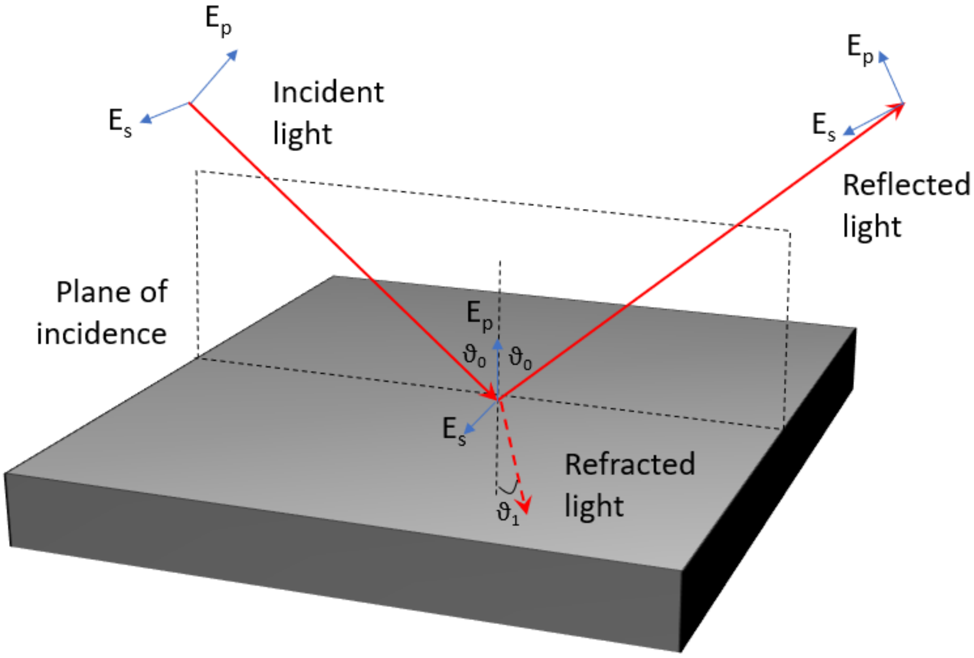

Figure 5.7 Illustration of the interaction between a monochromatic light beam and a surface, representing incident, refracted, and reflected components. The electric vectors of the plane-polarized light are denoted as "p" waves (in alignment with the plane of incidence) and "s" waves (perpendicular to the plane of incidence).

The transmitted light is refracted according to Snell's law, deviating from the incident angle. The electromagnetic field of the incident light can be decomposed into two distinct components: one aligned with the plane of incidence (p) and the other perpendicular to it (s). These two components experience different levels of attenuation and phase shift, dependent on the material's properties. The disparities in reflectivity are conventionally assessed using two parameters, namely, the amplitude and phase of the reflected waves. These parameters are obtained by employing the following equation [171], which quantifies the variations in reflectivity resulting from the differences in electromagnetic behavior at the surface-material interface:

$$\rho = \frac{R_P}{R_s} = \tan\psi e^{i\Delta} \tag{5.2}$$

In equation (5.2) the parameter Δ represents the disparity between the phase angles of the incoming and outgoing waves' parallel and perpendicular components, the angle ψ is defined as the tangent ratio of the magnitudes of the total reflection coefficients for the p- and s-polarized light. These quantities are interrelated with the ratio of the Fresnel amplitude reflection coefficients for the two types of polarized light [171].

Through ellipsometry, information regarding film thickness, roughness, crystal quality, chemical composition, and electrical conductivity can be extracted. This technique is capable of probing the optical depth of the sample, allowing for precise measurements of films as thin as a few tenths of nanometers up to several micrometers [171]. This characterization method played a crucial role throughout this thesis, serving not only to extract the optical constants required for accurate modeling and simulations, but also to assess the quality of the fabricated layers. As discussed in Section 3.2, different fabrication methods can introduce variations in layer quality, leading to differences in optical contrasts. For instance, in earlier studies, deposition tests of Ge layer depositions via HV/UHV evaporation (Plassys) were performed in order to choose the optimal Ge layer fabrication method. Figure 5.8 shows the extracted optical constants of Ge using mid-IR ellipsometry, highlighting the impact of different fluxes (0.1 nm/s and 0.5 nm/s) on the complex refractive index.

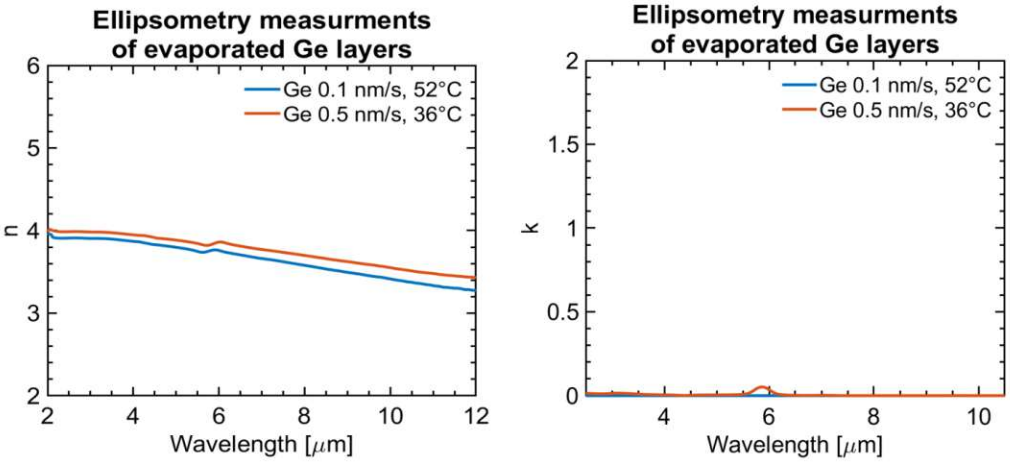

Figure 5.8 Extracted optical constants of Ge using mid-IR ellipsometry for deposition tests performed with different flux rates (0.1 nm/s and 0.5 nm/s). The results demonstrate the impact of flux variation on the optical contrasts of Ge layers.

5.2.2. Device Characterization

These techniques described in the previous section are limited to assessing the physical properties of the devices. In order to fully characterize the optical performance of the waveguides, it is crucial to evaluate their transmission losses. In our experiments, we selected the cut-back method to extract the coupling losses and to be able to single out the waveguide (material and fabrication) losses. This approach is widely used in integrated optics to determine the attenuation and coupling loss of a waveguide [29,195–198]. It consists of gradually shortening the length of the waveguide under test while measuring the corresponding optical transmission at each step. By comparing the measurements at different lengths, it is possible to estimate the optical losses and coupling efficiency of the waveguide. This measurement technique has several advantages over other methods for characterizing waveguide losses. Indeed, it is a simple and straightforward approach that can be easily implemented with basic optical equipment, and it can provide accurate and reliable measurements even for complex waveguide structures. However, one drawback is that performing the measurements can be quite time-consuming. For the analysis of the fabricated devices we assembled an end-fire coupling setup. Figure 5.9 illustrates the setup utilized to analyze DLSPPWs [141]. The setup used for analyzing all the other devices in this work was rather similar. The main difference consisted in the laser source, which changed the wavelength and the power used for performing the characterization. In some particular cases, additional modifications were required. For instance, when utilizing continuous wave (CW) distributed feedback (DFB) QCLs, it was necessary to incorporate a chopper along with a collimating lens, and an MC-5 lens cleaning tissue (from Thorlabs) placed in front of the detector, in order to protect it from saturation (as shown in Figure 5.10). Figure 5.10a illustrates a schematic example of this setup, where a movable mirror was occasionally employed instead of the ZnSe beam splitter, when the latter was not available. Details about the wavelengths used for the characterizations are discussed in more detail in their respective chapters.

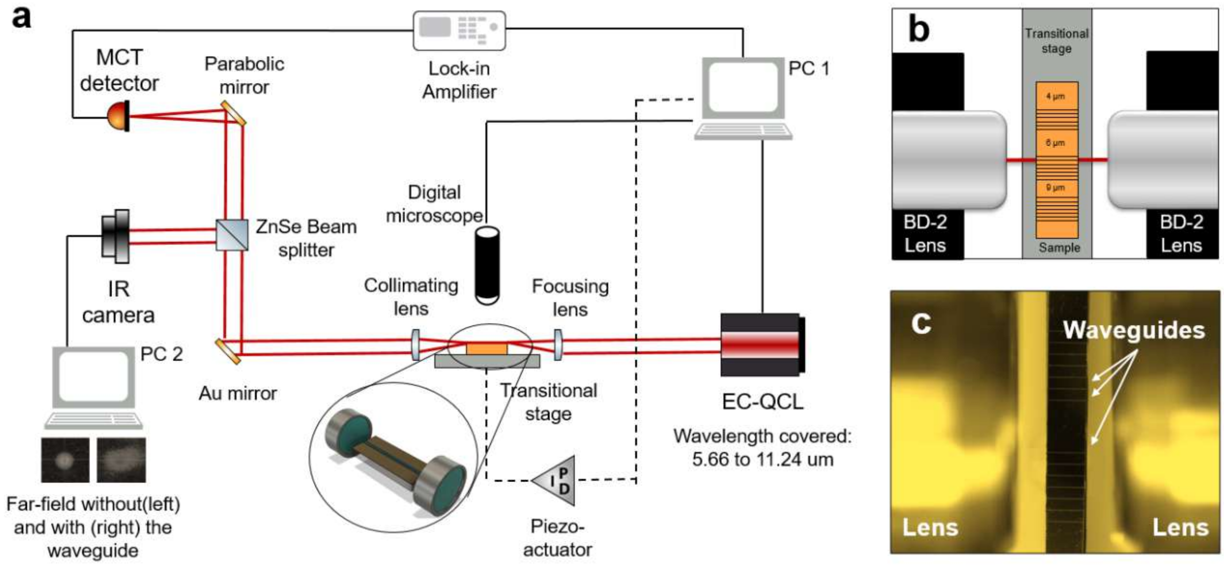

Figure 5.9 (a) Schematic diagram of the typical experimental setup used for the analysis of the fabricated devices. (b) Sketch and (c) topvieew optical image of the waveguide chip in the setup during the measurements showing the waveguide with respect to the lens. Image taken from [141]

The optical system consisted of two lenses (C037TME-F, Thorlabs) to couple light into and out of the waveguides. Initially, the waveguide was roughly aligned with the focal point of the lenses using a digital microscope ("Dino-Lite Edge" Digital

Microscope). Subsequently, the positioning of the waveguide relative to the lenses was achieved with nanometer precision via a piezoelectric transition stage. A 50:50 ZnSe beamsplitter (BSW711, Thorlabs) was utilized to project the beam profile on an IR camera (Pyrocam, Ophir-Spiricon, USA) and a thermoelectrically cooled (-78°C) Mercury Cadmium Telluride (MCT) detector ("PVI-4TE-10.6", Vigo Systems S.A., Poland) through the use of a parabolic mirror. The signal received by the detector was then amplified via a pre-amplifier, and the signal-to-noise ratio was improved by employing a lock-in amplifier. Since the plasmonic waveguides of this study have modest propagation lengths, they needed to be cleaved to very small lengths (1-2 mm). For this reason, it was difficult to cleave them after subsequent measurements. To overcome this challenge, we used a similar approach commonly employed in the analysis of other plasmonic waveguides [195–198]. Instead of performing measurements on the same waveguide, a series of measurements were taken on waveguides with different lengths that were nominally identical. The underlying assumption is that the coupling losses (in dB) and total losses (in dB/mm), are identical among waveguides of different lengths. To ensure the validity of the method, we conducted measurements on multiple waveguides that shared identical lengths and relevant parameters, such as the thickness and width of the Ge layer.

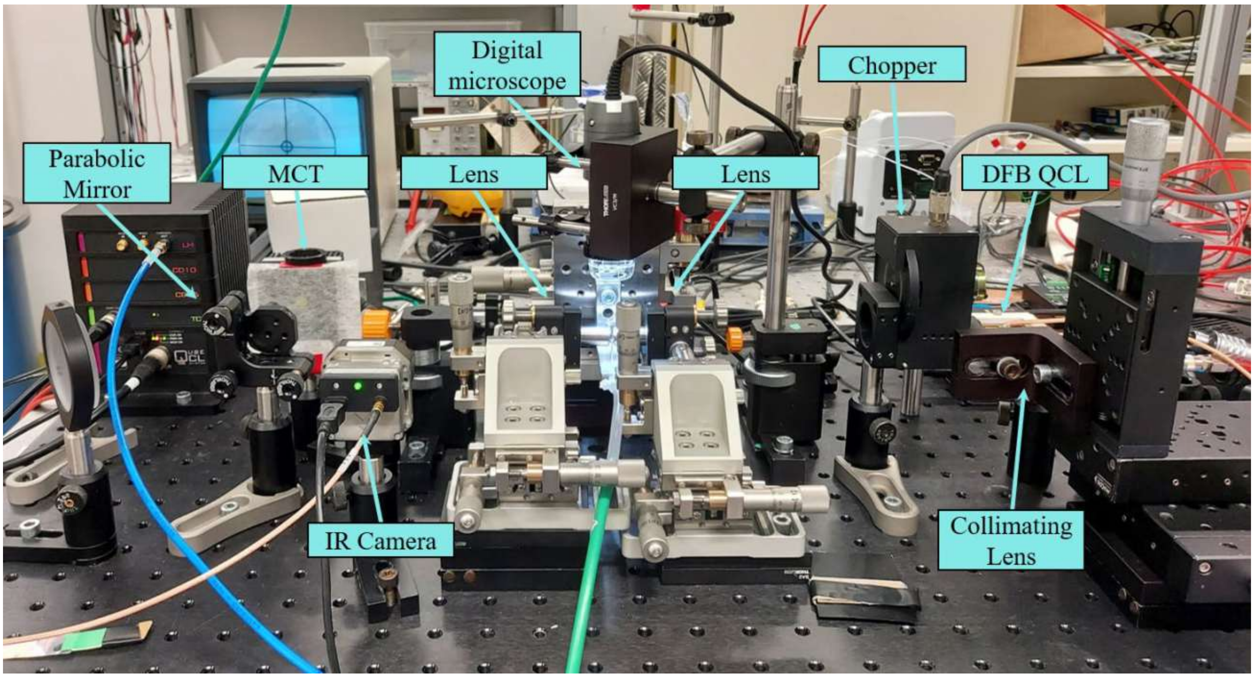

Figure 5.10 Picture of the experimental setup including a DFB QCL with a collimating lens, digital microscope, IR camera, parabolic mirror and MCT detector. In this setup, a movable mirror was used instead of the ZnSe beam splitter for the far-field analysis. The MCT detector was covered with an MC-5 lens cleaning tissue (from Thorlabs) to protect it from saturation.

We ensured that the resulting values were consistent within acceptable deviations that could be attributed to processing- and alignment-related variations. Furthermore, we assessed the goodness of fit of the measured data with a linear model and compared it with the simulation results.

The experimental procedure used to measure the losses involved taking a reference voltage measurement before each measurement and ensuring that the IR camera displayed a Gaussian beam. The use of the digital microscope and some custom-designed shutters, helped in the identification of the position of the beam in its focal spot. The waveguides were then properly aligned to the focal point of the lenses, and the intensity was measured at least three times per waveguide to obtain a more precise value. The average intensity was then calculated for each waveguide and for every length.

The insertion losses of a waveguide, measured in dB (y_i), are plotted against the corresponding sample lengths in millimeters (x_i). The resulting data is then fit to a linear model, $y = mx+b$, using a minimum least squares approach [195] to minimize the squared distance between the model and the data [199], where:

$$m = \frac{n\Sigma_{i=1}^{n} x_i y_i (\Sigma_{i=1}^{n} x_i)(\Sigma_{i=1}^{n} y_i)}{n\Sigma_{i}^{n} x_i^2 - (\Sigma_{i=1}^{n} x_i)^2}, \tag{5.3}$$

and

$$b = \frac{\Sigma_{i=1}^{n} y_i - m\Sigma_{i=1}^{n} x_i}{n}. \tag{5.4}$$

In this way, the attenuation coefficient of the waveguide, expressed in dB/mm, can be determined from the slope of the linear model. The parameter b, representing the y-intercept of the linear model, corresponds to the total mode power coupling losses due to both facets in dB.

5.2.3. Comparison Between Experimental Results and Theoretical Predictions

By comparing the experimental measurements obtained through the cut-back method with the theoretical predictions from simulations, it is possible to assess the accuracy of the theoretical models and identify any discrepancies between the predicted and measured values. If discrepancies are observed, further analysis may be conducted to investigate the underlying causes. This typically means starting by examining the waveguide structure and exploring the fabrication defects that may be affecting the results in terms of scattering losses. Among the possible causes of scattering losses, surface roughness is probably the most common one [195,200–202]. In fact, surface roughness can scatter light out of the waveguide and into the surrounding medium, resulting in a loss of the transmitted optical power. However, achieving perfectly smooth surfaces can be challenging, especially for waveguides with complex geometries or those fabricated using unconventional materials. Another possible cause of losses due to fabrication defects, is given by inhomogeneities of the waveguide core. If the core of the waveguide is not uniform in width or thickness, it can lead to a non-uniform distribution of the optical field along the core, resulting in higher attenuation along the device. Another common source of losses due to fabrication imperfections can happen at the facet. If the end-face of the waveguide is not perfectly flat or smooth, it can lead to increased reflection and consequent scattering losses. Finally, also material stress at the interfaces of different waveguide materials can lead to deformation or microcracks, which can increase scattering losses and reduce the overall efficacy of the waveguide. To minimize the impact of these factors on waveguide losses, it is therefore essential to carefully control the fabrication process and employ measures to detect and eliminate defects as early as possible. In cases where inspection fails to identify any obvious fabrication defects, it may be necessary to re-evaluate the theoretical model, assuming that other physical mechanisms are not involved. While numerical methods are generally highly accurate in predicting waveguide losses, their precision can be affected by the refractive indices of the materials. To ensure the accuracy of numerical simulations, it is therefore essential to obtain accurate and reliable refractive index values for the materials used in the waveguide. This can be achieved through careful characterization of the materials using ellipsometry.

Finally, it is worth mentioning that in some cases also environmental factors during the waveguide characterization, such as temperature [203] or humidity [204] flactuations, can affect the behavior of waveguides or the quality of the measurements leading to discrepancies between theoretical models and experimental measurements.

6

ORGANIC DIELECTRIC-LOADED PLASMONIC WAVEGUIDES

This chapter is based on the publications "Structure and mid-IR optical properties of spin-coated PE films developed for integrated photonics applications" [162] and "Advanced Mid-Infrared Plasmonic Waveguides based on Polymers for On-chip Integrated Photonics" [205].

6.1 Polyethylene

As discussed in Section 4.2.2, PE stands out as a highly promising organic material specifically suited for mid-IR frequencies. Different types of PE exist, generally categorized based on their density and branching characteristics. However, they can be classified into two fundamental types: High-Density PE (HDPE) and Low-Density PE (LDPE). HDPE is characterized by its highly ordered molecular arrangement, which results in the formation of well-defined crystalline domains, whereas LDPE exhibits a more amorphous phase with a less organized molecular structure. Nowadays, LDPE has almost entirely been replaced by linear LDPE (LLDPE) due to its higher crack strength and maximum operating temperature. In particular, LLDPE has superior UV stability [206,207]. The level of crystallinity has been observed to have a direct impact on the optical properties of these materials, with increasing degrees of crystallization generally leading to reduced transparency [208]. Table 6.1 summarizes the most important properties of various PE classes.

Spin coating is a widely used technique for creating uniform polymer films with controllable thicknesses on a flat substrate [209]. However, the method used to produce spin-coated PE films involves intricate and time-consuming procedures.

Property	HDPE	LDPE	LLDPE	VLDPE
Density (g/cm³)	0.94-0.97	0.91-0.94	0.90-0.94	0.86-0.90
Degree of crystallinity (% from density and calorimetry)	55-82	30-62	22-62	0-34
Melting temperature (°C)	125-132	98-115	100-125	60-100

Table 6.1 Primary properties of various PE classes, including High-Density Polyethylene (HDPE), Low-Density Polyethylene (LDPE), Linear Low-Density Polyethylene (LLDPE), and Very Low-Density Polyethylene (VLDPE). Data taken from [208]

These processes often require preheated equipment and the use of potentially harmful solvents such as Decalin, which are employed at their boiling point. Furthermore, the films typically necessitate several hours of annealing to achieve high-quality layers, including spherulites formations [210–212]. In the context of mid-IR integrated photonics applications, there is a critical need to accurately achieve thicknesses within the range of 100 nm to 6 µm. Surprisingly, this specific range was not extensively explored in the existing literature. Moreover, the available data on the mid-IR electrical and optical properties of PE is quite limited, and there is a complete absence of data for layers produced through spin-coating techniques [213]. In this chapter, we introduce an optimized fabrication method that enables the production of spin-coated LLDPE films. This method ensures to preserve the favorable optical properties of the material and to achieve consistent and controlled layer thickness by carefully controlling the ambient conditions. The remarkable optical characteristics of the resulting film, along with its resistance to solvent exposure, demonstrate the potential of thin PE films obtained through the presented spin-coating technique. These films can serve as key components in the fabrication of fundamental elements for PICs.

6.2 Polyethylene Thin Film Preparation

6.2.1. Film Fabrication

In most optoelectronic applications, achieving consistent results through a fabrication method is a crucial requirement. However, the properties of spin-coated films can be significantly influenced by ambient conditions, such as temperature and humidity, that can affect the drying kinetics of the solvent and impact the film formation. Spin-coating processes are frequently conducted within lab fume hoods, where factors such as relative humidity and temperature are prone to fluctuations. External meteorological conditions can also impact these changes. On the contrary, a glove box effectively minimizes variations in both temperature and humidity. The influence of humidity on film thickness is well-known [179,180]. Its effect can lead to unwanted variations in thickness, ultimately diminishing the quality of the layer. From some preliminary experiments conducted in a typical laboratory fume hood, we produced PE layers exhibiting significant thickness variability, ranging from 200 to 500 nm for a weight ratio of 2%. However, by transitioning the fabrication process to a glove box environment (see Figure 6.1), the humidity fluctuations that affect the thickness repeatability are avoided.

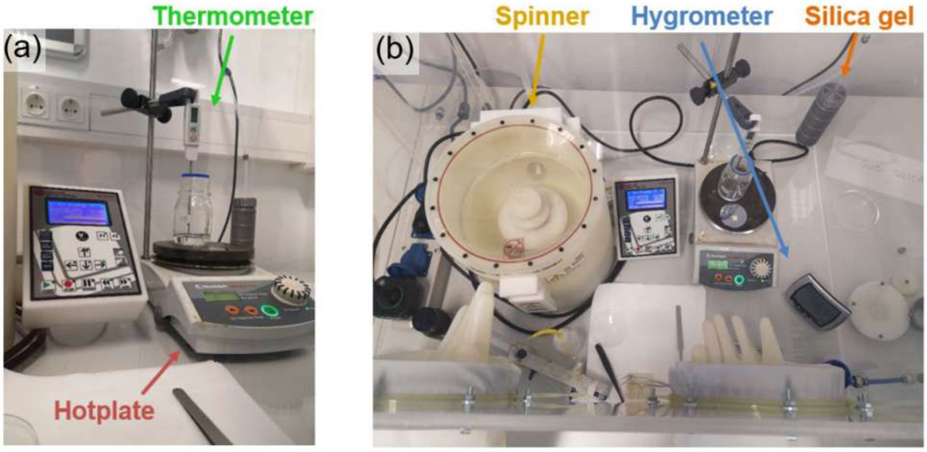

Figure 6.1 Side (a) and top-view (b) pictures of the fabrication setup in the glove box. Image taken from [162].

Synthesis of PE-based thin films is generally carried out at temperatures exceeding 100 °C, utilizing preheated equipment, and often involves extensive annealing periods post-synthesis [214,212,210,215,211]. State-of-the-art techniques necessitate heating all of the equipment involved - including the substrate, spin coater chuck, and pipette – to high temperatures (>100 °C), dissolving the polymer in boiling decalin(190 °C), [211] or boiling toluene(110 °C), [210] followed by long annealing steps. To avoid the need of a reflux condenser, we maintained the solution's temperature at 100°C, a value ten degrees from the solvent's boiling point. Under these conditions, we obtained inhomogeneous layers with low optical clarity by performing the deposition prior to spinning (static dispense method, see Section 5.1.1), as shown in Figure 6.2a and b. However, by using the dynamic dispense method, we effectively circumvent this issue. Through the utilization of this method, it becomes possible to create layers that are consistent and uniform. These films exhibit exceptional clarity, to the extent that they appear nearly invisible to the naked eye (Figure 6.2c and d). Moreover, to test the adhesion properties of the fabricated coatings, the synthesized films were immersed in acetone and deionized (DI) water after a post-baking treatment. The coatings produced through our optimized method demonstrated robust adhesion to the underlying substrate. In contrast, the layers fabricated outside the controlled environment of the glove box often encountered delamination issues and inadequate adhesion after the post-bake process.

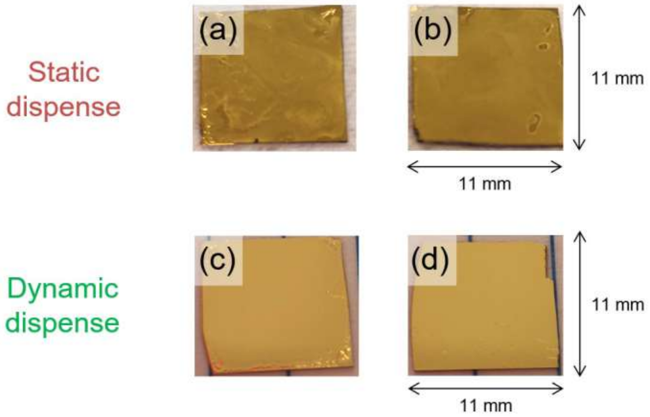

Figure 6.2 The figure displays macroscopic images of typically fabricated samples in a glove box, showing the difference in the layers obtained performing the deposition before spinning (a), (b), and during spinning (c), (d). Image taken from [162].

The optimized film fabrication process used for the final fabrication of the waveguides is illustrated in the flowchart of Figure 6.3. Initially, LLDPE powder was dissolved in toluene, with varying weight ratios ranging from 1% to 10%. The mixture was stirred at 100 °C until complete dissolution The temperature of the solution was monitored using a probe thermometer to ensure the desired temperature. Before depositing the polymer solution, the substrates were preheated on a hotplate set to 120 °C. The films were produced using the dynamic dispense method, depositing a fixed amount of the polymer solution (100 µL) during the spinning of an 11 x 11 mm Si substrate covered by 100-200 nm of Au. The spin-coating process was conducted at 1000 rpm for 35 seconds, with 5 seconds of acceleration for all coatings. To remove any remaining solvent, a post-baking step was performed at 120 °C for 15 minutes.

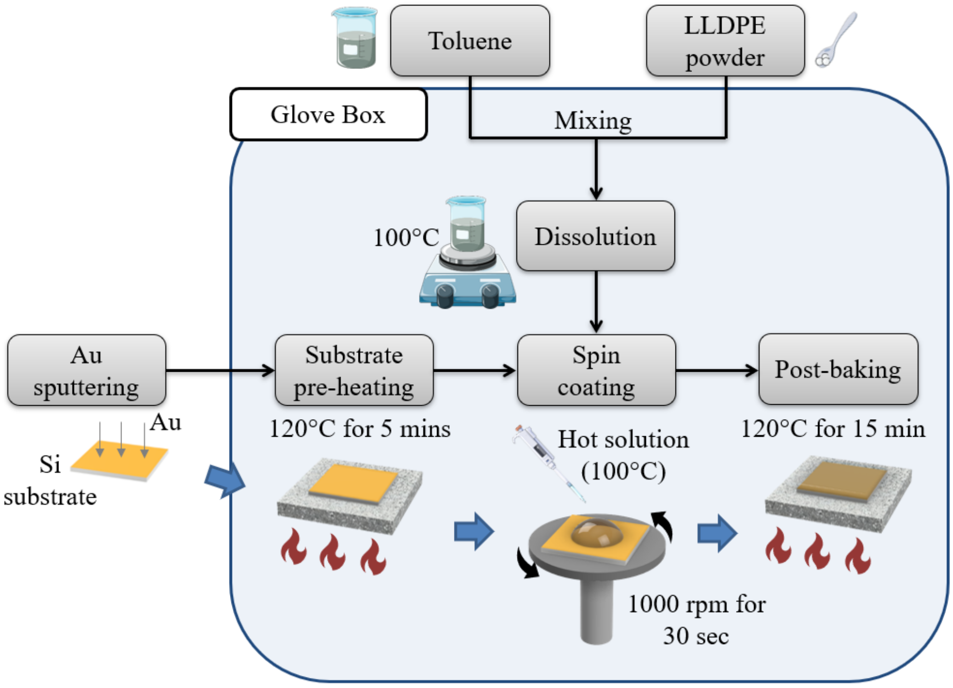

Figure 6.3 Process flowchart for film fabrication: LLDPE powder was dissolved in toluene at varying weight ratios and stirred at 100 °C until complete dissolution. The solution's temperature was monitored using a probe thermometer. Prior to depositing the polymer solution, substrates were preheated on a 120 °C hotplate. Using the dynamic dispense method, a fixed amount of solution (100 µL) was deposited on the substrate during spinning. Subsequently, a post-baking step at 120 °C for 15 minutes was performed to eliminate any remaining solvent.

6.2.2. Film Thickness and Concentration Dependence

In terms of device design, there is a need to accurately determine the thickness of fabricated layers using easily measurable quantities. The experimental results obtained through the use of our optimized method consistently demonstrated the typical nonlinear relationship between the concentration of polymer films and the layer thickness. In order to explain this phenomenon, we employed the equation introduced by Chen [179]. This model relates the thickness variation of a spin-coated layer to factors such as solvent type, solution composition, and spin-coating parameters:

$$D = K_0 \mu^{0.36} \omega^{-0.50} \left(\frac{E\lambda}{C_\mu}\right)^{0.6} \tag{6.1}$$

In the equation, the film thickness is denoted as D, K_0 represents a constant specific to volatile organic solvents, μ is the viscosity of the coating solution, E is the solvent-evaporation rate, λ is the latent heat of evaporation and C_μ denotes the solvent heat capacity. While the relation between polymer concentration and viscosity can be rather complex [214,216,217], it is possible to approximate it by a power-law function [214,218,219]. Therefore, the data were fitted to:

$$logD = C + 0.36\alpha(wt) \tag{6.2}$$

where C is a parameter that contains all the constants from equation (6.1), wt is the solution concentration, and α represents the coefficient describing the phenomenological power law that characterizes concentration and viscosity. The viscous behavior of a solution can be accurately estimated at higher concentrations by using a Taylor series expansion of the viscosity-concentration equation [217]:

$$\mu = \mu_0(1 + [\mu]wt + k_H[\mu]^2wt^2 + \cdots) \tag{6.3}$$

where $[\mu]$ is the intrinsic viscosity and k_H is the Huggins constant [220]. The results obtained from fitting the thickness to the model are shown in Figure 6.4.

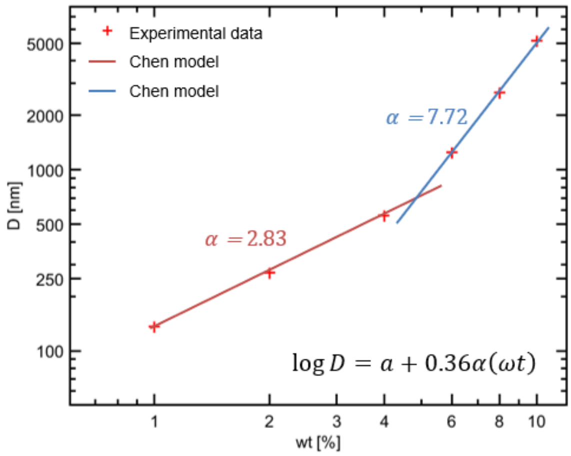

(a)

wt [%]	D [nm]	α
1	138 ± 1	2.83
2	271 ± 4	2.83
4	560 ± 11	2.83
6	1246 ± 13	7.72
8	2670 ± 2	7.72
10	5186 ± 17	7.72

(b)

Figure 6.4 (a) Film thickness dependence on LLDPE concentration. Experimental data points are depicted as red crosses, while the solid line represents the model fits for both observed regimes. All films were fabricated in a glove box. (b) Table with the thickness values. Image taken from [162].

Based on our measurements, two separate values of α can be identified that divide the solution into two distinct regimes. A value of $\alpha = 2.8$ was derived for concentrations ranging between 1 and 4%, suggesting that the behavior within this concentration range exhibits viscoelastic characteristics [219]. A value of $\alpha = 7.72$ was obtained for concentrations exceeding 5%. This relatively high value suggests that the solution is within a *highly concentrated regime*, which is typically associated with the presence of entangled macromolecules [216,217,219]. In order to evaluate the consistency of our fabrication technique, 10 coatings with a mass percentage of 10% were created. The average recorded thickness was 5159 ± 87 nm, demonstrating the exceptional reproducibility of the fabrication procedure.

6.2.3. Morphology Analysis of Films

The degree of crystallinity in LLDPE ranges from 20% to 50%, as reported in literature [208,221]. Crystallization of LLDPE can be achieved through two methods: non-isothermal and iso-thermal [210,211]. These processes require extended periods of annealing, specific timing, and precise temperature control. However, since our objective is to obtain homogeneous and transparent coatings, our focus was not on achieving maximum crystallization levels.

When a melt-crystallized polymer is prepared as a thin film and observed under an optical microscope using polarized light, characteristic structures known as spherulites are typically observed [220]. These spherulites typically exhibit a distinctive Maltese cross pattern, similar to the one shown in Figure 6.5.

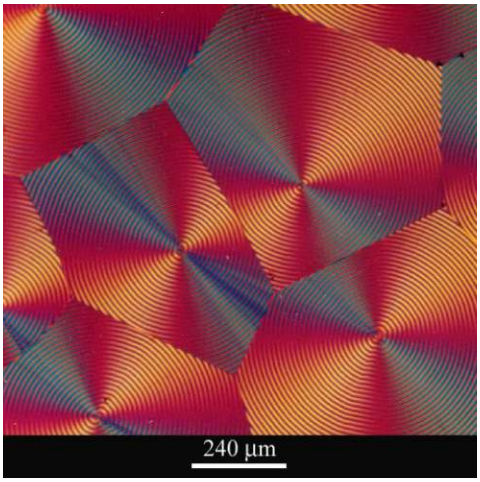

Figure 6.5 Image of a polyhydroxybutyrate (PHB) spherulite. When observed using a transmitted cross-polarized light microscope, spherulites exhibit a characteristic Maltese cross pattern, accompanied by a banded appearance in each spherulite [222]. Image by T.W. Clyne, Department of Materials Science and Metallurgy, University of Cambridge [223].

They form through nucleation at different points in the sample and grow as spherical entities, ceasing growth upon impingement with adjacent spherulites. While they may appear similar to grains in metals, spherulites in polymers consist of numerous crystals radiating from a central nucleus, unlike individual single crystals [220]. Analysis of the Maltese cross patterns indicates that the molecules in polymer spherulites are normally aligned tangentially. Some polymers, like poly(ethylene terephthalate) and isotactic polypropylene, have slow crystallization rates, which allows them to be obtained in an apparently amorphous state by rapidly quenching the melt [220]. Quenching does not provide sufficient time for crystals to form through regular nucleation and growth processes. Crystallization can be induced by annealing the quenched polymer at an elevated temperature [220]. During annealing, the diffraction patterns become more well-defined, indicating crystallization. The mechanism of crystallization during annealing is not entirely clear, as large-scale molecular diffusion cannot occur in the solid state. Thus, it remains challenging to determine whether the quenched polymers are truly amorphous or contain very small crystals [220].

Therefore, due to the absence of isothermal or non-isothermal crystallization processes in our study, the observation of highly structured and ordered morphology characterized by spherulites was not achieved [220]. Figure 6.6 shows the AFM surface scans for the fabricated LLDPE films with different polymer concentrations. The height profile obtained from the AFM measurements reveals distinct chain arrangements on the surface. The regions of higher brightness correspond to an increased density of polymer chains, indicating a greater level of crystallization achieved within those areas.

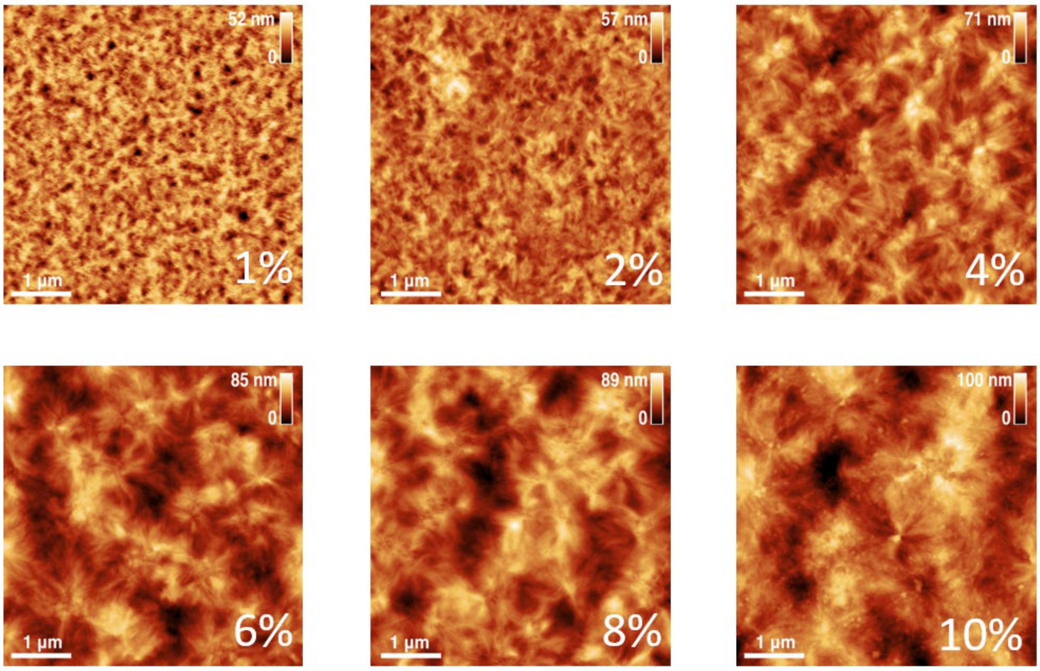

Figure 6.6 AFM images of LLDPE thin film surfaces for different mass concentrations. The change in ordering of the structures in the different regimes can be immediately observed. Image taken from [162].

From Figure 6.6, it is evident that a higher concentration of LLDPE in the solution leads to an increase in the size of the polymer microstructure. Specifically, as the concentration of LLDPE polymer increases, the surface features of the thin films become more prominent while maintaining the overall characteristics of the chain arrangement.

Additionally, the AFM measurements reveal an increase in surface height corresponding to the enlargement of the microstructure.

Figure 6.7 shows the relationship between polymer concentration and average film roughness extracted by the AFM scans. As the concentration increases, the surface roughness also increases. However, the surface roughness values remain relatively low, with all concentrations staying below 15 nm, for layer thicknesses that vary between 100 – 5200 nm, as reported in Figure 6.4b.

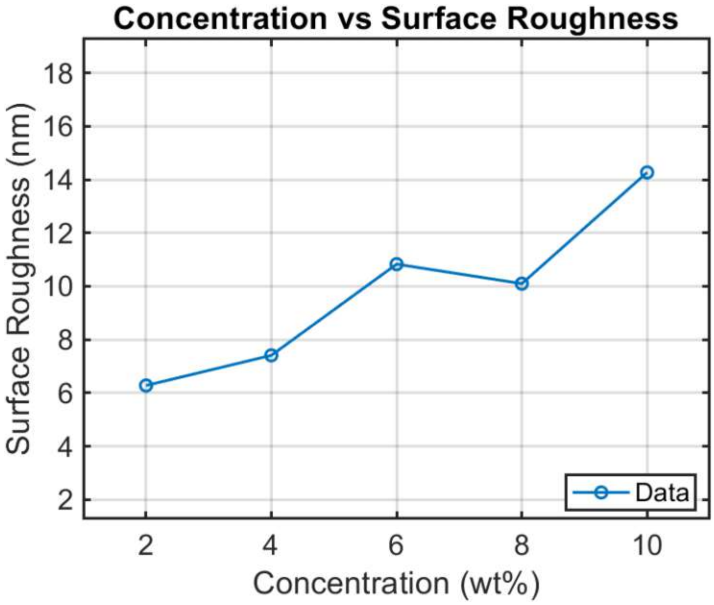

Figure 6.7 Mean roughness (Sa) as a function of concentration for various LLDPE concentrations. Image taken from [162].

The examination of the film surfaces using a profilometer demonstrates the absence of long-range (mm-scale) inhomogeneities across the samples. Previous research on PE coatings has reported thickness fluctuations characterized as "wavy-like" and attributed to the Gibbs-Marangoni effect [210], i.e., surface distribution heterogeneities driven by surface tension gradients [224]. These defects normally manifest as flower-like pattern. While these types of fabrication defects were absent in the films produced with the technique described in this thesis, AFM analysis showed a waviness-like behavior in the µm-scale, as illustrated in Figure 6.8. If we do not consider these fluctuations in the roughness analysis, the resulting RMS roughness would be 1.6 nm. Nevertheless, considering that these coatings are specifically designed for mid-IR wavelengths, where regions spanning from 100 to 1000 um are significant, we incorporate these µm fluctuations as part of the overall film's surface roughness, resulting in the rouhgness values plotted in Figure 6.7.

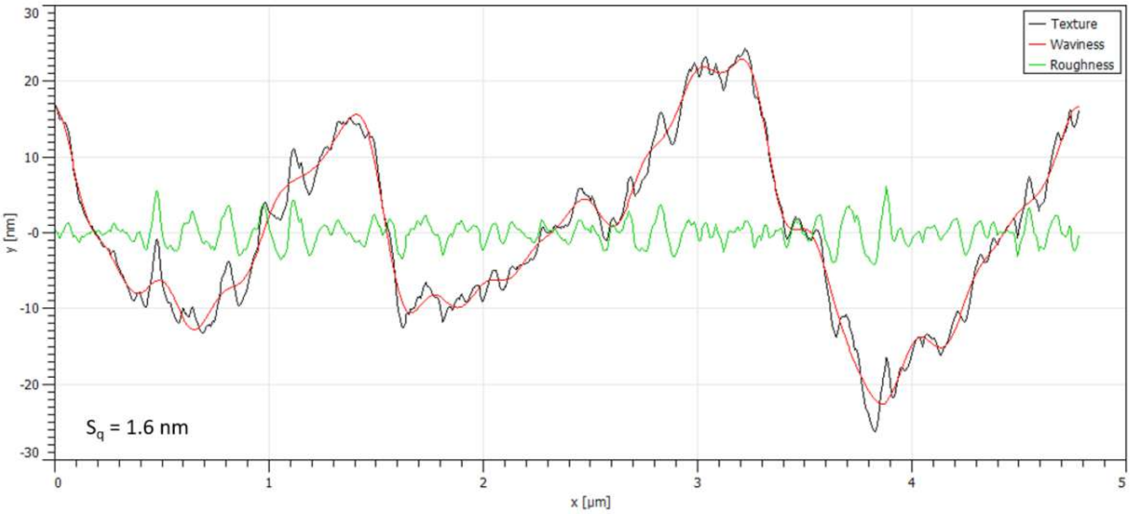

Figure 6.8 The AFM scans reveal µm-scale waviness in a 2.67 µm coating, which contributes to the overall surface roughness. If these fluctuations were eliminated, the resulting RMS roughness would be 1.6 nm. However, since the coatings are designed for mid-IR wavelengths, where regions spanning from 100 to 1000 µm are significant, we choose to retain these fluctuations as part of the overall surface roughness.

6.2.4. Film Crystallinity

The film's amorphous content exhibited a decrease as the concentration of LLDPE in the coating solution increased (see Figure 6.9a). At a 1% concentration, the amorphous content is approximately 80% (m/m), which gradually decreases to around 65% (m/m) at a 10% concentration. The corresponding Raman-fitted spectra are plotted in Figure 6.9b. Similarly, the variance of amorphous content is also decreasing with increasing PE concentration. Nevertheless, the reduction in standard deviation observed in Raman spectra, which probes an area smaller than 500 nm in diameter, can be attributed to the uniformity of the film, suggesting that employing higher concentrations of the stock solution not only decreases the fraction of amorphous films but also promotes the formation of more homogeneous films.

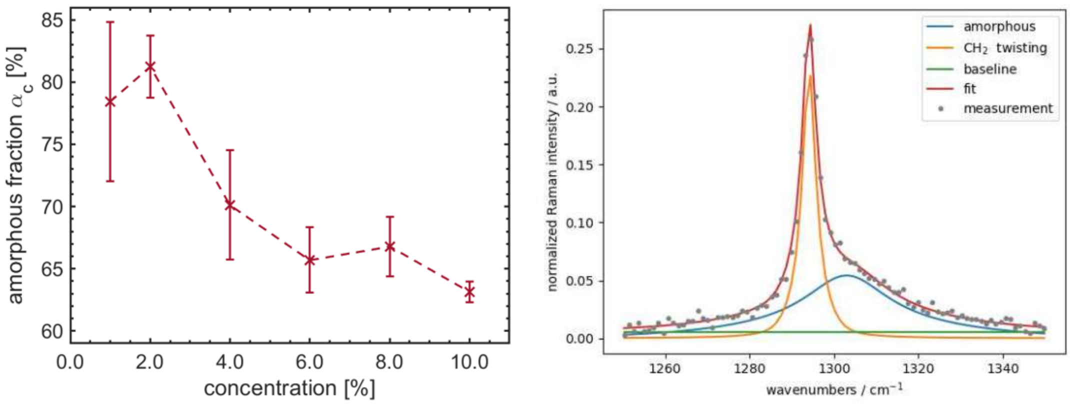

Figure 6.9 (left) The film's mass fraction of amorphous content was assessed using confocal Raman spectroscopy. The error bars indicate the standard deviation derived from measurements obtained at five distinct locations. (right) The spectrum obtained from Raman fitting. Image taken from [162]. Further details about these measurements can be found in the supporting information in reference [162].

6.2.5. Mid-IR Refractive Index

Figure 6.10 illustrates the profile of refractive index and permittivity in the mid-IR region for an LLDPE film fabricated in the glove box, measured wih an mid-IR ellipsometer. The presence of three distinct hydrocarbon peaks is well-known, located around 3.4, 3.5, and 6.8 µm (2923, 2849, and 1473 cm^{-1}). These peaks are consistent with the expected interband transitions inherent to the polymer structure[3]. The experimental results thereby confirm the high transparency of the fabricated films, validating the exceptional optical characteristics of the fabricated PE films within the mid-to-long-wave IR band.

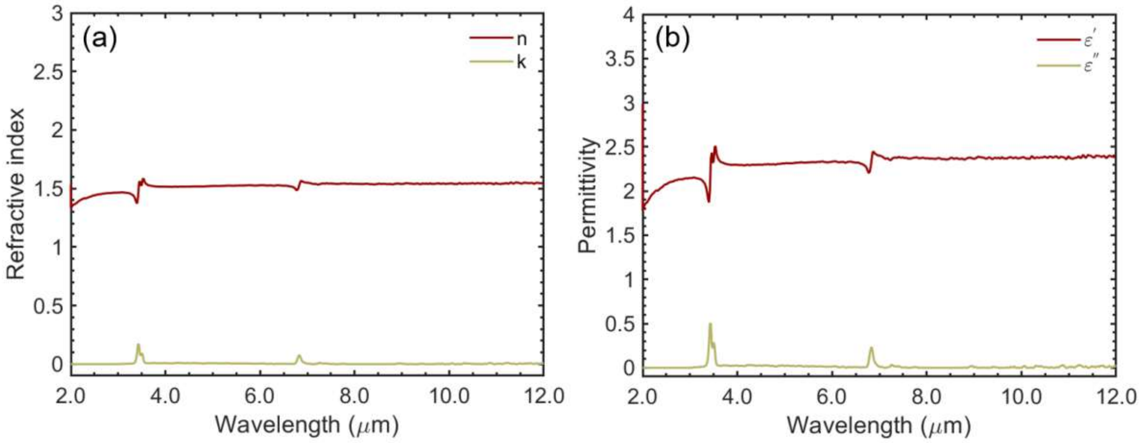

Figure 6.10 a) The refractive index profile of the fabricated PE film and b) its complex permittivity. Image taken from [162].

6.3 Fabrication of DLSPP Waveguides

After reaching a reliable material fabrication, the subsequent step involves modeling and fabricating the photonic device. The initial stage of the device design involves conducting simulations of different device structures using the eigenmode solver feature of COMSOL Multiphysics. The simulations were conducted at a specific wavelength of 9.26 µm, chosen as it is located in one of the spectral windows that can potentially be used in free-space optical telecommunication [225].

The plasmonic waveguide architecture is shown in Figure 6.11a, and consists of a PE ridge on top of a metal (Au) layer. Figure 6.11b shows the cross-sectional electric field confinement for a PE ridge of 3.6 x 3.6 µm^2, and Figure 6.11c illustrate its respective 3D simulation. In this specific design configuration, the mode is localized in the dielectric core of the waveguide, showing a good trade-off between propagation length (L_P ~ 455 µm) and confinement. The effective mode index is N_{eff}=1.20, demonstrating the promising performance characteristics of this material system for combining long-range L_P with high enough N_{eff} (1.20) for radiation guiding along the chip surface.

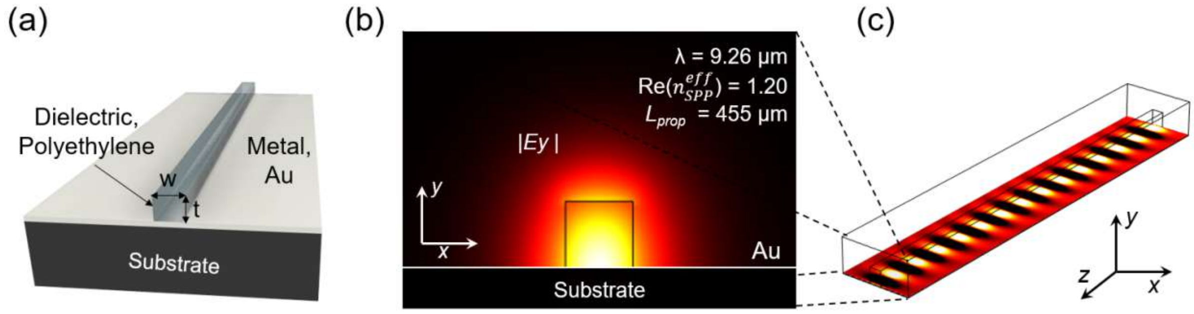

Figure 6.11 a) Cross section of the DLSPPW. b) $|E_y|$ 2D field profile of the TM_{00} SPP mode for a 3.6 x 3.6 µm^2 DLSPPW at λ = 9.26 µm. c) Top view of the 3D simulation of the waveguide. Image taken from [205].

Figure 6.12 shows how the ridge geometry impacts two important figures of merits, illustrating the inherent trade-off encountered in plasmonic waveguides. Figure 6.12a illustrates the influence of width and thickness on the effective mode index. As the ridge thickness increases, the N_{eff} monotonously increases, enhancing the ability to guide the plasmonic mode effectively. In the figure, the value of N_{eff} = 1.1 highlights the minimum refractive index contrast to achieve effective mode-guiding along waveguide bends when the surrounding medium is air. Figure 6.12b presents equivalent simulations, showing the impact of different ridge dimensions on the propagation length L_P. For thin ridge geometries (t < 1.2 µm), the propagation length is in the order of 1 mm, but, N_{eff} is too low to provide efficient mode guiding. Increasing the thickness of the ridge enlarges N_{eff}

and provides the necessary condition for light guiding, at the expense of the propagation length.

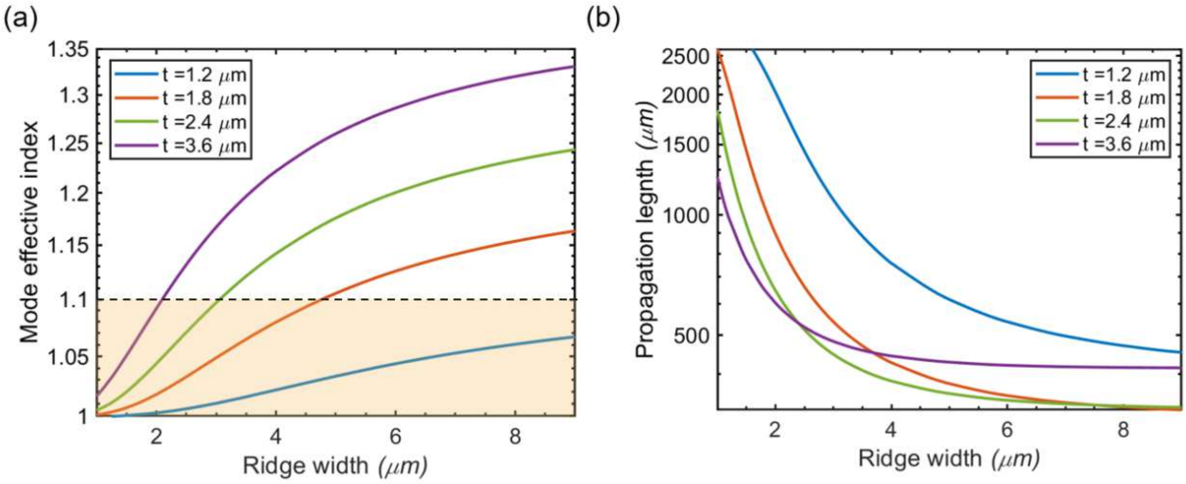

Figure 6.12 a) Mode effective index Neff for different ridge dimensions. b) Propagation length L_p for different ridge dimensions. Image taken from [205].

Figure 6.13a shows that an optimal ridge width exists (in the range of 2-5 µm) that minimizes mode size, here expressed in the form of normalized mode area A_{eff}/A_0. For smaller-than-optimal ridge widths, the mode is pushed outside of the dielectric ridge, increasing its extension. For larger ridge widths, the mode will occupy all the available dielectric space leading again to a lower degree of mode confinement [117] (see also inset in Figure 6.16b). These findings indicate a comparable performance between DLSPPWs based on PE in the LWIR band and previously documented numerical studies on PMMA-based DLSPPWs operating at telecommunications frequencies [226]. Figure 6.13b provides a clearer demonstration of this fact, where the simulated transmission $T_b = I_b/I_a$ (see also inset) for a 90° bend over a waveguide section of circular shape is compared for both the architectures at respective frequencies (PE at λ = 9.26 µm and PMMA at λ = 1.55 µm) as a function of normalized radius R/λ [114]. The plot (comparison between red and black curve) demonstrates that the optical characteristics of both polymers closely resemble each other at their specific operational wavelengths. Using these simulation results as design guidelines, we proceeded with the fabrication of the plasmonic devices.

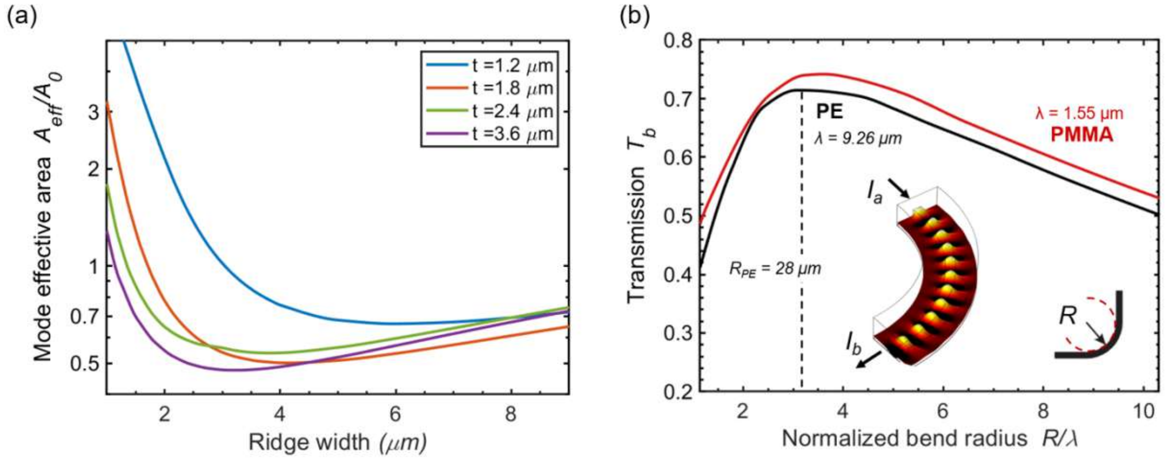

Figure 6.13 a) Impact of the PE ridge geometries on the effective mode area (Aeff/A0) as function of the PE thickness between 1.2 µm and 3.6 µm. b) Comparison of the transmission (Tb = Ib/Ia) of a 90° DLSPPW based on PE (cross-section of 3.6 x 3.6 µm^2) at a wavelength λ = 9.26 µm and based on PMMA (cross-section of 600 x 600 nm^2) at a wavelength λ = 1.55 µm, as a function of its normalized radius (R/λ). Inset: 3D modeling of the PE waveguide mode. Image taken from [205].

Figure 6.14 shows the schematic flowchart of the fabrication steps of the plasmonic devices. The films were deposited by spin-coating in a humidity- and temperature-controlled glove box, with the technique described in the previous section. The films were synthesized from linear LLDPE powder (Sigma-Aldrich, ρ = 0.906 g mL-1, average Mw ~ 35000 and Mn ~ 7700) dispersed in toluene (Sigma-Aldrich, anhydrous, purity 99.8%) with a mass portion of 10%, resulting in films of 5.0 µm thickness. The spin coating was conducted from a hot solution (100°C) at a rotation speed of 1000 rpm for 35 s, with 5 s of acceleration, using the dynamic dispense method. The samples were pre-heated to 120°C on a hotplate before spin-coating and post-baked at 120°C for 15 minutes right after spin-coating. The substrates employed were Si chips coated with Au, diced to dimensions of 11x11 mm^2 prior Au sputtering.

As PE is not inherently a UV-sensitive polymer [227], we performed the structuring of the ridges through the use of an inorganic hard mask during the lithographic process. When utilizing an Au hard mask (Figure 6.14a), an additional lithographic process is required to ensure the safe removal of the top layer of Au, while preserving the integrity of the underlying Au layer. In following attempts, a Cr hard mask was used (Figure 6.14b), which significantly reduced the number of "mouse-bite-type" defects at the bottom of the waveguide because the Cr etchant does not attack the bottom Au layer. Furthermore, this approach offers the added benefit of eliminating the necessity for a secondary lithography step. No significant difference in terms of roughness was observed when comparing the top of the fabricated devices and the spin-coated films prior to surface patterning for both methods.

After the device fabrication, the chips were cleaved into different lengths (ranging from 1 to 2.3 mm) for cut-back measurements.

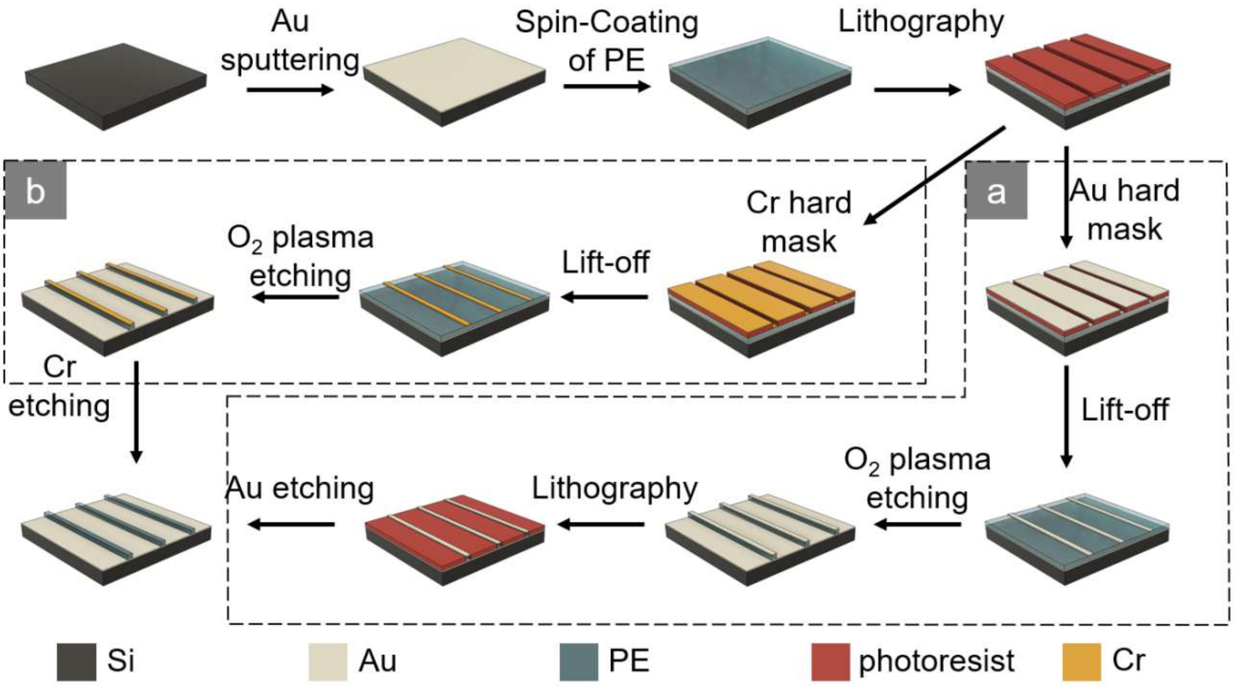

Figure 6.14 Schematic flow chart of the chip fabrication process, a) using an Au hard mask and b) using a Cr hard mask. Image taken from. Image taken from [205].

Figure 6.15 shows the SEM images of the typical fabricated PE-waveguides. The sidewalls exhibit a certain degree of roughness that can potentially lead to increased scattering losses and reduced efficiency of the device. Nevertheless, the upper edge of the waveguide exhibits a relatively flat profile, suggesting that the fabrication procedure attained a good level of precision.

We fabricated various geometries, ranging from 3 to 20 µm in width. The devices underwent etching using a plasma etching system (STS 320PC). However, this system did not have temperature control functionality, leading to some degree of uncertainty regarding the actual temperature of this processing step. Following the plasma etching process, we observed an inhomogeneous reduction in thickness. This phenomenon can be attributed to the combination of uncontrolled temperatures in the chamber and the low pressure during the etching process, which are particularly influential due to the polymer's relatively low melting point range of 110°C to 135°C.

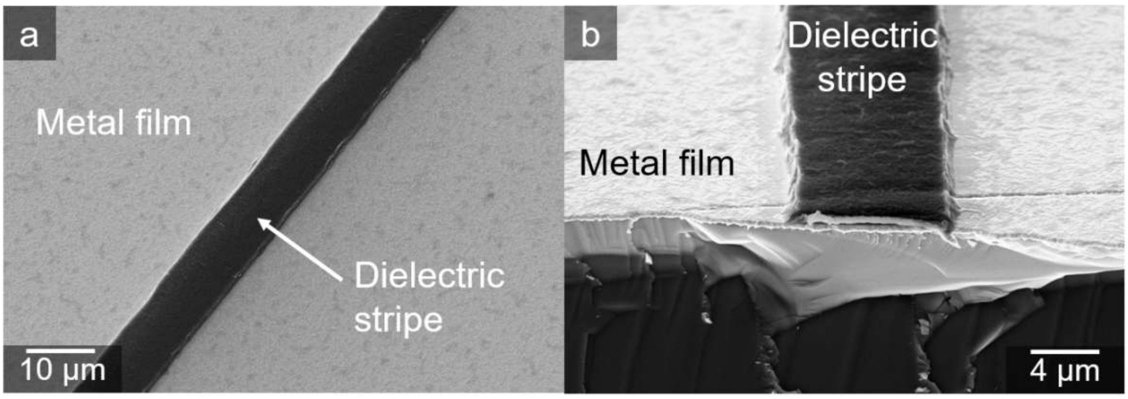

Figure 6.15 Scanning electron microscopy (SEM) image of a typical PE-ridge fabricated with a Au hard mask. a) Plasmonic waveguide and b) magnified view of its cleaved facet, for a 8 µm wide and 1 µm high PE ridge. Image taken from [205].

Devices fabricated using a 20 nm Cr-hard mask, instead of 100 nm of Au, exhibited a minor decrease in thickness. This suggests that the polymeric films may have reached their softening point (~110°C) during the etching process and were affected by the weight of the thicker hard mask. Nevertheless, these unforeseen variations in thickness enabled us to obtain devices with a broader range of geometric variations. Consequently, we were able to conduct a more comprehensive analysis, including different ridge geometries.

6.4 Characterization of DLSPP Waveguides

The propagation losses were determined using the cut-back method for each waveguide geometry [195–198]. The summary of the results in terms of waveguide and coupling losses is shown Figure 6.16a. The fabricated devices were then modeled in COMSOL, and the losses and normalized area results are displayed in the graph as dashed lines. The deviations between the measured and simulated losses shown in Figure 6.16a can be attributed to fabrication imperfections. Nevertheless, it is important to stress, that the measurements exhibit excellent agreement with simulations. The confinement of vertical and lateral modes in SPP waveguides strongly relies on geometric factors, as illustrated in Figure 6.16b. This relationship is empirically confirmed by comparing the measured coupling losses with the simulated normalized effective mode area (A_{eff}/A_0).

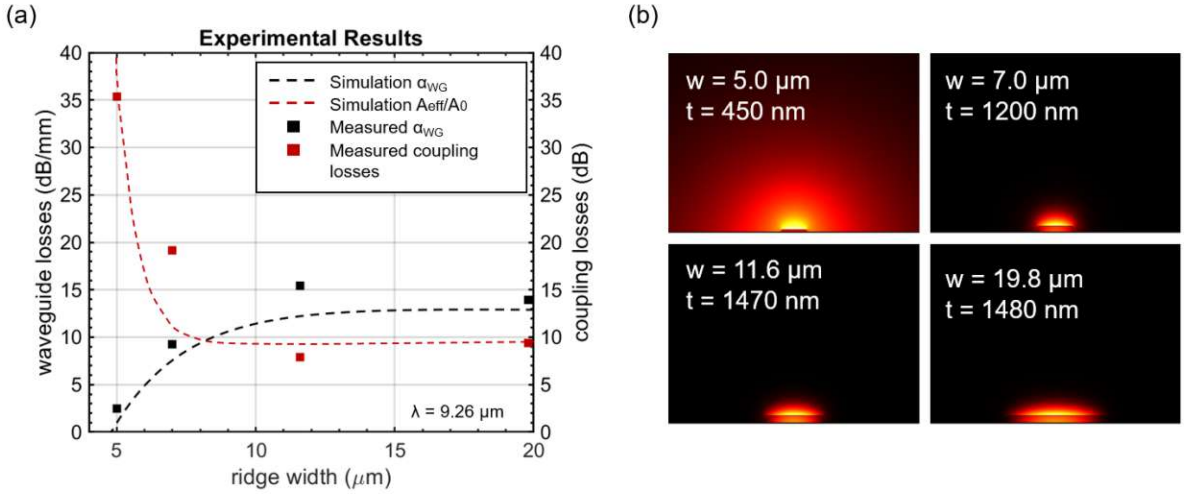

Figure 6.16 a) Summary of measured data. The values of the measured (squares) and simulated (dashed) waveguide losses are depicted in black, while the coupling losses extracted from the effective cut-back method (squares) are shown in red and compared with the mode effective area extracted from simulations. b) Cross-sectional profile simulations of the fabricated DLSPPWs, indicating the ridge geometrical factors, width (w) and thickness (t). Image taken from [205].

When performing end-fire coupling experiments, losses occur when the input light mode is not perfectly matched to the supported mode size of the receiving optical component. Consequently, larger effective mode areas lead to higher coupling losses, especially for lenses with small focal spot sizes (as seen in our case), as the spatial overlap between the lens and waveguide mode decreases. Conversely, smaller effective mode areas result in lower coupling losses due to increased spatial overlap between the two components. In conclusion, our measurements align well with the simulation results, providing an indirect validation of the measurement approach.

In order to investigate the bend losses, we fabricated 5 µm wide and 3 µm thick waveguides (Figure 6.17b) in the form of double S-bends (Figure 6.17a, between "A" and "B"). The design of the bends targeted the optimal bend radius of 28 µm (as shown in Figure 6.13b), ensuring adiabatic evolution of the mode throughout the bend. Two sets of devices were fabricated, with bend offsets (i.e., the difference between the two arms) of $d_1 = 50$ and $d_2 = 75$ µm. Table 6.2 presents a summary of the results. Figure 6.17b illustrates the excellent agreement between the experimental and theoretical transmission values.

Offset [µm]	Simulation [dB]	S-bend losses [dB]	Scattering (defects) [dB]	Bend losses [dB]
50	2.30	3.18	0.88	1.31
75	3.45	5.22	1.77	2.33

Table 6.2 The table presents the S-bend losses, both simulated and measured, for a 106 µm long S-bend. Additionally, it includes the scattering losses caused by fabrication defects, which are obtained by subtracting the simulated losses from the measured losses.

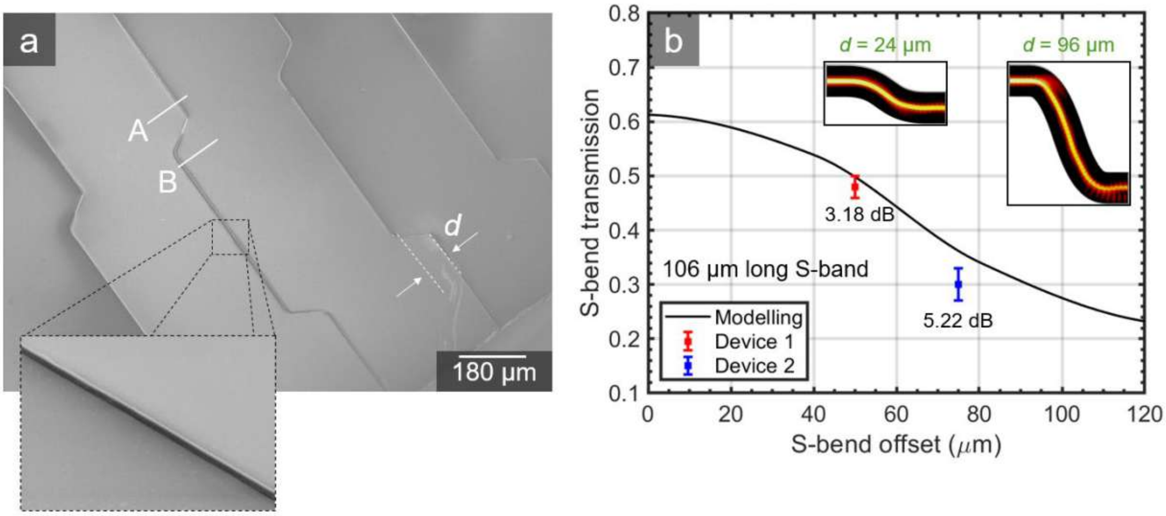

Figure 6.17 a) SEM images of the S-bend structures with an offset of d = 75 µm, (inset) straight section of the PE-waveguide. b) S-bend transmission dependence on the offset distance between the two arms. (inset) top-view of the 3D simulations for offsets of d = 24 µm and d = 96 µm. Image taken from [205].

The findings presented here have significant implications for the advancement of organic-based, bio-compatible photonic devices in the LWIR region. The remarkable low-loss properties exhibited by the PE offer a new, highly promising avenue for achieving fully integrated LWIR photonic systems.

The successful implementation of UV-lithography to pattern PE films opens up new opportunities for also creating other low-loss waveguide structures in the mid-to far-IR range. This includes other traditional photonic components such as dielectric or photonic crystal waveguides. Furthermore, the same fabrication process can be utilized for developing microfluidic chips with micrometer-scale features, providing a novel platform for fully-integrated lab-on-a-chip (LOC) systems that possess transparency in both the VIS and mid-IR spectra, thereby unlocking a wide array of biological and chemical sensing applications.

The broad transparency of PE, ranging approximately from 2 to 200 µm [163,228], opens up possibilities for developing devices beyond the LWIR range. This transparency enables applications in the THz range and paves the way for further advancements.

7
INORGANIC DIELECTRIC-LOADED PLASMONIC WAVEGUIDES

This chapter is based on the publications "Octave-spanning low-loss mid-IR waveguides based on semiconductor-loaded plasmonics" [141] and "Surface Protection and Activation of Mid-IR Plasmonic Waveguides for Spectroscopy of Liquids" [229].

7.1 Germanium

Ge, has a rich history within the semiconductor industry. While often overshadowed by Si, its vital role in the development and success of modern electronic devices. The transistor, invented in 1947, and the integrated circuit, introduced in 1958, initially were based on Ge rather than Si. In fact, the early years of solid-state technology heavily relied on Ge diodes and bipolar-junction transistors [230]. It was only later, with advancements such as the discovery of SiO_2 dielectric passivation and the introduction of the planar metal-oxide-semiconductor field-effect transistor (MOSFET) process in the mid-1960s, that Si surpassed Ge to become the dominant material in the semiconductor industry [230]. However, just a few years later, Ge found a new role in the advancement of Silicon photonics. Its compatibility with Si and optimal optical properties made it essential for developing integrated photonic devices like modulators, detectors, and waveguides [146].

Ge is a highly transparent material in the entire mid-IR spectral range, and it is fully compatible with complementary metal-oxide-semiconductor (CMOS) fabrication processes. It can be easily deposited in a suitable quality by a regular sputtering process and patterned by following state-of-the-art cleanroom fabrication techniques. In fact, it has already been investigated quite extensively for the development of many mid-IR devices [231–233]. Therefore, all these benefits motivate its investigation also in combination with metallic layers for the fabrication of efficient mid-IR plasmonic waveguides.

7.2 Design Optimization for Specific Applications

In addition to the aforementioned benefits, Ge possesses a notably high refractive index (n~4) [234]. This means that, for passive photonic devices, the light mode can be squeezed to very small sizes, offering a broad range of design freedom in terms of confinement and propagation length. The high refractive index offers flexibility in design, facilitating the implementation of multiple configurations (refer to Figure 7.1), customized for specific applications. It is possible to identify at least two separate optimal device geometries: a low-loss configuration with a tailorable surface evanescent field in the surrounding medium, capable of providing ideal design for surface sensing (Figure 7.1a), and an ultra-compact geometry with a high effective mode index, best for miniaturized, and high-speed modulators or radiation guiding on the sub-wavelength scale (Figure 7.1b).

Figure 7.1 shows the two configurations for a wavelength of 9 µm. When thin dielectric slabs (~200–300 nm) are applied, the plasmonic mode mostly (>96%) [48,141] propagates in the surrounding dielectric medium, making this approach highly suitable for, e.g., real-time in-situ sensing applications in liquids, as previously demonstrated for proteins, measured around 6.2 µm wavelength [49]. Under these conditions, the propagation length is nearly 1 mm, and the effective mode area is 26.7 μm^2, constituting a very good balance between on-chip low-loss propagation and a mode size that fits well to the facet of a QCL/QCD, minimizing coupling losses among all components. However, in this device architecture, the mode effective index is too low to provide radiation guiding, as shown in a preliminary simulation of Figure 7.2a. A significant loss of signal occurs when transmitting over a short adiabatic bend with a length of 50 µm. The optical mode escapes the lateral edges of the thin Ge stripe, resulting in signal loss at the second port. However, it must be noted that simulations with further improved boundary conditions (i.e., with perfectly matched layers) may reveal even inferior results.

On the other hand, if the Ge layer is thicker (Figure 7.1b), the mode effective index increases (up to $N_{eff} = 2.7$), allowing for a much more efficient guiding (see Figure 7.2b), as the mode is strongly confined in the Ge ridge.

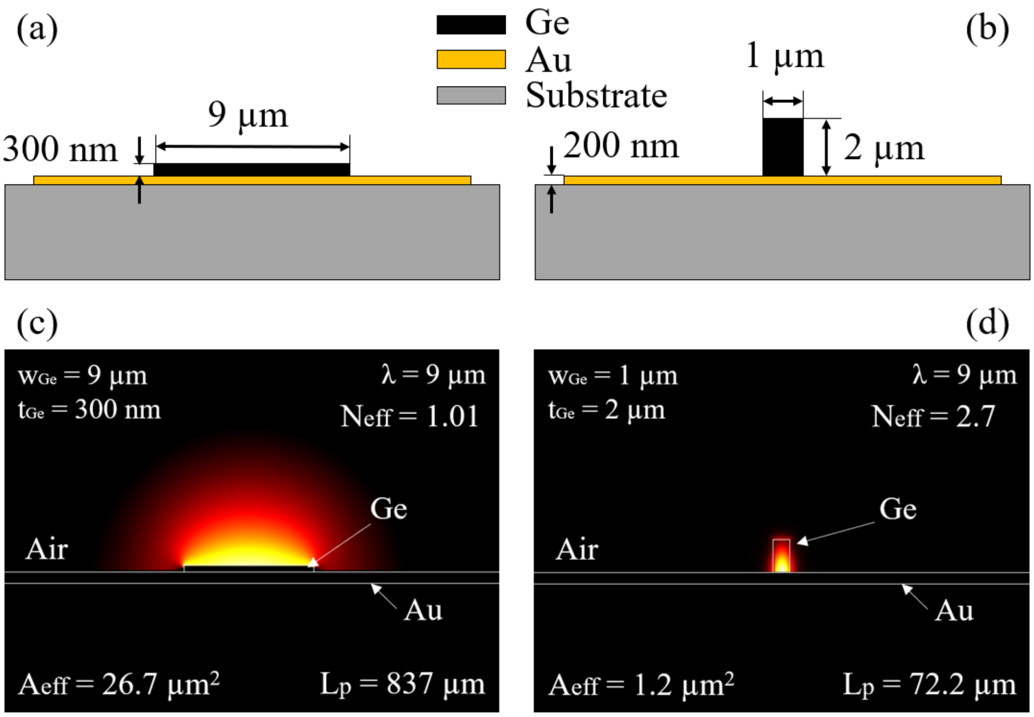

Figure 7.1 SLSPP waveguide cross sections. a) configuration and c) simulation of a Ge-based plasmonic waveguide optimized for sensing [48–50,141]. b) configuration and d) simulation of a Ge ridge SLSPP waveguide optimized for ultra-compact modulators and on-chip beam guiding

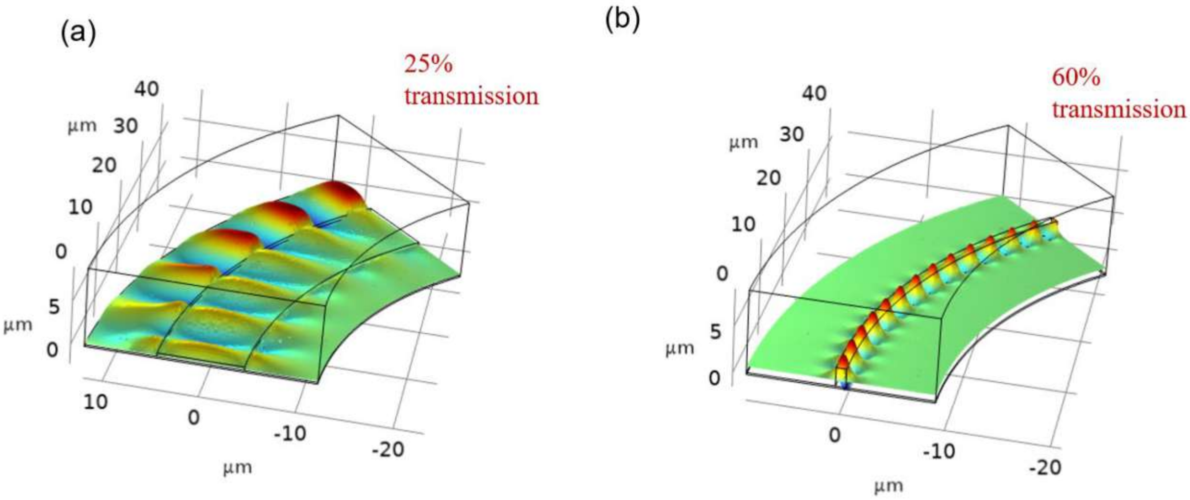

Figure 7.2 The figure shows the guiding capability of the two Ge-based SLSPP waveguide configurations at a wavelength λ = 9 μm, for a and a 45-degree angle, and a bend radius of 50 μm. a) The transmission of a 9 μm wide and 400 nm thick Ge slab results in only 25% of transmission, while b) the Ge-ridge configuration of a 2 μm high and 1 μm wide geometry allows a 60% transmission for the same bending geometry.

In this work, we focus on the low-loss configuration for sensing of Figure 7.1a, as for radiation guiding, the solution proposed in Chapter 6 is considered the best trade-off for low-loss and on-chip guiding for the LWIR range. However, at the end of this chapter, we will show an alternative approach that provides a competitive solution for achieving low-loss on-chip guiding and highly favorable fabrication feasibility through the utilization of on-chip integrated mirrors.

7.3 Semiconductor-Loaded SPP Waveguides for Broadband Sensing Application

In this and the following sections, we investigate the Ge-slab configuration as a sensing platform, focusing on its key properties. Our goal is to create a plasmonic platform that offers maximum flexibility and addresses several important feautures simultaneously. These include:

i) Large spectral bandwidth

ii) Compatibility with Si-integrated photonics and, to some extent, with CMOS processing

iii) Bio-compatibility for sensing applications

iv) Simplicity in the fabrication process

v) Feasibility of integration with active components

By addressing these points, we aim to show one of the most versatile and flexible plasmonic platform, particularly suitable for the LWIR spectral range and beyond.

7.3.1. Device Performance

Figure 7.3 illustrates the results of the simulations of the waveguide, showing the vertical mode confinement (Figure 7.3a), propagation length (Figure 7.3b), and the effective mode index (Figure 7.3d) for different Ge thicknesses and widths at a wavelength of 9.12 µm. Particularly, when the Ge layer thickness is approximately 300 nm, the plasmonic configuration enables mm-range propagation for Ge waveguides that are around 9 µm wide (to ensure sufficient suppression of higher-order lateral modes). This configuration provides excellent vertical confinement (L_y ~6 µm, which is below one wavelength extension) and lateral confinement (the mode profile remains well within the width, as shown by dashed vertical lines in Figure 7.3b (inset)). These findings highlight the suitability of this geometry for integrated sensing applications [48–50], where typically distances of some hundreds of microns need to be overcome, while a considerable portion (>95%) of the optical mode needs to be guided outside in the surrounding medium (i.e., air or liquids) for detecting specific molecular species of interest.

Figure 7.3c confirms the excellent mode confinement (both lateral and vertical) for a 300 nm thick and 9 µm wide Ge waveguide together with a mode propagation length of 663 µm, i.e., well within the range needed for liquid spectroscopy experiments [48]. Figure 7.3d shows that increasing the Ge thickness beyond 300 nm significantly increases the effective mode index, thus resulting in an also significantly reduced overlap of the mode with the surrounding medium.

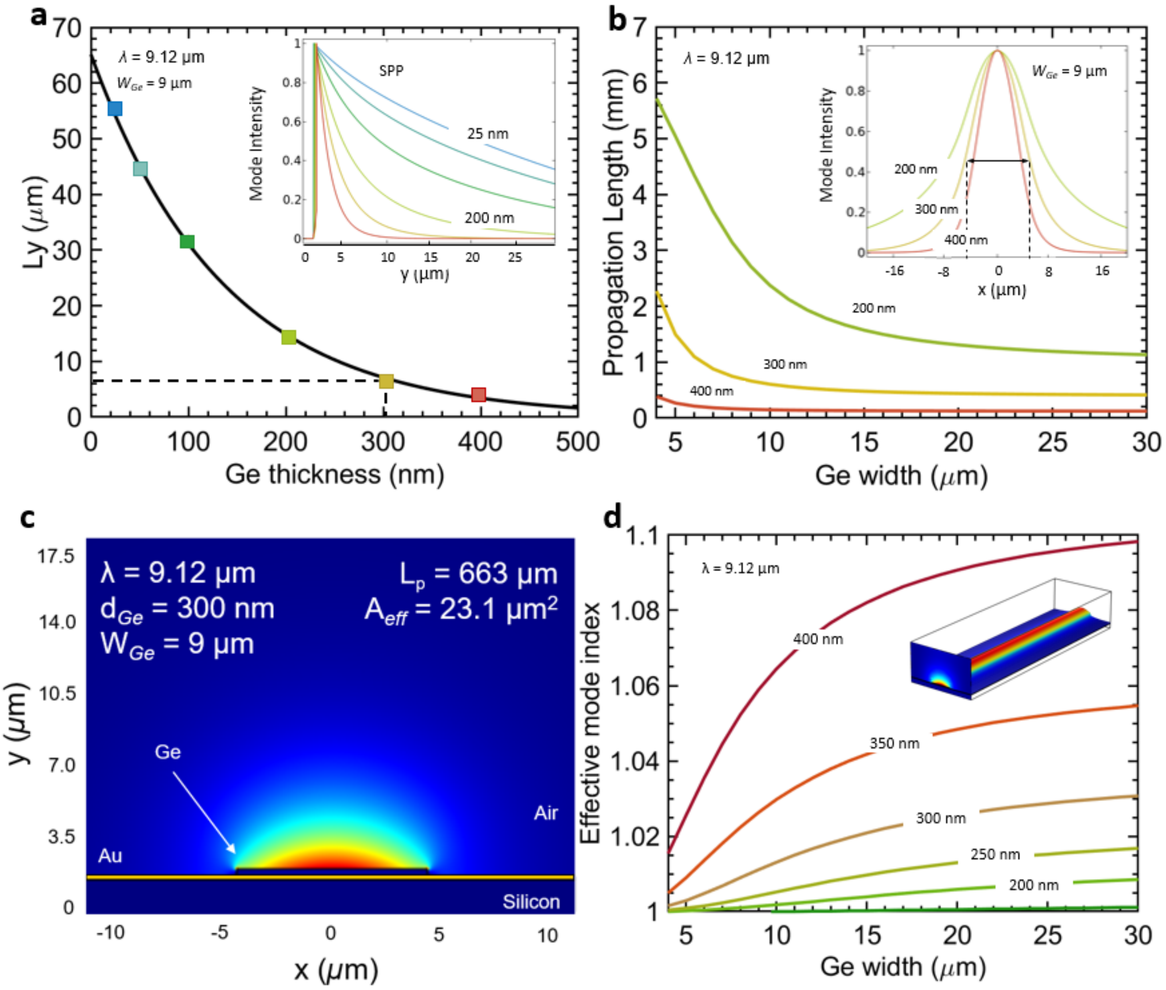

Figure 7.3 Simulation results at a wavelength of 9.12 µm. (a) Vertical mode confinement (L_y) as a function of the Ge layer thickness. The optimal design (width of 9 µm and thickness of 300 nm) is highlighted by dashed lines (inset: mode intensity profile with respect to vertical position y for different thicknesses of the Ge slab). (b) Propagation length for different Ge stripe widths (inset: lateral mode profile for different thicknesses for a 9 µm wide Ge stripe). (c) Cross-sectional facet view of the simulated mode profile for the $|E|^2$ distribution, showing the plasmonic mode. (d) Effective mode index for different Ge stripe widths and thicknesses. The inset shows a 3D simulation of the $|E|^2$ distribution for the waveguide design shown in (c). Figure taken from [141].

The simulations in Figure 7.4 show that it is possible to preserve similar device performances, in terms of N_{eff}, L_p, and A_{eff} for different mid-IR wavelengths, by simply adjusting geometrical factors. As shown in Figure 7.4c, a thicker and wider Ge waveguide can balance the effects of an increased wavelength in a way that L_p and A_{eff} remain comparable. Consequently, the simulations show that the entire LWIR range (6 – 12 µm) can be covered with this material system and concept at similar performance.

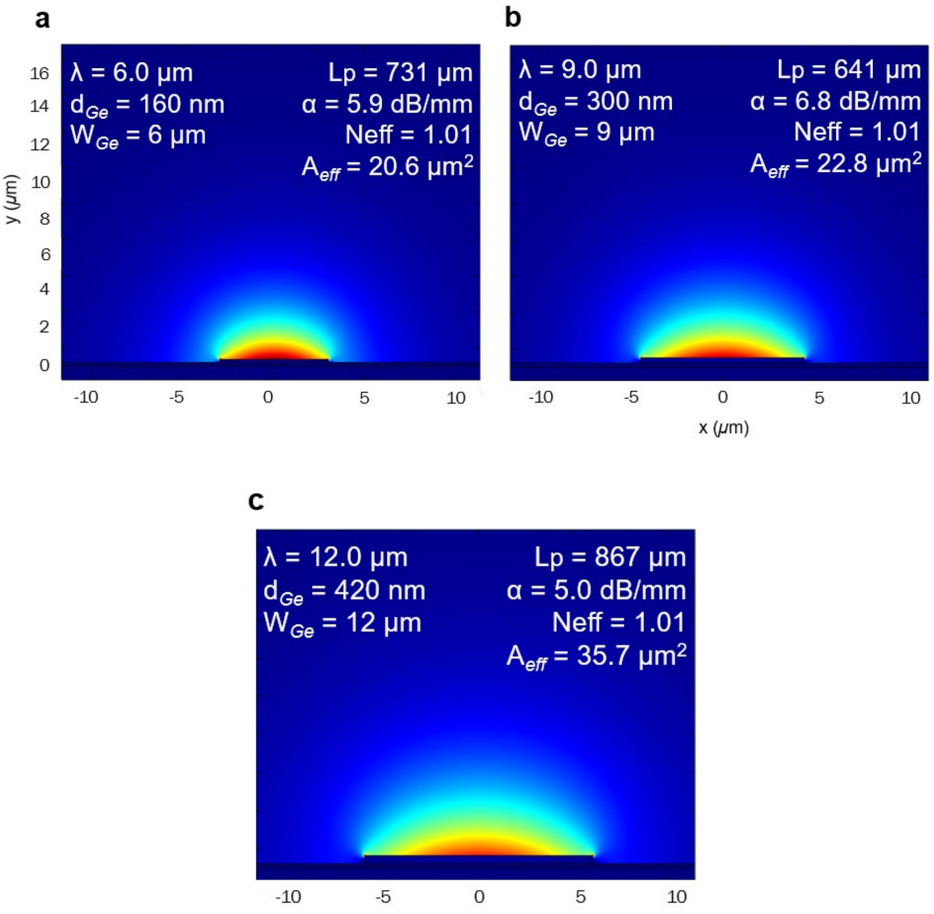

Figure 7.4 2D simulations of the mode profile facet with the respective FOM for different waveguide widths and wavelengths. Figure taken from [141].

By employing a similar concept, it can be demonstrated that these performance capabilities can be extended to cover the entire transparency band of Ge. Consequently, this allows for comprehensive coverage of the mid-IR range, especially important for sensing for biomedical applications, including body fluids analysis, glucose monitoring, breath analysis, and disease diagnostics, all with comparable performance levels [235,236].

Figure 7.5 demonstrates that by appropriately adjusting the geometry of the Ge slab in relation to the wavelength, it is possible to maintain consistent propagation characteristics of the plasmonic waveguide. The figure illustrates that the FOM (discussed in section 3.4), indicated by the blue line, remains nearly constant. To achieve this, the width of the waveguide is set equal to the wavelength ($w_{Ge} = \lambda$), while the thickness can be scaled linearly, as indicated by the green line.

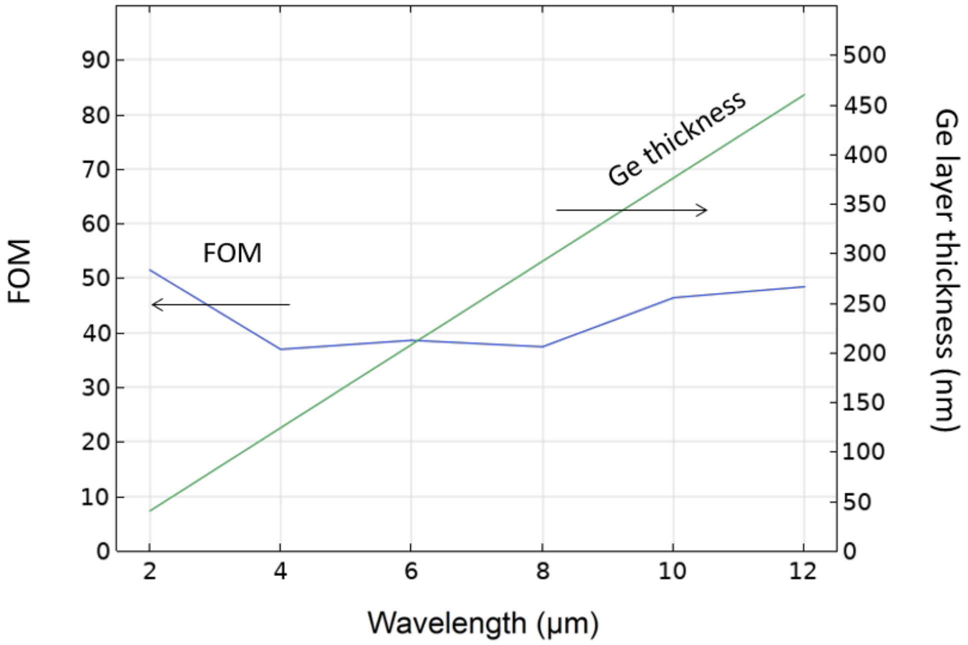

Figure 7.5 Simulations results obtained by sweeping the wavelength of a Ge-on-Au plasmonic waveguide. The waveguide was optimized for each wavelength to achieve comparable results as shown in Figure 7.4, demonstrating the feasibility of obtaining similar FOM (blue line) for each wavelength. In these simulations, the geometry of the Ge stripe was adjusted by maintaining the width equal to the wavelength ($w_{Ge} = \lambda$), while the thickness increased linearly from 40 nm to 460 nm (green line).

To assess the valitidy of the simulations results, the SLSPP waveguides were fabricated in our dedicated cleanroom facilities. Si substrates, specifically 2-inch wafers with 275 µm thickness, were used as carrier wafers. A 5 nm Ti adhesion layer and a 200 nm Au layer were deposited on the plasma-cleaned Si surface through high-vacuum e-beam evaporation. A 300 nm Ge layer was sputtered on top of the Au layer using a multiple cycle process. The Ge layer was patterned using a photoresist mask and selectively etched through an SF_6-O_2-based ICP-RIE process. After removing the remaining resist, individual waveguides of 1.0, 1.5, and 2.0 mm lengths were cleaved perpendicular to the ridges using a scribing and breaking technique. The fabrication process is sketched in Figure 7.6b, while Figure 7.6a illustrates a 3D schematic rendering of the proposed waveguide design.

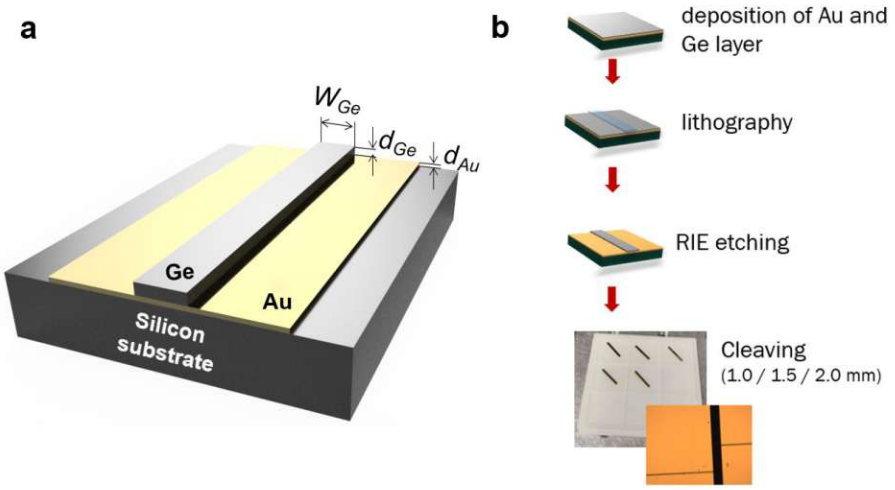

Figure 7.6 (a) 3D schematic of the Ge-based SLSPPW. (b) Process flow of the fabrication steps. Image adapted from [141].

Figure 7.7a displays the attenuation values obtained through the cut-back method for the Ge-SLSPP waveguides (width ~9.0 µm, thickness ~290 nm) with lengths of 1.0, 1.5, and 2.0 mm at λ = 9.12 µm. The experimentally extracted total propagation loss of the fabricated waveguides is 6.73 dB/mm, corresponding to a propagation length L_p of 645 µm. The correspondence between the regression line derived from the data (depicted by the solid red line) and the simulation results (illustrated by the blue dashed line) demonstrates a high level of agreement. The linear model is utilized to extract the total coupling losses from both facets. The calculated value for the total coupling losses is determined to be 6.28 dB. The comparison between the measurements of the lateral mode profile and the corresponding simulations is depicted in the inset of Figure 7.7a, revealing excellent agreement.

In our study, we performed the cut-back method at one selected wavelength of 9.12 µm. As mentioned earlier, when utilizing a different wavelength, it is necessary to adjust the geometry of the slab in order to ensure constant performance. Therefore, the use of a waveguide with a fixed geometry causes the mode size to vary with the excitation wavelength. This becomes significant in setups or integrated devices, where different components are coupled together. In such cases, the differences in mode sizes can lead to mode mismatch, resulting in variations in coupling losses (as also demonstrated in section 6.4). However, in the context of sensing devices, any variations or wavelength-dependent coupling losses can typically be effectively compensated for through calibration measurements.

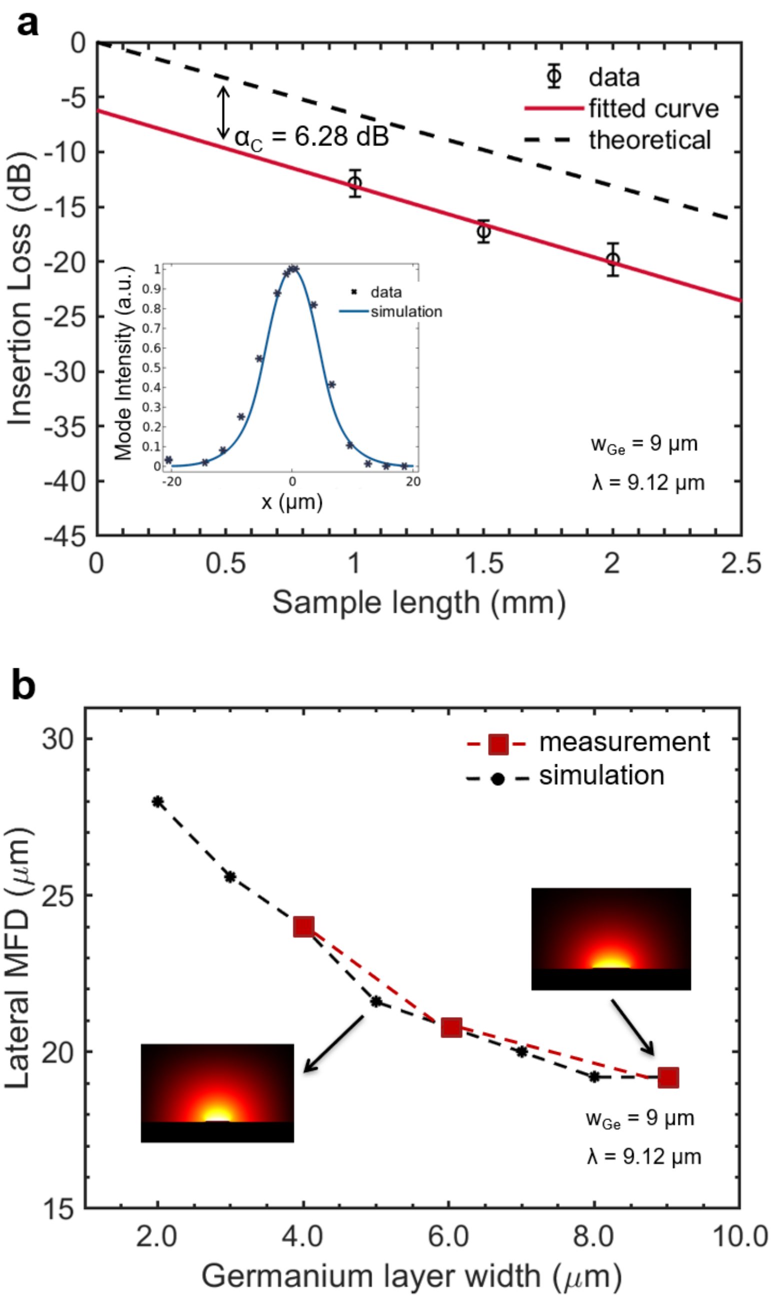

Figure 7.7 (a) The coupling losses at 9.12 μm for Ge-SLSPP waveguides were evaluated using the cut-back technique. Multiple devices were experimentally measured per length, and the averaged data points were obtained. The inset graph demonstrates the beam profile with excellent agreement between the measured data points (points) and the simulated results (solid line). (b) The lateral mode field diameter (MFD) depends on the width of the Ge layer. The insets show the modulus of the electric field distribution for various Ge stripe widths, providing further insights into the optical properties of the waveguide structure. Figure taken from [141].

This effect is shown in Figure 7.7b, where the lateral Mode Field Diameter (MFD), defined as the $1/e^2$ width of the lateral profile of the electric distribution, is plotted against the Ge-layer-width at a fixed wavelength.

To highlight the broad bandwidth capabilities of the proposed waveguide structure, we conducted loss measurements at different wavelengths. We specifically examined waveguides with widths of 9 µm and 6 µm, both with a Ge-thickness of 290 nm. Additionally, we analyzed a waveguide with a width of 4 µm and a thickness of 220 nm. The results are shown in Figure 7.8a, b, and c. The dashed lines represent the theoretical losses extracted from the 2D-simulations, while the solid lines are fitted to the measurement data (squares) "to guide the eye". The measurement points also include the subtraction of the coupling losses, measured at 9.12 µm.

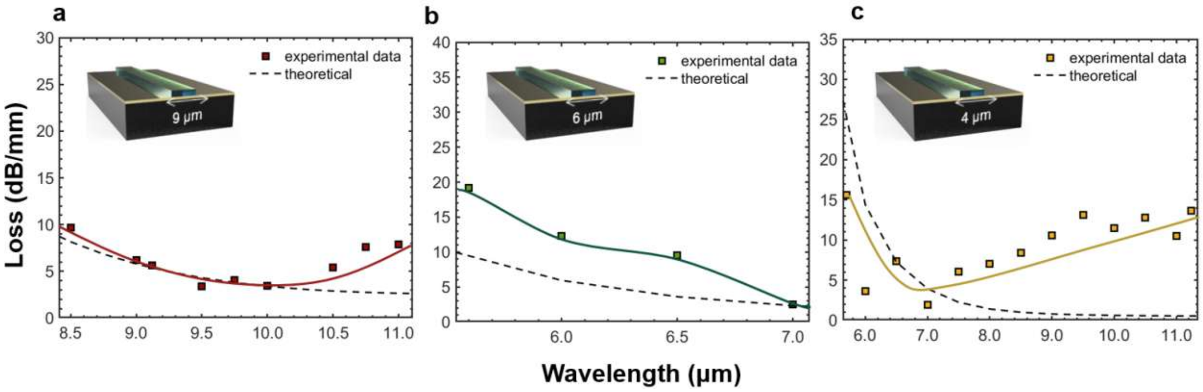

Figure 7.8 (a) Spectral bandwidth of a 9 µm wide and 290 nm thick Ge plasmonic waveguide in the spectral range of ~8.5 – 11 µm. (b) Spectral bandwidth of a 6 µm wide and 290 nm thick plasmonic waveguide in the spectral range of 5.5 – 7.0 µm (c) Spectral bandwidth of a 4 µm wide and 220 nm thick Ge plasmonic waveguide in the spectral range of ~5.7 – 11.2 µm. Figure taken from [141].

In Figure 7.8a we investigated a waveguide with a Ge width of 9 µm and examined its spectral bandwidth ranging from 8.5 µm to 11.2 µm. As anticipated, when calculating the theoretical losses for such waveguides and accounting for the coupling losses indicated in Figure 7.7a, we observe significant overlap in the wavelength range from 8.5 µm to approximately 10 µm. Beyond this threshold, the wavelength exceeds the waveguide width, resulting in a larger mode area and, consequently, higher coupling losses, as explained earlier (see Figure 7.7b).

Similarly, Figure 7.8b and c exhibit reasonable agreement between the measured and calculated values for the 6 µm and 4 µm wide waveguides, particularly in the wavelength range of approximately 5.6 µm to 7.5 µm. However, it is important to note that this spectral region is susceptible to strong absorption by water vapor in the atmosphere. As a result, fluctuations in humidity within the laboratory environment could contribute to increased variability or "scattering" of the measurements within this specific wavelength range.

In Figure 7.8c, it is evident that beyond this specific wavelength range, the experimental data consistently deviates from the theoretical values, even after accounting for the extracted coupling losses measured at 9.12 µm. It is important to note that in this case, the estimation of coupling losses is only an approximation due to the significant mismatch between the size of the waveguide used in the measurements and the excitation wavelength. This deviation can be attributed to the increasing mode size resulting from the width of the Ge stripe exceeding the wavelength, as discussed previously in Figure 7.7b and also shown in the case of PE (section 6.4). Nevertheless, the measured waveguide losses exhibit a weak spectral dependence, demonstrating the broad and low-loss capabilities of this waveguide geometry. These characteristics span a wide frequency range, covering almost the entire LWIR spectrum. Remarkably, the plasmonic waveguide consistently maintains low loss (<15 dB/mm) throughout the octave-spanning region of 5.6-11.2 µm. This shows the efficacy of this plasmonic waveguide design for achieving low-loss performance across a broad frequency range.

The results presented indicate that the proposed architecture have comparable, if not superior, performance when compared to previously suggested LWIR plasmonic waveguides. To date, theoretical investigations have primarily explored the potential of certain new materials for this purpose. These materials include heavily doped semiconductors, which have predicted losses from simulations of approximately 10.4 dB/mm at 10 µm [46], germanides with predicted Lp around 410 – 615 µm [237] and silicides [238] (predicted Lp in the millimeter range but mode extends >> 10 µm into the above dielectric, e.g. air).

Furthermore, our waveguide architecture allows for integration onto various standard substrates such as Si and III-V materials. As a result, the Ge-SLSPP geometry demonstrates compatibility with both back-end-of-line CMOS and III-V technologies. In contrast to alternative concepts that heavily rely on epitaxy and have restricted compatibility with specific carrier substrates, our proposed geometry offers a simpler implementation and deposition process, enabling broader compatibility with various substrate types.

7.3.2. Device Protection for Water-based Spectroscopic Applications

The solubility of Ge in water is a critical factor to consider when designing and realizing photonic sensors, especially for liquid analytes. When exposed to aqueous environments, Ge oxide can undergo dissolution [239], leading to performance degradation and reduced sensor lifespan. To overcome these problems, we tested the implementation of protective top-layers to enhance the durability and stability of Ge-based photonic sensors. Figure 7.9 shows the cross-sectional layer structure of the designed SLSPP waveguides, including a surface protection layer.

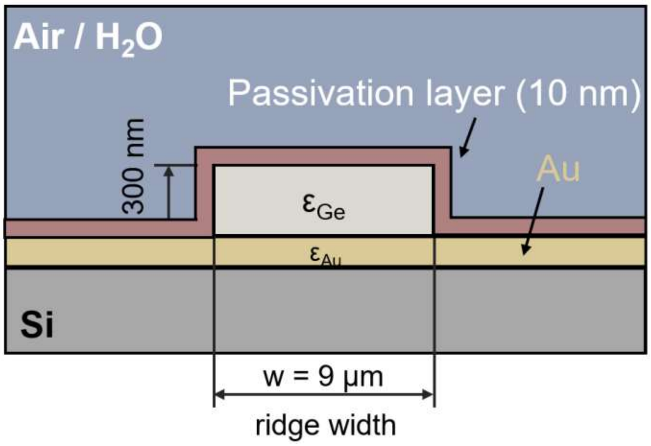

Figure 7.9 Cross-section of the waveguide layer structure. The Ge- based SLSPPW is protected by a passivation layer of nominally 10 nm with a dielectric. Figure taken from [229].

When working with semiconductor-based devices, especially those involving heterostructures or nanometer-thin layer sequences, precise control of material interfaces becomes crucial. This requirement is particularly significant, especially when dealing with surface-sensitive structures like those based on surface plasmons, which generally exhibit extraordinary sensitivity to the surrounding environment [240,241]. The challenge lies in protecting their surfaces while preserving their plasmonic functionality. To address this, coatings for mid-IR plasmonics used in liquid sensing applications must fulfill three main criteria: a) prevent physical penetration from the surrounding liquid, b) introduce minimal additional optical losses, and c) minimize the impact on the plasmonic characteristics. These criteria can be effectively met by utilizing high-quality dielectric materials commonly employed in CMOS transistors. These nanoscale dielectric layers can homogeneously encapsulate the Ge-slab underneath, exhibit relatively low losses, and have minimal interference with the underlying plasmonic structure due to their very low thickness.

Among different fabrication methods like sputtering or evaporation, ALD offers precise control over the thickness of monolayers and ensures excellent conformality of the deposited films [242]. Moreover, ALD exhibits high layer uniformity [243], therefore fully encapsulating the Ge layer, making it the preferred deposition technique for this purpose. Therefore, before conducting the experiments, we assessed the extra waveguide losses caused by the nanometer-scale passivation layers using FEM-simulations. However, to simulate the impact of the additional protective coatings and due to the lack of literature on the complex mid-IR refractive index of the coating materials [53], we first performed mid-IR ellipsometry measurements of different passivation materials on unstructured Au-coated Si wafers. A commercial ALD reactor (Savannah, Cambridge NanoTech Inc, USA) was used to deposit four protective coatings: HfO_2, ZrO_2, Al_2O_3, and TiO_2. Prior to the deposition process, the samples were inserted into the reactor and allowed to thermalize for 10 minutes [229]. The results of the complex refractive indices are shown in Figure 7.10a and b.

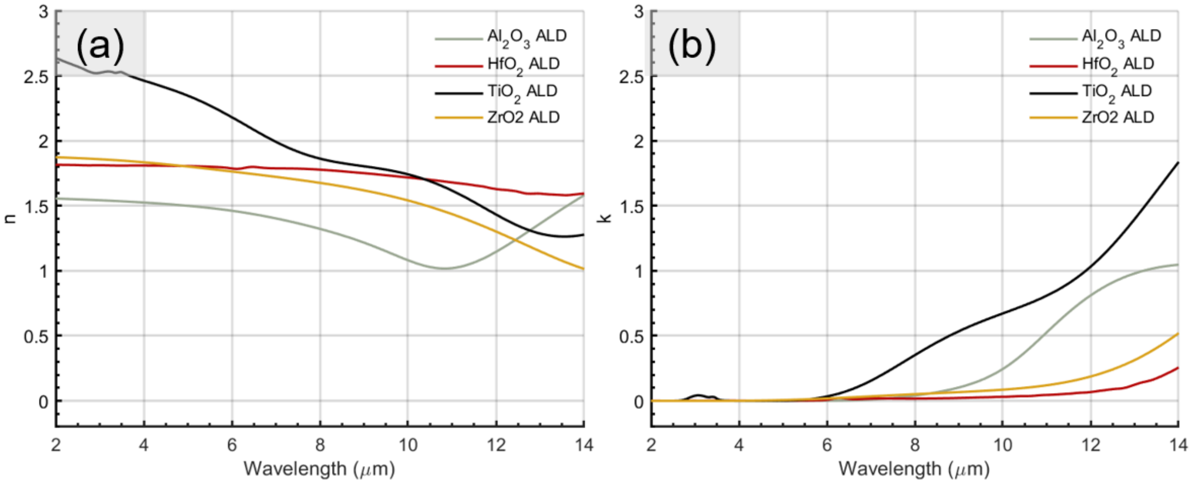

Figure 7.10 The refractive indices of four different ALD coatings (Al_2O_3, HfO_2, TiO_2, and ZrO_2) was determined using mid-IR ellipsometry measurements. The spectral dependence of the real (n) and imaginary (k) parts of the refractive index is depicted in Figure (a) and (b), respectively. Figure taken from [229].

Figure 7.11 illustrates the resulting increase in losses at 9.38 μm when considering the implementation of 10 nm thick passivation layers for the materials of Figure 7.10. These losses are presented as a relative increase compared to simulating bare Ge-slabs on Au without the protective coatings. The additional passivation layers contribute an increase in losses ranging from 2% (Al_2O_3) to 7% (TiO_2) for a typical SLSPP waveguide, compared to the scenario without these coatings. The increase in losses can be attributed to two factors: first, additional absorption losses caused by the imaginary part of the coating's refractive index, and second, Au-losses dependent on mode confinement, which in turn depends on the real part of the coating's refractive index.

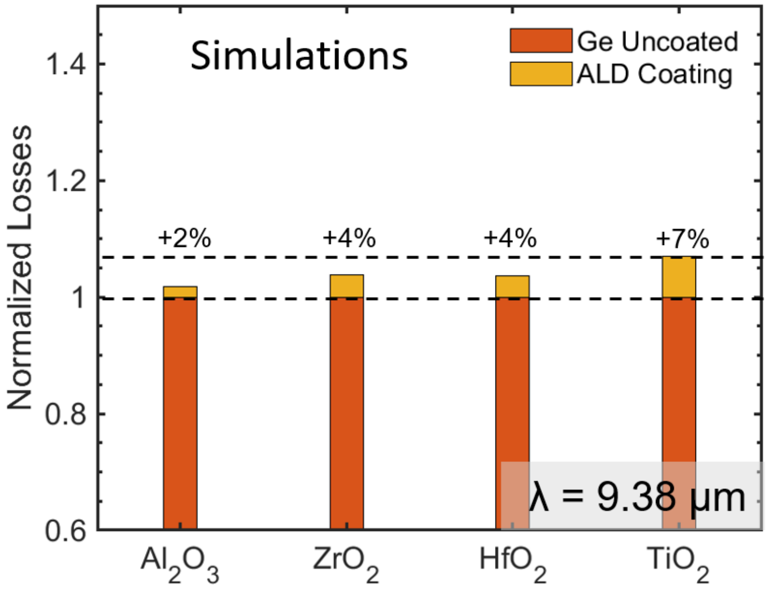

Figure 7.11 Additional losses of the coated SLSPP waveguides when simulating the impact of applying 10 nm thick layers of the different coatings at 9.38 µm wavelength. Figure taken from [229].

Despite some additional losses, the coatings seem well-suited for sensing applications in the mid-IR range, where state-of-the-art liquid sensors typically require very short plasmonic sensing sections (approximately 10 to 50 µm) [49,245,246]. In contrast, the propagation lengths for the presented devices are significantly longer, exceeding 500 µm [141].

To investigate the protective capabilities of the selected materials, we utilized a slightly modified fabrication method from the one described above, following the procedure outlined in Figure 7.12. After applying a 100 nm thick layer of Au via sputtering (7 cycles, $P_{base} \leq 1e{-}5$ mbar), on the Si substrate, the following stage involved a lithography and development step. Subsequently, a 300 nm thick Ge layer was sputtered onto the sample (12 cycles, $P_{base} \leq 1e{-}5$ mbar). The Ge stripes were obtained through a lift-off process and then cleaved to various waveguide lengths ranging from 1 mm to 2 mm.

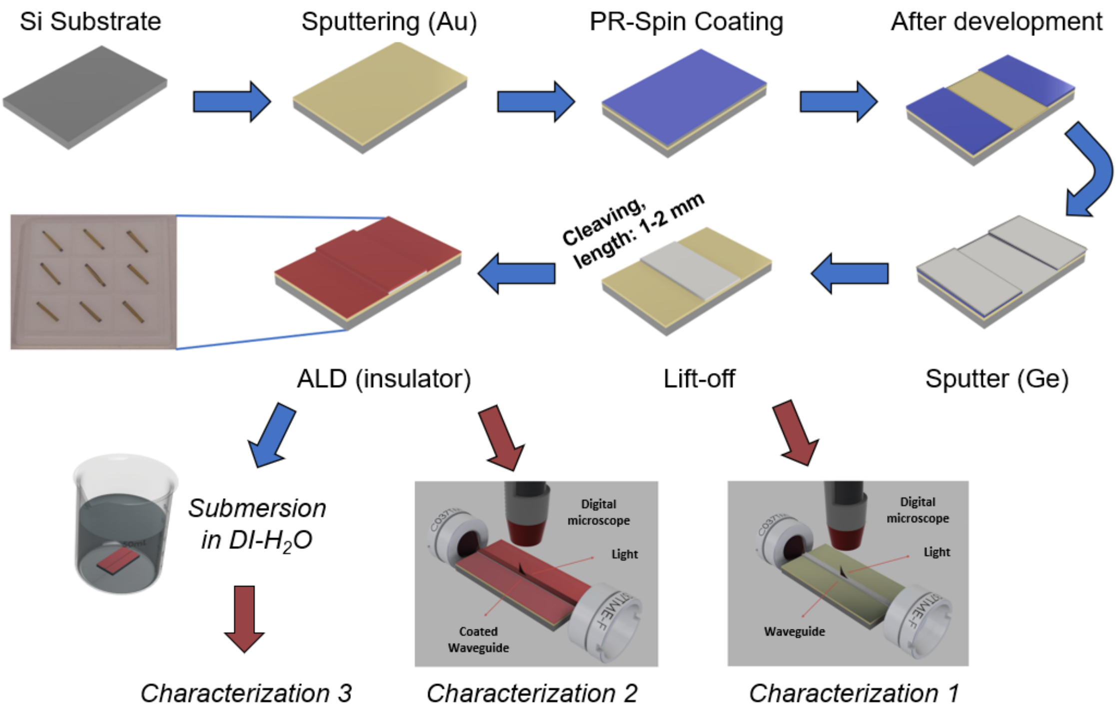

Figure 7.12 Process flow of the plasmonic waveguide fabrication and experimental characterization. Blue arrows represent fabrication steps. Red arrows represent characterization steps. Figure taken from [229].

The waveguides fabricated with the lift-off process exhibited slightly degraded sidewalls, increased line edge roughness, and round edges, as shown in Figure 7.13b, in contrast to the structures discussed in section 7.3.1 (Figure 7.13a), which resulted in smoother sidewalls, reduced line edge roughness, and sharper slab edges. Nevertheless, the devices fabricated through the lift-off process show satisfactory overall ridge smoothness and sidewall quality, which enables conducting the study as intended, while enabling faster prototyping compared to the RIE etching process. This is confirmed by the optical characterization of the waveguide losses, which align with the results from previous work (see Figure 7.7a and Figure 7.14).

The waveguides were characterized in the setup shown in Figure 5.8, using a CW single-mode DFB QCL emitting at a wavelength of 9.38 µm, and operated with an optical output power of 1.2 mW. The results indicated that the coupling losses were comparable to those observed in our previous study [141], suggesting that the mode size of the devices remained consistent, as expected, for nominally equal devices. However, the analysis revealed scattering losses (due to a more significant number of fabrication defects) of approximately 4.5 dB, a value that is significantly higher than the waveguide fabricated using the RIE etching process, which exhibited scattering losses of approximately 0.5 dB. This finding aligns with the observations made during the visual analysis of the SEM pictures (of which Figure 7.13 is a representative example).

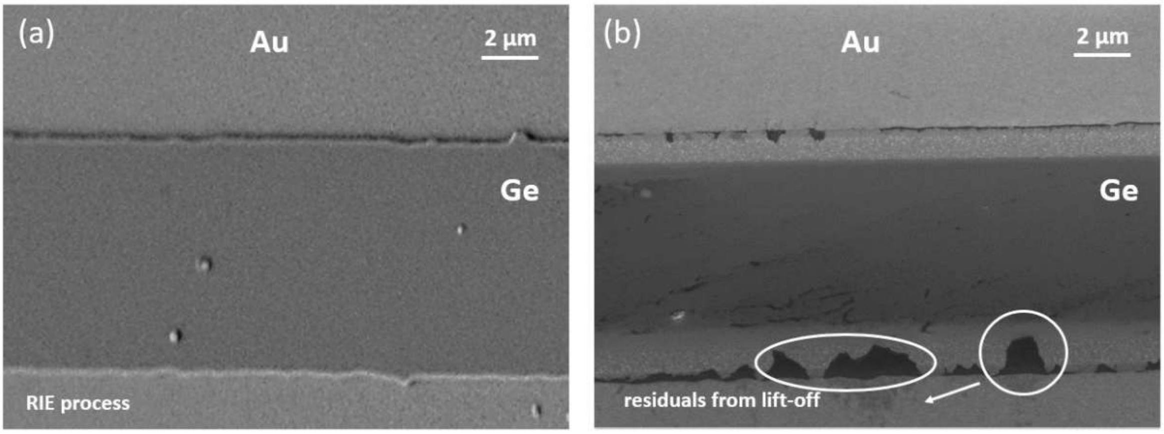

Figure 7.13 Comparison between the top-view of (a) a Ge waveguide fabricated with an RIE process and (b) through an acetone lift-off process. The waveguides exhibit slightly degraded sidewalls, increased line edge roughness, and round edges compared to the RIE etching process. Figure taken from the supplemental material of [229].

The total waveguide losses, including material and scattering (from roughness and fabrication defects) losses, were measured to be 9.7 dB/mm, as shown in Figure 7.14.

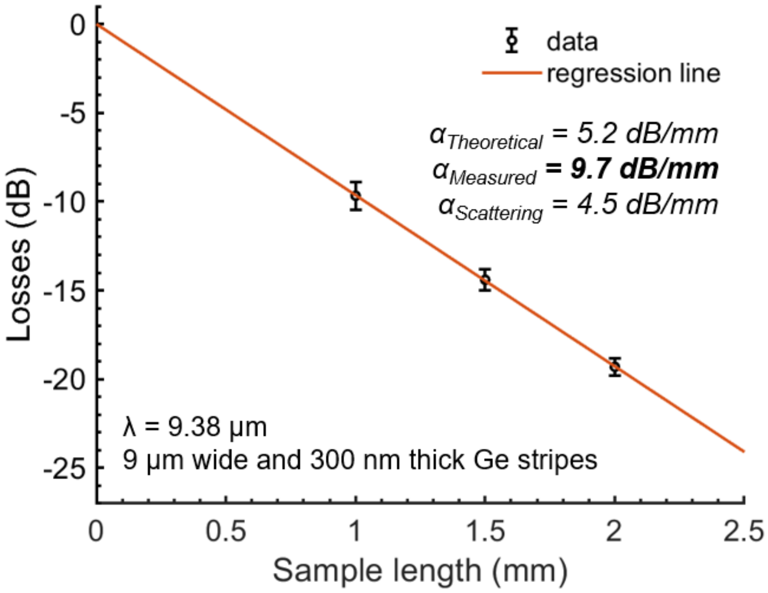

Figure 7.14 Cut-back measurements for a 9 µm wide and 300 nm thick Ge slab on Au processed via lift-off procedure. Figure adapted form [229].

Following the initial characterization (referred to as *characterization 1* in Figure 7.12), individual chips were coated with approximately 10 nm thickness of one of the four protective ALD materials. To ensure accurate measurement of the deposited layer thickness, a Si substrate was included alongside the waveguide samples and used as a reference for measuring the deposited thickness.

Table 7.1 reports the nominal and the measured thickness of the four coatings after fabrication. However, it was observed that the HfO_2 coating turned out to be significantly thinner than expected, measuring approximately 8.5 nm.

ALD coating material	**ZrO_2**	**Al_2O_3**	**TiO_2**	**HfO_2**
Nominal thickness (nm)	10	10	10	10
Measured thickness (nm)	10.1	10.2	9.8	8.5
Deviation (%)	+1	+2	-2	-15

Table 7.1 Nominal and measured thickness after deposition of the four coatings. The table reports the deviation in percentage from the intended design. The measurements were obtained from a Si substrate inserted as a reference during the process, using visible spectroscopic ellipsometry.

Subsequently, the waveguides underwent another round of characterization (*Characterization 2* of Figure 7.12) using the waveguide setup to examine the impact of the protective coatings on the waveguide losses.

In a third step we conducted a submersion experiment using pure DI water (DI-H_2O), followed by a third sample characterization (*Characterization 3* of Figure 7.12) in order to assess the protective capabilities of the ALD coatings. Since the Ge slabs of the waveguides had a relatively thick dimension of approximately 300 nm, the dissolution process was expected to occur over minutes to hours [239]. The experiment involved testing a total of 6 samples: two reference samples with uncoated Ge waveguides and four waveguide samples with additional ALD coatings.

The submersion experiment was carried out in two steps. Firstly, the samples were submerged in DI-H_2O for 30 minutes and then analyzed using an optical microscope and surface profilometry. Subsequently, the samples underwent a second submersion for an additional 60 minutes (a total of 90 minutes), and the waveguides were analyzed again. Figure 7.15 illustrates the comparison of surface profiles: before submersion (blue), after 30 minutes (red), and after 90 minutes (yellow).

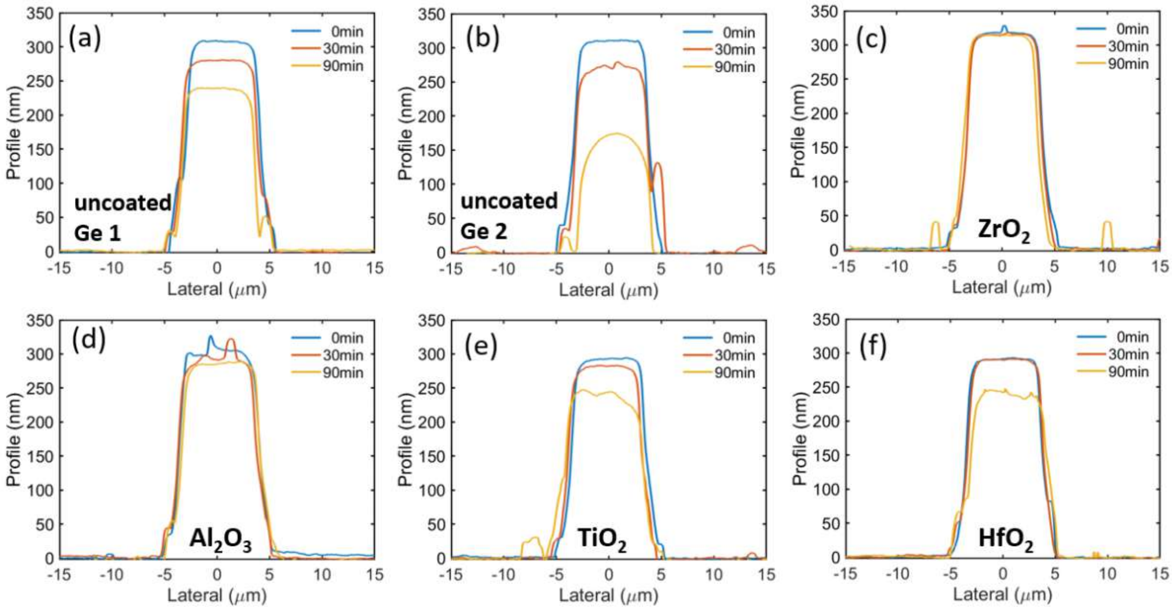

Figure 7.15 Profilometer measurements for the water submersion experiments of the SLSPP waveguides (pre: blue, 30 minutes: red, 90 minutes: yellow) of: (a),(b) uncoated, (c) ZrO_2 (d) Al_2O_3 (e) TiO_2 and (f) HfO_2 coated waveguides. Figure taken from [229].

All samples initially had a thickness of approximately 300 nm. However, after only 30 minutes of water exposure, the uncoated samples exhibited a significant reduction in the thickness of the Ge layer by approximately 30 nm, i.e., representing around 10% of the initial thickness. In contrast, the coated samples maintained a consistent thickness throughout the experiment, demonstrating the effectiveness of the ALD coatings in preventing Ge dissolution. After an additional 60 minutes in water, the uncoated samples exhibit a more pronounced removal of the Ge, with sample #2 (Figure 7.15b) being reduced to approximately half of its original thickness (around 150 nm), and the waveguide profile transitioned from rectangular to round-shaped geometry. From profilometry, it is possible to observe a difference in etch rates between the two uncoated devices. This result can be attributed to various factors related to surface conditions and material properties of the fabricated devices. Firstly, variations in surface morphology, as seen in the SEM pictures of Figure 7.13b, can create preferential etching sites, resulting in enhanced or slowed etching rates. Additionally, also the presence of surface defects as well as localized strain within the Ge layers may further affect reactant concentrations on the Ge surface, causing additional variations. Finally, different compositions of the native Ge oxide on the top surface may also contribute to varying etching rates.

In contrast, all the coatings initially provide a good level of protection, as evident from the absence of thickness reduction in the first 30 minutes and the calculated etch rates after 90 minutes from Figure 7.15: while for the uncoated Ge-slabs the etch rate is between 1-1.5 nm/min, it is 0.5 nm/min and 0.6 nm/min for TiO_2 and HfO_2, respectively. However, after 90 minutes of submersion, the ZrO_2 and Al_2O_3 coatings remain unaffected, while the TiO_2 and HfO_2 coatings show initial signs of degradation, characterized by a reduction in layer thickness of approximately 50 nm. A possible explanation for this effect is that the lack of a stable Ge surface oxide poses an additional challenge, potentially causing the etching of the samples with TiO_2 and HfO_2 coatings. This can be attributed to the diffusion of Ge into the dielectric coating layer [247], resulting in charge trapping and fixed charges [248,249]. Such diffusion processes can oxidize and, thus, contribute to slowly removing the HfO_2 passivation in water. Implementing a SiH_4 layer between Ge and HfO_2 can effectively suppress such diffusion processes [247]. Additionally, surface nitridation, S-passivation, or even simple air storage can improve the quality of the Ge surface [250]. For instance, storing an Al_2O_3 coated sample in air for 3 months demonstrated improved passivation quality, reducing the surface recombination velocity $S_{eff,max}$ by a factor of 3.5 [251].

To further enhance our understanding of the surface properties of the protective coatings, we conducted AFM measurements, scanning a 5x5 μm^2 area on the waveguide's surface after 90 minutes of water submersion. The scans are shown in Figure 7.16.

In conclusion, the observed degradation in HfO_2 can be attributed to a thinner deposited layer with a thickness of around 8.5 nm, while the poor protection of the TiO_2 coating can be explained by the presence of holes on its surface, as shown from the AFM measurements of Figure 7.16. One potential solution to circumvent these problems is to consider increasing the coating thickness to around 12-15 nm.

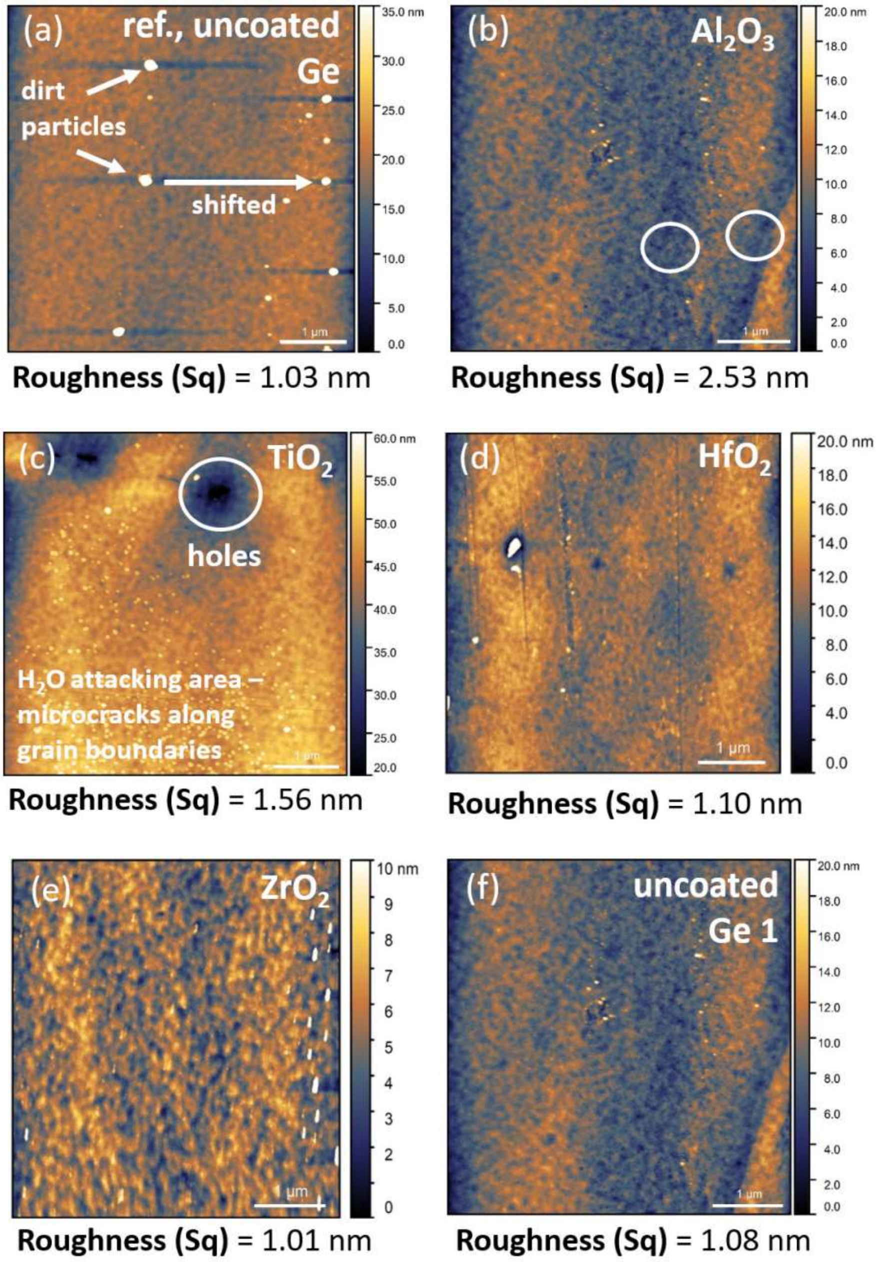

Figure 7.16 AFM analysis was conducted on samples that were either coated or uncoated and submerged in water for 90 minutes. The analysis included the following: (a) Ge reference without submersion, (b) Al_2O_3 coating (10.2 nm), (c) TiO_2 coating (9.8 nm), (d) HfO_2 coating (8.5 nm), (e) ZrO_2 coating (10.1 nm), and (f) Ge without coating after submersion. The RMS roughness was measured for each sample, and observations revealed the presence of particles, non-uniformity, and holes, which are marked accordingly. Figure taken from [229].

7.3.3. Experimental Results on Waveguide Protection

Finally, we conducted optical measurements to assess the impact of water exposure on the plasmonic properties of the coated waveguides at a wavelength of 9.38 µm. Figure 7.17a and b presents the final results of the coating and water exposure study. These graphs depict the absolute and normalized experimental losses, comparing the coated waveguides (yellow) to their uncoated counterparts (orange bars), both before and after the water submersion experiment (black). Notably, the addition of coatings resulted in an increase in losses that were approximately quadruple the expected simulation results shown in Figure 7.11. The increase ranged from around 10% for ZrO_2 to 19% for HfO_2.

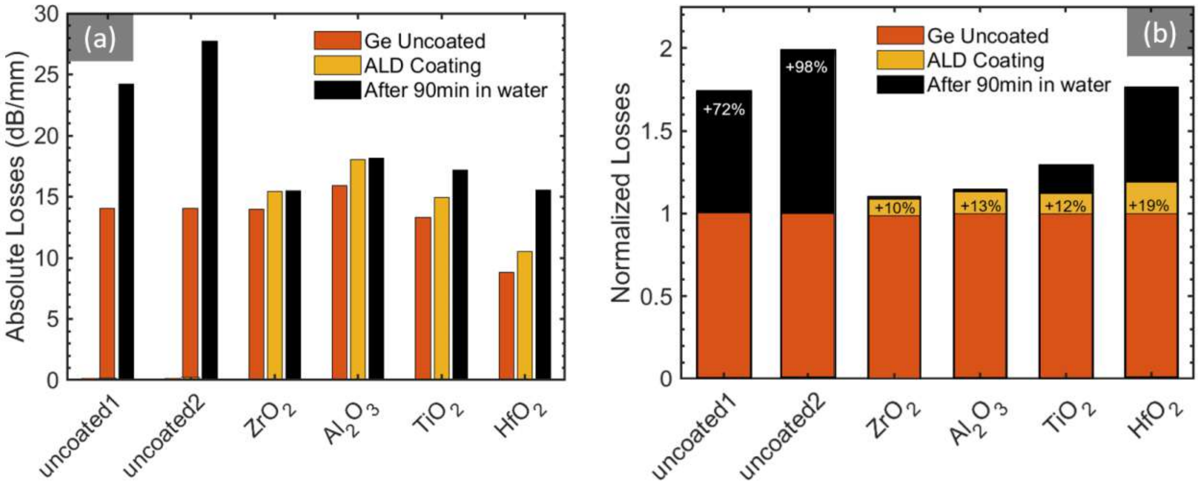

Figure 7.17 (a) The histogram illustrates the absolute losses at different experimental stages: prior to coating (orange bars), after coating (yellow bars), and after submersion (black bars). The variation in initial devices' absolute losses is attributed to differences in the thickness of the Ge layer and fabrication defects. (b) absolute normalized waveguide losses at different stages: before (orange), after ALD coatings (yellow), and after water submersion (black). Coating deposition adds approximately 10-20% losses, while water submersion increases losses for uncoated, HfO_2 coated, and TiO_2 coated waveguides, Figure adapted from [229].

After 90 min of submersion, we observe that the uncoated samples exhibit an expected significant increase in losses, with a rise of 72% and 98%, respectively, attributed to a significant decrease in layer thickness and lower coupling efficiency with respect to the lenses. Notably, this effect is even more pronounced in the "uncoated2" sample, consistent with the previously measured profile change. Conversely, our results demonstrate the excellent protective capabilities of ZrO_2 and Al_2O_3, as they exhibit negligible additional waveguide losses (~10%). However, TiO_2 displays an increase in losses by 17%, while HfO_2 experiences even more pronounced losses at 57%. Based on the data presented, we observe a noteworthy increase in loss in HfO_2 waveguides compared to TiO_2 waveguides, despite similar device degradation, as depicted in Figure

7.15. The discrepancy could potentially be attributed to a more pronounced degradation at the waveguide facets in the HfO_2-coated devices, leading to higher coupling losses. However, it is important to note that the device degradation illustrated in Figure 7.15 shows only a representative value, and does not provide a comprehensive analysis of the degradation along the entire waveguide length. As such, the measurements obtained from the profilometer should be regarded as indicative rather than definitive.

Based on our findings, it can be concluded that employing a 10 nm ALD-coating on a Ge-layer offers excellent protection against Ge-removal over time. This is achieved by selecting suitable materials (ZrO_2 and Al_2O_3) and ensuring a sufficient coating thickness (10 nm or greater). By increasing the thickness of less effective coatings like TiO_2 and HfO_2 (to 12-15 nm), comparable levels of protection should be able to be attained. This becomes particularly relevant for certain spectroscopic experiments where utilizing e.g., TiO_2 as a coating may yield specific benefits for Ge-based SLSPP waveguides [252]. Furthermore, TiO_2 exhibits additional desirable properties such as robustness, biocompatibility [253], and its use as a seed for activated surfaces [254], which can compensate for higher overall losses associated with a thicker coating in such cases.

7.3.4. Device Functionalization

In addition to providing basic protection through surface coatings for SPP waveguides, the activation, and functionalization of these surface-sensitive interfaces offers a powerful solution for the development of advanced liquid sensors. These sensors are designed to have a compact chip-scale footprint while enabling selective and highly sensitive detection capabilities, addressing the requirements of next-generation sensing technologies [149]. The utilization of surface-modified waveguides in mid-IR sensing has been extensively documented in literature. Various coating materials, including, for example, mesoporous materials [255,256] can be successfully used to enhance the sensitivity.

Surface modification aims to concentrate the analyte at the surface layer while simultaneously repelling undesirable substances, like water, and preventing their interference with the evanescent field [257–260]. Furthermore, these coatings have found applications in the field of catalysis [261,262]. Among the various materials, Zirconia is particularly intriguing due to its bio-compatibility [253,263–265] and potential for use as a host layer in surface functionalization approaches, such as those involving mesoporous coatings [256]. Studies have demonstrated that utilizing Zirconia membranes can significantly enhance the sensitivity of ATR sensors by over 160 times. This improvement would effectively surpass the current limit of detection in recently demonstrated monolithic SPP-based liquid sensors [49,50], enabling detection on the ppb-scale instead of the ppm-scale. Moreover, ZrO_2 exhibits excellent chemical and mechanical stability, making it an advantageous material for the application of such coatings in sensing schemes [266]. Therefore, instead of using the passivation coatings solely for protection, they can also serve as a means to activate the waveguide surface. It is becomes possible to effectively prevent unwanted water from reaching the evanescent field of light propagating through the plasmonic waveguide, while concurrently enhancing the selectivity of the surface layer towards specific molecules.

To enhance the hydrophobicity of the pristine ZrO_2 surface, a trimethylsilyl functionality was introduced, similar to the approach demonstrated in mesoporous ZrO_2 layers on Si-ATR crystals [256]. Initially, the surface of one of the SLSPP waveguide samples, which had a 12 nm ZrO_2 coating, was functionalized following the procedure described in literature [256]. However, this process resulted in surface damage to the waveguide, requiring a modification of the method. Instead of using an ultrasonic bath, the waveguides were submerged in the solvents for extended periods, and inspection with optical microscopy confirmed that the processed surface remained undamaged. The surface functionalization of the SLSPP waveguides was carried out using the procedure depicted in Figure 7.19. Initially, the sample underwent a series of immersion steps: acetone, ethanol, and DI water, each for a duration of 15 minutes. Following this, the waveguides were purged with dry air and then subjected to overnight drying at 110° C in a drying oven. Next, the sample was placed into a three-neck round bottom flask equipped with a reflux condenser, bubbler, N_2-inlet, and vacuum connection (see Figure 7.18). Drying was performed for 2 hours at approximately 15 mbar and 150° C. Subsequently, the flask was purged with N_2, and a mixture of 20 mL of $CHCl_3$ and 400 µL of chlorotrimethylsilane at 22° C was added. The solution was allowed to react in an inert atmosphere for 24 hours. Afterward, the solution was removed, and the waveguide sample was thoroughly washed with $CHCl_3$, followed by subsequent immersion in acetone, ethanol, and DI water, each for 15 minutes. Finally, the sample was purged with dry air, placed overnight in a drying oven at 90° C. The efficacy of the surface modification was assessed by comparing the contact angles of water drops on waveguides with and without surface functionalization, since a change from a hydrophilic to a hydrophobic surface is joined by a simultaneous change in the contact angle.

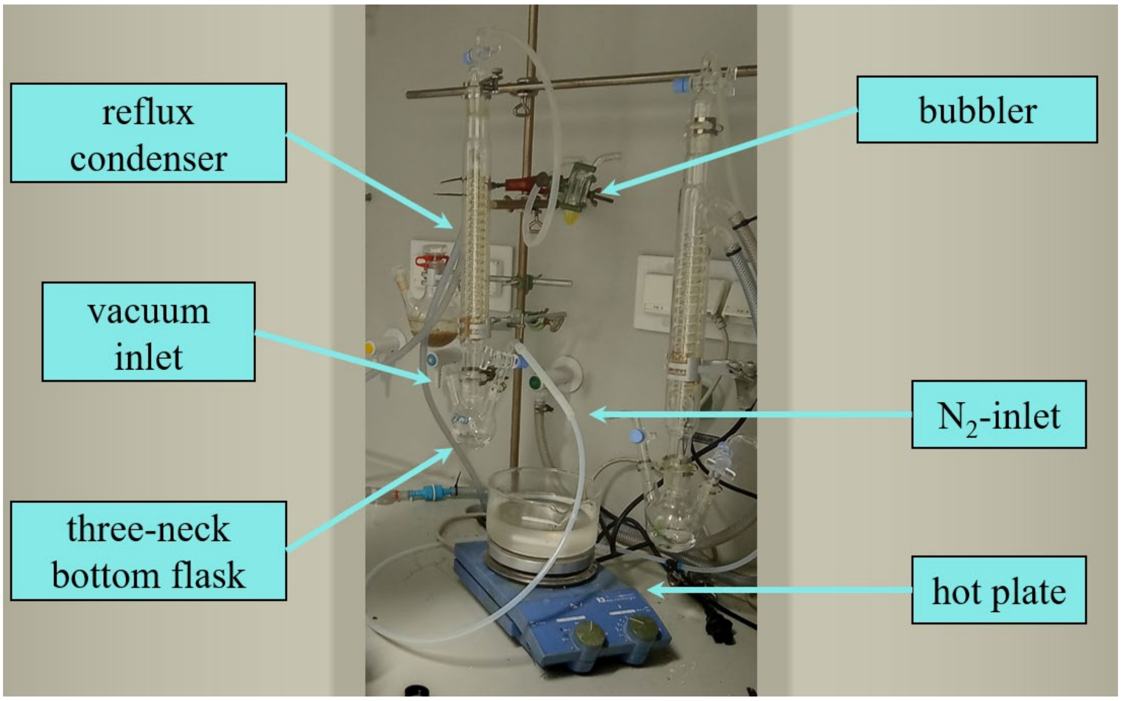

Figure 7.18 Chemical setup for functionalizing ZrO_2-coated plasmonic waveguides, featuring a reflux condenser, bubbler, and a three-neck bottom flask to contain the sample.

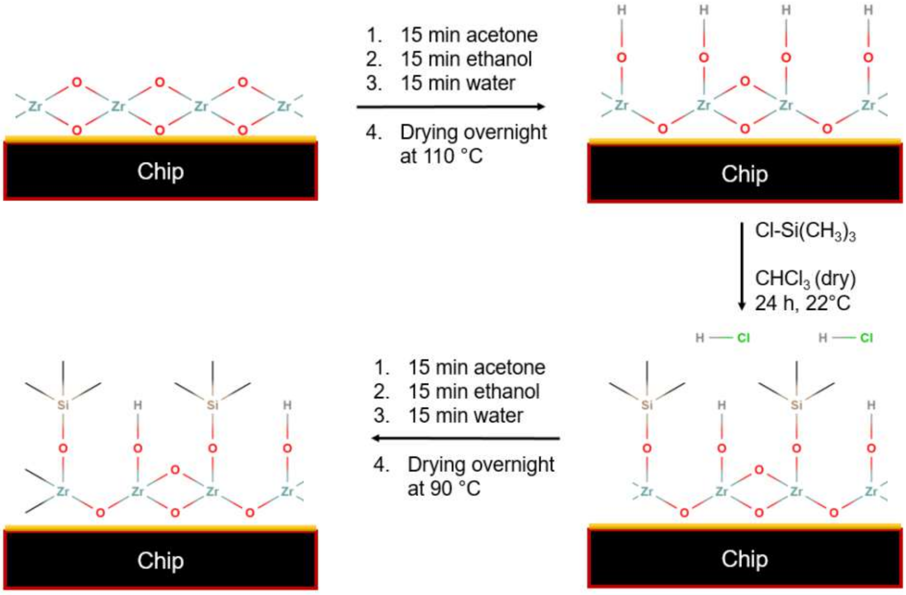

Figure 7.19 Procedure of the chemical treatment to activate the chip surface of ZrO_2-coated plasmonic surfaces. Figure taken from [229].

In Figure 7.20a, it can be observed that the non-functionalized ZrO_2 surface exhibits a lower contact angle compared to the functionalized ZrO_2 surface of Figure 7.20b. A lower contact angle indicates better surface wetting and higher hydrophilicity. Following the surface functionalization procedure, the contact angle significantly increases, indicating higher hydrophobicity. This change suggests the successful introduction of the trimethylsilyl moiety to the ZrO_2 surface. Moreover, the plasmonic mode losses of the waveguide were compared between the functionalized and non-functionalized surfaces.

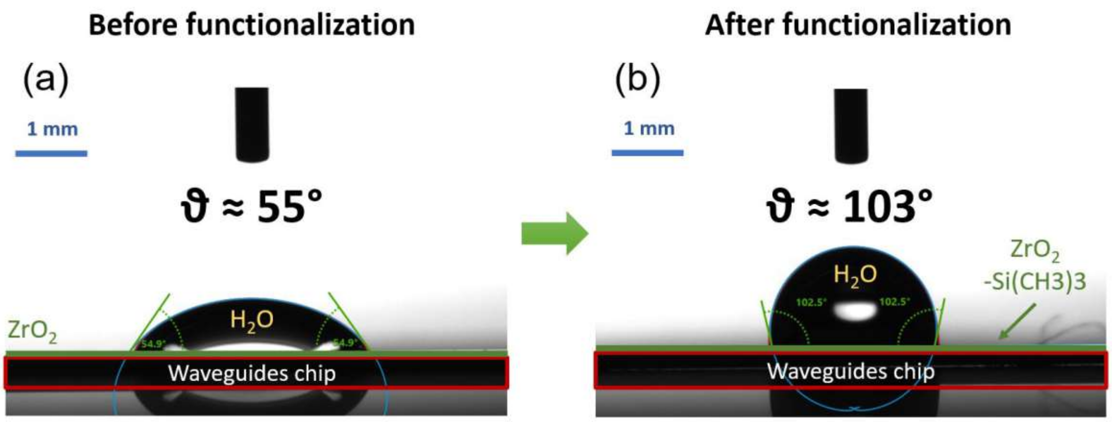

Figure 7.20 Contact angle measurements, using a water droplet on the (a) non-activated ZrO_2-coated SLSPPW (3 µL, hydrophilic: $\vartheta < 90^\circ$) and (b) activated (7 µL, hydrophobic: $\vartheta > 90^\circ$) SLSPP waveguide surface. Figure taken from [229].

Figure 7.21 clearly shows increased absorption losses resulting from the trimethylsilyl functionalization. The formation of Zr-O-Si bonds during functionalization contributes to the measured losses. This further confirms the successful modification of the ZrO_2 surface. Furthermore, the adsorption capabilities of a specific organic, apolar analyte on both the pristine and functionalized ZrO_2 surfaces were investigated using diethyl ether. Diethyl ether was chosen due to its absorption bands at the wavelength of interest (9.38 µm) and its rapid evaporation unless adsorbed or dissolved on a surface.

The investigation of the adsorption capabilities of waveguides was conducted using the experimental setup shown in Figure 5.10, employing a dipstick method procedure. Initially, the plasmonic losses of both non-functionalized and functionalized waveguides were experimentally determined. Subsequently, the waveguides were submerged in diethyl ether for a duration of 10 minutes, and plasmonic losses were measured again. To minimize the impact of solvent evaporation, measurements were taken immediately after exposure. The relative losses caused by adsorbed apolar analytes were calculated by comparing waveguide losses before and after diethyl ether submersion (see Figure 7.21).

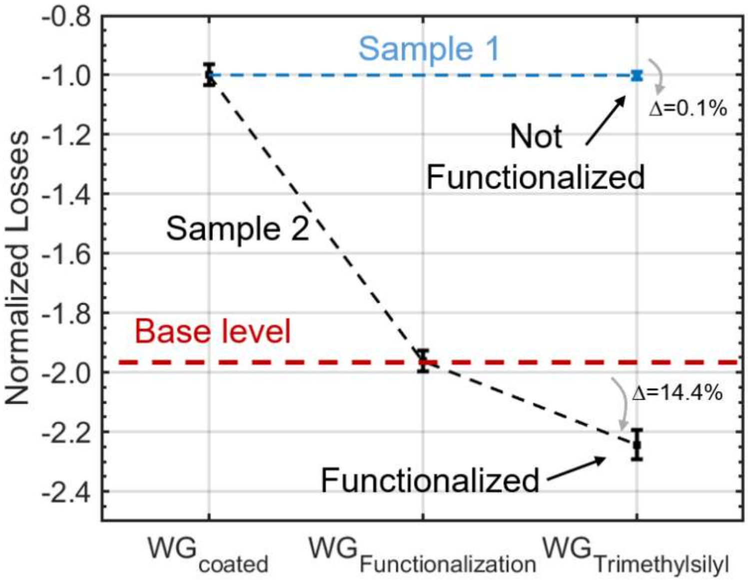

Figure 7.21 Results of the surface activation measurements on the activated ZrO_2 plasmonic surfaces for: no functionalization (Sample 1) and functionalization (Sample 2). Submerging the not functionalized waveguides into diethyl ether results in no significant changes for the plasmonic mode transmission. On the other hand, the functionalized surface shows increased losses of about 14.4 % because the molecules sticking to the surface absorb the 9.38 µm probe light. Figure taken from [229].

When comparing the non-functionalized waveguide (Sample 1) before and after submerging it in diethyl ether, there is hardly any noticeable difference. This indicates that the analyte evaporates quickly, preventing its measurement and suggesting no adsorption to the waveguide surface. On the other hand, when conducting the same experiment with the functionalized waveguides (Sample 2), a clear difference is observed. This implies surface adsorption of diethyl ether, leading to higher plasmonic losses due to the additional radiation absorption by the analyte. The plasmonic losses increase by approximately 14.4%. Interestingly, after around 5 minutes, the analyte fully evaporates from the surface, resulting in the same plasmonic losses as before the diethyl ether submersion. This suggests a complete recovery of the surface, a crucial characteristic for practical sensor applications.

As previously discussed, from Figure 7.21 it is possible to observe an increase in losses for sample 2 after functionalization. This effect can be attributed to the formation of Zr-O-Si bonds with absorption characteristics within this particular wavelength range. A detailed analysis of this phenomenon can be found in [267]. However, it is also possible that the functionalization process itself might contribute to some of the observed changes. Although we utilized non-aggressive chemicals, the immersion of waveguides in water after functionalization, accounting for over 2 hours at this stage, may have led to additional degradation of the waveguide structure.

This experiment highlights the suitability of surface-activated ZrO_2-coated SLSPP waveguides for spectroscopic analysis. By using various available silanes for surface modification and functionalization, the selectivity of these waveguides can be tailored to meet different application requirements. Additionally, higher sensitivity can be achieved by increasing film thickness and introducing porosity [256]. In conclusion, with their compact design and compatibility for chip-scale integration, these waveguides exhibit great potential for the next generation of miniaturized liquid sensors [49,50], offering enhanced selectivity and sensitivity.

7.4 On-chip Routing via Integrated Mirrors

As demonstrated earlier in this chapter, increasing the thickness of the Ge slab enables an increase in N_{eff}, enabling on-chip routing of the plasmonic mode. However, this approach leads to significant losses and requires extremely challenging geometries that may pose difficulties in their fabrication and integration with other active components. As an alternative approach, micro-optic concepts can be employed [268]. Microoptics refers to the design of optical components and systems at a microscale level, typically ranging from a few micrometers down to submicron dimensions. These elements may include lenses, gratings, diffractive elements, micro-mirrors, and micro-prisms, among others. The unique properties of micro-optical elements, such as small size, lightweight, and integration potential, make them suitable for compact and robust optical devices and systems. The integration of micro-optics with other photonic technologies, such as integrated photonics and optical fibers, has opened up new possibilities for miniaturization and system integration. In fact, the field of micro-optics has advanced significantly over the years, leading to the commercialization of various micro-optical components and systems [268].

By integrating thin Ge slabs with excellent low-loss propagation properties for sensing applications and incorporating on-chip integrated micro-mirrors, which are created by etching vertical facets into the substrate and covering them with a highly reflective material like Au, it becomes possible to achieve both, efficient radiation routing, and maintenance of the low-loss characteristics. Figure 7.22 provides a visual representation of this concept through a top view (Figure 7.22a) and a 3D simulation (Figure 7.22b). The on-chip mirror exhibits remarkable capability in redirecting light with minimal losses, as initial simulations predict around 1.5 dB for a 90° bend. However, it should be considered that any deviation from the ideal geometry, such as tilting of the mirror, the gap size between the Ge slab and mirror, and the mirror dimensions, can have an impact and potentially lead to increased losses.

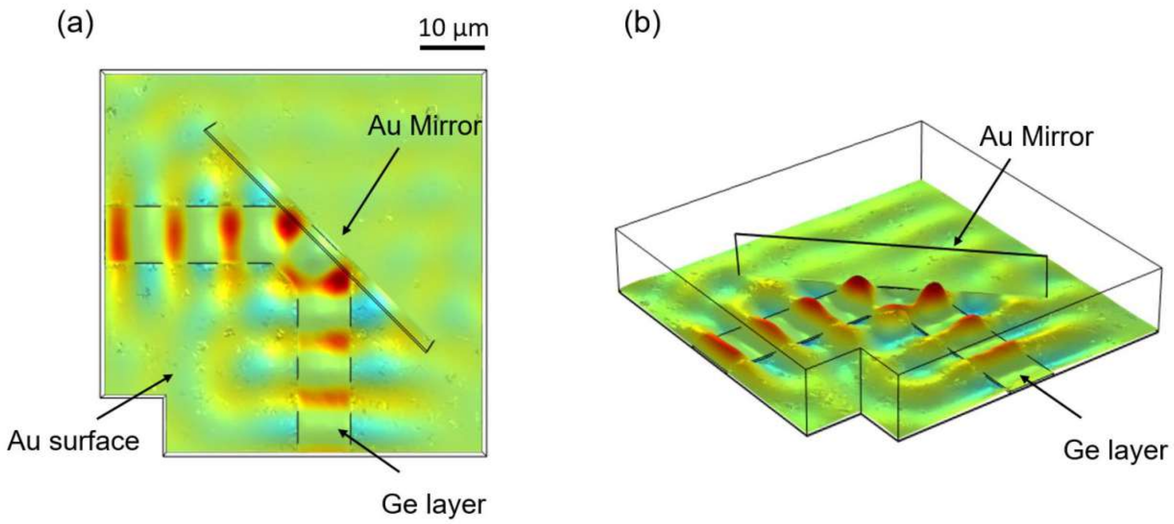

Figure 7.22 3D COMSOL simulations of the integrated micro-mirror concept with a Ge/Au plasmonic waveguide. (a) top view and (b) partial top view with angled perspectives from two sides.

Preliminary integration tests, shown by SEM images of fabricated devices in Figure 7.23, demonstrate the feasibility of this concept. The chips were fabricated on a (8.3 µm) QCLD material. Micro-mirrors, waveguides, lasers (QCLs), and detectors (QCDs) are successfully integrated on the same substrate, through an adapted fabrication technique described in [48].

Proof of concept measurements confirm the validity of the approach, showing good mode redirection over 90-degree bends with estimated losses of ~7.8 dB (Figure 7.23b). To estimate the waveguides and coupling losses on-chip, the effective cutback technique was reproduced by fabricating linear geometries similar to Figure 7.23a, with different waveguide lengths, and the values normalized by the laser power measured from butt-coupled QCL and QCD with 2 µm distance. To ensure measurement precision, the laser power was kept at the same value measured with an MCT detector from the back facet emission of the device. The mirror losses were then extracted by subtracting the calculated coupling losses (~7.2 dB) and waveguide losses (~18.4 dB/mm). The increased losses in the integrated waveguides stem from two main factors: the geometry employed, involving a 300 nm thick and 8 µm wide Ge at λ = 8.3 µm, and heightened losses due to the pronounced roughness of the evaporated Au layer. Therefore, the concepts presented in this thesis, demonstrate new pathways to seamlessly integrate mid-IR active elements, such as lasers (QCLs) and detectors (QCDs), into more sophisticated mid-IR PICs, as illustrated in Figure 7.23c. The incorporation of thin-slab Ge plasmonic waveguides and integrated micro-mirrors results in minimal on-chip losses, enabling the design of versatile PICs with advanced functionalities. As an example, Figure 7.23c shows a fully monolithically integrated heterodyne detector, achieved through the use of straight and tapered Ge SLSPPWs in combination with on-chip micro-mirrors.

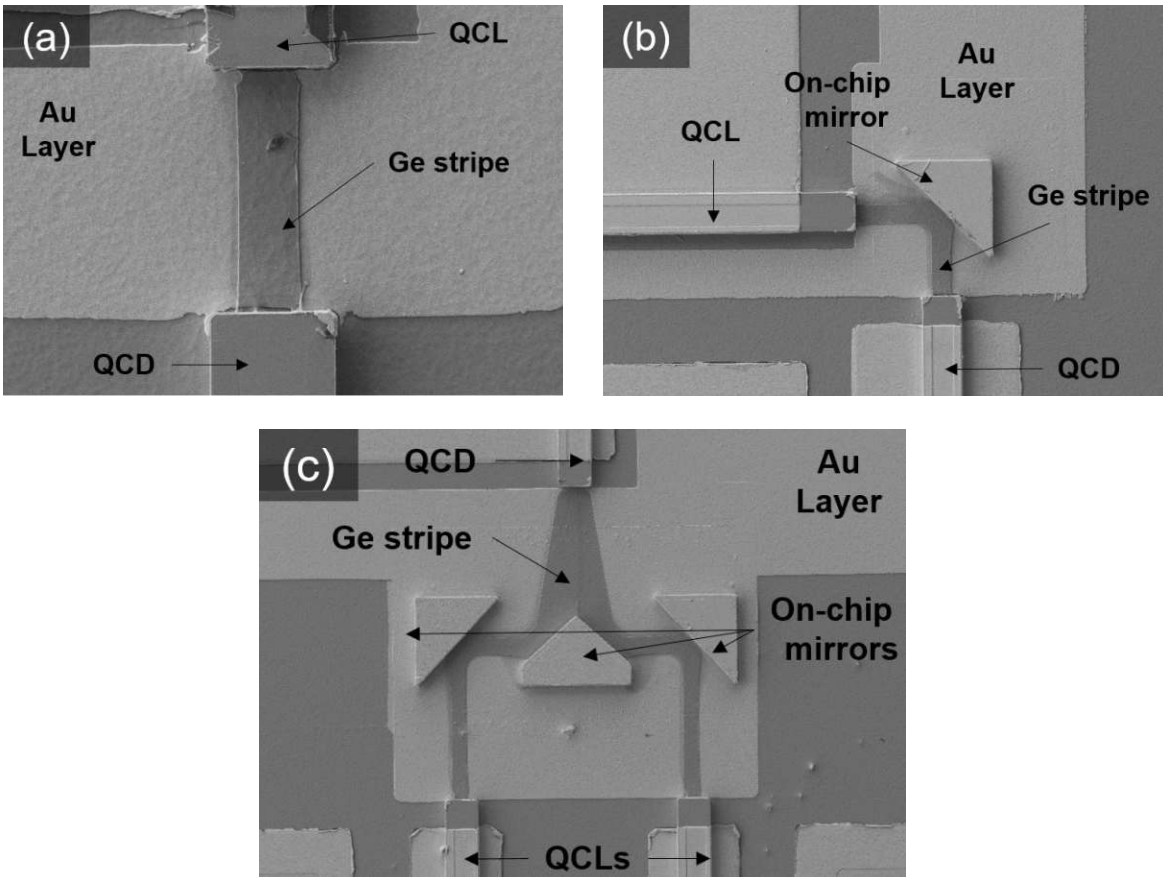

Figure 7.23 Monolithically integrated devices, including the micro-mirror for beam guiding, fabricated on a QCLD material designed for the LWIR (QCL emission at 8.3 µm at room temperature). (a) QCL and QCD in a straight configuration, coupled through a 8 µm-wide, 300 nm thick, and 25 µm long Ge-based SLSPPW. (b) Same design, with QCL and QCD at 90° with respect to each other. The light is redirected through the use of an Au-coated, 6 µm high micro-mirror. The integrated mirror has the same high of th QCL and QCD. (c) More complex design using the same PIC principle, resembling the configuration of an on-chip heterodyne detector (for more details, refer to section 8.2.2).

8

COMPARATIVE ANALYSIS OF LOADING MATERIALS AND FUTURE APPLICATIONS

8.1 Comparison of Different Loading Approaches

In this work, novel concepts for the next generation of fully integrated mid-IR PICs based on QCLD material were explored. Two distinct materials, Ge and PE, were investigated to analyze their potential application in dielectric-loaded plasmonic waveguides for mid-IR sensing and on-chip mode guiding purposes.

Table 8.1 presents a comparison of experimentally realized mid-IR plasmonic waveguide platforms based on DLSPP structures. The table demonstrates that PE can achieve comparable performance at above 9 µm wavelength as SiNx does up to approximately 6.5 µm, which is below the onset of its absorption band [269]. Importantly, this work introduces the first mid-IR plasmonic platform with guiding abilities.

Both materials present low-loss characteristics. However, their different refractive indices significantly impact the device's performance. PE is a low refractive index (~1.5) polymer, making it an attractive choice for dielectric loading, especially for the LWIR, where the availability of transparent materials is rather scarce. Its low refractive index allows for an efficient trade-off between propagation length and mode confinement while minimizing interface reflections. In this way, the replication of DLSPPW performance in the LWIR range is enabled, unlocking similar performance as compared to PMMA at telecom wavelengths. As a result, PE becomes a promising choice for various LWIR integrated applications. However, it is important to note that so far it has not been extensively utilized in microelectronics and photonics compared to some other materials. Therefore, there are fewer established fabrication techniques for its deposition and patterning compared to more commonly used materials like Ge.

Waveguide platform	Wavelength (μm)	Propagation length (mm)	Attenuation (dB/mm)	Guiding capabilities	Ref
60-μm-wide Au stripe	7.5	1.8	2.4	No	[270][a]
15-μm-wide and 200-nm-thick SiNx stripe on Au	6.5	2 - 4	2.1 – 1.1	No	[48][b]
15-μm-wide and 200-nm-thick SiNx stripe on Au	6.1 6.2	1.7 1.8	2.55 2.41	No	[271][b,c]
9-μm-wide and 290-nm-thick Ge stripe on Au	9.12	0.645	6.73	No	This work [141][a]
9-μm-wide and 300-nm-thick Ge stripe on Au	9.38	0.448	9.7	No	This work [229][a]
5-μm-wide and 450-nm-thick PE stripe on Au	9.26	2.0	2.5	No	This work [205][a]
5-μm-wide and 3-μm nm-thick PE ridge on Au	9.26	0.311	13.94	Yes	This work [205][a]

Table 8.1 Comparison of mid-IR plasmonic waveguide platforms. (a) experimentally measured losses, (b) losses estimated from simulations, (c) tapered waveguide.

In contrast, the implementation of transparent high-RI materials, such as Ge, requires the use of much smaller geometries in order to provide effective mode guiding (width and thickness in the order of 1x1 μm^2). However, achieving such low-loss propagation as in the case of PE is not feasible due to the higher degree of confinement that causes an increased contact with the lossy Au layer, amplifying the losses of the optical mode. Additionally, the fabrication and integration of these materials with active devices on a single chip can present significant challenges due to the small dimensions involved.

On the other hand, Ge opens other design possibilities. As it was shown, it is possible to tailor the evanescent field on the chip surface by changing the geometry, making thinner slabs extremely advantageous for sensing applications and low-loss propagation for highly integrated designs.

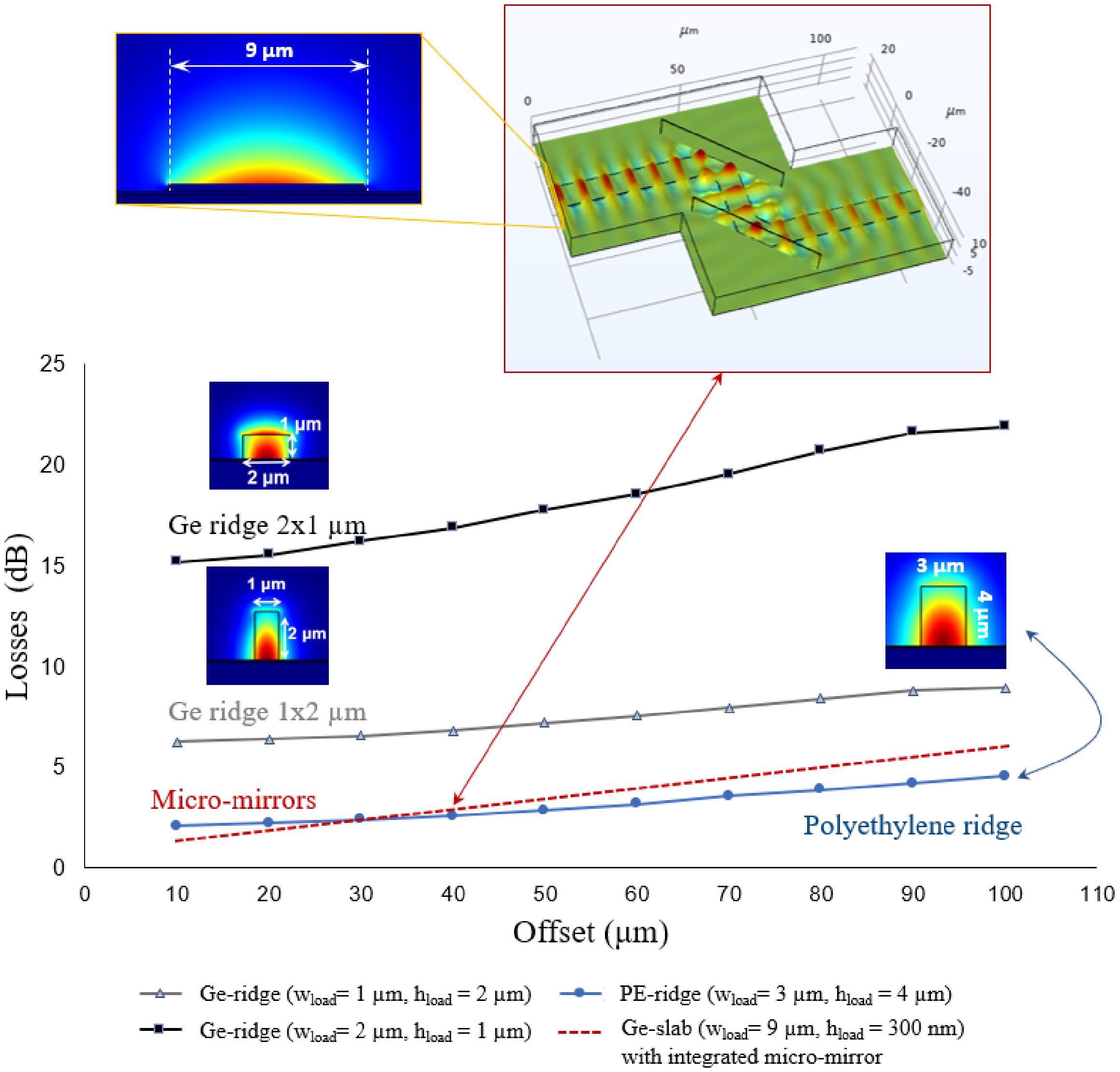

Figure 8.1 Simulation results for various guiding strategies, including Ge ridges with dimensions of 2x1 (width 2 µm, thickness 1 µm), Ge ridges with dimensions of 1x2 (width 1 µm, thickness 2 µm), PE ridges with dimensions of 3 µm width and 4 µm thickness, as well as a 300 nm Ge stripe integrated with micro-mirrors, for a 120 µm S-bend (double bend) at a wavelength of 9.12 µm. (insets) 3D simulation of a double bend designed with two micro-mirrors with an offset of 40 µm, and cross-sectional mode profile of the different waveguiding geometries.

Figure 8.1 shows the simulation results for the different waveguiding solutions proposed in this work, showing the advantages of the micro-mirror solution over the SLSPP waveguide with thick Ge ridges and how it compares with the use of PE-loading. To compare the different waveguide strategies, a 120 µm-long S-bend design (i.e., double bend) was selected, as it constitutes a typical building block element for many PIC configurations. The transmission between the two ports was calculated from 3D simulations for different offsets. By employing integrated micro-mirrors, it becomes possible to effectively replicate, with Ge-slab loading, the performance achieved with PE-loading, offering a versatile compromise between the two solutions. This enables significant benefits in terms of miniaturization, ease of fabrication, and improved functionality for several applications. However, this solution may not offer complete design versatility (as an example, for the fabrication of microrings).

Finally, Ge is a well-known CMOS-compatible material. This compatibility with CMOS technology enhances the potential for large-scale production and integration of Ge-based PICs. In our study, we employed Au as the plasmonic material. However, it is worth mentioning that the use of Pd can be beneficial in some applications where CMOS compatibility is a requirement. This is particularly significant for applications beyond 8 µm (refer to Figure 8.2), as indicated by evaluating the quality factor for plasmon propagation across various metals. The factor is computed as $Q_{SPP} = |\varepsilon'(\omega)| / \varepsilon''(\omega)$ [272].

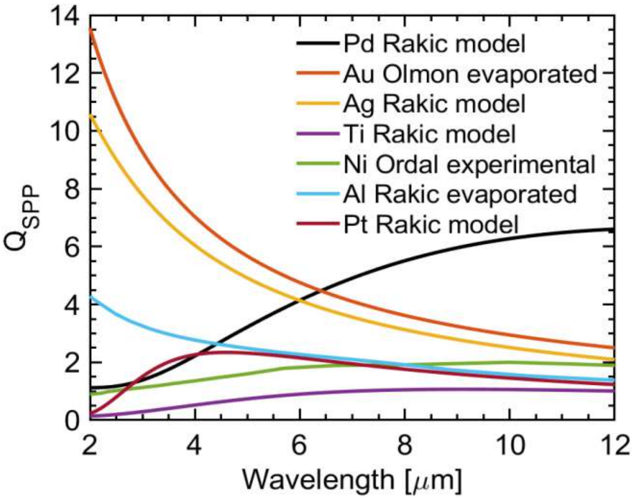

Figure 8.2 Plot of the Q_{SPP} for most commonly used metals in plasmonics. Image taken from [141]. Data taken from [75,273,274].

Figure 8.3 presents simulation results comparing Ge/Au and Ge/Pd combinations. The geometries of both material combinations were maintained, resulting in similar normalized mode sizes across all wavelengths. However, as can be seen from Figure 8.3a, the Ge/Pd waveguide exhibited an improved FOM (defined in equation (3.5)) due to the lower losses of Pd compared to Au at longer wavelengths (Figure 8.2). Consequently, this improvement in losses led to an enhanced propagation length (Figure 8.3b) for the Ge/Pd waveguide. Indeed, initial experiments performed in our labs have confirmed that plasmonic waveguides fabricated on Pd layers exhibit better performance than their respective ones on Au at a wavelength of 9.38 µm. However, further measurements are needed to conclusively validate these findings.

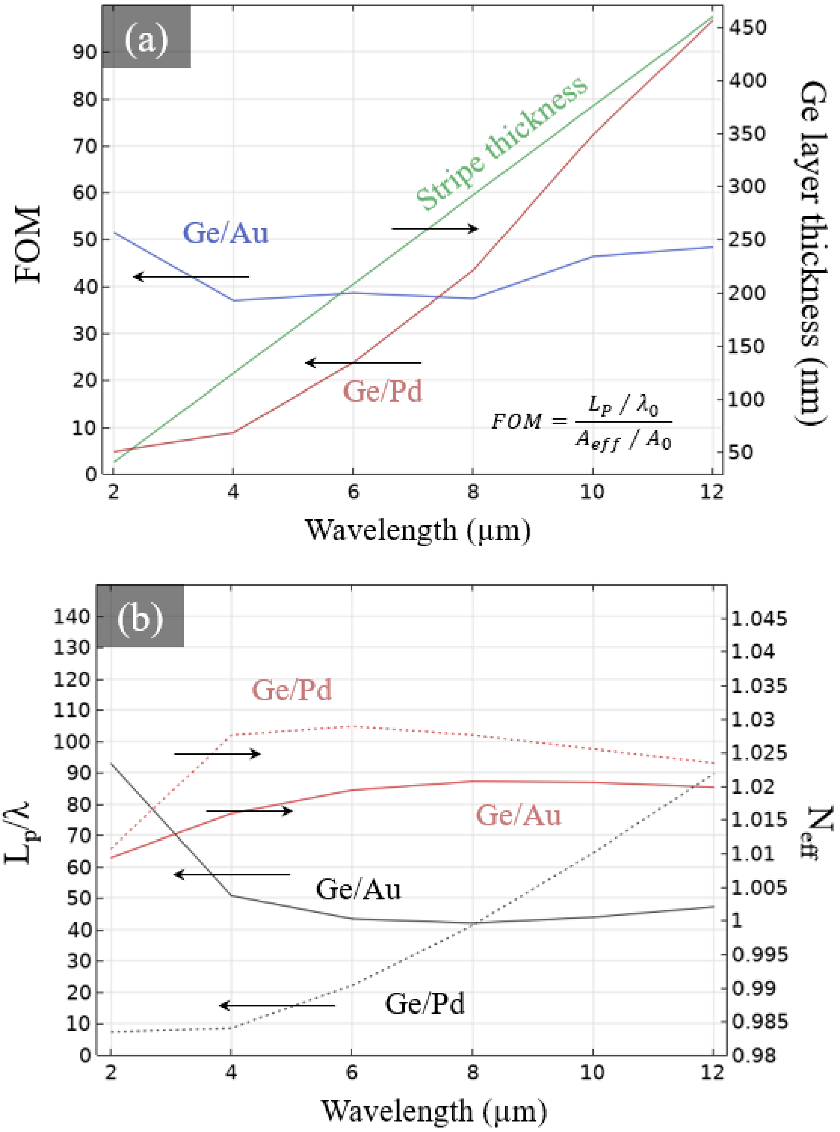

Figure 8.3 Simulation comparison of the performance of Ge stripes on both Au and Pd layers. In the simulations, the stripe width is set equal to the wavelength ($w = \lambda$) and the thickness is kept equal for both material combinations, indicated by (a) the green solid line (right axis). On the left axis, the FOM is displayed for the Ge/Au and Ge/Pd combinations in blue and red color, respectively (left axis). In (b), the comparison of L_p (in black) and N_{eff} (in red) is presented for the same material combinations (Ge/Au in solid lines, Ge/Pd in dotted lines). In the simulations, the materials properties from [274] are used for Pd.

8.2 Applications and Future Directions

This section aims to provide an overview of the recent advancements and possible future applications of the DLSPPWs presented in this thesis, in combination with QC technology for mid-IR PICs and LOCs.

8.2.1. Sensing Applications

DLSPPWs have shown exceptional sensitivity in detecting chemical species and biological analytes [275–277]. Integrating these waveguides with existing quantum cascade (QC) technology unlocks novel possibilities for high-performance, real-time sensing platforms in crucial fields like healthcare, environmental monitoring, and food safety. An exemplary achievement in this regard was shown by Schwarz et al. [48] in 2014, who demonstrated for the first time the integration of a QCL, QCD, and a plasmonic waveguide section, fabricated on the same epi-layer material, in a miniaturized LOC spectrometer, using a linear geometry (Figure 8.4).

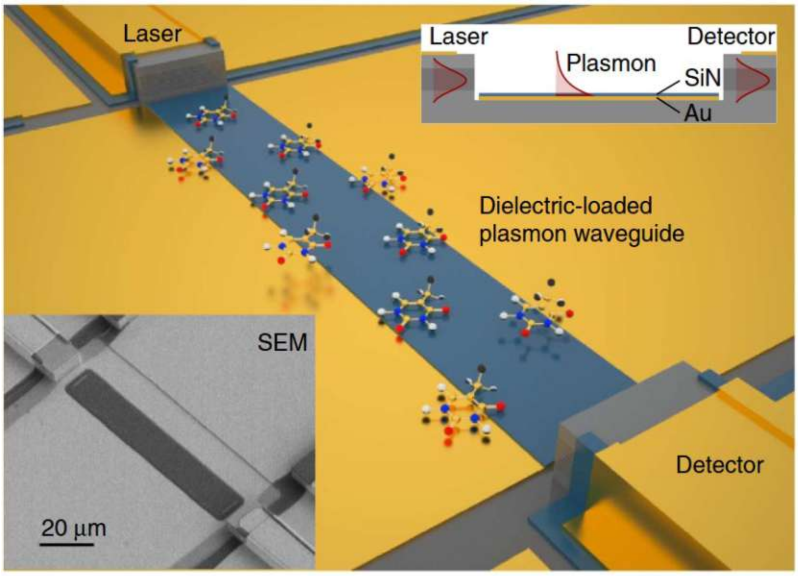

Figure 8.4 The first concept of monolithically integrated LOC consisted of a laser, a DLSPPW, and a detector, all integrated on a single substrate in a linear geometry. The upper inset illustrates the cross-section of the structure, while the lower inset displays the SEM image of the fabricated device. Image taken from [48].

In this configuration, it was shown that a thin SiNx layer enhances the light confinement on the chip surface and enables efficient coupling between laser and detector, offering high accuracy (within ppm) across a wide concentration range (0-60%) without complex integration or costly fabrication [48]. This groundbreaking novel LOC has later enabled real-time monitoring of bovine serum albumin (BSA) [49] and an organic solvent [50], with excellent sensing performance. Figure 8.5 shows the absorbance units (AU) of the QCLD sensor for BSA in D_2O with and without 18 mV crosstalk correction, along with a comparison to the single-reflection ATR-FTIR system using different scales for better visibility.

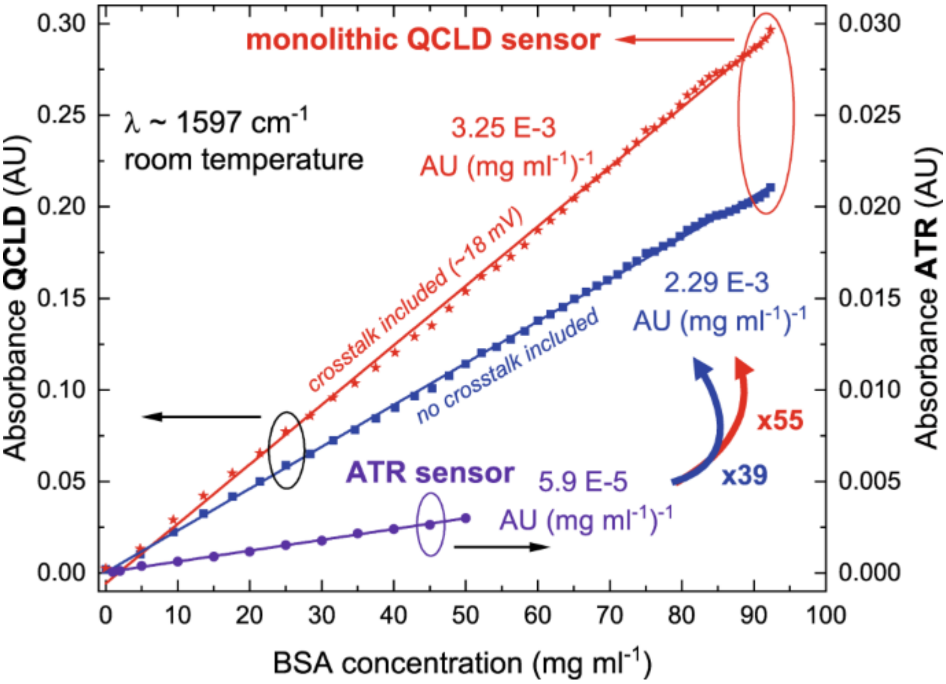

Figure 8.5 The results from the QCLD sensor's absorbance measurements for BSA in D_2O are represented in absorbance units (AU). The data is plotted with red stars indicating measurements with 18-mV crosstalk correction, while blue squares represent measurements without the correction (left scale). Additionally, the performance of the single-reflection ATR-FTIR system is illustrated with violet circles (right scale). To improve visibility of the ATR-FTIR signal, the right scale is divided by a factor of 10 in comparison to the left scale. Image taken from [271].

By replacing SiNx with Ge, this sensor concept can be expanded to longer wavelengths, specifically in the 6-12 µm band. This range is significant for detecting important molecules in medicine, disease diagnosis, and life sciences, such as glucose and body fluids [54]. Additionally, as shown in this thesis, the waveguides can be further enhanced by surface functionalization to increase sensor sensitivity and selectivity. By leveraging the broadband capabilities of the Ge-based waveguides, they can be integrated with mid-IR frequency combs [278] or EC-QCL-based systems, expanding the potential for chemical sensing. Infact, broadband sensing is particularly valuable as it provides additional information beyond quantitative measurements, facilitating a more comprehensive understanding of the chemical composition of the analyzed solution [244].

By incorporating PE ridges as presented in Chapter 6, or low-loss Ge slabs with integrated micro-mirrors (section 7.4), low-loss radiation guiding and routing can be achived over ranges of tens of wavelengths. This presents an opportunity to enhance the functionality of the aforementioned QCLD-based LOC through the implementation of more complex PIC schemes such as Mach-Zehnder Interferometers (MZIs) (Figure 8.6a) or Ring Resonators (Figure 8.6b).

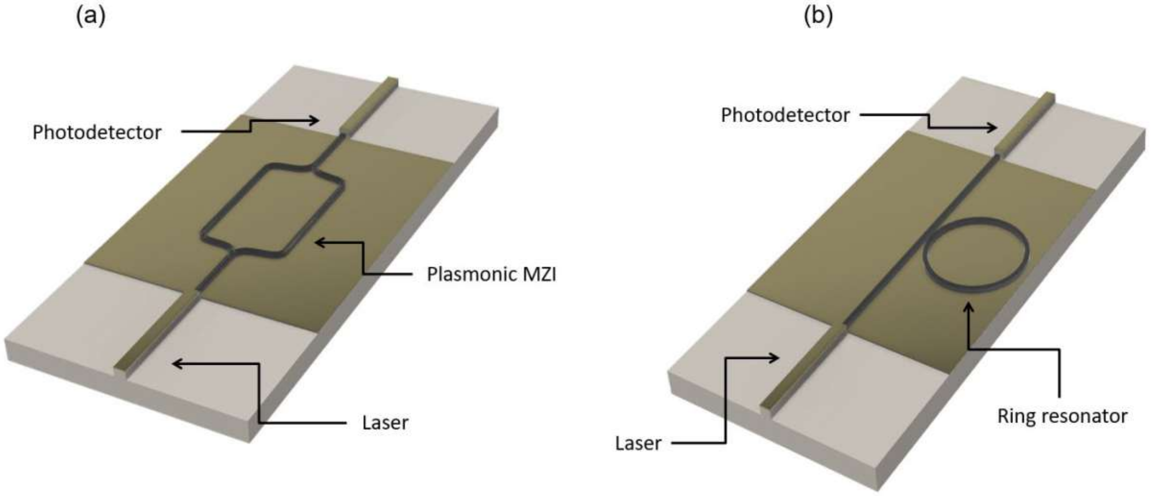

Figure 8.6 (a) Illustration of a monolithically integrated MZI fabricated on a QCLD material through the use of a PE-based DLSPPW. (b) Illustration of a QCLD-integrated plasmonic microring resonator sensor.

The technology presented in this thesis can be combined together into a fully integrated, miniaturized interferometric biosensor based on MZI (Figure 8.7a). This innovative system combines low-loss, broadband Ge-based plasmonic waveguides with a lithographically-based microfluidic chip made of transparent PE, where the incident light is divided into two arms (sensing and reference) and then recombined using on-chip Y-junctions based on micro-mirrors (Figure 8.7b). The beating signal observed at the output is directly linked to the refractive index changes occurring in the sensing arm.

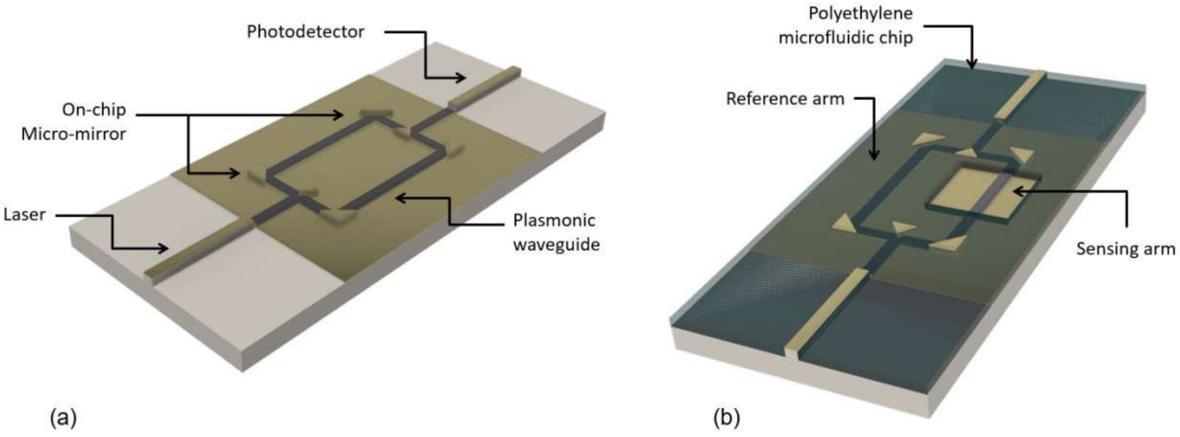

Figure 8.7 (a) 3D illustration of a fully integrated, miniaturized MZI biosensor based on Ge-based plasmonic waveguides and on-chip micro-mirrors. (b) The same device is combined with a lithographically-based microfluidic chip made of transparent PE.

8.2.2. Mid-IR Communications

Free-Space Optical (FSO) communication, also known as fiberless photonics, has emerged as a significant technology for various applications, including space and satellite communication, military data links, and mobile communications in crisis situations (referred to as "last mile" links within city regions, special data transmission such as between ships and terrestrial locations, as well as confidential military information) [279]. However, existing commercial FSO systems are highly sensitive to weather conditions due to their operation in the 780-850 nm and 1520-1600 nm range. In contrast, the LWIR band, specifically within the 8-12 μm range, offers a favorable atmospheric window with low sensitivity to turbulence and light scattering by aerosols (as it was shown in Figure 1.2). Unfortunately, the implementation of FSO systems in the LWIR range is limited by the availability of suitable components, such as laser emitters, detectors, and modulators, in the mid-IR spectral range. Although QC technology has facilitated the development of compact, tunable, high-speed mid-IR QCLs [280], the receiver part still often relies on MCT detectors, which have limited bandwidth (typically around 1 GHz), low saturation thresholds, and, under certain conditions, limited chemical stability. Moreover, it can not be integrated. The recent advancements in QCDs [281,282] offer a viable alternative. These devices exhibit room temperature operation and intrinsic bandwidth exceeding 100 GHz, constrained mainly by the device RC constant [283,284]. These characteristics make it well-suited for a heterodyne detection approach, where a robust local oscillator can generate a substantial photocurrent capable of coherently combining with a frequency-shifted signal relative to the local oscillator [285]. Leveraging the intrinsic speed of QCDs, combined with the ability to fabricate QCLs and QCDs with similar emission and detection wavelengths from the same active region (QCLD)[7] and the use of a PE-based DLSPPWs, it becomes possible to realize a compact, monolithic integrated LWIR heterodyne detector, operating at room temperature. Figure 8.8 presents a schematic representation of such a fully integrated heterodyne detector, and Figure 8.9 shows a 3D model of its possible realization.

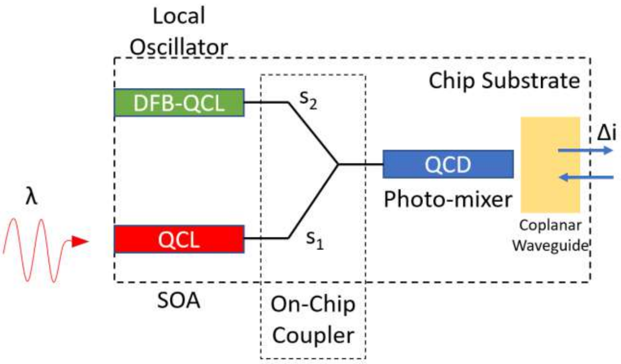

Figure 8.8 Scheme of an on-chip heterodyne detector. The external free-space light (λ) is amplified by a semiconductor optical amplifier (SOA) and mixed with a strong local oscillator on a QCD. The high-speed transmission is facilitated by a coplanar waveguide. Reprinted from [286].

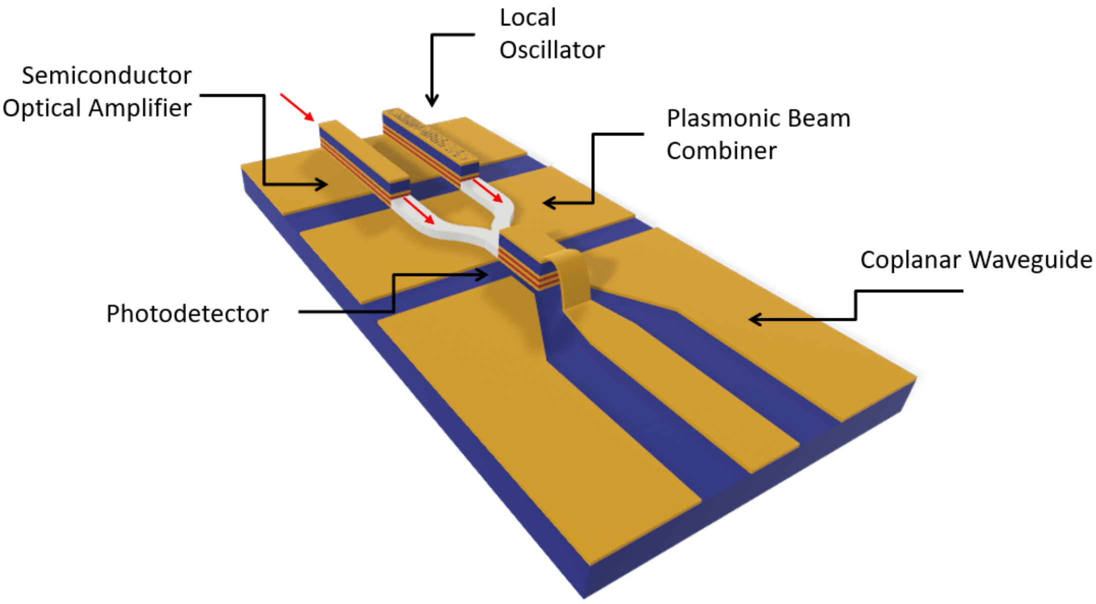

Figure 8.9 Example of an on-chip heterodyne detector design based on QCLD material and a PE-based integrated plasmonic waveguide.

9
CONCLUSION

In conclusion, this dissertation focuses on the design, fabrication, and characterization of surface plasmon waveguides for mid-IR applications, with particular attention on the LWIR band. The research aims to address the challenges in mid-IR integrated photonics and explore novel solutions for advanced PICs based on quantum intersubband devices. The primary objective is to develop DLSPPWs optimized for the mid-IR spectral range, for both, monolithic PIC, and optical-based LOCs.

Throughout this work, various materials and fabrication techniques were explored to achieve high-performance mid-IR plasmonic waveguides. The investigations include broadband SLSPP waveguides based on Ge, as well as novel techniques for fabricating high-quality and transparent PE thin films for DLSPP waveguides. The results demonstrate the potential of both materials for different applications, with PE being the first transparent polymer used in mid-IR integrated optics obtained through a lithography patterning technique. On the other hand, Ge enables efficient mode guiding throughout a broad range of wavelengths, offering low-loss and high tunability, specially tailorable for spectroscopy applications. Furthermore, the incorporation of Pd in combination with Ge offers the advantage of being a CMOS-compatible material, facilitating large-scale production of these plasmonic devices. The integration of the developed SLSPP waveguides with QCL, QCD, and micro-mirrors, also is demonstrated as a viable solution for balanced low-loss guiding and routing for the realization of monolithic mid-IR PICs.

The dissertation's contributions lay the groundwork for the next generation of fully integrated mid-IR PICs, which can open new avenues for cutting-edge technologies and impact various fields, not necessarily limited to plasmonic waveguides. As mid-IR photonics continues to evolve, these novel solutions offer new possibilities for the realization of compact, efficient, and cost-effective devices with a broad range of applications, revolutionizing the field of photonics in the mid-IR spectral region.

9.1 Outlook

The research presented in this dissertation demonstrates the potential of DLSPPWs in combination with QC technology for various applications, particularly in sensing and mid-IR communications. Building upon these findings, several research ideas could be pursued, a selection of which is presented below:

Improved PE Waveguides Processing:

While the PE-based DLSPPWs have shown promising results, there is room for further improvement in their fabrication processes. Refining and investigating novel manufacturing techniques could lead to reduced sidewall roughness and waveguide losses, ultimately enhancing the overall performance. Moreover, further research in the fabrication technique could aim to simplify the process and reduce the number of steps.

Exploration of Other Waveguide Types based on PE:

The lithographic patterning demonstrated in this thesis offers the possibility to develop other types of waveguides beyond the DLSPPWs, such as, for instance, dielectric and photonic crystal waveguides. Different waveguide configurations may offer unique advantages and open new application possibilities for low-loss mid-IR polymeric optical waveguides.

Integration with Mid-IR Frequency Combs and EC-QCL Systems:

Leveraging the broadband capabilities of Ge-based waveguides, future research can focus on integrating them with mid-IR frequency combs and EC-QCL systems. This integration could enable advanced chemical sensing, offering valuable information beyond single-color, quantitative measurements.

Surface Functionalization for Enhanced Sensing:

The plasmonic waveguides presented in this thesis have outstanding sensitivity to the surrounding media. Therefore, further research into surface functionalization of the waveguides can lead to improved sensor sensitivity and selectivity. Investigating various functionalization techniques and their impact on sensing performance will facilitate the development of highly sensitive and specific sensing platforms.

Cutting-edge PICs:

Incorporating PE ridges or low-loss Ge slabs with integrated micro-mirrors into QCLD designs enables low-loss radiation guiding and routing over large ranges. Future research can explore the implementation of more complex PIC schemes, such as MZIs and based on ring resonators, to enhance the functionality and versatility of DLSPPW-based devices.

Development of Compact LWIR Heterodyne Detectors:

To expand the application of FSO communication systems to the LWIR band, the development of compact, monolithic, integrated LWIR heterodyne detectors is essential. Research efforts can focus on optimizing the integration of QCLs and QCDs within the same active region (QCLD) and using PE-based DLSPPWs to realize efficient on-chip heterodyne detectors with room temperature operation.

REFERENCES

1. R. Soref, "The Past, Present, and Future of Silicon Photonics," IEEE Journal of Selected Topics in Quantum Electronics **12**, 1678–1687 (2006).
2. R. Sa, L. Bu, Q. Wang, and J. Zhou, "Spectral characteristics of polluted gases and their detection by mid-infrared differential absorption lidar," Optik **149**, 113–124 (2017).
3. J. Haas and B. Mizaikoff, "Advances in Mid-Infrared Spectroscopy for Chemical Analysis," Annual Review of Analytical Chemistry **9**, 45–68 (2016).
4. K. Isensee, N. Kröger-Lui, and W. Petrich, "Biomedical applications of mid-infrared quantum cascade lasers – a review," Analyst **143**, 5888–5911 (2018).
5. M. Mann, A. S. Rao, and R. C. Sharma, "Remote mid IR Photoacoustic Spectroscopy for the detection of explosive materials," Chemical Physics Letters **765**, 138231 (2021).
6. C. Bauer, A. K. Sharma, U. Willer, J. Burgmeier, B. Braunschweig, W. Schade, S. Blaser, L. Hvozdara, A. Müller, and G. Holl, "Potentials and limits of mid-infrared laser spectroscopy for the detection of explosives," Appl. Phys. B **92**, 327–333 (2008).
7. A. Elkhazraji, M. K. Shakfa, N. Abualsaud, M. Mhanna, M. Sy, M. Marangoni, and A. Farooq, "Laser-based sensing in the long-wavelength mid-infrared: chemical kinetics and environmental monitoring applications," Appl. Opt., AO **62**, A46–A58 (2023).
8. R. Kasahara, S. Kino, S. Soyama, and Y. Matsuura, "Noninvasive glucose monitoring using mid-infrared absorption spectroscopy based on a few wavenumbers," Biomed. Opt. Express, BOE **9**, 289–302 (2018).
9. F. Toor, S. Jackson, X. Shang, S. Arafin, and H. Yang, "Mid-infrared Lasers for Medical Applications: introduction to the feature issue," Biomed. Opt. Express, BOE **9**, 6255–6257 (2018).
10. J. S. Li, B. Yu, H. Fischer, W. Chen, and A. P. Yalin, "Contributed Review: Quantum cascade laser based photoacoustic detection of explosives," Review of Scientific Instruments **86**, 031501 (2015).
11. S. Law, V. Podolskiy, and D. Wasserman, "Towards nano-scale photonics with micro-scale photons: the opportunities and challenges of mid-infrared plasmonics," Nanophotonics **2**, 103–130 (2013).
12. O. US EPA, "Technical Air Pollution Resources," https://www.epa.gov/technical-air-pollution-resources.
13. S. Payan, J. de La Noë, A. Hauchecorne, and C. Camy-Peyret, "A review of remote sensing techniques and related spectroscopy problems," Comptes Rendus Physique **6**, 825–835 (2005).

14. J. Orphal, G. Bergametti, B. Beghin, P.-J. Hébert, T. Steck, and J.-M. Flaud, "Monitoring tropospheric pollution using infrared spectroscopy from geostationary orbit," Comptes Rendus Physique **6**, 888–896 (2005).
15. P. Drossart, "Infrared spectroscopy of planetary atmospheres," Comptes Rendus Physique **6**, 817–824 (2005).
16. N. S. Prasad, "Optical Communications in the mid-wave IR spectral band," in *Free-Space Laser Communications: Principles and Advances* (Springer New York, 2008), pp. 347–391.
17. D. P. Hutchinson and R. K. Richards, "All-weather long-wavelength infrared free space optical communications," in *Free-Space Laser Communications: Principles and Advances* (Springer New York, 2008), pp. 407–417.
18. H. Lin, L. Li, Y. Zou, O. Ogbuu, S. Danto, J. D. Musgraves, K. Richardson, and J. Hu, "Chalcogenide glass planar photonics: from mid-IR sensing to 3-D flexible substrate integration," in A. V. Kudryashov, A. H. Paxton, V. S. Ilchenko, L. Aschke, and K. Washio, eds. (2013), p. 86000K.
19. J. Faist, F. Capasso, D. L. Sivco, C. Sirtori, A. L. Hutchinson, and A. Y. Cho, "Quantum Cascade Laser," Science **264**, 553–556 (1994).
20. O. Cathabard, R. Teissier, J. Devenson, J. C. Moreno, and A. N. Baranov, "Quantum cascade lasers emitting near 2.6 µm," Applied Physics Letters **96**, 141110 (2010).
21. C. Walther, M. Fischer, G. Scalari, R. Terazzi, N. Hoyler, and J. Faist, "Quantum cascade lasers operating from 1.2to1.6THz," Applied Physics Letters **91**, 131122 (2007).
22. R. Q. Yang, "Infrared laser based on intersubband transitions in quantum wells," Superlattices and Microstructures **17**, 77–83 (1995).
23. W. W. Bewley, C. L. Canedy, C. S. Kim, M. Kim, C. D. Merritt, J. Abell, I. Vurgaftman, and J. R. Meyer, "Continuous-wave interband cascade lasers operating above room temperature at $\lambda = 4.7\text{-}5.6$ µm," Opt. Express, OE **20**, 3235–3240 (2012).
24. H. Knötig, B. Hinkov, R. Weih, S. Höfling, J. Koeth, and G. Strasser, "Continuous-wave operation of vertically emitting ring interband cascade lasers at room temperature," Appl. Phys. Lett. **116**, 131101 (2020).
25. J. R. Meyer, W. W. Bewley, C. L. Canedy, C. S. Kim, M. Kim, C. D. Merritt, and I. Vurgaftman, "The Interband Cascade Laser," Photonics **7**, 75 (2020).
26. H. Lin, Z. Luo, T. Gu, L. C. Kimerling, K. Wada, A. Agarwal, and J. Hu, "Mid-infrared integrated photonics on silicon: a perspective," Nanophotonics **7**, 393–420 (2018).
27. A. Yadav and A. M. Agarwal, "Integrated photonic materials for the mid-infrared," International Journal of Applied Glass Science **11**, 491–510 (2020).
28. V. M. Lavchiev and B. Jakoby, "Photonics in the Mid-Infrared: Challenges in Single-Chip Integration and Absorption Sensing," IEEE Journal of Selected Topics in Quantum Electronics **23**, 452–463 (2017).
29. A. Osman, M. Nedeljkovic, J. S. Penades, Y. Wu, Z. Qu, A. Z. Khokhar, K. Debnath, and G. Z. Mashanovich, "Suspended low-loss germanium waveguides for the longwave infrared," Opt. Lett., OL **43**, 5997–6000 (2018).
30. Y.-C. Chang, V. Paeder, L. Hvozdara, J.-M. Hartmann, and H. P. Herzig, "Low-loss germanium strip waveguides on silicon for the mid-infrared," Opt. Lett., OL **37**, 2883–2885 (2012).

31. J. S. Penadés, A. Sánchez-Postigo, M. Nedeljkovic, A. Ortega-Moñux, J. G. Wangüemert-Pérez, Y. Xu, R. Halir, Z. Qu, A. Z. Khokhar, A. Osman, W. Cao, C. G. Littlejohns, P. Cheben, I. Molina-Fernández, and G. Z. Mashanovich, "Suspended silicon waveguides for long-wave infrared wavelengths," Opt. Lett., OL **43**, 795–798 (2018).
32. J.-M. Fedeli and S. Nicoletti, "Mid-Infrared (Mid-IR) Silicon-Based Photonics," Proceedings of the IEEE **106**, 2302–2312 (2018).
33. T. Lewi and A. Katzir, "Silver halide single-mode strip waveguides for the mid-infrared," Opt. Lett., OL **37**, 2733–2735 (2012).
34. A. Gutierrez-Arroyo, E. Baudet, L. Bodiou, J. Lemaitre, I. Hardy, F. Faijan, B. Bureau, V. Nazabal, and J. Charrier, "Optical characterization at 7.7 µm of an integrated platform based on chalcogenide waveguides for sensing applications in the mid-infrared," Opt. Express, OE **24**, 23109–23117 (2016).
35. C. Xin, H. Wu, Y. Xie, S. Yu, N. Zhou, Z. Shi, X. Guo, and L. Tong, "CdTe microwires as mid-infrared optical waveguides," Opt. Express, OE **26**, 10944–10952 (2018).
36. S. Jung, D. Palaferri, K. Zhang, F. Xie, Y. Okuno, C. Pinzone, K. Lascola, and M. A. Belkin, "Homogeneous photonic integration of mid-infrared quantum cascade lasers with low-loss passive waveguides on an InP platform," Optica **6**, 1023 (2019).
37. R. Wang, P. Täschler, Z. Wang, E. Gini, M. Beck, and J. Faist, "Monolithic Integration of Mid-Infrared Quantum Cascade Lasers and Frequency Combs with Passive Waveguides," ACS Photonics **9**, 426–431 (2022).
38. M. R. Billah, M. Blaicher, T. Hoose, P.-I. Dietrich, P. Marin-Palomo, N. Lindenmann, A. Nesic, A. Hofmann, U. Troppenz, M. Moehrle, S. Randel, W. Freude, and C. Koos, "Hybrid integration of silicon photonics circuits and InP lasers by photonic wire bonding," Optica, OPTICA **5**, 876–883 (2018).
39. W. L. Barnes, A. Dereux, and T. W. Ebbesen, "Surface plasmon subwavelength optics," Nature **424**, 824–830 (2003).
40. M. Hochberg, T. Baehr-Jones, C. Walker, and A. Scherer, "Integrated plasmon and dielectric waveguides," Opt. Express, OE **12**, 5481–5486 (2004).
41. A. L. Pyayt, B. Wiley, Y. Xia, A. Chen, and L. Dalton, "Integration of photonic and silver nanowire plasmonic waveguides," Nature Nanotech **3**, 660–665 (2008).
42. S. Sederberg, V. Van, and A. Y. Elezzabi, "Monolithic integration of plasmonic waveguides into a complimentary metal-oxide-semiconductor- and photonic-compatible platform," Applied Physics Letters **96**, 121101 (2010).
43. M. Sistani, M. G. Bartmann, N. A. Güsken, R. F. Oulton, H. Keshmiri, M. S. Seifner, S. Barth, N. Fukata, M. A. Luong, M. I. den Hertog, and A. Lugstein, "Nanoscale aluminum plasmonic waveguide with monolithically integrated germanium detector," Applied Physics Letters **115**, 161107 (2019).
44. A. Rusina, M. Durach, and M. I. Stockman, "Theory of spoof plasmons in real metals," Appl. Phys. A **100**, 375–378 (2010).
45. B. N. Iii, D. Korobkin, C. Fietz, D. Carole, G. Ferro, and G. Shvets, "Critically coupled surface phonon-polariton excitation in silicon carbide," Opt. Lett., OL **34**, 2667–2669 (2009).
46. R. Soref, J. Hendrickson, and J. W. Cleary, "Mid- to long-wavelength infrared plasmonic-photonics using heavily doped n-Ge/Ge and n-GeSn/GeSn heterostructures," Opt. Express, OE **20**, 3814–3824 (2012).

47. A. V. Krasavin and A. V. Zayats, "Passive photonic elements based on dielectric-loaded surface plasmon polariton waveguides," Applied Physics Letters **90**, 211101 (2007).
48. B. Schwarz, P. Reininger, D. Ristanić, H. Detz, A. M. Andrews, W. Schrenk, and G. Strasser, "Monolithically integrated mid-infrared lab-on-a-chip using plasmonics and quantum cascade structures," Nature Communications **5**, 4085 (2014).
49. B. Hinkov, F. Pilat, L. Lux, P. L. Souza, M. David, A. Schwaighofer, D. Ristanić, B. Schwarz, H. Detz, A. M. Andrews, B. Lendl, and G. Strasser, "A mid-infrared lab-on-a-chip for dynamic reaction monitoring," Nat Commun **13**, 4753 (2022).
50. F. Pilat, B. Schwarz, B. Baumgartner, D. Ristanić, H. Detz, A. M. Andrews, B. Lendl, G. Strasser, and B. Hinkov, "Beyond Karl Fischer titration: a monolithic quantum cascade sensor for monitoring residual water concentration in solvents," Lab Chip (2023).
51. B. Schwarz, P. Reininger, H. Detz, T. Zederbauer, A. Maxwell Andrews, S. Kalchmair, W. Schrenk, O. Baumgartner, H. Kosina, and G. Strasser, "A bi-functional quantum cascade device for same-frequency lasing and detection," Appl. Phys. Lett. **101**, 191109 (2012).
52. B. Schwarz, D. Ristanic, P. Reininger, T. Zederbauer, D. MacFarland, H. Detz, A. M. Andrews, W. Schrenk, and G. Strasser, "High performance bi-functional quantum cascade laser and detector," Appl. Phys. Lett. **107**, 071104 (2015).
53. J. Kischkat, S. Peters, B. Gruska, M. Semtsiv, M. Chashnikova, M. Klinkmüller, O. Fedosenko, S. Machulik, A. Aleksandrova, G. Monastyrskyi, Y. Flores, and W. T. Masselink, "Mid-infrared optical properties of thin films of aluminum oxide, titanium dioxide, silicon dioxide, aluminum nitride, and silicon nitride," Appl. Opt., AO **51**, 6789–6798 (2012).
54. A. A. Bunaciu, Ş. Fleschin, V. D. Hoang, and H. Y. Aboul-Enein, "Vibrational Spectroscopy in Body Fluids Analysis," Critical Reviews in Analytical Chemistry **47**, 67–75 (2017).
55. T. Taliercio and P. Biagioni, "Semiconductor infrared plasmonics," Nanophotonics **8**, 949–990 (2019).
56. Y. Fang and M. Sun, "Nanoplasmonic waveguides: towards applications in integrated nanophotonic circuits," Light Sci Appl **4**, e294–e294 (2015).
57. J. Homola, S. S. Yee, and G. Gauglitz, "Surface plasmon resonance sensors: review," Sensors and Actuators B: Chemical **54**, 3–15 (1999).
58. S. Hayashi and T. Okamoto, "Plasmonics: visit the past to know the future," J. Phys. D: Appl. Phys. **45**, 433001 (2012).
59. S. Hayashi, K. Kozaru, and K. Yamamoto, "Enhancement of photoelectric conversion efficiency by surface plasmon excitation: A test with an organic solar cell," Solid State Communications **79**, 763–767 (1991).
60. S. A. Maier, *Plasmonics : Fundamentals and Applications* (Springer, 2007).
61. S. I. Bozhevolnyi, ed., *Plasmonic Nanoguides and Circuits* (Distributed by World Scientific Pub, 2009).
62. Y. Zhong, S. D. Malagari, T. Hamilton, and D. M. Wasserman, "Review of mid-infrared plasmonic materials," JNP **9**, 093791 (2015).
63. R. W. Wood, "XLII. On a remarkable case of uneven distribution of light in a diffraction grating spectrum," The London, Edinburgh, and Dublin Philosophical Magazine and Journal of Science **4**, 396–402 (1902).

64. J. C. M. Garnett and J. Larmor, "XII. Colours in metal glasses and in metallic films," Philosophical Transactions of the Royal Society of London. Series A, Containing Papers of a Mathematical or Physical Character **203**, 385–420 (1997).
65. G. Mie, "Beiträge zur Optik trüber Medien, speziell kolloidaler Metallösungen," Annalen der Physik **330**, 377–445 (1908).
66. R. H. Ritchie, "Plasma Losses by Fast Electrons in Thin Films," Phys. Rev. **106**, 874–881 (1957).
67. C. J. Powell and J. B. Swan, "Origin of the Characteristic Electron Energy Losses in Aluminum," Phys. Rev. **115**, 869–875 (1959).
68. A. Otto, "Excitation of nonradiative surface plasma waves in silver by the method of frustrated total reflection," Z. Physik **216**, 398–410 (1968).
69. E. Kretschmann and H. Raether, "Notizen: Radiative Decay of Non Radiative Surface Plasmons Excited by Light," Zeitschrift für Naturforschung A **23**, 2135–2136 (1968).
70. M. Fleischmann, P. J. Hendra, and A. J. McQuillan, "Raman spectra of pyridine adsorbed at a silver electrode," Chemical Physics Letters **26**, 163–166 (1974).
71. Y. Inouye and S. Kawata, "Near-field scanning optical microscope with a metallic probe tip," Opt. Lett., OL **19**, 159–161 (1994).
72. U. Ch. Fischer and D. W. Pohl, "Observation of Single-Particle Plasmons by Near-Field Optical Microscopy," Phys. Rev. Lett. **62**, 458–461 (1989).
73. T. W. Ebbesen, H. J. Lezec, H. F. Ghaemi, T. Thio, and P. A. Wolff, "Extraordinary optical transmission through sub-wavelength hole arrays," Nature **391**, 667–669 (1998).
74. F. T. Ulaby and U. Ravaioli, *Fundamentals of Applied Electromagnetics*, Seventh edition (Pearson, 2015).
75. R. L. Olmon, B. Slovick, T. W. Johnson, D. Shelton, S.-H. Oh, G. D. Boreman, and M. B. Raschke, "Optical dielectric function of gold," Phys. Rev. B **86**, 235147 (2012).
76. N. W. Ashcroft and N. D. Mermin, *Solid State Physics*, Holt-Saunders International Editions (Holt, Rinehart and Winston, 1976).
77. G. A. Reider, *Photonics* (Springer International Publishing, 2016).
78. A. Vial, A.-S. Grimault, D. Macías, D. Barchiesi, and M. L. De La Chapelle, "Improved analytical fit of gold dispersion: Application to the modeling of extinction spectra with a finite-difference time-domain method," Phys. Rev. B **71**, 085416 (2005).
79. "Introduction to Plasmonics," https://stepik.org/course/24660/promo.
80. "COMSOL: Multiphysics Software for Optimizing Designs," https://www.comsol.com/.
81. J. B. Pendry, L. Martín-Moreno, and F. J. Garcia-Vidal, "Mimicking Surface Plasmons with Structured Surfaces," Science **305**, 847–848 (2004).
82. K. S. Novoselov, A. K. Geim, S. V. Morozov, D. Jiang, Y. Zhang, S. V. Dubonos, I. V. Grigorieva, and A. A. Firsov, "Electric Field Effect in Atomically Thin Carbon Films," Science **306**, 666–669 (2004).
83. K. S. Novoselov, A. K. Geim, S. V. Morozov, D. Jiang, M. I. Katsnelson, I. V. Grigorieva, S. V. Dubonos, and A. A. Firsov, "Two-dimensional gas of massless Dirac fermions in graphene," Nature **438**, 197–200 (2005).
84. T. Low, A. Chaves, J. D. Caldwell, A. Kumar, N. X. Fang, P. Avouris, T. F. Heinz, F. Guinea, L. Martin-Moreno, and F. Koppens, "Polaritons in layered two-dimensional materials," Nature Mater **16**, 182–194 (2017).

85. G. V. Naik, J. Kim, and A. Boltasseva, "Oxides and nitrides as alternative plasmonic materials in the optical range [Invited]," Opt. Mater. Express, OME **1**, 1090–1099 (2011).
86. G. V. Naik, J. L. Schroeder, X. Ni, A. V. Kildishev, T. D. Sands, and A. Boltasseva, "Titanium nitride as a plasmonic material for visible and near-infrared wavelengths," Opt. Mater. Express, OME **2**, 478–489 (2012).
87. J. Tamayo-Arriola, E. M. Castellano, M. M. Bajo, A. Huerta-Barberà, E. Muñoz, V. Muñoz-Sanjosé, and A. Hierro, "Controllable and Highly Propagative Hybrid Surface Plasmon–Phonon Polariton in a CdZnO-Based Two-Interface System," ACS Photonics **6**, 2816–2822 (2019).
88. E. Martínez Castellano, J. Yeste, M. Abuin, M. del C. Martínez-Tomás, O. Klymov, V. Muñoz-Sanjosé, M. Montes Bajo, and A. Hierro, "Mid-IR Surface Plasmon Polaritons in CdZnO thin films on GaAs," Applied Surface Science **608**, 155060 (2023).
89. E. Martínez Castellano, "Transparent conductive oxide plasmonics for the infrared," PhD Thesis, Universidad Politécnica de Madrid (2022).
90. F. Marquier, K. Joulain, J. P. Mulet, R. Carminati, and J. J. Greffet, "Engineering infrared emission properties of silicon in the near field and the far field," Optics Communications **237**, 379–388 (2004).
91. J. C. Ginn, R. L. Jarecki Jr., E. A. Shaner, and P. S. Davids, "Infrared plasmons on heavily-doped silicon," Journal of Applied Physics **110**, 043110 (2011).
92. M. Shahzad, G. Medhi, R. E. Peale, W. R. Buchwald, J. W. Cleary, R. Soref, G. D. Boreman, and O. Edwards, "Infrared surface plasmons on heavily doped silicon," Journal of Applied Physics **110**, 123105 (2011).
93. D. Li and C. Z. Ning, "All-semiconductor active plasmonic system in mid-infrared wavelengths," Opt. Express, OE **19**, 14594–14603 (2011).
94. S. Law, D. C. Adams, A. M. Taylor, and D. Wasserman, "Mid-infrared designer metals," Opt. Express, OE **20**, 12155–12165 (2012).
95. C. R. Gubbin, S. De Liberato, and T. G. Folland, "Surface phonon polaritons for infrared optoelectronics," Journal of Applied Physics **131**, 030901 (2022).
96. J. D. Caldwell, A. V. Kretinin, Y. Chen, V. Giannini, M. M. Fogler, Y. Francescato, C. T. Ellis, J. G. Tischler, C. R. Woods, A. J. Giles, M. Hong, K. Watanabe, T. Taniguchi, S. A. Maier, and K. S. Novoselov, "Sub-diffractional volume-confined polaritons in the natural hyperbolic material hexagonal boron nitride," Nat Commun **5**, 5221 (2014).
97. S. Dai, Z. Fei, Q. Ma, A. S. Rodin, M. Wagner, A. S. McLeod, M. K. Liu, W. Gannett, W. Regan, K. Watanabe, T. Taniguchi, M. Thiemens, G. Dominguez, A. H. C. Neto, A. Zettl, F. Keilmann, P. Jarillo-Herrero, M. M. Fogler, and D. N. Basov, "Tunable Phonon Polaritons in Atomically Thin van der Waals Crystals of Boron Nitride," Science **343**, 1125–1129 (2014).
98. A. Hartstein, E. Burstein, E. D. Palik, R. W. Gammon, and B. W. Henvis, "Investigation of optic-phonon---magnetoplasmon-type surface polaritons on n-InSb," Phys. Rev. B **12**, 3186–3199 (1975).
99. R. Hillenbrand, T. Taubner, and F. Keilmann, "Phonon-enhanced light–matter interaction at the nanometre scale," Nature **418**, 159–162 (2002).
100. J.-C. Weeber, A. Dereux, C. Girard, J. R. Krenn, and J.-P. Goudonnet, "Plasmon polaritons of metallic nanowires for controlling submicron propagation of light," Phys. Rev. B **60**, 9061–9068 (1999).

101. M. L. Brongersma, J. W. Hartman, and H. A. Atwater, "Electromagnetic energy transfer and switching in nanoparticle chain arrays below the diffraction limit," Phys. Rev. B **62**, R16356–R16359 (2000).
102. S. I. Bozhevolnyi, V. S. Volkov, E. Devaux, and T. W. Ebbesen, "Channel Plasmon-Polariton Guiding by Subwavelength Metal Grooves," Phys. Rev. Lett. **95**, 046802 (2005).
103. E. Moreno, S. G. Rodrigo, S. I. Bozhevolnyi, L. Martín-Moreno, and F. J. García-Vidal, "Guiding and Focusing of Electromagnetic Fields with Wedge Plasmon Polaritons," Phys. Rev. Lett. **100**, 023901 (2008).
104. Z. Han and S. I. Bozhevolnyi, "Radiation guiding with surface plasmon polaritons," Rep. Prog. Phys. **76**, 016402 (2012).
105. E. Chatzianagnostou, A. Manolis, G. Dabos, D. Ketzaki, A. Miliou, N. Pleros, L. Markey, J.-C. Weeber, A. Dereux, B. Chmielak, A.-L. Giesecke, C. Porschatis, P. J. Cegielski, and D. Tsiokos, "Scaling the Sensitivity of Integrated Plasmo-Photonic Interferometric Sensors," ACS Photonics **6**, 1664–1673 (2019).
106. J. Homola, "Surface Plasmon Resonance Sensors for Detection of Chemical and Biological Species," Chem. Rev. **108**, 462–493 (2008).
107. R. Slavík and J. Homola, "Ultrahigh resolution long range surface plasmon-based sensor," Sensors and Actuators B: Chemical **123**, 10–12 (2007).
108. G. V. Naik, V. M. Shalaev, and A. Boltasseva, "Alternative Plasmonic Materials: Beyond Gold and Silver," Advanced Materials **25**, 3264–3294 (2013).
109. C. M. Miyazaki, F. M. Shimizu, and M. Ferreira, "6 - Surface Plasmon Resonance (SPR) for Sensors and Biosensors," in *Nanocharacterization Techniques*, A. L. Da Róz, M. Ferreira, F. de Lima Leite, and O. N. Oliveira, eds., Micro and Nano Technologies (William Andrew Publishing, 2017), pp. 183–200.
110. M. Fukui, V. C. Y. So, and R. Normandin, "Lifetimes of surface plasmons in thin silver films," physica status solidi (b) **91**, K61–K64 (1979).
111. A. E. Craig, G. A. Olson, and D. Sarid, "Experimental observation of the long-range surface-plasmon polariton," Opt. Lett., OL **8**, 380–382 (1983).
112. C. Reinhardt, S. Passinger, B. N. Chichkov, C. Marquart, I. P. Radko, and S. I. Bozhevolnyi, "Laser-fabricated dielectric optical components for surface plasmon polaritons," Opt. Lett., OL **31**, 1307–1309 (2006).
113. B. Steinberger, A. Hohenau, H. Ditlbacher, A. L. Stepanov, A. Drezet, F. R. Aussenegg, A. Leitner, and J. R. Krenn, "Dielectric stripes on gold as surface plasmon waveguides," Applied Physics Letters **88**, 094104 (2006).
114. B. Steinberger, A. Hohenau, H. Ditlbacher, F. R. Aussenegg, A. Leitner, and J. R. Krenn, "Dielectric stripes on gold as surface plasmon waveguides: Bends and directional couplers," Appl. Phys. Lett. **91**, 081111 (2007).
115. Z. Chen, T. Holmgaard, S. I. Bozhevolnyi, A. V. Krasavin, A. V. Zayats, L. Markey, and A. Dereux, "Wavelength-selective directional coupling with dielectric-loaded plasmonic waveguides," Opt. Lett., OL **34**, 310–312 (2009).
116. J. Grandidier, S. Massenot, G. C. des Francs, A. Bouhelier, J.-C. Weeber, L. Markey, A. Dereux, J. Renger, M. U. González, and R. Quidant, "Dielectric-loaded surface plasmon polariton waveguides: Figures of merit and mode characterization by image and Fourier plane leakage microscopy," Phys. Rev. B **78**, 245419 (2008).
117. A. V. Krasavin and A. V. Zayats, "Active Nanophotonic Circuitry Based on Dielectric-loaded Plasmonic Waveguides," Advanced Optical Materials **3**, 1662–1690 (2015).

118. J. Grandidier, G. C. des Francs, S. Massenot, A. Bouhelier, L. Markey, J.-C. Weeber, C. Finot, and A. Dereux, "Gain-Assisted Propagation in a Plasmonic Waveguide at Telecom Wavelength," Nano Lett. **9**, 2935–2939 (2009).
119. C. Garcia, V. Coello, Z. Han, I. P. Radko, and S. I. Bozhevolnyi, "Partial loss compensation in dielectric-loaded plasmonic waveguides at near infra-red wavelengths," Opt. Express, OE **20**, 7771–7776 (2012).
120. A. Kumar, J. Gosciniak, V. S. Volkov, S. Papaioannou, D. Kalavrouziotis, K. Vyrsokinos, J.-C. Weeber, K. Hassan, L. Markey, A. Dereux, T. Tekin, M. Waldow, D. Apostolopoulos, H. Avramopoulos, N. Pleros, and S. I. Bozhevolnyi, "Dielectric-loaded plasmonic waveguide components: Going practical," Laser & Photonics Reviews **7**, 938–951 (2013).
121. V. S. Volkov, Z. Han, M. G. Nielsen, K. Leosson, H. Keshmiri, J. Gosciniak, O. Albrektsen, and S. I. Bozhevolnyi, "Long-range dielectric-loaded surface plasmon polariton waveguides operating at telecommunication wavelengths," Opt. Lett., OL **36**, 4278–4280 (2011).
122. T. Holmgaard, J. Gosciniak, and S. I. Bozhevolnyi, "Long-range dielectric-loaded surface plasmon-polariton waveguides," Opt. Express, OE **18**, 23009–23015 (2010).
123. N. Kinsey, M. Ferrera, G. V. Naik, V. E. Babicheva, V. M. Shalaev, and A. Boltasseva, "Experimental demonstration of titanium nitride plasmonic interconnects," Opt. Express, OE **22**, 12238–12247 (2014).
124. S. M. García-Blanco, M. Pollnau, and S. I. Bozhevolnyi, "Loss compensation in long-range dielectric-loaded surface plasmon-polariton waveguides," Opt. Express, OE **19**, 25298–25310 (2011).
125. R. F. Oulton, V. J. Sorger, D. A. Genov, D. F. P. Pile, and X. Zhang, "A hybrid plasmonic waveguide for subwavelength confinement and long-range propagation," Nature Photon **2**, 496–500 (2008).
126. R. F. Oulton, V. J. Sorger, T. Zentgraf, R.-M. Ma, C. Gladden, L. Dai, G. Bartal, and X. Zhang, "Plasmon lasers at deep subwavelength scale," Nature **461**, 629–632 (2009).
127. M. Wu, Z. Han, and V. Van, "Conductor-gap-silicon plasmonic waveguides and passive components at subwavelength scale," Opt. Express, OE **18**, 11728–11736 (2010).
128. P. Berini, "Plasmon-polariton waves guided by thin lossy metal films of finite width: Bound modes of symmetric structures," Phys. Rev. B **61**, 10484–10503 (2000).
129. P. Berini, "Long-range surface plasmon polaritons," Adv. Opt. Photon., AOP **1**, 484–588 (2009).
130. D. F. P. Pile and D. K. Gramotnev, "Channel plasmon–polariton in a triangular groove on a metal surface," Opt. Lett., OL **29**, 1069–1071 (2004).
131. A. D. Boardman, G. C. Aers, and R. Teshima, "Retarded edge modes of a parabolic wedge," Phys. Rev. B **24**, 5703–5712 (1981).
132. D. K. Gramotnev, "Adiabatic nanofocusing of plasmons by sharp metallic grooves: Geometrical optics approach," Journal of Applied Physics **98**, 104302 (2005).
133. D. F. P. Pile, T. Ogawa, D. K. Gramotnev, T. Okamoto, M. Haraguchi, M. Fukui, and S. Matsuo, "Theoretical and experimental investigation of strongly localized plasmons on triangular metal wedges for subwavelength waveguiding," Applied Physics Letters **87**, 061106 (2005).

134. J. Takahara, S. Yamagishi, H. Taki, A. Morimoto, and T. Kobayashi, "Guiding of a one-dimensional optical beam with nanometer diameter," Opt. Lett., OL **22**, 475–477 (1997).
135. L. Tong, R. R. Gattass, J. B. Ashcom, S. He, J. Lou, M. Shen, I. Maxwell, and E. Mazur, "Subwavelength-diameter silica wires for low-loss optical wave guiding," Nature **426**, 816–819 (2003).
136. K. Tanaka and M. Tanaka, "Simulations of nanometric optical circuits based on surface plasmon polariton gap waveguide," Applied Physics Letters **82**, 1158–1160 (2003).
137. G. Veronis and S. Fan, "Guided subwavelength plasmonic mode supported by a slot in a thin metal film," Opt. Lett., OL **30**, 3359–3361 (2005).
138. A. Banerjee, *Optical Waveguides Analysis and Design* (Springer International Publishing, 2022).
139. K. Kawano and T. Kitoh, *Introduction to Optical Waveguide Analysis* (John Wiley & Sons, Inc., 2001).
140. R. F. Oulton, G. Bartal, D. F. P. Pile, and X. Zhang, "Confinement and propagation characteristics of subwavelength plasmonic modes," New J. Phys. **10**, 105018 (2008).
141. M. David, A. Dabrowska, M. Sistani, I. C. Doganlar, E. Hinkelmann, H. Detz, W. M. Weber, B. Lendl, G. Strasser, and B. Hinkov, "Octave-spanning low-loss mid-IR waveguides based on semiconductor-loaded plasmonics," Opt. Express **29**, 43567 (2021).
142. J. Gosciniak, T. Holmgaard, and S. I. Bozhevolnyi, "Theoretical Analysis of Long-Range Dielectric-Loaded Surface Plasmon Polariton Waveguides," Journal of Lightwave Technology **29**, 1473–1481 (2011).
143. R. Buckley and P. Berini, "Figures of merit for 2D surface plasmon waveguides and application to metal stripes," Opt. Express, OE **15**, 12174–12182 (2007).
144. T. Schädle and B. Mizaikoff, "Mid-Infrared Waveguides: A Perspective," Appl Spectrosc **70**, 1625–1638 (2016).
145. G. Pellegrini, L. Baldassare, V. Giliberti, J. Frigerio, K. Gallacher, D. J. Paul, G. Isella, M. Ortolani, and P. Biagioni, "Benchmarking the Use of Heavily Doped Ge for Plasmonics and Sensing in the Mid-Infrared," ACS Photonics **5**, 3601–3607 (2018).
146. R. Soref, "Mid-infrared photonics in silicon and germanium," Nature Photon **4**, 495–497 (2010).
147. G. Z. Mashanovich, M. M. Milošević, M. Nedeljkovic, N. Owens, B. Xiong, E. J. Teo, and Y. Hu, "Low loss silicon waveguides for the mid-infrared," Opt. Express, OE **19**, 7112–7119 (2011).
148. P. T. Lin, V. Singh, H.-Y. G. Lin, T. Tiwald, L. C. Kimerling, and A. M. Agarwal, "Low-Stress Silicon Nitride Platform for Mid-Infrared Broadband and Monolithically Integrated Microphotonics," Advanced Optical Materials **1**, 732–739 (2013).
149. B. Mizaikoff, "Waveguide-enhanced mid-infrared chem/bio sensors," Chem. Soc. Rev. **42**, 8683–8699 (2013).
150. S. Bhagyaraj, O. S. Oluwafemi, and I. Krupa, "Chapter 13 - Polymers in optics," in *Polymer Science and Innovative Applications*, M. A. A. AlMaadeed, D. Ponnamma, and M. A. Carignano, eds. (Elsevier, 2020), pp. 423–455.
151. J. Loste, J.-M. Lopez-Cuesta, L. Billon, H. Garay, and M. Save, "Transparent polymer nanocomposites: An overview on their synthesis and advanced properties," Progress in Polymer Science **89**, 133–158 (2019).

152. H. Ma, A. k.-Y. Jen, and L. r. Dalton, "Polymer-Based Optical Waveguides: Materials, Processing, and Devices," Advanced Materials **14**, 1339–1365 (2002).
153. G. Cao and Y. Wang, *Nanostructures and Nanomaterials: Synthesis, Properties, and Applications*, 2nd ed., World Scientific Series in Nanoscience and Nanotechnology (WORLD SCIENTIFIC, 2011), Vol. 2.
154. M. W. Alam, S. Islam Bhat, H. S. Al Qahtani, M. Aamir, M. N. Amin, M. Farhan, S. Aldabal, M. S. Khan, I. Jeelani, A. Nawaz, and B. Souayeh, "Recent Progress, Challenges, and Trends in Polymer-Based Sensors: A Review," Polymers **14**, 2164 (2022).
155. X.-Y. Han, Z.-L. Wu, S.-C. Yang, F.-F. Shen, Y.-X. Liang, L.-H. Wang, J.-Y. Wang, J. Ren, L.-Y. Jia, H. Zhang, S.-H. Bo, G. Morthier, and M.-S. Zhao, "Recent Progress of Imprinted Polymer Photonic Waveguide Devices and Applications," Polymers (Basel) **10**, 603 (2018).
156. S. N. Khonina, G. S. Voronkov, E. P. Grakhova, N. L. Kazanskiy, R. V. Kutluyarov, and M. A. Butt, "Polymer Waveguide-Based Optical Sensors—Interest in Bio, Gas, Temperature, and Mechanical Sensing Applications," Coatings **13**, 549 (2023).
157. M. A. Sefunc, M. Pollnau, and S. M. García-Blanco, "Low-loss sharp bends in polymer waveguides enabled by the introduction of a thin metal layer," Opt. Express, OE **21**, 29808–29817 (2013).
158. A. Block, C. Etrich, T. Limboeck, F. Bleckmann, E. Soergel, C. Rockstuhl, and S. Linden, "Bloch oscillations in plasmonic waveguide arrays," Nature communications **5**, 3843 (2014).
159. T. J. Davis, D. E. Gómez, and A. Roberts, "Plasmonic circuits for manipulating optical information," Nanophotonics **6**, 543–559 (2017).
160. X. Zhang, J. Qiu, J. Zhao, X. Li, and L. Liu, "Complex refractive indices measurements of polymers in infrared bands," Journal of Quantitative Spectroscopy and Radiative Transfer **252**, 107063 (2020).
161. S. Ashraf, I. Niskanen, B. Kanyathare, E. Vartiainen, C. Mattsson, R. Heikkilä, and G. Thungström, "Determination of complex refractive index of SU-8 by Kramers–Kronig dispersion relation method at the wavelength range 2.5–22.0 µm," Journal of Quantitative Spectroscopy and Radiative Transfer **224**, 309–311 (2019).
162. M. David, D. Disnan, A. Lardschneider, D. Wacht, H. Hoang, G. Ramer, H. Detz, B. Lendl, U. Schmid, G. Strasser, and B. Hinkov, "Structure and mid-infrared optical properties of spin-coated polyethylene films developed for integrated photonics applications," Optical Materials Express (2022).
163. D. R. Smith and E. V. Loewenstein, "Optical constants of far infrared materials 3: plastics," Appl. Opt. **14**, 1335 (1975).
164. H. I. Song, H. Jin, and H.-M. Bae, "Plastic straw: future of high-speed signaling," Sci Rep **5**, 16062 (2015).
165. M. Geiger, M. Hitzler, J. Iberle, and C. Waldschmidt, "A dielectric lens antenna fed by a flexible dielectric waveguide at 160 GHz," in *2017 11th European Conference on Antennas and Propagation (EUCAP)* (2017), pp. 3380–3383.
166. B. You, J.-Y. Lu, T.-A. Liu, and J.-L. Peng, "Hybrid terahertz plasmonic waveguide for sensing applications," Opt. Express, OE **21**, 21087–21096 (2013).
167. X. Y. He, Q. J. Wang, and S. F. Yu, "Analysis of dielectric loaded surface plasmon waveguide structures: Transfer matrix method for plasmonic devices," Journal of Applied Physics **111**, 073108 (2012).

168. B. Zhang, Y. Bian, L. Ren, F. Guo, S.-Y. Tang, Z. Mao, X. Liu, J. Sun, J. Gong, X. Guo, and T. J. Huang, "Hybrid Dielectric-loaded Nanoridge Plasmonic Waveguide for Low-Loss Light Transmission at the Subwavelength Scale," Scientific Reports **7**, 40479 (2017).
169. B. You, J.-Y. Lu, W.-L. Chang, C.-P. Yu, T.-A. Liu, and J.-L. Peng, "Subwavelength confined terahertz waves on planar waveguides using metallic gratings," Opt. Express, OE **21**, 6009–6019 (2013).
170. D. Ren, C. Dong, S. J. Addamane, and D. Burghoff, "High-quality microresonators in the longwave infrared based on native germanium," Nat Commun **13**, 5727 (2022).
171. P. M. Martin, *Handbook of Deposition Technologies for Films and Coatings: Science, Applications and Technology*, 3rd ed (Elsevier, 2010).
172. M. J. Madou, *Fundamentals of Microfabrication and Nanotechnology*, 3. ed. (CRC, n.d.).
173. J. Clark and G. Lanzani, "Organic photonics for communications," Nature Photon **4**, 438–446 (2010).
174. S. Landis, *Lithography : Main Techniques*, ISTE (ISTE ; Wiley, 2011).
175. D. Meyerhofer, "Characteristics of resist films produced by spinning," Journal of Applied Physics **49**, 3993–3997 (2008).
176. "Spin Coating: Complete Guide to Theory and Techniques," https://www.ossila.com/en-eu/pages/spin-coating.
177. M. A. Butt, "Thin-Film Coating Methods: A Successful Marriage of High-Quality and Cost-Effectiveness—A Brief Exploration," Coatings **12**, 1115 (2022).
178. K. T. Chaudhary, "Thin Film Deposition: Solution Based Approach," in *Thin Films* (IntechOpen, 2021).
179. B. T. Chen, "Investigation of the solvent-evaporation effect on spin coating of thin films," Polymer Engineering & Science **23**, 399–403 (1983).
180. P. N. Plassmeyer, G. Mitchson, K. N. Woods, D. C. Johnson, and C. J. Page, "Impact of Relative Humidity during Spin-Deposition of Metal Oxide Thin Films from Aqueous Solution Precursors," Chem. Mater. **29**, 2921–2926 (2017).
181. D. P. Sanders, "Advances in Patterning Materials for 193 nm Immersion Lithography," Chem. Rev. **110**, 321–360 (2010).
182. D. M. Mattox, "Introduction," in *Handbook of Physical Vapor Deposition (PVD) Processing* (Elsevier, 2010), pp. 1–24.
183. S. M. George, "Atomic Layer Deposition: An Overview," Chem. Rev. **110**, 111–131 (2010).
184. R. C. Jäger, *Introduction to Microelectronic Fabrication*, 2. ed., Modular Series on Solid State Devices (Addison-Wesley, 2002).
185. M. Christophersen, V. Fadeyev, S. Ely, B. F. Phlips, and H. F.-W. Sadrozinski, "The effect of different dicing methods on the leakage currents of n-type silicon diodes and strip sensors," Solid-State Electronics **81**, 8–12 (2013).
186. A. Hooper, J. Ehorn, M. Brand, and C. Bassett, "Review of wafer dicing techniques for via-middle process 3DI/TSV ultrathin silicon device wafers," in *2015 IEEE 65th Electronic Components and Technology Conference (ECTC)* (2015), pp. 1436–1446.
187. R. Casquel, M. Holgado, J. J. García-Ballesteros, K. Zinoviev, C. Férnandez-Sánchez, F. J. Sanza, C. Molpeceres, M. F. Laguna, A. Llobera, J. L. Ocaña, and C. Domínguez, "UV laser-induced high resolution cleaving of Si wafers for micro–nano devices and

polymeric waveguide characterization," Applied Surface Science **257**, 5424–5428 (2011).

188. P. Kaur, A. Boes, G. Ren, T. G. Nguyen, G. Roelkens, and A. Mitchell, "Hybrid and heterogeneous photonic integration," APL Photonics **6**, 061102 (2021).
189. C.-Y. Hsu, G.-Z. Yiu, and Y.-C. Chang, "Free-Space Applications of Silicon Photonics: A Review," Micromachines **13**, 990 (2022).
190. S. M. Sze and K. K. Ng, *Physics of Semiconductor Devices*, 3. ed., Wiley-Interscience (Wiley, 2007).
191. M. E. Levinštein, *Handbook Series on Semiconductor Parameters : 2. Ternary and Quaternary III-V Compounds* (World Scientific, 1999).
192. L. Chen, Q. Xu, M. G. Wood, and R. M. Reano, "Hybrid silicon and lithium niobate electro-optical ring modulator," Optica, OPTICA **1**, 112–118 (2014).
193. J. Justice, C. Bower, M. Meitl, M. B. Mooney, M. A. Gubbins, and B. Corbett, "Wafer-scale integration of group III–V lasers on silicon using transfer printing of epitaxial layers," Nature Photon **6**, 610–614 (2012).
194. K. Yamada, "Silicon Photonic Wire Waveguides: Fundamentals and Applications," in *Silicon Photonics II: Components and Integration*, D. J. Lockwood and L. Pavesi, eds., Topics in Applied Physics (Springer, 2011), pp. 1–29.
195. P. Berini, R. Charbonneau, N. Lahoud, and G. Mattiussi, "Characterization of long-range surface-plasmon-polariton waveguides," Journal of Applied Physics **98**, 043109 (2005).
196. S.-T. Huang, C.-C. Lai, F.-W. Sheu, and W.-S. Tsai, "Characterization of long-range plasmonic waveguides at visible to near-infrared regime," AIP Advances **7**, 125221 (2017).
197. T. Nikolajsen, K. Leosson, I. Salakhutdinov, and S. I. Bozhevolnyi, "Polymer-based surface-plasmon-polariton stripe waveguides at telecommunication wavelengths," Appl. Phys. Lett. **82**, 668–670 (2003).
198. R. Zektzer, B. Desiatov, N. Mazurski, S. I. Bozhevolnyi, and U. Levy, "Experimental demonstration of CMOS-compatible long-range dielectric-loaded surface plasmon-polariton waveguides (LR-DLSPPWs)," Opt. Express, OE **22**, 22009–22017 (2014).
199. R. E. Walpole, R. H. Myers, S. L. Myers, and K. Ye, *Probability and Statistics for Engineers and Scientists* (Macmillan New York, 1993), Vol. 5.
200. Y. Shi, L. Ma, Y. Zhuang, and Z. He, "Investigation on roughness-induced scattering loss of small-core polymer waveguides for single-mode optical interconnect applications," Opt. Express, OE **28**, 38733–38744 (2020).
201. R. Wolf, I. Breunig, H. Zappe, and K. Buse, "Scattering-loss reduction of ridge waveguides by sidewall polishing," Opt. Express, OE **26**, 19815–19820 (2018).
202. L. Zou, Y. Ge, G. Wang, J. Fu, and F. Liu, "Effect of annealing treatment on refractive index and optical propagation in fluorinated polyimide film waveguide," Optik **126**, 2470–2473 (2015).
203. T. Baehr-Jones, M. Hochberg, C. Walker, E. Chan, D. Koshinz, W. Krug, and A. Scherer, "Analysis of the tuning sensitivity of silicon-on-insulator optical ring resonators," Journal of Lightwave Technology **23**, 4215–4221 (2005).
204. K. Peters, "Polymer optical fiber sensors—a review," Smart Mater. Struct. **20**, 013002 (2011).
205. M. David, D. Disnan, E. Arigliani, A. Lardschneider, G. Marschick, H. Hoang, H. Detz, B. Lendl, U. Schmid, G. Strasser, and B. Hinkov, "Advanced Mid-Infrared

Plasmonic Waveguides based on Polymers for On-chip Integrated Photonics," Photonics Research (2023).

206. C. Vasile and M. Pascu, *Practical Guide to Polyethylene* (iSmithers Rapra Publishing, 2005).
207. P. N. Khanam and M. A. A. AlMaadeed, "Processing and characterization of polyethylene-based composites," Advanced Manufacturing: Polymer & Composites Science **1**, 63–79 (2015).
208. A. Peacock, *Handbook of Polyethylene: Structures: Properties, and Applications* (CRC Press, 2000).
209. R. Das and A. Chanda, "Fabrication and Properties of Spin-Coated Polymer Films," in (2016), pp. 283–306.
210. Y. Wang, S. Ge, M. Rafailovich, J. Sokolov, Y. Zou, H. Ade, J. Lüning, A. Lustiger, and G. Maron, "Crystallization in the Thin and Ultrathin Films of Poly(ethylene−vinyl acetate) and Linear Low-Density Polyethylene," Macromolecules **37**, 3319–3327 (2004).
211. K. Jeon and R. Krishnamoorti, "Morphological Behavior of Thin Linear Low-Density Polyethylene Films," Macromolecules **41**, 7131–7140 (2008).
212. O. Mellbring, S. Kihlman Øiseth, A. Krozer, J. Lausmaa, and T. Hjertberg, "Spin Coating and Characterization of Thin High-Density Polyethylene Films," Macromolecules **34**, 7496–7503 (2001).
213. Y. Wang, Y. Abe, Y. Matsuura, M. Miyagi, and H. Uyama, "Refractive indices and extinction coefficients of polymers for the mid-infrared region," Appl. Opt. **37**, 7091 (1998).
214. K. A. Dill, "Concentration Dependence of the Viscosity and Viscoelasticity of Polymer Solutions: Application of the Theory of Muthukumar and Freed," Macromolecules **13**, 620–622 (1980).
215. A. C. Wirtz, M. Dokter, C. Hofmann, and E. J. J. Groenen, "Spincoated polyethylene films for single-molecule optics," Chemical Physics Letters **417**, 383–388 (2006).
216. N. Chapman, M. Chapman, and W. B. Euler, "Modeling of Poly(methylmethacrylate) Viscous Thin Films by Spin-Coating," Coatings **11**, 198 (2021).
217. S. Matsuoka and M. K. Cowman, "Equation of state for polymer solution," Polymer **43**, 3447–3453 (2002).
218. E. Hedl, I. Fabijanić, I. Šrut Rakić, I. Vadla, and J. Sancho-Parramon, "Fabrication by Spin-Coating and Optical Characterization of Poly(styrene-co-acrylonitrile) Thin Films," Coatings **11**, 1015 (2021).
219. A. Weill and E. Dechenaux, "The spin-coating process mechanism related to polymer solution properties," Polymer Engineering & Science **28**, 945–948 (1988).
220. R. J. Young and P. A. Lovell, *Introduction to Polymers*, 3. ed. (CRC, 2011).
221. W. Lin, M. Cossar, V. Dang, and J. Teh, "The application of Raman spectroscopy to three-phase characterization of polyethylene crystallinity," Polymer Testing **26**, 814–821 (2007).
222. "Spherulites and optical properties," https://www.doitpoms.ac.uk/tlplib/polymers/spherulites.php.
223. "Full Record for Micrograph 601," https://www.doitpoms.ac.uk/miclib/full_record.php?id=601.

224. M. Roché, Z. Li, I. M. Griffiths, S. Le Roux, I. Cantat, A. Saint-Jalmes, and H. A. Stone, "Marangoni Flow of Soluble Amphiphiles," Phys. Rev. Lett. **112**, 208302 (2014).
225. L. Flannigan, L. Yoell, and C. Xu, "Mid-wave and long-wave infrared transmitters and detectors for optical satellite communications—a review," J. Opt. **24**, 043002 (2022).
226. T. Holmgaard and S. I. Bozhevolnyi, "Theoretical analysis of dielectric-loaded surface plasmon-polariton waveguides," Phys. Rev. B **75**, 245405 (2007).
227. K. Q. Nguyen, P. Cousin, K. Mohamed, M. Robert, A. El-Safty, and B. Benmokrane, "Effects of Ultraviolet Radiation on Recycled and Virgin HDPE Corrugated Pipes Used in Road Drainage Systems," J Polym Environ **30**, 3391–3408 (2022).
228. M. David, D. Disnan, A. Lardschneider, D. Wacht, H. Hoang, G. Ramer, H. Detz, B. Lendl, U. Schmid, G. Strasser, and B. Hinkov, "Structure and mid-infrared optical properties of spin-coated polyethylene films developed for integrated photonics applications," Optical Materials Express **12**, 2168 (2022).
229. M. David, C. D. Ismail, D. Nazzari, E. Arigliani, D. Wacht, M. Sistani, H. Detz, G. Ramer, B. Lendl, M. W. Weber, G. Strasser, and B. Hinkov, "Surface Protection and Activation of Mid-IR Plasmonic Waveguides for Spectroscopy of Liquids," Journal of Lightwave Technology (Under review) (2023).
230. R. Pillarisetty, "Academic and industry research progress in germanium nanodevices," Nature **479**, 324–328 (2011).
231. D. Marris-Morini, V. Vakarin, J. M. Ramirez, Q. Liu, A. Ballabio, J. Frigerio, M. Montesinos, C. Alonso-Ramos, X. L. Roux, S. Serna, D. Benedikovic, D. Chrastina, L. Vivien, and G. Isella, "Germanium-based integrated photonics from near- to mid-infrared applications," Nanophotonics **7**, 1781–1793 (2018).
232. M. P. Fischer, A. Riede, K. Gallacher, J. Frigerio, G. Pellegrini, M. Ortolani, D. J. Paul, G. Isella, A. Leitenstorfer, P. Biagioni, and D. Brida, "Plasmonic mid-infrared third harmonic generation in germanium nanoantennas," Light Sci Appl **7**, 106 (2018).
233. L. Baldassarre, E. Sakat, J. Frigerio, A. Samarelli, K. Gallacher, E. Calandrini, G. Isella, D. J. Paul, M. Ortolani, and P. Biagioni, "Midinfrared Plasmon-Enhanced Spectroscopy with Germanium Antennas on Silicon Substrates," Nano Lett. **15**, 7225–7231 (2015).
234. T. Amotchkina, M. Trubetskov, D. Hahner, and V. Pervak, "Characterization of e-beam evaporated Ge, YbF_3, ZnS, and LaF_3 thin films for laser-oriented coatings," Appl. Opt., AO **59**, A40–A47 (2020).
235. A. Schwaighofer, M. Brandstetter, and B. Lendl, "Quantum cascade lasers (QCLs) in biomedical spectroscopy," Chem. Soc. Rev. **46**, 5903–5924 (2017).
236. D. I. Ellis and R. Goodacre, "Metabolic fingerprinting in disease diagnosis: biomedical applications of infrared and Raman spectroscopy," Analyst **131**, 875 (2006).
237. J. W. Cleary, W. H. Streyer, N. Nader, S. Vangala, I. Avrutsky, B. Claflin, J. Hendrickson, D. Wasserman, R. E. Peale, W. Buchwald, and R. Soref, "Platinum germanides for mid- and long-wave infrared plasmonics," Opt. Express, OE **23**, 3316–3326 (2015).
238. R. Soref, R. E. Peale, and W. Buchwald, "Longwave plasmonics on doped silicon and silicides," Opt. Express, OE **16**, 6507–6514 (2008).
239. W. W. Harvey and H. C. Gatos, "The Reaction of Germanium with Aqueous Solutions," JOURNAL OF THE ELECTROCHEMICAL SOCIETY **105**, (1958).

240. Q. Duan, Y. Liu, S. Chang, H. Chen, and J. Chen, "Surface Plasmonic Sensors: Sensing Mechanism and Recent Applications," Sensors **21**, 5262 (2021).
241. J. Divya, S. Selvendran, A. S. Raja, and A. Sivasubramanian, "Surface plasmon based plasmonic sensors: A review on their past, present and future," Biosensors and Bioelectronics: X **11**, 100175 (2022).
242. M. Nayak, S. Ezhilvalavan, and T. Y. Tseng, "Chapter 2 - High-Permittivity (Ba, Sr)TiO3 thin films," in *Handbook of Thin Films, Five-Volume Set* (Elsevier Inc, 2002), pp. 99–167.
243. O. Bethge, S. Abermann, C. Henkel, C. J. Straif, H. Hutter, and E. Bertagnolli, "Impact of Germanium Surface Conditioning and ALD-growth Temperature on Al2O3 / ZrO2 High-k Dielectric Stacks," J. Electrochem. Soc. **156**, G168 (2009).
244. A. Dabrowska, M. David, S. Freitag, A. M. Andrews, G. Strasser, B. Hinkov, A. Schwaighofer, and B. Lendl, "Broadband laser-based mid-infrared spectroscopy employing a quantum cascade detector for milk protein analysis," Sensors and Actuators B: Chemical **350**, 130873 (2022).
245. A. Schwaighofer, C. K. Akhgar, and B. Lendl, "Broadband laser-based mid-IR spectroscopy for analysis of proteins and monitoring of enzyme activity," Spectrochimica Acta Part A: Molecular and Biomolecular Spectroscopy **253**, 119563 (2021).
246. A. Barth, "Infrared spectroscopy of proteins," Biochimica et Biophysica Acta (BBA) - Bioenergetics **1767**, 1073–1101 (2007).
247. N. Wu, Q. Zhang, C. Zhu, D. S. H. Chan, M. F. Li, N. Balasubramanian, A. Chin, and D.-L. Kwong, "Alternative surface passivation on germanium for metal-oxide-semiconductor applications with high-k gate dielectric," Applied Physics Letters **85**, 4127–4129 (2004).
248. E. P. Gusev, H. Shang, M. Copel, M. Gribelyuk, C. D'Emic, P. Kozlowski, and T. Zabel, "Microstructure and thermal stability of HfO2 gate dielectric deposited on Ge(100)," Applied Physics Letters **85**, 2334–2336 (2004).
249. M. M. Frank, S. J. Koester, M. Copel, J. A. Ott, V. K. Paruchuri, H. Shang, and R. Loesing, "Hafnium oxide gate dielectrics on sulfur-passivated germanium," Applied Physics Letters **89**, 112905 (2006).
250. Q. Xie, S. Deng, M. Schaekers, D. Lin, M. Caymax, A. Delabie, X.-P. Qu, Y.-L. Jiang, D. Deduytsche, and C. Detavernier, "Germanium surface passivation and atomic layer deposition of high-k dielectrics—a tutorial review on Ge-based MOS capacitors," Semicond. Sci. Technol. **27**, 074012 (2012).
251. W. J. H. Berghuis, J. Melskens, B. Macco, R. J. Theeuwes, M. A. Verheijen, and W. M. M. Kessels, "Surface passivation of germanium by atomic layer deposited Al2O3 nanolayers," Journal of Materials Research **36**, 571–581 (2021).
252. W. Gong, "A real time in situ ATR-FTIR spectroscopic study of linear phosphate adsorption on titania surfaces," International Journal of Mineral Processing **63**, 147–165 (2001).
253. F. Hofmann, B. Eversmann, M. Jenkner, A. Frey, M. Merz, T. Birkenmaier, P. Fromherz, M. Schreiter, R. Gabl, K. Plehnert, M. Steinhauser, G. Eckstein, and R. Thewes, "Technology aspects of a CMOS neuro-sensor: back end process and packaging," in *ESSDERC '03. 33rd Conference on European Solid-State Device Research, 2003.* (2003), pp. 167–170.

254. F. Frank, "Development of a micromolar sensitivity dipstick mid-IR ATR sensor for phosphate in water," presented at ICAVS, Krakow, Poland (2021).
255. B. Baumgartner, J. Hayden, A. Schwaighofer, and B. Lendl, "*In Situ* IR Spectroscopy of Mesoporous Silica Films for Monitoring Adsorption Processes and Trace Analysis," ACS Appl. Nano Mater. **1**, 7083–7091 (2018).
256. D. Wacht, M. David, B. Hinkov, H. Detz, A. Schwaighofer, B. Baumgartner, and B. Lendl, "Mesoporous Zirconia Coating for Sensing Applications Using Attenuated Total Reflection Fourier Transform Infrared (ATR FT-IR) Spectroscopy," Appl Spectrosc **76**, 141–149 (2022).
257. L. Han, T. M. Niemczyk, Y. Lu, and G. P. Lopez, "Chemical Sensors Based on Surface-Modified Sol-Gel-Coated Infrared Waveguides," Appl Spectrosc **52**, 119–122 (1998).
258. E. Wijaya, C. Lenaerts, S. Maricot, J. Hastanin, S. Habraken, J.-P. Vilcot, R. Boukherroub, and S. Szunerits, "Surface plasmon resonance-based biosensors: From the development of different SPR structures to novel surface functionalization strategies," Current Opinion in Solid State and Materials Science **15**, 208–224 (2011).
259. K.-J. Kim, P. Lu, J. T. Culp, and P. R. Ohodnicki, "Metal–Organic Framework Thin Film Coated Optical Fiber Sensors: A Novel Waveguide-Based Chemical Sensing Platform," ACS Sens. **3**, 386–394 (2018).
260. N. T. Benéitez, B. Baumgartner, J. Missinne, S. Radosavljevic, D. Wacht, S. Hugger, P. Leszcz, B. Lendl, and G. Roelkens, "Mid-IR sensing platform for trace analysis in aqueous solutions based on a germanium-on-silicon waveguide chip with a mesoporous silica coating for analyte enrichment," Opt. Express, OE **28**, 27013–27027 (2020).
261. A. Taguchi and F. Schüth, "Ordered mesoporous materials in catalysis," Microporous and Mesoporous Materials **77**, 1–45 (2005).
262. A. Bavykina, N. Kolobov, I. S. Khan, J. A. Bau, A. Ramirez, and J. Gascon, "Metal–Organic Frameworks in Heterogeneous Catalysis: Recent Progress, New Trends, and Future Perspectives," Chem. Rev. **120**, 8468–8535 (2020).
263. S. Affatato, G. Bersaglia, I. Foltran, D. Emiliani, F. Traina, and A. Toni, "The influence of implant position on the wear of alumina-on-alumina studied in a hip simulator," Wear **256**, 400–405 (2004).
264. S. Shankar, R. Nithyaprakash, and B. R. Santhosh, "Short term tribological behavior of ceramic and polyethylene biomaterials for hip prosthesis," Materials Testing **63**, 470–473 (2021).
265. A. Tchinda, L. Chézeau, G. Pierson, R. Kouitat-Njiwa, B. H. Rihn, and P. Bravetti, "Biocompatibility of ZrO2 vs. Y-TZP Alloys: Influence of Their Composition and Surface Topography," Materials **15**, 4655 (2022).
266. J. Nawrocki, M. Rigney, A. McCormick, and P. W. Carr, "Chemistry of zirconia and its use in chromatography," Journal of Chromatography A **657**, 229–282 (1993).
267. D. Wacht, "Development of a mesoporous ZrO2-coating for sensing applications using ATR-FTIR spectroscopy," (n.d.).
268. S. Sinzinger and J. Jahns, *Microoptics*, 2nd rev. and enlarged ed (Wiley-VCH, 2003).
269. J. Kischkat, S. Peters, B. Gruska, M. Semtsiv, M. Chashnikova, M. Klinkmüller, O. Fedosenko, S. Machulik, A. Aleksandrova, G. Monastyrskyi, Y. Flores, and W. T. Masselink, "Mid-infrared optical properties of thin films of aluminum oxide, titanium

dioxide, silicon dioxide, aluminum nitride, and silicon nitride," Appl. Opt., AO **51**, 6789–6798 (2012).

270. J.-P. Tetienne, A. Bousseksou, D. Costantini, R. Colombelli, A. Babuty, I. Moldovan-Doyen, Y. De Wilde, C. Sirtori, G. Beaudoin, L. Largeau, O. Mauguin, and I. Sagnes, "Injection of midinfrared surface plasmon polaritons with an integrated device," Applied Physics Letters **97**, 211110 (2010).
271. B. Hinkov, F. Pilat, L. Lux, P. L. Souza, M. David, A. Schwaighofer, D. Ristanić, B. Schwarz, H. Detz, A. M. Andrews, B. Lendl, and G. Strasser, "A mid-infrared lab-on-a-chip for dynamic reaction monitoring," Nat Commun **13**, 4753 (2022).
272. P. R. West, S. Ishii, G. V. Naik, N. K. Emani, V. M. Shalaev, and A. Boltasseva, "Searching for better plasmonic materials," Laser & Photonics Reviews **4**, 795–808 (2010).
273. M. A. Ordal, R. J. Bell, R. W. Alexander, L. L. Long, and M. R. Querry, "Optical properties of Au, Ni, and Pb at submillimeter wavelengths," Appl. Opt. **26**, 744 (1987).
274. A. D. Rakić, A. B. Djurišić, J. M. Elazar, and M. L. Majewski, "Optical properties of metallic films for vertical-cavity optoelectronic devices," Appl. Opt. **37**, 5271 (1998).
275. P. Berini, "Long-range surface plasmon-polariton waveguide biosensors for disease detection," in *2015 International Topical Meeting on Microwave Photonics (MWP)* (2015), pp. 1–2.
276. O. Krupin and P. Berini, "Biosensing using long-range surface plasmon-polariton waveguides," in *2012 International Conference on Optical MEMS and Nanophotonics* (2012), pp. 17–18.
277. O. Krupin and P. Berini, "Long-Range Surface Plasmon-Polariton Waveguide Biosensors for Human Cardiac Troponin I Detection," Sensors **19**, 631 (2019).
278. J. Faist, G. Villares, G. Scalari, M. Rösch, C. Bonzon, A. Hugi, and M. Beck, "Quantum Cascade Laser Frequency Combs," Nanophotonics **5**, 272–291 (2016).
279. J. Piotrowski, A. Prokopiuk, W. Gawron, J. Mikołajczyk, Z. Bielecki, M. Bugajski, J. Wojtas, and D. Szabra, "Analysis of Free-Space Optics Development," Metrology and Measurement Systems; 2017; vol. 24; No 4; 653–674 (2017).
280. M. S. Vitiello, G. Scalari, B. Williams, and P. D. Natale, "Quantum cascade lasers: 20 years of challenges," Opt. Express, OE **23**, 5167–5182 (2015).
281. A. Delga, "8 - Quantum cascade detectors: A review," in *Mid-Infrared Optoelectronics*, E. Tournié and L. Cerutti, eds., Woodhead Publishing Series in Electronic and Optical Materials (Woodhead Publishing, 2020), pp. 337–377.
282. G. Marschick, M. David, E. Arigliani, N. Opačak, B. Schwarz, M. Giparakis, A. Delga, M. Lagree, T. Poletti, V. Trinite, A. Evirgen, B. Gerard, G. Ramer, R. Maulini, J. Butet, S. Blaser, A. M. Andrews, G. Strasser, and B. Hinkov, "High-responsivity operation of quantum cascade detectors at 9 µm," Opt. Express, OE **30**, 40188–40195 (2022).
283. B. Hinkov, A. Hugi, M. Beck, and J. Faist, "Rf-modulation of mid-infrared distributed feedback quantum cascade lasers," Opt. Express **24**, 3294 (2016).
284. H. Dely, T. Bonazzi, O. Spitz, E. Rodriguez, D. Gacemi, Y. Todorov, K. Pantzas, G. Beaudoin, I. Sagnes, L. Li, A. G. Davies, E. H. Linfield, F. Grillot, A. Vasanelli, and C. Sirtori, "10 Gbit s−1 Free Space Data Transmission at 9 µm Wavelength With Unipolar Quantum Optoelectronics," Laser & Photonics Reviews **16**, 2100414 (2022).
285. D. Palaferri, Y. Todorov, A. Bigioli, A. Mottaghizadeh, D. Gacemi, A. Calabrese, A. Vasanelli, L. Li, A. G. Davies, E. H. Linfield, F. Kapsalidis, M. Beck, J. Faist, and C.

Sirtori, "Room-temperature nine-µm-wavelength photodetectors and GHz-frequency heterodyne receivers," Nature **556**, 85–88 (2018).

286. M. David, G. Marschick, E. Arigliani, N. Opacak, B. Schwarz, G. Strasser, and B. Hinkov, "Towards Fully Integrated Mid-Infrared Heterodyne Detection Based on Quantum Cascade Technology," in *2022 European Conference on Optical Communication (ECOC)* (2022), pp. 1–3.

LIST OF PUBLICATIONS

Peer Reviewed Journal Publications

1. **M. David**, D. Disnan, E. Arigliani, A. Lardschneider, G. Marschick, H. Hoang, H. Detz, B. Lendl, U. Schmid, G. Strasser, and B. Hinkov, "Advanced Mid-Infrared Plasmonic Waveguides based on Polymers for On-chip Integrated Photonics," *Photonics Research*, Jul. 2023. doi:10.1364/PRJ.495729.

2. B. Hinkov, **M. David**, G. Strasser, B. Schwarz, and B. Lendl, "On-chip liquid sensing using mid-IR plasmonics," *Frontiers in Photonics*, vol.4, 2023. Doi: 10.3389/fphot.2023.1213434.

3. **M. David**, C. D. Ismail, D. Nazzari, E. Arigliani, D. Wacht, M. Sistani, H. Detz, G. Ramer, B. Lendl, M. W. Weber, G. Strasser, and B. Hinkov, "Surface Protection and Activation of Mid-IR Plasmonic Waveguides for Spectroscopy of Liquids," *Journal of Lightwave Technology (Under review)*, Jan. 2023.

4. G. Marschick, **M. David**, E. Arigliani, N. Opačak, B. Schwarz, M. Giparakis, A. Delga, M. Lagree, T. Poletti, V. Trinite, A. Evirgen, B. Gerard, G. Ramer, R. Maulini, J. Butet, S. Blaser, A. M. Andrews, G. Strasser, and B. Hinkov, "High-responsivity operation of quantum cascade detectors at 9 µm," *Opt. Express*, vol.30, no. 22, p.40188, Oct. 2022. doi:10.1364/OE.470615.

5. D. Wacht, **M. David**, B. Hinkov, H. Detz, A. Schwaighofer, B. Baumgartner, and B. Lendl, "Mesoporous Zirconia Coating for Sensing Applications Using Attenuated

Total Reflection Fourier Transform Infrared (ATR FT-IR) Spectroscopy," *Appl Spectrosc*, vol.76, no. 1, pp.141–149, Jan. 2022. doi:10.1177/00037028211057156.

6. B. Hinkov, F. Pilat, L. Lux, P. L. Souza, **M. David**, A. Schwaighofer, D. Ristanić, B. Schwarz, H. Detz, A. M. Andrews, B. Lendl, and G. Strasser, "A mid-infrared lab-on-a-chip for dynamic reaction monitoring," *Nat Commun*, vol.13, no. 1, p.4753, Aug. 2022. doi:10.1038/s41467-022-32417-7.

7. **M. David**, D. Disnan, A. Lardschneider, D. Wacht, H. T. Hoang, G. Ramer, H. Detz, B. Lendl, U. Schmid, G. Strasser, and B. Hinkov, "Structure and mid-infrared optical properties of spin-coated polyethylene films developed for integrated photonics applications," *Opt. Mater. Express*, vol.12, no. 6, p.2168, Jun. 2022. doi:10.1364/OME.458667.

8. **M. David**, A. Dabrowska, M. Sistani, I. C. Doganlar, E. Hinkelmann, H. Detz, W. M. Weber, B. Lendl, G. Strasser, and B. Hinkov, "Octave-spanning low-loss mid-IR waveguides based on semiconductor-loaded plasmonics," *Opt. Express*, vol.29, no. 26, p.43567, Dec. 2021. doi:10.1364/OE.443966.

9. A. Dabrowska, **M. David**, S. Freitag, A. M. Andrews, G. Strasser, B. Hinkov, A. Schwaighofer, and B. Lendl, "Broadband laser-based mid-infrared spectroscopy employing a quantum cascade detector for milk protein analysis," *Sensors and Actuators B: Chemical*, vol.350, p.130873, Jan. 2022. doi:10.1016/j.snb.2021.130873.

10. **M. David** and G. Schmid, "Dosimetric analysis of hands exposure during handling of strong permanent magnets," *J. Radiol. Prot.*, vol.40, no. 2, pp.520–529, Jun. 2020. doi:10.1088/1361-6498/ab6b9b.

Invited Oral Presentations

1. B. Hinkov, F. Pilat, **M. David**, A. Schwaighofer, P. L. Souza, E. Arigliani, G. Marschick, I. C. Doganlar, L. Lux, D. Ristanic, A. Dabrowska, D. Wacht, M. Sistani, D. Disnan, H. Detz, A. M. Andrews, B. Schwarz, U. Schmid, W. M. Weber, B. Lendl,

and G. Strasser, “A mid-infrared lab-on-a-chip for dynamic reaction monitoring”, *Optica Sensing Congress,* Munich, Germany, 31. July – 03. Aug., 2023.

2. B. Hinkov, F. Pilat, **M. David**, A. Schwaighofer, P. L. Souza, E. Arigliani, G. Marschick, I. C. Doganlar, L. Lux, D. Ristanic, A. Dabrowska, D. Wacht, M. Sistani, D. Disnan, H. Detz, A. M. Andrews, B. Schwarz, U. Schmid, W. M. Weber, B. Lendl, and G. Strasser, “Monitoring liquid dynamics on the chip-scale”, *Seminar ISOM, Universidad Politécnica de Madrid*, Madrid, Spain, Dec 16, 2022.

3. B. Hinkov, F. Pilat, **M. David**, A. Schwaighofer, P. L. Souza, E. Arigliani, G. Marschick, I. C. Doganlar, L. Lux, D. Ristanic, A. Dabrowska, D. Wacht, M. Sistani, D. Disnan, H. Detz, A. M. Andrews, B. Schwarz, U. Schmid, W. M. Weber, B. Lendl, and G. Strasser, “Mid-IR photonic integration concepts: realizing tailored lab-on-a-chip sensors for monitoring of liquids”, *Ipswich Research Centre Workshop on Mid-IR Devices & Technologies*, Cambridge, UK, Nov 24–25, 2022.

4. B. Hinkov, **M. David**, G. Marschick, E. Arigliani, F. Pilat, P. Lustoza Souza, H. Knötig,
   I. C. Doganlar, A. Lardschneider, N. Brandacher, D. Koukola, A. Schwaighofer, B. Lendl, and G. Strasser, „Mid-IR photonic integrated circuits for on-chip applications in liquid sensing and telecom“, *PASSEPARTOUT & OPTAPHI joint Workshop,* Wien, Austria, April 21., 2022.

5. B. Hinkov, **M. David**, F. Pilat, L. Lux, P. Lustoza Souza, A. Schwaighofer, B. Schwarz, H. Detz, A. M. Andrews, B. Lendl, and G. Strasser, „ Next generation of liquid spectroscopy: a monolithic sensor for protein denaturation “, *3rd IR Sessions by LC Week,* online workshop*, December 8., 2021.

6. B. Hinkov, F. Pilat, **M. David**, L. Lux, P. Lustoza Souza A. Schwaighofer, B. Schwarz, H. Detz, A. M. Andrews, B. Lendl, and G. Strasser, „Liquid sensing 2.0: a monolithic mid-IR lab-on-a-chip for measuring protein denaturation and beyond“, Workshop *Procad Defesa (Sao Paulo),* online workshop*, November 25., 2021.

7. B. Hinkov, **M. David**, F. Pilat, L. Lux, P. Lustoza Souza A. Schwaighofer, B. Schwarz, H. Detz, A. M. Andrews, B. Lendl, and G. Strasser, „Mid-IR plasmonics for next generation liquid sensing“, *10th SciX conference (47th Federation of Analytical*

Chemistry & Spectroscopy Societies (FACSS) conference), Providence (Rhode Island), USA, Sept. 26. – Oct. 01., 2021.

Oral Presentations

1. B. Hinkov, A. Dabrowska, **M. David**, A. Schwaighofer, S. Freitag, A. M. Andrews, G. Strasser, and B. Lendl, „Broadband mid-infrared milk protein analysis based on quantum cascade technology", *Quantum Sensing and Nano Electronics and Photonics XIX (Photonics West)*, San Francisco, USA, 31. January – 02. February, 2023.

2. E. Arigliani, **M. David**, E. Hinkelmann, H. Knötig, V. Butera, A. Konecny, F. Pilat, B. Schwarz, G. Strasser, H. Detz, and B. Hinkov, „A novel miniaturized mid-IR sensor for glucose detection using on-chip plasmonics and quantum cascade detectors", *Oxide-based Materials and Devices XIV (Photonics West)*, San Francisco, USA, 31. January – 02. February, 2023.

3. **M. David**, G. Marschick, E. Arigliani, N. Opacak, B. Schwarz, G. Strasser, and B. Hinkov, „Merging mid-IR QC technology with plasmonic interconnects: a monolithically integrated mid-infrared heterodyne receiver", *Integrated Optics: Devices, Materials, and Technologies XXVII (Photonics West)*, San Francisco, USA, 31. January – 02. February, 2023.

4. G. Marschick, **M. David**, A. Delga, N. Opacak, B. Schwarz, M. Lagree, T. Poletti, A. Evirgen, B. P. Gerard, G. Strasser, and B. Hinkov, "Quantum cascade detectors: A 9-µm device optimized for low-attenuation free-space optical communication," Novel In-Plane Semiconductor Lasers XXI, vol.PC12021, p.PC120210K, Mar. 2022.

5. **M. David**, I. C. Doganlar, D. Nazzari, M. Sistani, H. Detz, W. M. Weber, G. Strasser, and B. Hinkov, „Functionalization of mid-IR plasmonic waveguides for novel lab-on-a-chip biosensors", *71st Annual Meeting of the Austrian Physical Society (ÖPG) 2022*, Leoben, Austria, Sept 26 – 30, 2022.

6. B. Hinkov, F. Pilat, **M. David**, A. Schwaighofer, P. L. Souza, L. Lux, B. Schwarz, D. Ristanić, H. Detz, A. M. Andrews, B. Lendl, and G. Strasser, „Next generation of

liquid sensing based on monolithic mid-IR sensors for real-time reaction monitoring“, *71st Annual Meeting of the Austrian Physical Society (ÖPG) 2022*, Leoben, Austria, Sept 26 – 30, 2022.

7. E. Arigliani, **M. David**, A. Lardschneider, G. Marschick, D. Disnan, H. T. Hoang, H. Detz, B. Lendl, U. Schmid, G. Strasser, and B. Hinkov, „Low-loss polyethylene-based plasmonics for mid-infrared photonic integrated circuits”, *71st Annual Meeting of the Austrian Physical Society (ÖPG) 2022*, Leoben, Austria, Sept 26 – 30, 2022.

8. **M. David**, G. Marschick, E. Arigliani, N. Opacak, B. Schwarz, G. Strasser, and B. Hinkov, „Towards Fully Integrated Mid-Infrared Heterodyne Detection Based on Quantum Cascade Technology“, 48*th European Conf. on Optical Communication (ECOC)*, Basel, Switzerland, 18 – 22 Sept., 2022.

9. B. Hinkov, F. Pilat, **M. David**, A. Schwaighofer, P. L. Souza, L. Lux, B. Baumgartner, D. Ristanić, B. Schwarz, H. Detz, A. M. Andrews, B. Lendl, and G. Strasser, „Mid-IR Plasmonics for Monolithic Photonic Integrated Circuits“, 48*th European Conference on Optical Communication (ECOC)*, Basel, Switzerland, 18 – 22 Sept., 2022.

10. G. Marschick, E. Arigliani, **M. David**, N. Opacak, B. Schwarz, A. Delga, T. Poletti, M. Lagree, V. Trinité, A. Evirgen, B. Gerard, M. Giparakis, G. Ramer, J. Butet, R. Maulini, S. Blaser, A. M. Andrews, G. Strasser, and B. Hinkov, , „High performance quantum cascade detectors for long-wave infrared detection”, 10*th International Quantum Cascade Laser School & Workshop*, ETH Zürich & Monte Verità, Switzerland, 23 – 28 Aug., 2022.

11. **M. David**, G. Marschick, N. Opacak, E. Arigliani, A. Dabrowska, A. Schwaighofer, B. Lendl, B. Schwarz, G. Strasser, and B. Hinkov, „Broadband mid-infrared spectroscopy employing quantum cascade optoelectronics and integrated plasmonic“, 10*th International Quantum Cascade Laser School & Workshop*, ETH Zürich & Monte Verità, Switzerland, 23 – 28 Aug., 2022.

12. B. Hinkov, F. Pilat, L. Lux, P. Lustoza Souza, **M. David**, A. Schwaighofer, B. Baumgartner, D. Ristanić, B. Schwarz, H. Detz, A. M. Andrews, B. Lendl, and G. Strasser, „A Monolithic Lab-on-a-Chip for Real Time Liquid Spectroscopy“, *OPTICA Optical Sensors and Sensing Congress*, Vancouver (British Columbia), Canada, July

11. – 15., 2022.

13. E. Arigliani, **M. David**, A. Lardschneider, G. Marschick, D. Disnan, H. T. Hoang, H. Detz, B. Lendl, U. Schmid, G. Strasser and B. Hinkov, „ Loss compensation in novel Polyethylene-metal plasmonics for Mid-Infrared photonic integration“, *8th PLASMONICA Workshop*, Turin, Italy, 7 – 8 July, 2022.

14. B. Hinkov, G. Marschick, F. Pilat, **M. David**, A. Schwaighofer, P. L. Souza, B. Schwarz, D. Ristanić, L. Lux, H. Detz, A. M. Andrews, B. Lendl, and G. Strasser, „Real-time reaction monitoring of liquids on the chip-scale“, *19th International Conference on Nanoscience and Nanotechnologies (Nanotexnology)*, Thessaloniki, Greece, 5 – 8 July, 2022.

15. **M. David**, M. Sistani, F. Frank, I. C. Doganlar, D. Nazzari, A. Dabrowska, G. Marschick, E. Arigliani, H. Detz, B. Lendl, W. M. Weber, G. Strasser and B. Hinkov, „Surface-enhancement of ultra-broadband mid-IR plasmonic waveguides for liquid spectroscopy applications“, *3rd School of Plasmonics and Nano-Optics*, Turin, Italy, 4 – 6 July, 2022.

16. G. Marschick, E. Arigliani, **M. David**, N. Opacak, B. Schwarz, A. Delga, T. Poletti, M. Lagree, V. Trinité, A. Evirgen, B. Gerard, M. Giparakis, G. Ramer, J. Butet, R. Maulini, S. Blaser, A. M. Andrews, G. Strasser and B. Hinkov, „High performance quantum cascade detectors for long-wave infrared detection”, *19th International Conference on Nanoscience and Nanotechnologies (Nanotexnology)*, Thessaloniki, Greece, 5 – 8 July, 2022.

17. B. Hinkov, F. Pilat, **M. David**, G. Marschick, E. Arigliani, P. Lustoza Souza, A. Schwaighofer, L. Lux, B. Baumgartner, D. Ristanić, B. Schwarz, H. Detz, A. M. Andrews, B. Lendl, and G. Strasser, „(Postdeadline) Real-time reaction monitoring of liquids based on monolithic mid-IR sensors“, *Conference on Lasers and Electro-Optics (CLEO)*, San José, USA, May 15 – 20, 2022.

18. B. Hinkov, F. Pilat, L. Lux, P. L. Souza, A. Schwaighofer, B. Schwarz, H. Detz, A. M. Andrews, B. Baumgartner, B. Lendl, G. Strasser, and **M. David**, “Mid-infrared lab-on-a-chip for protein sensing in real-time,” Novel In-Plane Semiconductor Lasers XXI, vol.PC12021, p.PC120210M, Mar. 2022.

19. **M. David**, A. Dabrowska, M. Sistani, E. Hinkelmann, I. C. Doganlar, H. Detz, W. M. Weber, B. Lendl, G. Strasser and B. Hinkov, „Octave-spanning long-range plasmonic waveguide based on semiconductor-loading for mid-infrared monolithic sensors", *Novel In-Plane Semiconductor Lasers XXI (Photonics West)*, San Francisco, USA, 9th March 2022, https://doi.org/10.1117/12.2610311

20. G. Marschick, **M. David**, A. Delga, N. Opacak, B. Schwarz, M. Lagree, T. Poletti, A. Evirgen, B. Gerard, G. Strasser and B. Hinkov, „Quantum cascade detectors: a novel 9 µm device optimized for low-attenuation free-space optical communication", *Novel In-Plane Semiconductor Lasers XXI (Photonics West)*, San Francisco, USA, 9th March 2022, https://doi.org/10.1117/12.2609902

21. **M. David**, A. Dabrowska, M. Sistani, E. Hinkelmann, I. C. Doganlar, H. Detz, W. M. Weber, B. Lendl, G. Strasser, B. Hinkov, „Hybrid semiconductor-metal plasmonic waveguide for on-chip sensors in the longwave infrared", *Joint Annual Meeting of the Swiss Physical Society (SPS) and Austrian Physical Society (ÖPG) 2021*, Innsbruck, Austria, Aug 30 – Sept 03, 2021.

22. G. Marschick, **M. David**, S. Isceri, A. Delga, N. Opacak, B. Schwarz, M. Lagree, T. Poletti, A. Evirgen, B. Gerard, A. M. Andrews, G. Strasser, B. Hinkov, „Novel quantum cascade detectors (QCD) for telecommunication applications between 9 – 10 µm wavelength", *Joint Annual Meeting of the Swiss Physical Society (SPS) and Austrian Physical Society (ÖPG) 2021*, Innsbruck, Austria, Aug 30 – Sept 03, 2021.

23. G. Marschick, **M. David**, A. Delga, N. Opacak, B. Schwarz, M. Lagree, T. Poletti, A. Evirgen, B. Gerard, G. Strasser, B. Hinkov, „A novel quantum cascade detector (QCD) for low attenuation free-space telecommunication around 9 µm wavelength", *15th International Conference on Mid-Infrared Optoelectronic Materials and Devices (MIOMD) 2021*, virtual (formerly planned in Surrey, UK), Sept 01 – 03, 2021.

24. ***M. David**, A. Dabrowska, M. Sistani, E. Hinkelmann, I. C. Doganlar, H. Detz, W. M. Weber, B. Lendl, G. Strasser and B. Hinkov, „LWIR dielectric-loaded surface-plasmon-polariton waveguide for optical sensing", *15th Int. Conference on Mid-Infrared Optoelectronic Materials & Devices (MIOMD) 2021*, virtual (formerly planned in Surrey, UK), Sept 01 – 03, 2021.

*best presentation award

25. A. Dabrowska, **M. David**, A. Schwaighofer, S. Freitag, A. M. Andrews, G. Strasser, B. Hinkov, and B. Lendl, "Broadband Mid-Infrared Spectroscopy employing a Quantum Cascade Laser and a Quantum Cascade Detector for Milk Protein Analysis," 2021 , Providence, Rhode Island, USA, International.

26. A. Dabrowska, **M. David**, A. Schwaighofer, S. Freitag, B. Hinkov, A. Harrer, G. Strasser, and B. Lendl, "Broadband laser-based mid-infrared spectroscopy employing a quantum cascade detector for protein analysis in aqueous solution," 2021.

27. A. Dabrowska, **M. David**, A. Schwaighofer, S. Freitag, A. M. Andrews, G. Strasser, B. Hinkov and B. Lendl „Broadband Mid-Infrared Sensor employing a Quantum Cascade Laser and Quantum Cascade Detector for Milk Protein Analysis", *11th International Conference on Advanced Vibrational Spectroscopy (ICAVS)*, virtual (formerly planned in Krakow, Poland), August 23 - 26, 2021.

28. **M. David**, A. Dabrowska, M. Sistani, E. Hinkelmann, I. C. Doganlar, B. Schwarz, H. Detz, W. M. Weber, B. Lendl, G. Strasser, and B. Hinkov, „Germanium-based dielectric loaded plasmonic waveguides for the long-wave infrared spectral range", *Compound Semiconductor Week (CSW) – (Joint 47th International Symposium on Compound Semiconductors (ISCS) and 32nd International Conference on Indium Phosphide and Related Materials (IPRM))*, online conference* (formerly planned in Stockholm, Sweden), May 9 – 13, 2021.

29. A. Dabrowska, **M. David**, A. Schwaighofer, B. Hinkov, A. Harrer, G. Strasser and B. Lendl „Towards Broadband Mid-Infrared Fully Integrated Protein Sensor employing a Quantum Cascade Laser and Quantum Cascade Detector", *Conference on Lasers and Electro-Optics/Europe (CLEO/Europe) and European Quantum Electronics Conference (EQEC)*, online conference* (formerly planned in Munich, Germany), May 20 – 24, 2021.

Poster Presentations

1. E. Arigliani, **M. David**, A. Lardschneider, D. Disnan, G. Marschick, H. T. Hoang, D. Wacht, G. Ramer, H. Detz, B. Lendl, U. Schmid, G. Strasser, B. Schwarz and B.

Hinkov, „Low loss polyethylene-loaded plasmonic waveguides for mid-infrared photonic integrated circuits“, International Nano-Optoelectronics Workshop (iNOW), Würzburg, Germany, 16 – 27 July, 2023.

2. **M. David**, E. Arigliani, A. Dabrowska, A. Lardschneider, M. Sistani, D. Nazzari, D. Disnan, I. C. Doganlar, H. T. Hoang, G. Marschick, H. Detz, U. Schmid, B. Lendl, W. M. Weber, G. Strasser, and B. Hinkov, „Low loss mid-infrared plasmonic waveguides: extending the limits of noble metals”, *2022 MRS Fall Meeting & Exhibit*, Boston, Massachusetts, USA, Nov 27 – Dec 02, 2022.

3. B. Hinkov, F. Pilat, **M. David**, A. Schwaighofer, P. L. Souza, B. Schwarz, D. Ristanić, E. Arigliani, L. Lux, D. Wacht, F. Frank, H. Detz, A. M. Andrews, B. Lendl, and G. Strasser, „A surface-plasmon enhanced mid-infrared lab-on-a-chip for real-time reaction monitoring of liquids“, *2022 MRS Fall Meeting & Exhibit*, Boston, Massachusetts, USA, Nov 27 – Dec 02, 2022.

4. N. Brandacher, E. Arigliani, **M. David**, G. Marschick, D. Koukola, G. Strasser, and B. Hinkov, „Fiber-coupled mid-IR plasmonic sensors for chemical analysis of liquids”, *71st Annual Meeting of the Austrian Physical Society (ÖPG) 2022*, Leoben, Austria, Sept 26 – 30, 2022.

5. D. Koukola, G. Marschick, **M. David**, E. Arigliani, A. Dabrowska, B. Lendl, G. Strasser,and B. Hinkov, „New material systems for mid-IR photonic integrated circuits”, *71st Annual Meeting of the Austrian Physical Society (ÖPG) 2022*, Leoben, Austria, Sept 26 – 30, 2022.

6. B. Hinkov, F. Pilat, **M. David**, P. L. Souza, A. Schwaighofer, L. Lux, B. Schwarz, D. Ristanić, H. Detz, A. M. Andrews, B. Lendl, and G. Strasser, „Lab-on-a-chip for real-time reaction monitoring of liquids“, 10th *International Quantum Cascade Laser School & Workshop*, ETH Zürich & Monte Verità, Switzerland, 23 – 28 Aug., 2022.

7. *E. Arigliani, **M. David**, A. Lardschneider, D. Disnan, G. Marschick, H. T. Hoang, D. Wacht, G. Ramer, H. Detz, B. Lendl, U. Schmid, G. Strasser and B. Hinkov, „Polyethylene-loaded plasmonic waveguides for mid-infrared photonic integrated circuits“, 10th *International Quantum Cascade Laser School & Workshop*, ETH Zürich

& Monte Verità, Switzerland, 23 – 28 Aug., 2022.
*3rd best paper award

8. B. Hinkov, F. Pilat, **M. David**, A. Schwaighofer, P. L. Souza, B. Schwarz, D. Ristanić, E. Arigliani, L. Lux, H. Detz, A. M. Andrews, B. Lendl, and G. Strasser, „A mid-infrared lab-on-a-chip for real-time reaction monitoring of liquids“, *3rd School of Plasmonics and Nano-Optics & 8th PLASMONICA Workshop*, Turin, Italy, 4 – 8 July, 2022.

9. H. T. Hoang, **M. David**, D. Disnan, I. C. Doganlar, H. Detz, U. Schmid, G. Strasser, B. Hinkov, „Modelling, fabrication and characterization of low-density polyethylene based plasmonic waveguides for mid-IR photonic networks”, *Joint Annual Meeting of the Swiss Physical Society (SPS) and Austrian Physical Society (ÖPG) 2021*, Innsbruck, Austria, Aug 30 – Sept 03, 2021.

10. I. C. Doganlar, **M. David**, M. Sistani, D. Nazzari, H. Detz, A. Lugstein, W. M. Weber, G. Strasser, B. Hinkov, „Material Analysis for Mid-IR Dielectric Loaded Plasmonic Waveguides and Their Application in Chemical Sensing”, *Joint Annual Meeting of the Swiss Physical Society (SPS) and Austrian Physical Society (ÖPG) 2021*, Innsbruck, Austria, Aug 30 – Sept 03, 2021.

11. **M. David**, A. Dabrowska, M. Sistani, E. Hinkelmann, I. C. Doganlar, B. Schwarz, H. Detz, W. M. Weber, B. Lendl, G. Strasser and B. Hinkov, „Towards long-wave infrared lab-on-chip sensors using plasmonic and quantum cascade technology”, *11th International Conference on Advanced Vibrational Spectroscopy (ICAVS)*, virtual (formerly planned in Krakow, Poland), August 23 - 26, 2021.

12. F. Frank, B. Baumgartner, **M. David**, C. I. Doganlar, G. Strasser, B. Hinkov, G. Ramer and B. Lendl, „Development of a micromolar sensitivity dipstick mid-IR ATR sensor for phosphate in water”, *11th International Conference on Advanced Vibrational Spectroscopy (ICAVS)*, virtual (formerly planned in Krakow, Poland), August 23 - 26, 2021.

13. D. Wacht, **M. David**, B. Hinkov and B. Lendl, „A Mesoporous Zirconia Coating for Sensing Applications using ATR-FTIR Spectroscopy”, *11th International Conference*

on Advanced Vibrational Spectroscopy (ICAVS), virtual (planned in Krakow, Poland), August 23 - 26, 2021.

14. **M. David**, A. Dabrowska, M. Sistani, E. Hinkelmann, I. C. Doganlar, B. Schwarz, H. Detz, W. M. Weber, B. Lendl, G. Strasser, and B. Hinkov, „Low loss dielectric loaded plasmonic waveguides for sensing applications above nine microns", *Conference on Lasers and Electro-Optics/Europe (CLEO/Europe) and European Quantum Electronics Conference (EQEC)*, Munich, Germany, May 20 - 24, 2021.

15. **M. David** *et al.*, "High speed and high bandwidth quantum cascade detectors," in *21st International Winterschool New Developments in Solid State Physics*, 2020.

16. *__M. David__ and G. Schmid, Dosimetric analysis of hands exposure during handling of strong permanent magnets. *BioEm 2019*, Montpellier, France, June 23-28, 2019.
*1st place poster award

APPENDIX A: PUBLISHED SCIENTIFIC PAPERS

Peer-Reviewed Scientific Publications of the Thesis:.

1 **David, M.**; Dabrowska, A.; Sistani, M.; Doganlar, I. C.; Hinkelmann, E.; Detz, H.; Weber, W. M.; Lendl, B.; Strasser, G.; Hinkov, B. Octave-Spanning Low-Loss Mid-IR Waveguides Based on Semiconductor-Loaded Plasmonics. Opt. Express 2021, 29 (26), 43567. https://doi.org/10.1364/OE.443966.

Contributions:

- *conceived and designed the study,*
- *device design and simulations*
- *material characterization*
- *device fabrication*
- *characterization setup development*
- *data acquisition*
- *data analysis*
- *manuscript writing*

2 Dabrowska, A.; **David, M.**; Freitag, S.; Andrews, A. M.; Strasser, G.; Hinkov, B.; Schwaighofer, A.; Lendl, B. Broadband Laser-Based Mid-Infrared Spectroscopy Employing a Quantum Cascade Detector for Milk Protein Analysis. Sensors and Actuators B: Chemical 2022, 350, 130873. https://doi.org/10.1016/j.snb.2021.130873.

Contributions:

- *characterization setup development*
- *part of data acquisition*
- *part of the data analysis*

3 **David, M.**; Disnan, D.; Lardschneider, A.; Wacht, D.; Hoang, H. T.; Ramer, G.; Detz, H.; Lendl, B.; Schmid, U.; Strasser, G.; Hinkov, B. Structure and Mid-Infrared

Optical Properties of Spin-Coated Polyethylene Films Developed for Integrated Photonics Applications. Opt. Mater. Express 2022, 12 (6), 2168. https://doi.org/10.1364/OME.458667.

Contributions:

- *conceived and designed the study,*
- *part of film fabrication*
- *material characterization*
- *data analysis and interpretation*
- *manuscript writing*

4 Hinkov, B.; Pilat, F.; Lux, L.; Souza, P. L.; **David, M**.; Schwaighofer, A.; Ristanić, D.; Schwarz, B.; Detz, H.; Andrews, A. M.; Lendl, B.; Strasser, G. A Mid-Infrared Lab-on-a-Chip for Dynamic Reaction Monitoring. Nat Commun 2022, 13 (1), 4753. https://doi.org/10.1038/s41467-022-32417-7.

Contributions:

- *simulations*
- *a minor part of device fabrication*
- *part of interpretation*

5 Marschick, G.; **David, M**.; Arigliani, E.; Opačak, N.; Schwarz, B.; Giparakis, M.; Delga, A.; Lagree, M.; Poletti, T.; Trinite, V.; Evirgen, A.; Gerard, B.; Ramer, G.; Maulini, R.; Butet, J.; Blaser, S.; Andrews, A. M.; Strasser, G.; Hinkov, B. High-Responsivity Operation of Quantum Cascade Detectors at 9 Mm. Opt. Express 2022, 30 (22), 40188. https://doi.org/10.1364/OE.470615.

Contributions:

- *part of the design of the study,*
- *device simulations*
- *part of device fabrication*
- *part of characterization setup development*
- *part of data acquisition*
- *part of interpretation*

6 Wacht, D.; **David, M**.; Hinkov, B.; Detz, H.; Schwaighofer, A.; Baumgartner, B.; Lendl, B. Mesoporous Zirconia Coating for Sensing Applications Using Attenuated Total Reflection Fourier Transform Infrared (ATR FT-IR) Spectroscopy. Appl Spectrosc 2022, 76 (1), 141–149. https://doi.org/10.1177/00037028211057156.

Contributions:

- *part of device fabrication*
- *material characterization*

7 **David, M**.; Ismail, C. D.; Nazzari, D.; Arigliani, E.; Wacht, D.; Sistani, M.; Detz, H.; Ramer, G.; Lendl, B.; Weber, M. W.; Strasser, G.; Hinkov, B. Surface Protection and Activation of Mid-IR Plasmonic Waveguides for Spectroscopy of Liquids. Journal of Lightwave Technology (Under review).

Contributions:

- *conceived and designed the study,*
- *device design and simulations*
- *material characterization*
- *part of device fabrication*
- *characterization setup development*
- *data analysis*
- *part of manuscript writing*

8 **David, M**.; Disnan, D.; Arigliani, E.; Lardschneider, A.; Marschick, G.; Hoang, H. T.; Detz, H.; Lendl, B.; Schmid, U.; Strasser, G.; Hinkov, B. Advanced Mid-Infrared Plasmonic Waveguides For On-Chip Integrated Photonics. arXiv May 5, 2023. https://doi.org/10.48550/arXiv.2305.03586.

Contributions:

- *conceived and designed the study,*
- *device design and simulations*
- *material characterization*
- *part of device fabrication*
- *characterization setup development*
- *data analysis*
- *manuscript writing*

9 Hinkov, B.; **David, M**.; Strasser, G.; Schwarz, B.; Lendl, B.; On-chip liquid sensing using mid-IR plasmonics. Frontiers in Photonics May 5, 2023. https://doi.org/10.48550/arXiv.2305.03586.

Contributions:

- *manuscript writing*

APPENDIX B: CLEAN ROOM TOOLS

The following are the fabrication tools and equipment for the manufacturing of photonic devices presented in this thesis:

- Oxford Instruments PECVD
- Oxford Instruments ICP RIE
- Dektak profilometer
- Suess Microtec MJB4 mask aligner
- Von Ardenne Sputtering system
- J.A. Wollam Alpha-SE Ellipsometer
- J.A. Wollam IR-Vase Ellipsometer
- Microtechnic Scriber S100
- Plasma Etching System (STS 320PC)
- HV/UHV evaporation (Plassys)
- Covac Spinner (for polyethylene films deposition)
- ALD reactor (Savannah, Cambridge NanoTech Inc, USA)

Mauro David

PhD Candidate

Strong background in the research and development of electronic systems, photonic devices, and optical sensors. Naturally investigative, I foster a collaborative mindset and excel in lateral thinking.

Education

2019-2023
PhD, Electrical Engineering
TU Wien

2017-2019
MSc, Biomedical Engineering
(with distinction)
FH Technikum Wien

2013-2017
BSc, Electronic Engineering
Politecnico di Milano

Achievements

- **9 publications in scientific journals**
Citations: 86
h-index: 6 (Google Scholar)
- **52 conference contributions**
- **1st place presentation award at MIOMD 2021**
- **1st place poster award at BioEm 2019**
- **Scholarship for academic excellence at FH Technikum Wien(2018)**

Languages

Italian (C2)
English (C1)
German (B1)

Work experience

2019 - Present
TU Wien - Institute of Solid State Electronics, Vienna, AT

Project Assistant

- Integrated Photonics & Plasmonics
- Material Science & FEM Simulations
- Photonic Devices Fabrication & Characterization
- Experience in working in Eurpean Projects (H2020)
- Training & supervision of students to cleanroom and optical lab work
- Teaching Assistant (Semiconductor Physics)

Jan 2019 - Dec 2019
EURIKOS - Startup, Milano, IT

Chief Technology Officer (CTO)

- Research activities related to Acoustic Energy Harvesting (AEH)
- Design of AEH prototypes
- Project management and feasability studies
- Assisting in the overall technology strategy and vision of the startup

Sep 2018 - Aug 2019
AIT - EMC & Optics Department, Seibersdorf, AT

EMF engineer

- Electromagnetic Fields Exposure Assessment
- Dosimetry & FEM Simulations
- Human body modeling & Image Analysis

Jan 2017 - Jun 2017
TPL Informatica - Milano, IT

Embedded Hardware Engineer

- Sensors System Developer
- AVR Microcontrollers Programming

Sep 2008 - Jun 2013
La Sorgente Music School - Belluno, IT

Musician & Music Teacher

- Guitar and music theory teacher
- Guitarist and composer
- Studio recordings and live audiences